Selective Gas Adsorption on Functionalized Metal Organic Frameworks

A Thesis Submitted in Partial Fulfillment of the Requirements for the Degree of

DOCTOR OF PHILOSOPHY

by

MEDIKONDA. PRUDHVIRAJ

Roll No: 136107025

Department of Chemical Engineering

Indian Institute of Technology Guwahati

Guwahati 781039, INDIA

November, 2022

Department of Chemical Engineering

Indian Institute of Technology Guwahati

Guwahati–781039 (INDIA)

CERTIFICATE

It is certified that the work contained in the thesis entitled **"Selective Gas Adsorption on Functionalized Metal Organic Frameworks"**, by **Medikonda. Prudhviraj** has been carried out under our supervision and that this work has not been submitted elsewhere for a degree.

Prof. Sasidhar Gumma
Professor
Department of Chemical Engineering
Indian Institute of Technology Tirupati
Tirupati 517506, India

Prof. Chivukula V Sastri
Professor
Department of Chemistry
Indian Institute of Technology Guwahati
Guwahati 781039, India

Dedicated to my family

ACKNOWLEDGEMENTS

I would like to take this opportunity to express my utmost gratitude to my supervisors Prof. Sasidhar Gumma and Prof. Chivukula Vasudeva Sastri for their immense guidance during the PhD study. Their guidance and patience throughout the project have been very indispensable for completion of this thesis and I am grateful for all the opportunities that they provided me.

I would like to express my gratitude to doctoral committee chairman Prof. Bishnupada Mandal and doctoral committee members Prof. Mihir Kumar Purkait and Dr. Amit Kumar for their valuable suggestions during my progress review seminars. Their valuable suggestions have really helped me to make necessary improvements towards various stages of my research work.

I must also thank the faculty members of the Department of Chemical Engineering, for their consistent encouragements and supports to me. My sincere thanks to Prof. Anugrah Singh (HOD, Department of Chemical Engineering) and Prof. Ashok Kumar Dasmahapatra (DPPC Secretary, Department of Chemical Engineering) for their assistance on administrative proceedings.

I am extremely thankful to my seniors at the Department of Chemical Engineering Dr. Prashant Mishra, Dr. Debjyoti Sahu, Dr. Satyannarayana Edubilli, and Dr. Abhik Bhattacharjee for their voluble suggestions. Many discussions I have made with them benefited me considerably. Special thanks to my friends and colleagues at the Department of Chemistry, Dr. Sayanta Sekhar Nag and Dr. Gourab Mukherjee who helped me throughout this period.

I would like to thank the Department of Chemical Engineering and Central Instruments Facility, IIT Guwahati for providing the facilities to carry out BET, TGA, and powder XRD analysis.

I express my thanks to the technical staffs of my department Mr. Harsaraj Biswanath, Mr. Pankaj Kumar, Dr. Lukumoni Borah, Mr. Debajit Borah and Mr. Prasun Bhattacharjee for their assistance during characterization of samples. I would like to thank Mr. Deep Jyoti Sinha (Junior Assistant), Mr. Sailen Das (Junior Superintendent) and Mr. Bhagya Boro (Senior Attendant) for their support in various forms.

I would like to thank my lab mates Ramesh Tellagorla, Dr. Pradip Das, Sagar Kokkiligadda, Rajashekar Pilli, Nitun Das, Manik dutta, Mudit Baruai, and Geetanjali Bhati for their support in completing this work. I am also thankful to my friends Mallikarjuana Reddy, Narasimha Rao, Bharat, Sudarshan Konidena, Durga Prasad Kelli, Rambabu, and Hanumanth Reddy for their enriching friendship and support during the course of my stay in IIT Guwahati.

Finally, I would like to express my heartfelt thanks to my beloved parents for their love, affections, support, and blessings. I would also like to acknowledge my brothers Ravikondala Rao and Durga Prasad being my best friends. I will always be thankful to the GOD for having such a wonderful family.

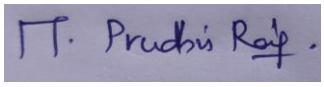

Prudhviraj Medikonda

Guwahati, India

ABSTRACT

This work focuses on to study the effect of functionality on gas adsorption properties of various categories of MOFs *viz.* [{Cu_2(abtc)}$_3$] (functional groups N=N and NH–NH), Cu–BTC (–H, –Br, and –I), and UiO–66 (–H, –NH_2, –NO_2, –COOH, and –$(COOH)_2$). The equilibrium adsorption measurements of gases varying polarity were measured over a wide range of temperature and pressure to understand the role of functionality, pore volume, and presence of accessible metal sites on physical properties of gases.

In the first part of the work, the adsorption characteristics of CO_2, CO, N_2, CH_4, C_2H_6, C_3H_8 and O_2 on Cu–abtc and Cu–hbtc MOFs were evaluated at three different temperatures *viz*. 294, 317, and 356 K and pressures ranging from 0–80 bar. Due to the presence of accessible open metal sites in both frameworks, electrostatic interactions are likely to be present. Thus, CO with significant dipole moment has higher adsorption capacity at lower pressures compared to that of CH_4. However, at higher pressures these metal sites are occupied and adsorption occurs mainly due to dispersion interactions. As a result, the adsorption uptake for CH_4 (which has higher polarizability) is more than that of CO in the high pressure region. This "cross-over" in selectivity between CO and CH_4 occurs at about 4 bar pressure. The adsorption enthalpy for CO_2 is slightly higher on Cu–hbtc compared to that Cu–abtc, indicating grater affinity of the NH–NH bond for the adsorbates. However, in the case of N_2, adsorption enthalpy on Cu–hbtc is only slightly lower compared to that on Cu–abtc. As a result of this behavior, the selectivity of for CO_2 over N_2 will be significantly higher for Cu–hbtc compared to that on Cu–abtc.

In the second part, the role of functionality on adsorption characteristics of well-known Cu–BTC MOF and its derivatives were analyzed. The presence of halo-functional groups *viz.* Cu–(bromo)BTC and Cu–(iodo)BTC and their effect on industrially important gases such as CO_2, CO, CH_4, and N_2 at three different temperatures (294, 317, 356 K) and up to high pressures was studied. Cu–BTC exhibits increased gravimetric uptake capacity (at saturation) for CO_2 (15.4 mol kg^{-1}) followed by Cu–(iodo)BTC (13.2 mol kg^{-1}) and Cu–(bromo)BTC (10.4 mol kg^{-1}). On the other hand, compared on a unit cell basis the uptake capacities increase due to functionalization. This can be readily explained by increased molar mass of the MOFs after addition of functional groups. Similar trends also followed for other gases such as CH_4 and CO as well. Minor variations in the enthalpy of adsorption for various gases were also observed.

In the final part of this work, the effect of functionalization on pure gas adsorption of CO_2, CH_4, CO, and N_2 on a series of functionalized UiO–66 *viz.* UiO–66–NH_2, UiO–66–NO_2, UiO–66–COOH, and UiO–66–$(COOH)_2$ was studied. Among the studied gases, the highest up take capacity observed for CO_2 followed by CH_4, CO, and N_2. For CO_2 adsorption, we observed two distinct effects with respect to organic linker functionalization. At low pressure region, the CO_2 uptake increases by the introduction of polar functional groups and such improvement are more pronounced for functional groups with larger polarity. This kind of consistent behavior observed in previously reported IRMOFs. The main reason is that at pressures up to ~2 bar (low pressure region) larger functional groups in framework provides optimized pore diameter, then CO_2 molecules in the pores were tightly attached, attributing to the interactions between CO_2 molecules and complex functionalized framework play the dominant role. So, at low pressure region the highest adsorption for UiO–66–$(COOH)_2$ followed by UiO–66–COOH, UiO–66–NO_2, UiO–66–NH_2 and UiO–66. At upon substantial increment of increasing pressure up to saturation

(~ 30 bars) levels, the advantage of the polar functional groups becomes less evident and highest uptake capacity was followed with respect to pore volume of the MOF. At 294 K, up to saturation pressure, the highest up take was observed for UiO–66 followed by UiO–66–NH_2, UiO–66–COOH, UiO–66–NO_2, and UiO–66–$(COOH)_2$. The selectivity of CO_2 over N_2 following order UiO–66–$(COOH)_2$>UiO–66–COOH>UiO–66–NH_2>UiO–66>UiO–66–NO_2 at saturation. In CO_2 selectivity over CO, UiO–66–$(COOH)_2$ shows ~2.2 times more selective over unfunctionalized UiO–66. In case of UiO–66–COOH and UiO–66–NH_2 is ~2 fold more selective over UiO–66. Initially, for UiO–66–COOH and UiO–66–NO_2 having more selective over UiO–66, as gradually pressure increases the selectivity is decreased, for UiO–66–$(COOH)_2$ is small increment in selectivity and whereas in UiO–66 and UiO–66–NH_2 does not change appreciably.

CONTENTS

		Page No.
Certificate		
Acknowledgements		
Abstract		i–iii
List of Tables		xi–xii
List of Figures		xiii–xxv
Nomenclature		xxvi–xxix
CHAPTER 1: Introduction		**1–20**
1.1	Overview on adsorption	1
1.2	Adsorbents of Industrial Importance	4
	1.2.1 Important Factors on Sorbent Selection	6
	1.2.2 Novel Adsorbents	7
1.3	Overview on CO_2 Emissions and Importance of CH_4 Storage	9
	1.3.1 Different Pathways of CO_2 Capture and CH_4 Storage	10
1.4	Background of Present Research Work	13
1.5	Research Objectives	14
	References	17
CHAPTER 2: Literature Survey		**21–64**
2.1	Metal Organic Frameworks (MOFs)	21
	2.1.1 Background on MOFs	22

		Page No.
	2.1.2 Design and Synthesis of MOFs	23
2.2	Potential Applications of MOFs	26
	2.2.1 Gases Storage	27
	2.2.2 Gasses Separation	29
2.3	Modification of MOF Structures	31
	2.3.1 Functionalization of MOFs	31
	2.3.2 Post–synthetic Modification of MOF structures	33
2.4	Open metal sites in MOFs	34
2.5	Simulation Studies on MOFs	35
2.6	A Review on Adsorption of the Gases of our Interest	36
	References	45
CHAPTER 3: Theory		**65–75**
3.1	Phase Rule	65
3.2	Equilibrium Adsorption Isotherm	65
3.3	Henry's Constant	66
3.4	Models for Pure Gas Isotherms	66
	3.4.1 Langmuir Isotherm	66
	3.4.2 Dual Site Langmuir (DSL) Isotherm	67
	3.4.3 Virial Isotherm	68
	3.4.4 Langmuir-virial (VL) Isotherm	69
3.5	Enthalpy of Adsorption	70

		Page No.
3.6	Spreading Pressure	71
3.7	Ideal Adsorbed Solution Theory (IAST)	73
	References	75
CHAPTER 4: Experimental		**76–97**
4.1	General Synthesis procedure for MOFs	76
4.2	Synthesis of MOFs Studied	77
	4.2.1 Synthesis of Cu–abtc	77
	4.2.2 Synthesis of Cu–hbtc	78
	4.2.3 Synthesis of Cu–BTC	79
	4.2.4 Synthesis of Cu–(bromo)BTC	79
	4.2.5 Synthesis of Cu–(iodo)BTC	81
	4.2.6 Synthesis of UiO–66	81
	4.2.7 Synthesis of UiO–66–NH_2	82
	4.2.8 Synthesis of UiO–66–NO_2	82
	4.2.9 Synthesis of UiO–66–COOH and UiO–66– $(COOH)_2$	83
4.3	Characterization	83
4.4	Experimental System Used for Pure Gas Measurements	84
4.5	Equilibrium Adsorption Measurement	87
	4.5.1 Calculation of Amount Adsorbed	88
4.6	Different Types of Amount Adsorbed	89

		Page No.
	4.6.1 Determination of Buoyancy Volume for Various Reference States	91
4.7	Conversion of Units	91
4.8	Experimental Conditions	92
4.9	Details of Used Gases	94
4.9	Physical Properties of Studied Gases	95
	References	96
CHAPTER 5: A Comparison of Adsorption Capacities of Cu–abtc Versus Cu–hbtc MOFs		**98–132**
5.1	Background	98
5.2	Characterization of Frameworks Synthesized	100
	5.2.1 Powder X-ray Diffraction (PXRD) Analysis	100
	5.2.2 Thermogravimetric Analysis (TGA)	101
	5.2.3 Surface Area and Pore Volume Analysis	101
5.3	Adsorption Isotherms	102
	5.3.1 CO_2 Isotherms	103
	5.3.2 CO Isotherms	104
	5.3.3 CH_4 Isotherms	106
	5.3.4 N_2 Isotherms	107
	5.3.5 C_2H_6 Isotherms	109
	5.3.6 C_3H_8 Isotherms	110

Page No.

5.3.7 O_2 Isotherms 111

5.4 Isotherm Modelling 113

5.5 Effect of physical properties of gases 116

5.6 Henry's Constants and Adsorption Enthalpy 118

5.7 Prediction of Binary Selectivity using IAST 121

5.8 Summary 123

References 125

CHAPTER 6: Selective Gas Adsorption on HKUST–1 Derivatives: Cu–BTC Versus Cu–(bromo)BTC Versus Cu–(iodo)BTC **133–155**

6.1 Background 133

6.2 Characterization of Frameworks Synthesized 135

6.2.1 Powder X–ray Diffraction (PXRD) 135

6.2.2 Thermogravimetric Analysis (TGA) 135

6.2.3 Surface Area and Pore Volume Analysis 136

6.3 Adsorption Isotherms 137

6.3.1 CO_2 Isotherms 138

6.3.2 N_2 Isotherms 139

6.3.3 CO Isotherms 140

6.3.4 CH_4 Isotherms 141

6.4 Isotherm Modeling 142

Page No.

6.5 Effect of functionality on framework 144

6.6 Effect of physical properties of gases 145

6.7 Henry's Constants and Adsorption Enthalpy 147

6.8 Prediction of Binary Selectivity using IAST 148

6.9 Summary 150

References 151

CHAPTER 7: A Comparative Study of Effect of Functionality on CO_2, CH_4, CO and N_2 Adsorption in UiO–66 Derivative **156–191**

7.1 Background 156

7.2 Characterization of Frameworks Synthesized 158

7.2.1 Powder X–Ray Diffraction (PXRD) 158

7.2.2 Thermogravimetric Analysis (TGA) 159

7.2.3 Surface Area and Pore Volume Analysis 160

7.3 Adsorption Isotherms 161

7.3.1 CO_2 Isotherms 161

7.3.2 CH_4 Isotherms 164

7.3.3 CO and N_2 Isotherms 167

7.4 Isotherm Modeling 171

7.5 Effect of organic linker functionality 174

7.5.1 On CO_2 adsorption 174

Page No.

7.5.2 On CH_4 adsorption 175

7.5.3 On CO and N_2 adsorption 176

7.6 Henry's Constants and Adsorption Enthalpy 178

7.7 Prediction of Binary Selectivity using IAST 180

7.8 Summary 183

References 185

CHAPTER 8: Conclusions and Future Scope **192–196**

8.1 Conclusions 192

8.1.1 Affinity of functional group HN–NH in Cu–hbtc over N=N in Cu–abtc 193

8.1.2 A comparative study of gas adsorption on Cu–BTC versus Cu–(bromo)BTC versus Cu–(iodo)BTC 194

8.1.3 Effect of functionality (functional groups: –H, $–NH_2$, $–NO_2$, –COOH, $–(COOH)_2$) on adsorption characteristics of UiO–66 derivatives 195

8.2 Recommendation for Future Works 196

Page No.

APPENDIX A: Detail of the Experimental Protocol followed for Adsorption Measurement **197**

APPENDIX B: Measured Isotherm Data on MOFs Studied in this Work **198–216**

LIST OF TABLES

Table	Caption of the table	Page No.
2.1	Some commonly used organic linkers in MOF synthesis	25
2.2	Representative literature for CO_2 adsorption	37
2.3	Representative literature for CH_4 adsorption	38
2.4	Representative literature for CO adsorption	40
2.5	Representative literature for N_2 adsorption	41
2.6	Representative literature for C_2H_6 adsorption	42
2.7	Representative literature for C_3H_8 adsorption	43
2.8	Representative literature for O_2 adsorption	44
3.1	Enthalpy of Adsorption of relevant isotherm models	71
3.2	Spreading pressure for relevant isotherm models	73
4.1	List of instruments used in the gravimetric experimental setup	86
4.2	Details of activation protocols used for different MOFs	88
4.3	Second virial coefficients for different gases	90
4.4	Experimental ranges for various adsorptions isotherm measurements	93
4.5	Details of gases used in this study	94
4.6	Physical properties of gases used in this study	95
5.1	BET surface area and pore volume of Cu–abtc and Cu–hbtc	102

Table	Caption of the table	Page No.
5.2	Fit parameters of Virial–Langmuir isotherm of CO_2	114
5.3	Fit parameters of Virial–Langmuir isotherm of CO	114
5.4	Fit parameters of Langmuir isotherm of CH_4	115
5.5	Fit parameters of Langmuir isotherm of N_2	115
5.6	Fit parameters of Langmuir isotherm of C_2H_6	115
5.7	Fit parameters of Langmuir isotherm of C_3H_8	116
5.8	Fit parameters of Langmuir isotherm of O_2	116
6.1	BET surface area and pore volume of Cu–BTC, Cu–(bromo)BTC, and Cu–(iodo)BTC	137
6.2	Fit parameters of Langmuir isotherm of CO_2	143
6.3	Fit parameters of Langmuir isotherm of N_2	143
6.4	Fit parameters of Langmuir isotherm of CO	144
6.5	Fit parameters of Langmuir isotherm of CH_4	144
7.1	BET surface area and pore volume UiO–66 derivatives used in this chapter	161
7.2	Fit parameters of Virial isotherm of CO_2	172
7.3	Fit parameters of Virial isotherm of CH_4	172
7.4	Fit parameters of Virial isotherm of CO	173
7.5	Fit parameters of Virial isotherm of N_2	173

LIST OF FIGURES

Figure	Caption of the Figure	Page No.
1.1	IUPAC classifications of adsorption isotherms	3
2.1	MOF–5 structure with topology. ZnO_4 tetrahedral (blue polyhedral) are connected by benzene dicarboxylate linkers (O, red and C, black) to form MOF–5 structure	24
2.2	Framework structure of Cu–BTC (Blue: Cu, red: oxygen, black: carbon)	24
4.1	Synthesis of H_4abtc organic linker	77
4.2	Synthesis of H_4hbtc organic linker	78
4.3	Synthesis procedure for H_3 bromo BTC	80
4.4	Synthesis procedure for H_3 iodo BTC	81
4.5	Schematic of gravimetric adsorption measurement unit used in this work	85
5.1	DFT optimized structures of (a) abtc, (b) hbtc organic linkers; After Cu metalation (c) Cu–abtc and (d) Cu–hbtc (Cu, orange; C, gray; O, red; H, white; N, blue)	99
5.2	Powder X–ray diffractogram of Cu–abtc (red) and Cu–hbtc (blue)	100
5.3	TGA analysis of Cu–abtc (red) and compound Cu–hbtc (blue) at heating rate of 5 K min^{-1} under argon flow	101

Figure	Caption of the Figure	Page No.
5.4	N_2 adsorption of Cu–abtc (red) and Cu–hbtc (blue) at 77 K	102
5.5	CO_2 isotherms of Cu–abtc and Cu–hbtc MOFs. Symbols are experimental data at 294 K (●), 317 K (■), and 356 K (▲); lines are fits obtained using Langmuir-virial isotherm parameters from Table 5.2	104
5.6	CO_2 isotherms of Cu–abtc and Cu–hbtc MOFs in Langmuir-virial domain. Symbols are experimental data at 294 K (●), 317 K (■), and 356 K (▲); lines are fits obtained using Langmuir-virial isotherm parameters from Table 5.2	104
5.7	CO isotherms of Cu–abtc and Cu–hbtc MOFs. Symbols are experimental data at 294 K (●), 317 K (■), and 356 K (▲); lines are fits obtained using Langmuir-virial isotherm parameters from Table 5.3	105
5.8	CO isotherms of Cu–abtc and Cu–hbtc MOFs in Langmuir-virial domain. Symbols are experimental data at 294 K (●), 317 K (■), and 356 K (▲); lines are fits obtained using Langmuir-virial isotherm parameters from Table 5.3	105

Figure	Caption of the Figure	Page No.
5.9	CH_4 isotherms of Cu–abtc and Cu–hbtc MOFs in Langmuir domain. Symbols are experimental data at 294 K (●), 317 K (■), and 356 K (▲); lines are fits obtained using Langmuir isotherm parameters from Table 5.4	106
5.10	CH_4 isotherms of Cu–abtc and Cu–hbtc MOFs in Langmuir domain. Symbols are experimental data at 294 K (●), 317 K (■), and 356 K (▲); lines are fits obtained using Langmuir isotherm parameters from Table 5.4	107
5.11	N_2 isotherms of Cu–abtc and Cu–hbtc MOFs in Langmuir domain. Symbols are experimental data at 294 K (●), 317 K (■), and 356 K (▲); lines are fits obtained using Langmuir isotherm parameters from Table 5.5	108
5.12	N_2 isotherms of Cu–abtc and Cu–hbtc MOFs in Langmuir domain. Symbols are experimental data at 294 K (●), 317 K (■), and 356 K (▲); lines are fits obtained using Langmuir isotherm parameters from Table 5.5	108
5.13	C_2H_6 isotherms of Cu–abtc and Cu–hbtc MOFs. Symbols are experimental data at 294 K (●), 317 K (■), and 356 K (▲); lines are fits obtained using Langmuir isotherm parameters from Table 5.6	109

Figure	Caption of the Figure	Page No.
5.14	C_2H_6 isotherms of Cu–abtc and Cu–hbtc MOFs in Langmuir domain. Symbols are experimental data at 294 K (●), 317 K (■), and 356 K (▲); lines are fits obtained using Langmuir isotherm parameters from Table 5.6	110
5.15	C_3H_8 isotherms of Cu–abtc and Cu–hbtc MOFs in Langmuir domain. Symbols are experimental data at 294 K (●), 317 K (■), and 356 K (▲); lines are fits obtained using Langmuir isotherm parameters from Table 5.7	110
5.16	C_3H_8 isotherms of Cu–abtc and Cu–hbtc MOFs in Langmuir domain. Symbols are experimental data at 294 K (●), 317 K (■), and 356 K (▲); lines are fits obtained using Langmuir isotherm parameters from Table 5.7	111
5.17	O_2 isotherms of Cu–abtc and Cu–hbtc MOFs. Symbols are experimental data at 294 K (●), 317 K (■), and 356 K (▲); lines are fits obtained using Langmuir isotherm parameters from Table 5.8	112
5.18	O_2 isotherms of Cu–abtc and Cu–hbtc MOFs in Langmuir domain. Symbols are experimental data at 294 K (●), 317 K (■), and 356 K (▲); lines are fits obtained using Langmuir isotherm parameters from Table 5.8	112

Figure	Caption of the Figure	Page No.
5.19	Adsorption Isotherms of CO_2 (▲), CO (■), and CH_4 (●) at 294 K for Cu–abtc and Cu–hbtc MOFs	117
5.20	Adsorption Isotherms of C_3H_8(●), C_2H_6 (■), CH_4 (▲), N_2(♦), and O_2(-) at 294 K on Cu–abtc and Cu–hbtc MOFs	118
5.21	Henry's constant at 294 K and enthalpy of adsorption at zero occupancy as a function of polarizability of the adsorbate for Cu–abtc; linear trend lines for nonpolar gases are also shown	118
5.22	Henry's constant at 294 K and enthalpy of adsorption at zero occupancy as a function of polarizability of the adsorbate for Cu–hbtc; linear trend lines for nonpolar gases are also shown	119
5.23	Variation of adsorption enthalpy of CO_2 (●) and N_2 (▲) with loading for Cu–abtc (open symbol) and Cu–hbtc (closed symbol)	120
5.24	Adsorption enthalpy at zero coverage for N_2, O_2, CH_4, C_2H_6, and C_3H_8 on Cu–abtc (hatch pattern) and Cu–hbtc (solid fill)	121
5.25	Variation of CO_2 selectivity over N_2 for Cu–abtc (open symbol) and Cu–hbtc (closed symbol). CO_2 mole fraction in all binary mixtures is 20%; lines are drawn as a guide to the eyes	122

Figure	Caption of the Figure	Page No.
5.26	Effect of temperature on CO_2 selectivity (for 20% molar composition of CO_2) over N_2 for Cu–abtc (open symbol) and Cu–hbtc (closed symbol) at 1 bar; lines are drawn as a guide to the eyes	122
5.27	Effect of temperature on CO_2 selectivity (for 20% molar composition of CO_2) over CO (green) and CH_4 (yellow) for Cu–abtc (open symbol) and Cu–hbtc (closed symbol) at 1 bar; lines are drawn as a guide to the eyes	123
6.1	Functionalized organic linkers used to synthesize Cu–BTC, Cu–(bromo)BTC, and Cu–(iodo)BTC	134
6.2	Framework structure of Cu–BTC (Brown: metal, red: oxygen, black: carbon, white: oxygen). Redrawn from CCDC deposition 943008	134
6.3	Powder X-ray diffractogram of Cu–BTC (blue), Cu–(bromo)BTC (red), and Cu–(iodo)BTC (green)	135
6.4	TGA analysis of compound Cu–BTC (blue), Cu–(bromo)BTC (red), and Cu–(iodo)BTC (green) at a heating rate of 5 K min^{-1}	136
6.5	N_2 adsorption (closed symbol) and desorption (open symbol) of Cu–BTC (blue), Cu–(bromo)BTC (red), and Cu–(iodo)BTC (green) at 77 K	137

Figure	Caption of the Figure	Page No.
6.6	CO_2 isotherms of Cu–BTC, Cu–(bromo)BTC, and Cu–(iodo)BTC MOFs. Symbols are experimental data at 294 K (●), 317 K (■), and 356 K (▲); lines are fits obtained using Langmuir isotherm parameters from Table 6.2	139
6.7	N_2 isotherms of Cu–BTC, Cu–(bromo)BTC, and Cu–(iodo)BTC MOFs. Symbols are experimental data at 294 K (●), 317 K (■), and 356 K (▲); lines are fits obtained using Langmuir isotherm parameters from Table 6.3	140
6.8	CO isotherms of Cu–BTC, Cu–(bromo)BTC, and Cu–(iodo)BTC MOFs. Symbols are experimental data at 294 K (●), 317 K (■), and 356 K (▲); lines are fits obtained using Langmuir isotherm parameters from Table 6.4	141
6.9	CH_4 isotherms of Cu–BTC, Cu–(bromo)BTC, and Cu–(iodo)BTC MOFs. Symbols are experimental data at 294 K (●), 317 K (■), and 356 K (▲); lines are fits obtained using Langmuir isotherm parameters from Table 6.5	142
6.10	Adsorption Isotherms of (a) CO_2, (b) N_2, (c) CO, and (d) N_2 on Cu–BTC (▲), Cu–(bromo)BTC (●), and Cu–(iodo)BTC (■) at 294 K; adsorption capacities compared in molecules/unit cell	145

Figure	Caption of the Figure	Page No.
6.11	Due to the presence of open metal sites in framework, CH_4 isotherm overtake over CO; CO_2 (■), CH_4 (▲), CO (●), and N_2 (♦) at 294 K for Cu–(bromo)BTC; adsorption capacities compared in molecules/unit cell	146
6.12	Due to the presence of open metal sites in the framework, CH_4 isotherm overtake over CO; CO_2 (■), CH_4 (▲), CO (●), and N_2 (♦) at 294 K for (a) Cu–BTC and (b) Cu–(iodo)BTC; adsorption capacities compared in molecules/unit cell	146
6.13	Variation of adsorption enthalpy at zero coverage on Cu–BTC versus Cu– (bromo)BTC versus Cu–(iodo)BTC	147
6.14	Variation of CO_2 selectivity over N_2 for Cu–BTC (▲), Cu–(bromo)BTC (●), and Cu–(iodo)BTC (■). CO_2 at 294 K and 1 bar; lines are drawn as a guide to the eyes	149
6.15	Variation of CO_2 selectivity over CH_4 for Cu–(iodo)BTC (■) over Cu–BTC (▲) and Cu–(bromo)BTC (●). CO_2 at 294 K and 1 bar; lines are drawn as a guide to the eyes	149
7.1	Organic linkers used for synthesize UiO–66 derivatives	157

Figure	Caption of the Figure	Page No.
7.2	Crystal structure of UiO–66 MOF (Twelve BDC linkers coordinate to the metal atoms of the cluster with one of their carboxylate groups)	158
7.3	Powder X-ray diffractogram of UiO–66 (red), UiO–66–NO_2 (brown), UiO–66–NH_2 (blue), UiO–66–COOH (yellow) and UiO–66–$COOH)_2$ (green)	159
7.4	TGA analysis of UiO–66 (red), UiO–66–NO_2 (brown), UiO–66–NH_2 (blue), UiO–66–COOH (yellow), and UiO–66–$(COOH)_2$ (green)	160
7.5	N_2 adsorption isotherms at 77 K on UiO–66 (○), UiO–66–NH_2 (□), UiO–66–NO_2 (×), UiO–66–COOH (◊), and UiO–66–$(COOH)_2$ (Δ)	161
7.6	CO_2 isotherms of UiO–66, UiO–66–NH_2, UiO–66–NO_2, UiO–66–COOH, and UiO–66–$(COOH)_2$ MOFs. Symbols are experimental data at 294 K (●), 317 K (■), and 356 K (▲); lines are fits obtained using Virial isotherm parameters from Table 7.2	163

Figure	Caption of the Figure	Page No.
7.7	CO_2 isotherms of UiO–66, UiO–66–NH_2, UiO–66–NO_2, UiO–66–COOH, and UiO–66–$(COOH)_2$ MOFs in the Virial domain. Symbols are experimental data at 294 K (●), 317 K (■), and 356 K (▲); lines are fits obtained using the Virial isotherm parameters from Table 7.2	164
7.8	CH_4 isotherms of UiO–66, UiO–66–NH_2, UiO–66–NO_2, UiO–66–COOH, and UiO–66–$(COOH)_2$ MOFs. Symbols are experimental data at 294 K (●), 317 K (■), and 356 K (▲); lines are fits obtained using Virial isotherm parameters from Table 7.3	165
7.9	CH_4 isotherms of UiO–66, UiO–66–NH_2, UiO–66–NO_2, UiO–66–COOH, and UiO–66–$(COOH)_2$ MOFs in the Virial domain. Symbols are experimental data at 294 K (●), 317 K (■), and 356 K (▲); lines are fits obtained using Virial isotherm parameters from Table 7.3	166
7.10	CO isotherms of UiO–66, UiO–66–NH_2, UiO–66–NO_2, UiO–66–COOH, and UiO–66–$(COOH)_2$ MOFs. Symbols are experimental data at 294 K (●), 317 K (■), and 356 K (▲); lines are fits obtained using Virial isotherm parameters from Table 7.4	168

Figure	Caption of the Figure	Page No.
7.11	CO isotherms of UiO–66, UiO–66–NH_2, UiO–66–NO_2, UiO–66–COOH, and UiO–66–$(COOH)_2$ MOFs in the Virial domain. Symbols are experimental data at 294 K (●), 317 K (■), and 356 K (▲); lines are fits obtained using Virial isotherm parameters from Table 7.4	169
7.12	N_2 isotherms of UiO–66, UiO–66–NH_2, UiO–66–NO_2, UiO–66–COOH, and UiO–66–$(COOH)_2$ MOFs. Symbols are experimental data at 294 K (●), 317 K (■), and 356 K (▲); lines are fits obtained using Virial isotherm parameters from Table 7.5	170
7.13	N_2 isotherms of UiO–66, UiO–66–NH_2, UiO–66–NO_2, UiO–66–COOH, and UiO–66–$(COOH)_2$ MOFs in the Virial domain. Symbols are experimental data at 294 K (●), 317 K (■), and 356 K (▲); lines are fits obtained using Virial isotherm parameters from Table 7.5	171
7.14	Adsorption isotherms of CO_2 at 294 K on UiO–66 (●), UiO–66–NH_2 (■), UiO–66–NO_2 (×), UiO–66–COOH (♦), and UiO–66– $(COOH)_2$ (▲)	175

Figure	Caption of the Figure	Page No.
7.15	Adsorption isotherms of CH_4 at 294 K on UiO–66 (●), UiO–66–NH_2 (■), UiO–66–NO_2 (×), UiO–66–COOH (♦), and UiO–66–$(COOH)_2$ (▲)	176
7.16	Adsorption isotherms of CO at 294 K on UiO–66 (●), UiO–66–NH_2 (■), UiO–66–NO_2 (×), UiO–66–COOH (♦), and UiO–66–$(COOH)_2$ (▲)	177
7.17	Adsorption isotherms of N_2 at 294 K on UiO–66 (●), UiO–66–NH_2 (■), UiO–66–NO_2 (×), UiO–66–COOH (♦), and UiO–66–$(COOH)_2$ (▲)	177
7.18	Henry's constant at 294 K as a function of the polarizability of the adsorbate for the UiO–66–$(COOH)_2$ adsorbent	178
7.19	Variation of enthalpy of adsorption of CO_2 on UiO–66 (●), UiO–66–NH_2 (■), UiO–66–COOH (×), UiO–66–NO_2 (♦), and UiO–66– $(COOH)_2$ (▲)	179
7.20	Variation of enthalpy of adsorption at zero coverage of N_2 on UiO–66 (red), UiO–66–NH_2 (blue), UiO–66–COOH (yellow), UiO–66–NO_2 (brown), and UiO–66–$(COOH)_2$ (green)	179

Figure	Caption of the Figure	Page No.
7.21	Variation of CO_2 selectivity over N_2 for UiO–66 (●), UiO–66–NH_2 (■), UiO–66–COOH (♦), UiO–66–NO_2 (×), and UiO–66–$(COOH)_2$ (▲); CO_2 mole fraction in all binary mixture is 20%; lines are drawn as a guide to the eyes	181
7.22	Variation of CO_2 selectivity over CO for UiO–66 (●), UiO–66–NH_2 (■), UiO–66–COOH (♦), UiO–66–NO_2 (×), and UiO–66–$(COOH)_2$ (▲). CO_2 mole fraction in all binary mixtures is 20%; lines are drawn as a guide to the eyes	182
7.23	Effect of temperature on CO_2 selectivity (for 20% molar composition of CO_2) over N_2 for UiO–66 (●), UiO–66–NH_2 (■), UiO–66–COOH (♦), UiO–66–NO_2 (×), and UiO–66–$(COOH)_2$ (▲); lines are drawn as a guide to the eyes	182

Nomenclature

a	Molar area of the adsorbent, $m^2\ mol^{-1}$
A	Specific area of the adsorbent, $m^2\ kg^{-1}$
b	Second virial coefficients for adsorption, $mol^{-1}\ kg$
$b^{(0)}$ and $b^{(1)}$	Temperature independent second virial coefficients, $mol^{-1}\ kg$ and $mol^{-1}\ kg\ K$, respectively
B^{gas}	Gas phase second virial coefficient, $m^3\ Kmol^{-1}$
B_1, B_2, B_3, B_4, B_5	Parameters used for describing temperature dependency of second virial coefficient of gas
c	Third virial coefficients for adsorption, $mol^{-2}\ kg^2$
$c^{(0)}$ and $c^{(1)}$	Temperature independent parameters of third virial coefficients, $mol^{-2}\ kg^2$ and $mol^{-2}\ kg^2\ K$, respectively
C	Number of chemical species
f	Fugacity, bar
F	Number of degrees of freedom
Δh_{ads}	Enthalpy of adsorption, $kJ\ mol^{-1}$
$\Delta h_{ads,0}$	Enthalpy of adsorption at zero coverage, $kJ\ mol^{-1}$
I_1, I_2	Isotherm models relating N_i^0 and P_i^0
I_3, I_4	Equations relating spreading pressure ψ, excess amount adsorbed N and fugacity P
M	Metal cation in an adsorbent
M_0	True adsorbent weight including bucket weight in vacuo, g
M_{eq}	Adsorbent plus bucket weight at equilibrium, g

M_f	Molecular weight of unit cell of adsorbent, g mol^{-1}
M_t	Gibbs' amount adsorbed, g
M_w	Molecular weight of the gas, g mol^{-1}
n	Number of metal atoms in one unit cell
N	Excess amount adsorbed, mol kg^{-1}
N^{max}	Saturation capacity, mol kg^{-1}
N_1^{max}, N_2^{max}	Saturation capacities of sites 1 and 2 in DSL model, mol kg^{-1}
Ni^0	Excess amount adsorbed of pure component *'i'* at fugacity f_i^0
N_m	Amount adsorbed per metal atom in the adsorbent, molecules $atom^{-1}$
N_u	Excess amount adsorbed on a unit cell basis, molecules $unit\ cell^{-1}$
N_v	Excess amount adsorbed on volumetric basis, mol L^{-1}
P	Pressure, bar
P_i^0	Standard state pressure of component *'i'*
R	Universal gas constant, J mol^{-1} K^{-1}
T	Temperature, K
V	Volume, m^3
V_{bucket}, V_s	Buoyancy volume of bucket and impenetrable solid volume, cm^3
V_p	Pore volume of adsorbent, cm^3 g^{-1}
$V_{buoyancy}$	Buoyancy volume of the sample, cm^3
x_i	Equilibrium mole fraction of the component *'i'* in adsorbed phases
y_i	Equilibrium mole fraction of the component *'i'* in bulk gas phases

Greek letters

α_{ij}	Selectivity of the adsorbent for species ***i*** over species ***j***
β	Henry's constant, mol kg^{-1} bar^{-1}
$\beta^{(0)}$	Parameter related to entropy used for describing temperature dependency of Henry's constant, mol kg^{-1} bar^{-1}
$\beta^{(1)}$	Parameter related to enthalpy used for describing temperature dependency of Henry's constant, K
β_1 *and* β_2	Affinity parameters for sites 1 and 2 respectively in Dual Site Langmuir model, bar^{-1}
$\beta_1^{(0)}$ *and* $\beta_2^{(0)}$	Parameters related to entropy for sites 1 and 2 respectively in Dual Site Langmuir model, bar^{-1}
$\beta_1^{(1)}$ *and* $\beta_2^{(1)}$	Parameters related to adsorption enthalpy for sites 1 and 2 in Dual Site Langmuir model, respectively, K
γ_i	Activity coefficient in the adsorbed phase
π	Spreading pressure, N m^{-1}
ρ_c	Crystal density of the adsorbent, g cm^{-3}
ρ^{gas}	Bulk gas density, g cm^{-3}
$\emptyset_i^{gas}$	Fugacity coefficient of bulk gas
χ	Number of phases
ψ	Reduced spreading pressure, mol kg^{-1}

Abbreviations

MOF	Metal organic framework
BDC	Benzene 1,4–dicarboxylic acid
BTC	Benzene 1,3,5–tricarboxylic acid
IAST	Ideal adsorption solution theory
cus	Coordinatively unsaturated
H_4abtc	3,3′,5,5′–azobenzenetetracarboxylic acid
H_4hbtc	3,3′,5,5′–hydrazinebenzenetetracarboxylic acid

CHAPTER 1

Introduction

In the last few decades, porous materials have been subjected to extensive research that has widened their application arena to energy storage, sorption and separation, catalysis, and drug delivery, etc. this chapter outlines a brief overview on adsorption, includes a history of the adsorption process, adsorption characteristics, advantages and disadvantages of various industrially important conventional adsorbents, factors to be considered in the selection of adsorbent were discussed. CO_2 emissions, existing CO_2 capture technologies, and the importance of CH_4 storage were included. The focus of this study and research objectives were also mentioned.

1.1 Overview on Adsorption

Adsorption is a surface phenomenon where the density of a fluid adsorbate increases at a phase boundary or adsorbent surface [1]. The term adsorption is strictly distinguished from absorption by its limitation to the surface or interface of the sorbent; upon diffusion beyond the interface into the bulk of the sorbent, the adsorbate becomes the absorbate. The phenomenon of adsorption has been known since antiquity [2]. However, a quantitative investigation began in the 18th century by Scheele, Priestley, and Fontana [3, 4]. The theory of adsorption was first focused on the solid surface by Herbert Freundlich in 1907 [5]. Later Irving Langmuir's monolayer-based theory was reported in 1916, and Langmuir described monolayer formation occurs based on binding interaction between solid surface and adsorbate. Later monolayer theory was broadly generalized to multilayer adsorption, ranging from highly regular surfaces to completely

amorphous surfaces containing different adsorption sites. The six fundamental cases of adsorption identified by Langmuir laid the foundation for surface science [2]. Later significant research on adsorption was continued by Stephen Brunauer, Paul Emmett, Edward Teller [6] and Paul Kisliuk [7], etc.

Based on the strength of interaction between adsorbate and adsorbent, adsorption can be divided into two categories

(i) Physisorption: When the interaction between adsorbate and adsorbent takes place purely based on intermolecular forces or van der Waals forces, the process is called physisorption. Physisorption is a reversible process that does not involve a significant change in the electronic orbital patterns of the species. So the binding energy is typically low [8]. However, in the case of polar molecules like H_2O and NH_3, adsorption on zeolite usually may be high (100–130 kJ mol^{-1}). Under appropriate conditions of temperature and pressure, multilayer adsorption may be possible.

(ii) Chemisorption: The interaction between adsorbate and adsorbent in which valence forces are involved, and the formation of a chemical substance is called chemisorption. Based on the chemical nature of adsorption, surface dissociation or desorption might not be possible; in this sense, the chemisorption is irreversible. Since the adsorbed molecules are linked to the surface by valence bonds, they will usually occupy certain adsorption sites on the surface, so only a mono layer is possible. In this process, the magnitudes of the energy changes are very large (100–1000 kJ mol^{-1}) [9]. Usually, heterogeneous catalysis mostly involves this type of adsorption.

Since Langmuir laid the foundation for six fundamental cases of adsorption, modifications and new theories were added to design and describe complex and real-word adsorption phenomena [10]. In six different types of adsorption isotherms, Type–I represents the adsorption characteristics of microporous adsorbent in which the molecular diameter of the adsorbate matches exactly with the pore diameter of the adsorbent. This type of isotherms has a definite saturation limit corresponding to the complete filling of the micro pores. Non–porous or macro-porous adsorbents show types II, III, and VI isotherms, whereas mesoporous adsorbents exhibit types IV and V isotherms. The shape of isotherms itself indicates that there are stronger gas-solid interactions for type II and IV and weaker ones for type III and V. Shape of type VI suggests the multilayer formation either on a plane surface or on the walls of pores which are much larger than the molecular diameter of the adsorbate molecule.

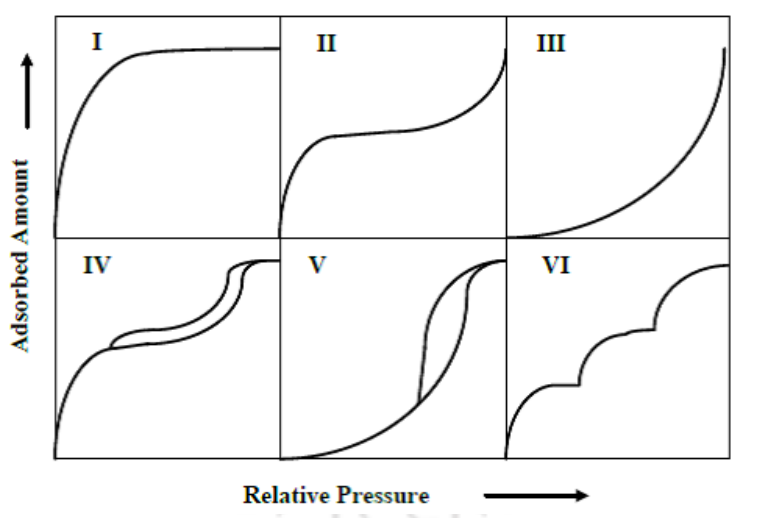

Figure 1.1: IUPAC classifications of adsorption isotherms [9].

1.2 Adsorbents of Industrial Importance

The success of any industrial-based adsorption process largely depends upon the selection of a proper adsorbent for a particular application. Since a large number of adsorbents were reported in the literature, only a few are feasible to study in adsorption processes. Silica gel, activated carbon, carbon molecular sieve, activated alumina, and zeolites are the most studied adsorbent materials. Based on elemental composition, adsorbents are classified into two distinguished categories.

(i) Organic porous adsorbents: Activated carbons, carbon molecular sieves, and microporous organic polymers come under this category. These materials are widely used for industrial gas separations [2]. Activated carbons usually synthesized by pyrolysis of carbon-rich materials give higher pore volume, which results in good saturation capacities. However, the main disadvantage of these materials has poor selectivity. To overcome these issues, carbon adsorbents with a narrow distribution of micro pore sizes are prepared using special activation procedures known as carbon molecular sieves. However, porosity and saturation adsorption capacities are lower for these materials. Microporous polymers synthesize using various binder polymers like polyfurfuryl alcohols and polyacrylonitrile.

(ii) Inorganic porous adsorbents: These materials structures are formed entirely based on inorganic elementary structures. Silica gel, activated alumina, and zeolites are examples of inorganic porous adsorbents.

Silica gel: Silica gel is an amorphous and porous form of silicon dioxide (SiO_2). The structure is consisting of an irregular tridimensional framework of alternating silicon and oxygen with

nanometer-scale voids and pores. It often uses to adsorb water moisture, making it useful as a desiccant (or drying agent).

Activated alumina: Activated alumina (Al_2O_3) manufactured by dihydroxylation of aluminum hydroxide ($Al(OH)_3$) produces highly porous material having acidic and basic properties. It is often used for a wide range of applications, including adsorbents in adsorption of catalysts in polyethylene production, selective removal of fluorine and arsenic from hydrogen peroxide production, and sulfur removal from fluid streams Claus Catalyst process.

Zeolites: Natural zeolites are formed from alkaline volcanic sediments under hydrothermal conditions of saline lake groundwater-based systems. Examples are mordenite, natrolite, etc. Due to overwhelming industrial demand, the inability to supply natural zeolites, synthetic zeolites development was started. Usually, synthetic zeolites are made by hydrothermal sol-gel method in an aqueous solution at low pressure and moderate temperatures (up to 300°C). Examples are Zeolite A (based on Na, Ca, K), zeolite X (based on Na, K, Ba), etc. Synthetic zeolites are commercially used for gases adsorption and separation processes [10–12]. For example, zeolite 4A ($Na_{12}Al_{12}Si_{12}O_{48}$) forms a porous solid permeated by channels 4Å in diameter resulting from eight tetrahedral coordinated silicon/aluminum atoms and 8 oxygen atoms. Zeolite 4 Å commonly is used as a drying agent due to the size-selective specificity and hydrophilic nature of the channels for absorbing water, the high loading capacity of the bulk material, and the ability to reactivate the zeolite once it becomes saturated by removing the absorbed water at elevated temperatures. Another application of zeolites as porous adsorbent was demonstrated when silicalite–1 was used to remove gasoline from drinking water [13]. Despite their widespread use, zeolites have several potential drawbacks that limit their utility as porous solids. Those drawbacks include syntheses that can be difficult to control, a limited number of structural and

channel architectures available, and crystalline structures based on covalently-bonded networks of atoms that cannot be modified.

1.2.1 Important Factors on Sorbent Selection

Adsorption has several advantages over other conventional techniques, such as distillation, absorption, membrane-based systems, etc. It is worthy of discussing some of the important factors to be considered to choose an adsorbent for adsorption application [14].

(A) Adsorption capacity: Adsorption capacity or loading is the most important characteristic of any adsorbent. The adsorbent is taken up by the adsorbent per unit mass or volume of the adsorbent, which is measured in mol kg^{-1} or mol cm^{-3}. Adsorption capacity is a paramount factor in estimating the capital cost because it dictates the amount of adsorbent required, which also fixes the volume of the adsorber column. The adsorption loading depends upon the fluid-phase concentration, temperature, and other conditions (especially the initial condition of the adsorbent). Typically, adsorption capacity data are measured at a fixed temperature with various partial pressures, and the data are plotted as an isotherm.

(B) Selectivity: Selectivity is related to adsorption capacity; it is a ratio of the capacity of one component to that of another at a given fluid pressure or concentration. Selectivity is defined as

$$a_{ij} = \frac{x_i/y_i}{x_j/y_j} \qquad 1.1$$

Where x_i and y_i are equilibrium mole fractions of component 'i ' in adsorbed and bulk gas phases, respectively. The x_j and y_j are equilibrium mole fractions of component 'j ' in adsorbed and bulk gas phases. The selectivity generally approaches a constant value as concentration drops towards zero.

(C) Adsorbent regeneration: Adsorbent Regenerability means that the adsorbent can operate in repeat cycles with uniform performance, where adsorbed material must be relatively weakly adsorbed. The heat of adsorption measures the energy required for adsorbent regeneration, and in this regard, low values are desirable. Regeneration can be accomplished by a temperature swing, pressure swing, and chemical swing (e.g., CO_2 supercritical extraction) or sometimes by combining these. The regeneration affects the fraction of the original adsorbent capacity for the first few cycles, often followed by a gradual decay, perhaps over hundreds of cycles due to aging, poisoning, etc.

(D) Compatibility: Different possible ways of physical and chemical attacks on adsorbent could reduce the life expectancy of the adsorbent, such as biological fouling and attrition. For example, the adsorbent, binder, and surface groups should be inert to the carrier or solvent and should not irreversibly react with the adsorbate. Likewise, operating conditions such as temperature, pressure, and vibration should not cause undue disintegration of the adsorbent particles.

(E) Cost: Cost is the most subtle characteristic to understand because it may vary from day to day based on particular material production capacity and market availability. Price changes from one vendor to another vendor for the same material. So cost may be significant if not dominant.

1.2.2 Novel Adsorbents

Within the class of ordered porous solids, zeolites have been the widely studied porous inorganic materials for gases adsorption and separation processes [10–12]. Activated carbons, carbon molecular sieves, and microporous organic polymers come under porous organic solids widely used for various applications such as gases storage, separation, drug delivery, catalysis etc. [2].

However, adsorption is primarily a material-driven technology, and it is essential to develop porous materials with better characteristics for the development of efficient adsorptive processes.

In the search for development, a new class of hybrid ordered structures was discovered. In this hybrid structure, both inorganic and organic components were introduced to evolve the hybrid structure to incorporate organic and inorganic porous structures properties. The concept of reticular synthesis has been adopted to connect building blocks to form a bigger network. Based on this concept, a large volume of novel porous structures have been synthesized during the last decade. These novel structures are called in different names, such as hybrid organic-inorganic materials, porous coordination polymers, metal-organic frameworks (MOFs), etc. MOFs are considered organic analogs of inorganic zeolites in which oxygen atoms are replaced by rigid organic ligands that bridge the metal ions. The resulting crystalline solids are comprised of rigid frameworks of molecules coordinated to metal ions in two or three dimensions that form open networks that render the crystalline structure highly porous. MOFs represent a promising new class of porous crystalline solids because they exhibit some of the largest pore volumes and highest surface areas known.

MOFs have attracted the attention of researchers largely because they offer several significant advantages over zeolites resulting from the organic ligands present in the backbone of the framework namely, the dimensions and properties of channels can be controlled at the molecular level via synthetic modification of the ligand either before or after the MOF is prepared [15−17]. Consequently, the structures and physical properties of MOFs can be controlled to a far greater extent relative to zeolites. In addition, the void volumes and diameters of channels in some MOFs (i.e., up to 29 Å) far exceed those observed in the most highly porous zeolites, which allows small to medium-sized organic compounds both to diffuse

through channels and to be covalently appended to reactive groups on the walls of channels [18]. Since their discovery, MOFs have received the greatest interest in the scientific community due to their suitability as host materials for gas storage [19–21], gas separation [22–25], drug delivery [26,27], ion exchanging [28], catalysis [29] and micro sensing [30,31], etc.

1.3 Overview on CO_2 Emissions and Importance of CH_4 Storage

The last century has witnessed humanity actively using organic fossil fuels like coal and petroleum products as energy sources, causing considerable carbon dioxide emissions in the atmosphere [32]. Approximately 80% of total CO_2 emission is responsible for energy generation, and the remaining 20% is emitted from industrial sources such as cement production plants (~7%), refineries (~6%), and the iron and steel industry (~5%) [33]. A chemically stable CO_2 molecule can remain in the atmosphere for about 120 years so that CO_2 emitted from fossil fuels gradually accumulates in the atmosphere. These excessive amounts of CO_2 in the atmosphere may adversely affect the earth's climate, resulting in the planet's surface overheating, permafrost being destroyed, polar ice caps melting, rising sea levels, etc. [32]. Therefore, CO_2 capture technologies on these sources could be an important early opportunity application.

On the other hand, the demand for alternative fuels is a greater concern due to national and regional energy security, ground-level air quality, and climate change. Methane is the primary component of natural gas. However, natural gas is not renewable energy, and it mainly comprises methane which has a potential bridging fuel to a low carbon energy future. Methane delivers roughly twice the energy of coal in terms of the amount of carbon dioxide released. In contrast to coal, methane does so without dissipating mercury or producing uranium and thorium-rich ash. Methane containing natural gas is more widespread globally than those of

petroleum, and its refinement to an energy fuel is much simpler than crude petroleum. Methane is also produced by the decomposition of organic waste and by bacteria in the guts of ruminants and termites. Methane and natural gas are often considered waste products in crude oil collection and refining and other industrial processes and are often burned off in giant flares with no secondary energy capture. Recently inexpensive new technologies are developed to the recovery of natural gas from shale. So, environmental considerations boosted natural gas as a fuel for transportation, especially as a replacement for petrol.

1.3.1 Different Pathways of CO_2 Capture and CH_4 Storage

CO_2 Capture: There are several approaches that can be adopted to reduce the total CO_2 emission into the atmosphere, such as a reduction in energy intensity by the efficient use of energy, a reduction of carbon intensity by using alternatives to fossil fuels like hydrogen and renewable energy, and enhancement of carbon dioxide sequestration by developing new carbon capture technologies.

From the above mentioned approaches, the most promising approach is carbon capture from point source emissions such as power generation plants. There are three different pathways for CO_2 capture. They are post-combustion, pre-combustion, and oxy-fuel combustion.

(1) Post-combustion: CO_2 is the end product of the combustion of any carbonaceous fuel. The capture of CO_2 downstream of a combustion unit is referred to as the post-combustion capture system. In these systems, the fossil fuels are combusted in excess air, resulting in a flue gas stream that contains low concentrations of CO_2 (coal-fired power plants: 10–15 v/v, natural gas-fired plants: 5–8 v/v %). In some cases, such as cement kilns and blast furnaces where flue gases contain process-related CO_2 and fuel-related CO_2, the CO_2 concentration in the flue gases may

vary from 14–33%. CO_2 from the post-combustion flue gases can be captured by various techniques such as absorption by amines, membrane separation, and cryogenic separation. With the current state of technology, only absorption and, to some extent, membranes are considered to be economically viable technologies.

(2) Pre–combustion: In the pre-combustion capture system, carbonaceous fuels are converted to syngas through gasification, partial oxidation, or steam reforming. Next, the CO is converted to CO_2 through the water gas shift conversion process:

$$CO + H_2O \rightarrow CO_2 + H_2$$

The concentration of CO_2 in this stream is around 25–40%, and the total pressure is typically in the range of 2.5–5 MPa. Thus, the partial pressure of CO_2 in the pre-combustion process is very high compared to conventional combustion systems. This makes it easier to separate the CO_2 by techniques such as scrubbing through physical solvents. The CO_2 can then be used or disposed of. The H_2 can be used as a feedstock in a chemical plant or combusted in a gas turbine to produce electricity. Because the CO_2 is captured prior to the utilization of the hydrogen product, the system is classified as a "pre-combustion" CO_2 capture procedure.

(3) Oxy-fuel combustion: As oxy-fuel combustion inherently produces a flue gas stream concentrated in CO_2, the CO_2 can readily be captured without the use of post-combustion solvents. Therefore, oxy-fuel technology is neither a "pre-combustion" nor a "post-combustion" process. Consequently, it is generally classified as a "combustion" process. Oxy-fuel combustion is widely used in glass and metal industries where very high temperatures are required for the process. Compared to the glass and metal industries, oxy-fuel combustion for power generation and other large industrial boilers is relatively new. The approach consists of separating O_2 from

the air and using the O_2 as the oxidant for fossil fuel combustion. With the nitrogen removed (78% of the air) from the combustion process, the result is a highly concentrated flue gas stream composed mainly of CO_2 (> 80 v/v%) water vapour and other minor amounts of contaminants, such as particulates, NO_x, SO_x and trace elements. The contaminants can be easily removed to further concentrate the CO_2 through physical gas purification techniques, such as cryogenic separation. Since the combustion occurs in an O_2/CO_2 environment, this variant of the oxy-fuel technology is sometimes called O_2/CO_2 recycle combustion. Several oxy-fuel combustion systems have been proposed and are under development for retrofit or new applications in power plants. One variant is the O_2/CO_2 recycles process. In this process, CO_2 is recycled to the combustor to control the flame temperature. This is currently the most advanced oxy-fuel combustion approach and has attracted the interest of the industry for applications in conventional furnaces, process heaters, and power plants.

CH_4 Storage: Methane is considered an ideal energy for future applications. Compared to petroleum oil, methane can provide much more energy because of its higher hydrogen to carbon ratio and has much lower carbon emissions. It appears to be a more promising alternative for mobile applications in terms of practical utilization. In vehicular transportation, methane is used as compressed natural gas (CNG) and, in few cases, as liquefied natural gas (LNG). A potential key challenge of natural gas storage and delivery should be mass efficient and volume efficient at ambient temperature. The US Department of Energy has initiated a new methane storage program with the following ambitious targets:

(i) Gravimetric target is 0.5 g of CH_4 per gram of adsorbent.

(ii) Volumetric target is equivalent to 263 cm^3 (STP: 273.15 K, 1atm) per cm^3 of adsorbent. If we consider 25% packing loss, the required volumetric target becomes 350 cm^3 (STP).

1.4 Background of Present Research Work

MOFs are a new class of ordered porous solids that have been investigated in the past 15 years. MOFs are crystalline coordination polymers composed of metal clusters and organic linkers that self-assembled into one, two, or three-dimensional frameworks. The advantage of this class of materials is that by carefully choosing metal ions and organic ligands, it is possible to tailor the structures and sizes of pores within MOFs by design. Because of the wide variety of coordination geometries offered by transition and lanthanide metal ions and the rich number of structures and reactive functionalities that can be incorporated into organic linkers via organic synthesis, MOFs provide a means to generate a diverse range of framework architectures. A characteristic feature of MOFs is their extremely high surface areas and void volumes and pore openings ranging from 3 Å up to 20 Å that is highly accessible to organic guests.

In general, adsorption is primarily governed by the availability of high binding energy sites at low pressures and larger surface area and pore volume at higher pressures attributes to higher adsorption. In addition, the physical properties of the adsorbates, such as polarity, polarizability, and kinetic diameter, also play an important role. To exploit the structural diversity of MOFs for targeted applications, it is essential to understand the role of each of the constituents in the adsorbent framework.

1.5 Research Objectives

The main object of this research work focuses on the study of the effect of the functionality on gas adsorption properties of various categories of metal-organic frameworks (MOFs) *viz.* $[\{Cu_2(abtc)\}_3]$ (functional groups N=N and NH–NH), Cu–BTC (–H, –Br, and –I) and UiO–66 (–H, $–NH_2$, $–NO_2$, –COOH and $–(COOH)_2$). A significant improvement in adsorption uptakes was obtained for selective gas adsorption on these MOFs. It covers the following topics:

(1) Role of functional groups presented in the above mentioned MOFs on adsorption capacities.
(2) Evaluation of adsorption properties by measurement of gas adsorption with varying physical properties such as polarity, kinetic diameter, polarizability, dipole, and quadrupole moments.

(3) Effect of open metal sites presence on adsorption characteristics of the MOFs. Ideal Adsorbed Solution Theory was used to predict the selectivity of binary mixtures.

A Comparison of Adsorption Capacities of Cu–abtc versus Cu–hbtc Metal Organic Frameworks

Till date, different types of aromatic polycarboxylate ligands such as 1,3–benzenedicarboxylate (BDC), 1,3,5–benzenetricarboxylate (BTC), and 3,3′,5,5′–biphenyltetracarboxylate (BPTC) are well studied for adsorptive and separation processes, while there is limited literature on MOFs formed from the ligand 3,3′,5,5′–azobenzenetetracarboxylate (abtc). In addition to the abtc linker having photo-chromatic in nature, luminescence properties, the binding modes and geometrical configuration of the MOF resulting from the four carboxylic groups on the ligand increase the thermal stability and rigidity of the MOF. Our research interest lies in understanding the effect of the functional groups present on the ligand on the gas adsorption properties of the MOF. We reasoned that a subtle change by reducing the azo group in the abtc linker to form 3,3′,5,5′–

hydrazinebenzenetetracarboxylate (hbtc) would influence the structure and the adsorption characteristics of the resultant MOF. In this work, adsorptive characteristics of [{Cu_2(abtc)}$_3$] (also known as Cu–abtc) and [{Cu_2(hbtc)}$_3$] (also known as Cu–hbtc) are investigated for gases CO_2, CO, N_2, CH_4, C_2H_6, C_3H_8, and O_2 with varying wide range of polarity and polarizability. Adsorption isotherms are measured for a wide range of temperature and pressure. Modeling of obtained isotherms is done to get more insights into adsorbate–adsorbent interactions. The model parameters are utilized to calculate important thermodynamic parameters such as enthalpy of adsorption and Henry's constants. Ideal Adsorbed Solution Theory (IAST) predicts selectivity for binary mixtures at various conditions.

Selective Gas Adsorption on HKUST–1 Derivatives: Cu–BTC Versus Cu–(bromo)BTC Versus Cu–(iodo)BTC MOFs

Among the studied MOFs, Cu–BTC is one of the widely studied materials which comprised of Cu^{2+} metal clusters coordinated to 1,3,5–benzenetricarboxylate (BTC) organic linker makes three-dimensional structure with open metal sites. The resultant structure has big cavities with octahedral cages having a pore diameter of 9 Å. Several studies revealed that Cu–BTC having good thermal stability as well as without damage in crystal structure upon adsorption and desorption cycles. However, limited work has been done to modify the H_3BTC ligand for functionalizing Cu–BTC to optimize its properties for gases adsorption and separation. This work shows the effect of functionalization by comparing the gas adsorption properties of Cu–BTC versus Cu–(bromo)BTC versus Cu–(iodo)BTC over a wide range of temperature and pressure on industrially important gases CO_2, CO, CH_4, and N_2. IAST was performed to find potential separation of CO_2/N_2, CO_2/CH_4, and CO/CH_4 mixture for targeted applications, including natural gas processing, coal gasification, partial oxidation of hydrocarbons, etc.

The role of Functionality on CO_2, CH_4, CO, and N_2 Adsorption in UiO–66 Derivatives

In an industrial scale of synthesis, the adsorbent must possess stable, low cost, high uptake capacity, easily generable, and selective towards targeted applications. One MOF that satisfies above all the requirements is UiO–66 (UiO = University of Oslo). This work focuses on the effect of organic linker functionality on adsorption characteristics of CO_2, CH_4, CO, and N_2 over UiO–66, UiO–66–NH_2, UiO–66–NO_2, UiO–66–COOH, and UiO–66–$(COOH)_2$. By introducing polar and complex functional groups such as –NH_2, –NO_2, –COOH, and –$(COOH)_2$ improved the adsorption capacity initially, and it also caused the reduction of free volume, and which negatively contributed to adsorption at saturation levels.

References

(1) Swenson, H.; Stadie, N. P. Langmuir's Theory of Adsorption: A Centennial Review. *Langmuir* **2019**, *35*, 5409−5426.

(2) Rouquerol, F.; Rouquerol, J.; Sing, K. S. W. Adsorption by Powders and Porous Solids: Principles, Methodology, and Applications. *Academic Press: San Diego,* **1999**.

(3) Dabrowski, A. Adsorption from Theory to Practice. *Advance Colloid Interface Sci.* **2001**, *93*, 135−224.

(4) Kiefer, S.; Robens, E. Some Intriguing Items in the History of Volumetric and Gravimetric Adsorption Measurements. *J. Therm. Anal. Calorim.* **2008**, *94*, 613−618.

(5) Freundlich, H. Über die Adsorption in Lösungen. *Z. Phys. Chem.* **1907**, *57*, 385−470.

(6) McMillan, W. G.; Teller, E. The Assumption of the BET Theory. *J. Phys. Chem.* **1951**, *55*, 17–20.

(7) Kisliuk, P. The Sticking Probabilities of Gases Chemisorbed on the Surfaces of Solids. J. Phys. Chem. Solids **1957**, 3, 95–101.

(8) http://en.wikipedia.org/wiki/Physisorption.

(9) Barton, T. J.; Bull, L. M.; Klemperer, W. G.; Loy, D. A.; McEnaney, B.; Misono, M.; Monson, P. A.; Pez, G.; Scherer, G. W.; Vartuli, J. C.; Yaghi, O. M. Tailored Porous Materials. *Chem. Mater.* **1999**, *11*, 2633–2656.

(10) Virta, R. L (2011). 2009 Minerals Yearbook-Zeolites (PDF). USGS. Retrieved 8 Feb **2019**.

(11) Earl, D. J.; Deem M. W. Toward a Database of Hypothetical Zeolite Structures. *Ind. Eng. Chem. Res.* **2006**, *45*, 5449–5454.

(12) Szostak, R. Molecular Sieves-Principles of Synthesis and Identification. *Van Nostrand Reinhold Electrical/Computer Science and Engineering Series*, **1989**.

(13) Roth,W. J; Nachtigall, P; Morris, R. E. A Family of Zeolites With Controlled Pore Size Prepared Using A Top-Down Method. *Nat. Chem.* **2013**, *5*, 628–633.

(14) Knaebel, K. S. Adsorbent Selection. *Adsorption Research, Inc. Dublin, Ohio 43016,* **2003**.

(15) Zou, R.Q.; Sakurai, H.; Xu, Q. Preparation, Adsorption Properties, and Catalytic Activity of 3D Porous Metal-Organic Frameworks Composed of Cubic Building Blocks and Alkali-Metal Ions. *Angew Chem. Int. Ed Engl.* **2006,** *45*, 2542–2546.

(16) Alkordi, M. H.; Liu, Y.; Larsen, R. W.; Eubank, J. F.; Eddaoudi, M. Zeolite-like Metal-organic Frameworks as Platforms for Applications: on Metalloporphyrin-based Catalysts. *J. Am. Chem. Soc.* **2008**, *130*, 12639–12641.

(17) Xie, Z.; Guo, L.; Zheng, X.; Lin, X.; Chen, G. A New Porous Plastic Fiber Probe for Ammonia Monitoring. *Sensors and Actuators B: Chemical* **2005**, *104*, 173–178.

(18) Peppas, C.; Xergen, B.; Robert, W. C.; Merton, C. F.; Bernard, I.; Edward, J. K.; Subhash, M.; Patrick, V. *Elsevier: Oxford*, **2001**, 3492.

(19) Zhou, W.; Wu, H.; Yildirim, T. Enhanced H_2 Adsorption in Isostructural Metal-Organic Frameworks with Open Metal Sites: Strong Dependence of the Binding Strength on Metal Ions. *J. Am. Chem. Soc.* **2008**, *130*, 15268–15269.

(20) Collins, D. J.; Zhou, H. C. Hydrogen Storage in Metal-Organic Frameworks. *J. Mater Chem* **2007**, *17*, 3154–3160.

(21) Peng, Y.; Krungleviciute, V.; Eryazici, I.; Hupp, J. T.; Farha, O. K.; Yildirim, T. Methane Storage in Metal-Organic Frameworks: Current Records, Surprise Findings, and Challenges. *J. Am. Chem. Soc.* **2013**, *135*, 11887–11894.

(22) Herm, Z. R.; Swisher, J. A.; Smit, B.; Krishna, R.; Long, J. R. Metal-Organic Frameworks as Adsorbents for Hydrogen Purification and Pre-combustion Carbon Dioxide Capture. *J. Am. Chem. Soc*. **2011**, *133*, 5664–5667.

(23) Mason, J. A.; Sumida, K.; Herm, Z. R.; Krishna, R.; Long, J. R. Evaluating Metal-Organic Frameworks for Post-Combustion Carbon Dioxide Capture via Temperature Swing Adsorption. *Energy Environ. Sci.* **2011**, *4*, 3030–3040.

(24) Bloch, E. D.; Murray, L. J.; Queen, W. L.; Chavan, S.; Maximoff, S. N.; Bigi, J. P.; Krishna, R.; Peterson, V. K.; Grandjean, F.; Long, G. J. Selective Binding of O_2 over N_2 in a Redox-Active Metal-Organic Framework with Open Iron(II) Coordination Sites. *J. Am. Chem. Soc*. **2011**, *133*, 14814–14822.

(25) Couck, S.; Denayer, J. F. M.; Baron, G. V.; Remy, T.; Gascon, J.; Kapteijn, F. An Amine Functionalized MIL-53 Metal-Organic Framework with Large Separation Power for CO_2 and CH_4. *J. Am. Chem. Soc.* **2009**, *131*, 6326–6327.

(26). Zhao, C ; Dai, X ; Yao, T ; Chen, C ; Wang, X ; Wang, J ; Yang, J ; Wei, S ; Wu, Y ; Li, Y Ionic Exchange of Metal-Organic Frameworks to Access Single Nickel Sites for Efficient Electro-reduction of CO_2. *J. Am. Chem. Soc.* **2017**, *139*, 8078–8081.

(27) Horcajada, P.; Serre, C.; Vallet-Regi, M.; Sebban, M.; Taulelle, F.; Férey, G. Metal Organic Frameworks as Efficient Materials for Drug Delivery. *Angew. Chem. Int. Ed.* **2006**, *45*, 5974–5978.

(28) Fei, H.; Rogow, D. L.; Oliver, S. R. J. Reversible Anion Exchange and Catalytic Properties of Two Cationic Metal-Organic Frameworks Based on Cu(I) and Ag(I). *J. Am. Chem. Soc.* **2010**, *132*, 7202–7209.

(29) Loiseau, T.; Serre, C.; Huguenard, C.; Fink, G.; Taulelle, F.; Henry, M.; Bataille, T.; Férey, G. A Rationale for the Large Breathing of the Porous Aluminum Terephthalate (MIL-53) upon Hydration. *Chem. Eur. J.* **2004**, *10*, 1373–1382.

(30) Bourrelly, S.; Llewellyn, P. L.; Serre, C.; Millange, F.; Loiseau, T.; Ferey, G. Different Adsorption Behaviors of Methane and Carbon Dioxide in the Isotypic Nanoporous Metal-Terephthalates MIL-53 and MIL-47. *J. Am. Chem. Soc.* **2005**, *127*, 13519–13521.

(31) Yazaydin, A. O.; Snurr, R. Q.; Park, T.-H.; Koh, K.; Liu, J.; LeVan, M. D.; Benin, A. I.; Jakubczak, P.; Lanuza, M.; Galloway, D. B.; Low, J. J.; Willis, R. R. Screening of Metal-Organic Frameworks for Carbon Dioxide Capture from Flue Gas Using a Combined Experimental and Modeling Approach. *J. Am. Chem. Soc.* **2009**, *131*, 18198–18199.

(32) Ezhova, N. N.; Sudareva, S. V. Modern Methods for Removing Carbon Dioxide from Flue Gases Emitted by Thermal Power Stations. *Therm. Eng.* **2009**, *56*, 15–21.

(33) Romano, M. C.; Anantharaman, R.; Arastoc, A.; Ozcan, D. C.; Ahn, H.; Dijkstra, J. W.; Carbo, M.; Boavida. D. Application of Advanced Technologies for CO_2 Capture from Industrial Sources. *Energy Procedia* **2013**, *37*, 7176–7185.

CHAPTER 2

Literature Survey

This chapter presents a brief review of the history and state of the art progress of metal organic frameworks. Various methods were followed to synthesize MOFs, importance of MOF functionalization and post-synthesis modifications were explained. A review on adsorption uptakes of several important gases of our interest on MOFs is also included.

2.1 Metal Organic Frameworks (MOFs)

Metal organic frameworks (MOFs) are a novel crystalline microporous materials formed indefinitely from organic linkers and metal clusters [1–3]. The term 'MOF' first appeared in the literature around 1995 [4]. Prior to this, other acronyms such as porous coordination polymers (PCPs) [5] and porous coordination networks (PCNs) [6], metal azolate framework (MAF) [7], and ZIF (zeolite imidazolate framework) [8] terms used to represent MOFs. Due to a wide choice of metal ions and organic linkers a large number of MOFs can be designed and synthesized. The number of possible structures can further be increased through post-synthesis modification [9]. In addition to the high surface area, controllable pore size can also be achieved by functionalization resulting in good selectivity and capacity for adsorptive separations. These versatilities make MOFs highly promising materials for gas storage [10–12], gas separation [13–16], drug delivery [17,18], ion exchanging [19], catalysis [20], and micro sensing [21,22], etc. Over the past two decades, the research on MOF materials was exponentially increased due to their promising and interesting characteristics. According to Cambridge Structural Database

(CSD), thousands of extended crystalline metal-containing compounds are cataloged from 1978 through 2020 [23].

2.1.1 Background on MOFs

The first microporous materials began to appear in 1990 when Robson and co-workers recorded porous coordination polymers which displayed ion exchange properties [24]. In the meantime, Omar M. Yaghi and co-workers prepared a revolutionary compound that has been reported to be the first robust and highly porous material MOF–5 [1], which synthesized from zinc acetate building block and benzene 1, 4–dicarboxylic acid. Since then, MOF–5 and Cu–BTC are known to be widely studied structures due to their robust porosity and flexibility [25]. To extend the number of possible MOF structures, a new concept of isoreticular chemistry was introduced where IRMOFs [26] were synthesized by using a 1,4–benzenedicarboxylate acid (BDC) and other elongated dicarboxylate acids with functional groups such as phenols, alkyl amines and thiols [27]. Férey et al. created and designed a porous crystal structure, MIL–101, with a very large pore size and surface area, known for high chemical stability [28]. Mg–DOBDC and Ni–DOBDC materials have emerged as promising materials for low-pressure CO_2 adsorption and Methane storage, respectively [29]. Due to variability in the potential geometry, pore size, porosity, and functionality have opened the door for more than 20,000 various MOFs over the past few decades. However, successful synthetic strategies are still a formidable challenge for the preparation of MOFs with promising applications because the self-assembly of MOF is heavily influenced by structural characteristics of the ligands, coordination nature of metal ion, solvent system, pH value of the solution, reaction temperature and the ratio of metal source to organic ligand.

2.1.2 Design and Synthesis of MOFs

MOF materials possess tunable pore sizes, and structure diversity makes potential advantages over conventional adsorbents. So it is very important to know how these metal ions and organic linkers are connected to form MOF structures. In general, MOFs can be synthesized by the self–assembly of organic ligands and metal ions under hydro or solvothermal conditions to form crystals. The essential requirement to form a MOF is organic ligands coordination bonds with a central metal cluster to form secondary building unit (SBU). The extended structure of SBU is known as MOF. The surface area, pore size, pore-volume, and selective adsorption sites towards targeted application of MOFs can be controlled by choosing different metal ions and organic ligands [30]. The design of a MOF structure is always complicated, and it highly depends upon the mercy of intermolecular forces that limits our predictability. However, a combinatorial approach by making subtle changes in concentration, solvent polarity, pH, and temperature can lead to optimal MOF structure for targeted applications [31]. Some commonly used organic linkers in MOF synthesis explained in Table 2.1.

Firstly, Yaghi and co-workers locked metal ions and organic linkers into rigid metal-oxygen-carbon SBU clusters. MOF–2 [32] and MOF–5 [1] are synthesized based on this concept of SBUs. In MOF–5 (Figure 2.1), octahedral Zn_4O SBU clusters are connected by terephthalate ligands, resulting in a cubic network of MOF with exceptional porosity. In the majority of MOFs reported, organic ligands act as points of attachment to the inorganic metal clusters. The structural features of MOFs allow them to be predesigned; by a precise selection of the organic and inorganic components, materials can achievable desired topologies, structures, and properties known as reticular chemistry. An isoreticular series of MOFs (IRMOFs) contain the same underlying connectivity, and as a result, they share the same overall framework structure.

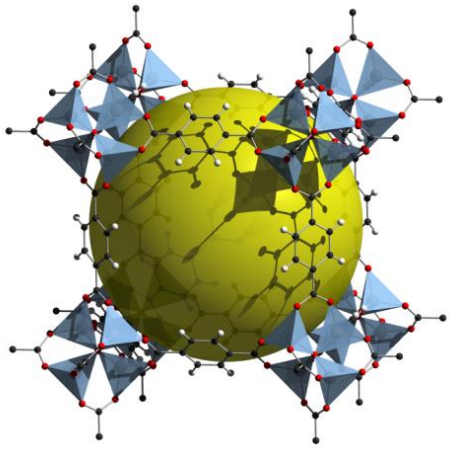

Figure 2.1: MOF–5 structure with topology. ZnO_4 tetrahedra (blue polyhedra) are connected by benzene dicarboxylate linkers (O, red, and C, black) to form MOF–5 structure [3].

In another well–known MOF is Cu–BTC (BTC = 1, 3, 5–benzenetricarboxylate), also commonly known as HKUST–1 (Figure 2.2). The Cu–BTC framework contains Cu^{2+} paddlewheel units with each Cu atom connected by 4 oxygen atoms of the bridging organic ligands. The resultant structure has big cavities with octahedral cages having a pore diameter of 9 Å. Several studies revealed that Cu–BTC has good thermal stability and is without damage in crystal structure upon adsorption and desorption cycles.

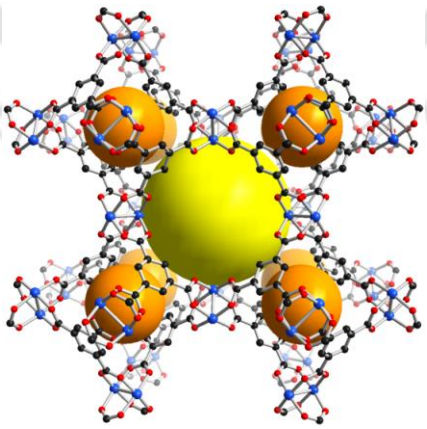

Figure 2.2: Framework structure of Cu–BTC (Blue: Cu, red: oxygen, black: carbon) [33].

Table 2.1: Some commonly used organic linkers in MOF synthesis.

Organic linker		MOF	Ref.
Name	**Structure**		
benzene 1,4–dicarboxylic acid	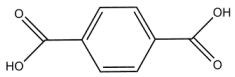	MOF–5	[34]
		MIL–53	[20]
		MIL–101	[35]
2–amino, benzene 1,4–dicarboxylic acid	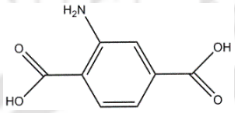	NH_2–MIL–53	[36]
		IRMOF–3	[37]
2,5–dihydroxy, benzene 1,4–dicarboxylic acid	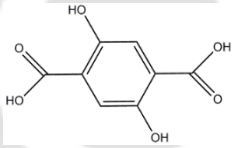	M/DOBDC (M = Mg, Zn, Co, Ni)	[13, 38]
naphthalene 2,6–dicarboxylic Acid	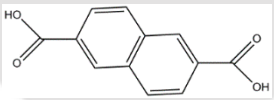	Al–NDC	[39]
azo benzene tetracarboxylic acid	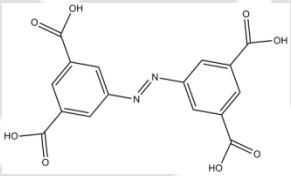	Cu–abtc	In this work
benzene 1,3,5–tricarboxylic acid	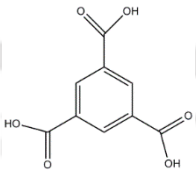	Cu–BTC or HKUST–1	[40]
		MIL–100	[41]
4,4',4''–benzene–1,3,5–triyltribenzoic acid	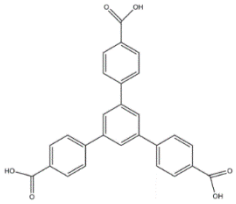	MOF–177	[37]
		MOF–519	[42]

MOFs are generally synthesized in self–assembly reaction between a metal salt and organic ligand. To synthesize MOFs, two different methods were followed. The popular method is solvothermal, and the other being non–solvothermal. The reaction in a closed container under autogenous pressure above the solvent boiling point is known as a solvothermal reaction [43]. On the other hand, nonsolvothermal reactions occur below or at the solvent's boiling temperature under ambient pressure [44], including centrifugal separation, ultrasonic irradiation and microwave–induced thermal method, etc. In the conventional solvothermal process, the reactants and solvent are mixed, and then seal them in a Teflon reactor and heat reactor at a temperature of usually below 573 K. The mixture will react under autogenous pressure above the boiling point the solvent. The reactants dissolve slowly with the increased temperature and react to form nice crystalline products. This method requires less time, and the equipment is simple and can be used for certain reactants. The product formation in this technique is greatly determined by the reaction temperature. Usually, more condensed structures are observed at higher temperatures. In order to get proper crystals and reaction rates, the increasing reaction temperature is needed for certain MOFs, especially if kinetically more inert ions are used. This method can be used for the synthesis of a wide variety of MOFs, which are among the most extensively studied. These include, among others: MOF–5, MOF–74, MOF–177, Cu–BTC (HKUST–1), and ZIF–8 etc.

2.2 Potential Applications of MOFs

The MOF materials possess versatile characteristics include tunable pore sizes, structural diversity, and surface areas, made researchers keen to investigate their potential applications in the field of gases adsorption, gases separation, drug delivery, ion exchanging, catalysis, and micro sensing, etc. Being porous materials, the application of MOFs on gas is of paramount importance. The most significant disadvantages of conventional technologies for gas absorption

are that equipment sizes are too large and energy is consumed too high. In contrast to this, MOFs are cost-effective, flexible and relatively easy to regenerate.

2.2.1 Gases Storage

Methane is the primary component of natural gas which has a potential for low carbon future energy. However, several challenges were prevented by the widespread use of natural gas in commercial vehicles. Most importantly, the volumetric energy density of natural gas at ambient temperature and pressure is only 0.04 MJ L^{-1}, compared to 32.4 MJ $L^{-1}$for gasoline or petrol [45]. Either compression or liquefaction can increase the volumetric energy density, but both solutions are costly and poorly suited for light-duty passenger vehicles. Compressed natural gas (CNG) requires expensive multi-stage compressors that consume energy and heavy, bulky fuel tanks that reduce passenger and cargo space. Even with compression to 250 bar, the energy density of CNG is 9MJL^{-1}, very low compared to 32.4 MJL^{-1} for gasoline (only 26% in gasoline). Moreover, CNG refueling stations are not yet common enough and are costly to build [46, 47]. Due to the low critical temperature of CH_4 (190.6 K), natural gas cannot be liquefied by compression alone, and cryogenic cooling is necessary to store liquefied natural gas (LNG). While the volumetric energy density of LNG can reach 20.8 MJL^{-1}(64% of gasoline) [45], the overall system energy density is reduced due to the insulation required to maintain a low temperature and prevent boil-off. Additionally, the high cost of cooling systems and complications of handling a cryogenic fuel make LNG unlikely to find much application in the transportation sector beyond commercial trucking and public transportation [48].

An alternative to CNG and LNG, to store natural gas in adsorbents is an emerging research area since the early 1970s [49]. Several types of research revealed that the ideal way of maximizing

the volumetric energy density of CH_4 is storing at 35 bar and 298 K [50]. The US Department of Energy CH_4 volumetric target is 263 cm^3 (STP: 273.15 K, 1atm) per cm^3 of adsorbent. If we consider 25% packing loss, the required volumetric target is 350 cm^3 (STP). The same gravimetric target is 0.5 g of CH_4 per gram of adsorbent. Over the last decade, MOFs have received significant attention as a new class of adsorbents potential for CH_4 storage. Some widely used MOFs for methane storage were illustrated in Table 2.2. In a major contribution, Yaghi and co-workers have synthesized a series of new high surface areas MOFs such as MOF–177, MOF–200, MOF–205, and MOF–210, which exhibited excellent gravimetric methane storage (293–331 cm^3g^{-1}) at 35 bar and ambient temperature. However, their volumetric capacities at the same conditions are considerably lower (only 67–126 cm^3 (STP)/ cm^3 of adsorbent) due to the poor crystal densities [51]. PCN–14 has been widely studied MOF for CH_4 storage which has a volumetric capacity of 230 v/v at 35 bar and 290 K [52], lower than the DOE target. Later, gravimetric CH_4 uptake capacities are measured on exceptionally high surface area MOFs DUT–49, NU–111, and PCN–68 having uptake capacities of 0.26, 0.24, and 0.24 g/g, respectively [53–55]. In 2013, Peng et al. [56] reported CH_4 uptake at 35 bar and 298 K on Ni/DOBDC was found to be 228 cm^3/cm^3, slightly higher than that on Cu–BTC (227 cm^3/cm^3) and PCN–14 (195 cm^3/cm^3). In the same work, Peng et al. [56] reported the highest total volumetric capacity of 267cm^3/cm^3 on Cu–BTC at 65 bar and 298 K, meeting the DOE volumetric target of 263 cm^3/cm^3. In 2014, Gandara et al. [57] reported high CH_4 volumetric storage capacity for MOF–519 found to be 279cm^3/cm^3 at 298 K and 80 bar. Mason et al. [58], performed the CH_4 adsorption on six different MOFs such as Cu–BTC, Ni/DOBDC, Mg/DOBDC, Co/DOBDC, PCN–14, and MOF–5 and compared with benchmark activated carbon AX–21. Ni/DOBDC and CO/ DOBDC exhibited the highest uptakes at lower pressures

regions. However, Ni/DOBDC and Cu–BTC have the highest total volumetric uptakes of 230 and 225 cm^3/cm^3 respectively at 35 bar and 298 K. Although PCN–14 has been widely cited as the best existing MOF for volumetric CH_4 storage (202 cm^3/cm^3 at 35 bar, 298 K), Ni/DOBDC and Cu–BTC have significantly higher volumetric capacities at 35 bar and 298 K.

2.2.2 Gasses Separation

Owing to their tunable structures and uniform pore size distributions, MOF materials were widely investigated to study their effectiveness in adsorptive separation applications. In 2011, Herm et al. [59] investigated on five different MOFs MOF–177, Be–BTB, Co–BDP, Cu–BTTri, and Mg/DOBDC for hydrogen purification and pre-combustion CO_2 capture. The single-component adsorption isotherms of CO_2 and H_2 were measured at 313 K upto 40 bar and compared with NaX and Carbon JX101. An IAST prediction says that exceptional CO_2 selectivity was observed over H_2 on Mg/DOBDC for a binary mixture containing 80% hydrogen at 313 K. Interestingly, both gravimetric as well as volumetric working capacities on Cu–BTTri, were higher than those on other adsorbents, including Mg/DOBDC. In another work, Herm et al. [60] analyzed Mg/DOBDC MOF for high-pressure $CO_2/CH_4/H_2$ separation, which resulted in significant enhancement in separation for Mg/DOBDC over benchmark NaX. Next, Mason et al. [61] evaluated the performance of MOF–177 and Mg/DOBDC for temperature swing adsorption process of CO_2 capture from flue gas by measuring the single-component adsorption isotherms of CO_2 and N_2 across the entire temperature range (293–473 K). They calculated working capacity, which says that the actual amount of CO_2 can be captured during a full adsorption/desorption cycle). A maximum working capacity of 17.6 wt.% was obtained for MOF–177 at 473 K desorption temperature. Interestingly, NaX exhibited higher working capacity than Mg/DOBDC for desorption temperature less than 353 K, but for higher desorption

temperatures, the working capacity of NaX was lower. CO_2 selectivity over N_2 at 313 K for a mixture of 0.15 bar CO_2 and 0.75 bar N_2 was also significantly higher on Mg/DOBDC (175) than that on MOF–177 (5) and NaX (115). Krishna et al. [62] examined Cu–BTC, MIL–101, Zn/DABCO, and Zeolite NaX for separation of CO_2 from a mixture of CH_4/CO for the pressure swing adsorption process. NaX exhibited the highest selectivity for CO_2 over CO and CH_4. For lower pressures (up to 10 bar), NaX exhibited the best performance due to its highest working capacity; however, at higher pressures (around 60 bar), Cu–BTC was better. Among all the adsorbents studied, MIL–101 exhibited the lowest working performance even though it has the highest surface area. Xiang et al. [63] compared CO_2 adsorptive separation on UTSA–16 with Mg/DOBDC, Cu–BTC, MIL–101, and many more adsorbents for CO_2/CH_4 and CO_2/N_2 gas mixture. Initially, Mg/DOBDC performed better than UTSA–16. However, after exposing both the adsorbents towards moisture, the performance of Mg/DOBDC decreases. On the other hand, CO_2 sorption was repeatable and reversible for UTSA–16 even after further exposing the adsorbent sample to air for three days.

The separation of O_2/N_2 is useful for medical and industrial applications. Bloch et al. [64] demonstrated newly synthesized MOF (Fe/DOBDC) having open metal sites. At 298 K and 1 bar, Fe/DOBDC binds O_2 preferentially over N_2, with an irreversible capacity of 9.3 wt.%. At 211 K, O_2 uptake was fully reversible, and the capacity increases to 18.2 wt.%. They reported that the highest O_2 over N_2 selectivity (7.5) for equimolar mixture at 1 bar and 298 K. However, high temperature (473K) was needed for desorption of O_2, which resulted in the decomposition of the structure. So they identified 226 K to be more suitable for separation of O_2/N_2 using Fe/DOBDC.

MOFs have shown extraordinary performance for lower olefin/paraffin separations. Bae et al. [65] performed an IAST study for propene/propane selectivity over Mg/DOBDC, Mn/DOBDC, and Co/DOBDC. They obtained selectivity for Co/DOBDC is 46 at 1 bar, 298 K for the equimolar mixture. In another work, Bloch et al. [66] measured equilibrium adsorption isotherms of methane, ethane, ethylene, acetylene, propane, and propylene on Fe/DOBDC at 318, 333, and 353 K to investigate its ability for C_1–C_3 separation. This material exhibits a very strong affinity for unsaturated acetylene, ethylene, and propylene hydrocarbons. For equimolar mixture at 318 K, ethylene selectivity over ethane on Fe/DOBDC ranges from 13 to 18, higher than that on NaX (9 to 14) and Mg/DOBDC (4 to 7). Similarly, the selectivity of propylene over propane on Fe/DOBDC (13 to 15) was also significantly higher than to other adsorbents.

2.3 Modification of MOF Structures

To improve the adsorption capacity, separation performance, physical and chemical properties of MOFs for targeted applications, modification of MOF structures are essential. The MOF structures can be modified by a variety of techniques as follows

2.3.1 Functionalization of MOFs

Functionalization of MOFs can be achieved by modifying the organic ligand with specific substituents and then using the modified ligand directly to synthesize the desired MOF. Biswas et al. [67] synthesized six vanadium-based MOFs MIL–47–X (X= −Cl, −Br, $-CH_3$, $-CF_3$, −OH, $-OCH_3$) along with the parent vanadium MIL–47. Among the six functionalized compounds, MIL–47–OCH_3 obtained the highest value of CO_2 loading found to be 5.9 mmol g^{-1} at 1 bar and 273 K, mainly driven by pore size and the nature of the functional group and CO_2 molecule interaction.

In 2012, Jasuja et al. [68] demonstrated an interesting research work on water vapour adsorption. By the introduction of polar functional groups in Zn(BDC–X)(DABCO) (X= –Br, –Cl, –OH, NO_2) results in water unstable MOFs compared to parent Zn(BDC)(DABCO). Polar functional groups presented in framework causing negative shielding effect; i.e., they facilitate hydrolysis of the Zn−O bond. On the other hand, placing non–polar groups ($–CH_3$) in the ligand enhances the stability of the MOF at 80% relative humidity compared to the parent MOF. This result shows that ligand functionalization is possible to adjust the water stability on MOFs. Lin et al. [69] worked on a series of isostructural MOFs $[Cu_2(X)(H_2O)_2]$ (X=tetra carboxylate ligands), named as NOTT–X series (NOTT–100 to NOTT–110). Among them, NOTT–103 exhibited very high gravimetric H_2 adsorption of 77.8 mg/g at 77K and 60 bar pressure, mainly driven by controlled pore size, enhancing the isosteric heat of adsorption and improving the H_2 adsorption. Lan et al. [70] demonstrated a family of diamondoid metal-organic frameworks (DMOF–X). DMOF–6 exhibited the highest surface area and H_2 adsorption capacity among this family of MOFs. N_2 and H_2 adsorption results show that the surface areas and hydrogen uptake capacities are determined by the most optimal combination of functional groups, interpenetration, and free volume in the system.

Wang et al. [71] demonstrated on the porous metal-organic frameworks Zn_4O(4–[N, N–bis(4–methylbenzoic acid)amino])–X benzoic acid (X= $–CH_3$, –Cl) and its functionalized derivatives. The H_2 adsorption capacities are highest for –Cl (266 $cm^3 g^{-1}$) followed by $–CH_3$ (259 $cm^3 g^{-1}$) and –H (250 $cm^3 g^{-1}$) at 77 K, 1 bar. Interestingly the CH_4 adsorption also showed that highest for –Cl (29.0 $cm^3 g^{-1}$) followed by $–CH_3$ (27.4 $cm^3 g^{-1}$) and –H (25.3 $cm^3 g^{-1}$) at 293 K, 1 bar. For CO_2 adsorption also exhibited slightly high for –Cl (96.2 $cm^3 g^{-1}$) followed by $–CH_3$ (85.4 $cm^3 g^{-1}$) and –H (82.0 $cm^3 g^{-1}$) at 273 K, 1 bar. This work revealed that the adsorbate-adsorbent

interaction plays an essential role in the gas-adsorption properties of these samples at low pressure, whereas the effects of the pore volumes and surface areas dominate the gas-adsorption properties at high pressure.

2.3.2 Post–synthetic Modification of MOF structures

In order to improve the performance of certain aspects of MOFs, post-synthetic modification has become a focus. Post-synthetic modification involves multiple approaches such as doping with metal ions, organic ligands, and solvents. In most cases, the pore size and pore shape of a MOF can be controlled through this approach, which can modify the selectivity of a MOF on adsorbed gases and the gas uptake capacities. Wang et al. [72] successfully reacted acetic anhydride with amino groups of IRMOF–3 (also known as $Zn_4O(H_2N–BDC)_3$) becomes amino-substituted version of IRMOF–1($Zn_4O(BDC)_3$). This process is realized by treating IRMOF–3 with dilute acetic anhydride solution in the presence of $CdCl_3$ under ambient conditions.

It was found that metal doping could greatly improve the H_2 uptake capacity near ambient conditions. Himsl et al. [73] exchanged the protons of hydroxyl pendants in MIL–53(Al) with lithium; it was found that 15% of the acidic framework protons were exchanged with lithium.

The H_2 uptake capacities at 77 K and 1 bar were 0.5 wt% and 1.7 wt% for pure MIL–53(Al) and MIL–53 (Al)/Li. In another work, Xiang et al. [74] reported that the effect of Li doping in Cu–BTC and Cr–BDC on H_2 adsorption properties. Due to doping, the pore volume and surface area of the MOFs were decreased significantly. However, H_2 uptake capacity increased by more than 40% compared to undoped MOFs. This work reveals appropriate loading of metal ions plays an important role at higher loadings of H_2.

2.4 Open metal sites in MOFs

Metal centers in a MOF system have a fixed number of coordination vacancies through which they connect to the organic ligands. If some of these positions can be opened, the material will have open metal sites or coordinatively unsaturated metal sites. These open metal sites possess additional electrostatic interactions for polar gases. Due to the presence of open metal sites, these MOFs exhibit high Henry's constants compared to without open metal sites MOFs. MIL–101is the one of the first synthesized MOF having open metal sites [75]. However, due to the small number of open metal sites present a bigger pore diameter of MIL–101, the effect is not pronounced, and Cu–BTC with a smaller pore size seems to be better for CO_2/CH_4 separation [76].

In the M/DOBDC series (M= Mg, Ni, Co, Zn, etc.) of MOFs, metal atoms are coordinatively bonded to the hydroxylate groups of the organic ligand [77]. This coordination results in the occupation of five coordination positions by the oxygen atoms, and the sixth position is occupied by water molecules. Water molecules can be removed after the activation or thermal treatment, resulting in one open metal site presence in the framework [78]. Zhang et al. [79] demonstrated CO_2 adsorption on Zn/DOBDC and Mg/DOBDC having open metal and Lewis basic sites that interact strongly with CO_2 and particularly effectively capture and separation of CO_2 from binary mixtures of CO_2/ N_2. CO_2 adsorption capacities for Zn/DOBDC and Mg/DOBDC are 19.8 and 26.0 wt.% respectively at 1 bar and 296 K. The CO_2 uptake on Mg/DOBDC represents the highest low pressure gravimetric and volumetric adsorption capacity among known MOFs.

2.5 Simulation Studies on MOFs

Due to the vast choices of metal atoms and organic linkers, a large number of MOFs can be synthesized. However, it is infeasible to design the optimal MOF structure for a targeted application only by experimentation. Experimental methods cannot obtain macroscopic properties, and simulations can provide molecular-level insights into the underlying mechanism involved [80, 81]. Simulations can help screen the large number of MOFs for a particular application and can also provide the ability to hypothesize the structure of the best performing MOF. In most simulation studies, the Grand Canonical Monte Carlo (GCMC) method estimates the adsorption isotherms. Wilmer et al. [82] demonstrated a computational approach for better CH_4 storage and generated many MOFs from a given chemical library of building blocks and rapidly screened them to find the best candidates for a specific application. From a library of 102 building blocks, generated 137,953 hypothetical MOFs and for each one, calculated the pore–size distribution, surface area, and CH_4 storage capacity. Over 300 MOFs were predicted for better CH_4 storage capacity, which reveals structure-property relationships. Methyl, ethyl, and propyl functionalized MOFs were frequently top performers. Krishna [83] presented a review on diffusion characteristics of single gas and a mixture of gases in a wide spectrum of MOFs. Jhon et al. [84] demonstrated a simulation study on the effect of alkoxy-functionalization on IRMOFs, which results in the highest CH_4 uptake at low and moderate pressure on IRMOF–6 due to the stronger potential overlap of smaller pores. In 2012, Watanabe et al. [85] screened more than 30,000 synthesized MOFs from the CSD database and finally sorted out 359 MOFs with appropriate pore sizes for CO_2/N_2 separations. Later, Snurr and co-workers [86] screened 20,000 MOFs, excluded highly disordered materials, and ended up having 4,764 MOFs. In this way, they prepared a very useful database called computation-ready experimental MOFs.

2.6 A Review on Adsorption of the Gases of our Interest

One important parameter to screen an adsorbent for gases adsorption and separation applications always widens the scope to study other various gases. This section focuses on single gas adsorptions of various gases that have so far been reported. An overview of literature data on representative adsorption uptakes of several adsorbates used in this study on various MOFs is presented in Tables 2.2–2.8.

Table 2.2: Representative literature for CO_2 adsorption.

Adsorbent	BET Surface Area ($m^2 g^{-1}$)	At 1 bar pressure		At 40 bar pressure		Enthalpy of adsorption at zero coverage (kJ mol^{-1})	Ref.
		Amount adsorbed (mol kg^{-1})	Temp (K)	Amount adsorbed (mol kg^{-1})	Temp (K)		
MOF–2	345	0.6	298	3.2	298	–	[37]
MOF–5	2833	1.0	298	22	298	14.5	[37, 87]
MIL–53(Al)	1500^{L}	2.3	304	10.4 (25 bar)	304	35 – 17	[21]
MIL–100	1900	–	–	17.5	303	62	[88]
MIL–101	4230	–	–	37	304	44	[88]
IRMOF–3	2160	1.1	298	18.8	198	–	[37]
IRMOF–6	2516	1.05	298	19.7	298	–	[37]
IRMOF–11	2096	1.5	298	14.8	298	–	[37]
Cu–btc	1663	5.8	295	15.4	295	23	[89]
NOTT–100	1547	3.2	298	10.4	298	–	[37]
Mg/DOBDC	1800	8.0	293	15	313	–	[13]
Ni/DOBDC	1218	6.9	298	12	298	36	[90]
Co/DOBDC	1080	6.7	296	–	–	–	[91]
Zn/DOBDC	816	4.6	298	10.4	298	–	[37]
Ni/DABCO	1705	2.0	298	12 (15 bar)	298	20.4	[92]
Zn/DABCO	1725	2.0	298	14 (15 bar)	298	21.6	[92]
MOF–200	4530	–	–	55	298	–	[51]
MOF–205	4460	–	–	33	298	–	[51]
MOF–210	6240	–	–	53	298	–	[51]
Zeolite 13X	616	4.7	298	6.9	298	49	[93]
Silicalite	440	1.4	308	2.9	304	28	[94, 95]

L: Langmuir surface area

Table 2.3: Representative literature for CH_4 adsorption.

Adsorbent	BET Surface Area ($m^2\ g^{-1}$)	Pore volume ($cc\ g^{-1}$)	Excess amount adsorbed ($mol\ kg^{-1}$)	Total amount adsorbed		Pressure (bar)	Temp (K)	Ref.
				($mol\ kg^{-1}$)	($mol\ L^{-1}$)			
Ni/DOBDC	1593^{L}	0.56	7.77	8.62	10.27	35	298	[58]
Cu-BTC	2203^{L}	0.77	10.23	11.38	10.04	35	298	[58]
Co/DOBDC	1433^{L}	0.51	7.63	8.39	9.87	35	298	[58]
PCN-14	2360^{L}	0.83	9.64	10.89	9.02	35	298	[58]
Mg/DOBDC	1957^{L}	0.69	8.78	9.82	8.93	35	298	[58]
NJU-Bai10	2883	1.11	11.49	13.21	8.79	35	290	[96]
NOTT-109	2110	0.85	9.89	11.16	8.79	35	300	[97]
UTSA-20	1156	0.63	8.75	9.69	8.79	35	300	[98]
NOTT-101	2805	1.08	11.16	12.77	8.75	35	300	[97]
PCN-11	1931	0.91	10.20	11.56	8.66	35	298	[99]
NOTT-100	1661	0.68	8.32	9.33	8.66	35	300	[97]
NOTT-103	2958	1.16	11.71	13.44	8.66	35	300	[97]
PCN-16	2273	1.06	10.25	11.83	8.57	35	300	[100]
NOTT-107	1770	0.77	10.10	11.25	8.53	35	298	[101]
Zn/DOBDC	885	0.41	6.21	6.83	8.39	35	298	[38]
MIL-53(Al)	1235	0.54	7.69	8.48	8.30	35	303	[102]
NOTT-102	3342	1.27	11.86	13.75	8.08	35	300	[91]
NU-125	3120	1.29	11.90	13.84	7.99	35	298	[103]
IRMOF-6	2630^{L}	0.92	10.70	12.14	7.90	36.5	298	[26]
Mn/DOBDC	1102	0.50	11.39	12.14	7.90	35	298	[38]
UIO-66-NH_2	1080	0.40	4.90	5.49	7.46	35	303	[104]
IRMOF-1	3995^{L}	1.40	8.65	10.76	6.70	35	298	[58]
UIO-66	970	0.36	4.38	4.91	6.52	35	303	[104]
IRMOF-3	2160	1.07	8.57	10.18	6.43	36.5	298	[62, 105]

L: Langmuir surface area

Contd. (Representative literature for CH_4 adsorption)

Adsorbent	BET Surface Area ($m^2\ g^{-1}$)	Pore volume ($cc\ g^{-1}$)	Excess amount adsorbed ($mol\ kg^{-1}$)	Total amount adsorbed		Pressure (bar)	Temp. (K)	Ref.
				($mol\ kg^{-1}$)	($mol\ L^{-1}$)			
MIL-125	1820	0.67	6.78	7.77	6.29	35	303	[104]
UTSA-62	2190	0.91	9.17	10.54	6.21	35	298	[106]
NU-111	4930	2.09	11.72	14.87	6.07	35	298	[107]
PCN-66	4000	1.63	11.12	13.57	5.98	35	298	[108]
DUT-23 (Co)	4850	2.03	11.72	14.78	5.94	35	298	[109]
SNU-71	1770	0.71	5.85	6.92	5.80	35	298	[110]
PCN-68	5109	2.13	11.62	14.82	5.63	35	298	[108]
MOF-177	4500	1.89	10.24	13.08	5.63	35	298	[51]
ZIF-8	1445	0.59	4.00	4.87	5.54	35	303	[111]
MIL-125	1820	0.67	6.78	7.77	6.29	35	303	[104]
UTSA-62	2190	0.91	9.17	10.54	6.21	35	298	[106]
NU-111	4930	2.09	11.72	14.87	6.07	35	298	[107]
PCN-66	4000	1.63	11.12	13.57	5.98	35	298	[108]
DUT-23 (Co)	4850	2.03	11.72	14.78	5.94	35	298	[109]
SNU-71	1770	0.71	5.85	6.92	5.80	35	298	[110]
PCN-68	5109	2.13	11.62	14.82	5.63	35	298	[108]
MOF-177	4500	1.89	10.24	13.08	5.63	35	298	[51]
ZIF-8	1445	0.59	4.00	4.87	5.54	35	303	[111]
MIL-100	1900	1.10	6.01	7.63	5.36	35	303	[88]
MOF-205	4460	2.16	10.77	14.02	5.31	35	298	[51]
IRMOF-8	4326	1.83	8.59	11.34	5.09	35	298	[112]
NOTT-119	4118	2.35	9.59	13.13	4.73	35	298	[113]
MIL-101	4230	2.15	7.10	10.27	4.51	35	303	[88]

Contd. (Representative literature for CH_4 adsorption)

Adsorbent	BET Surface Area ($m^2\ g^{-1}$)	Pore volume ($cc\ g^{-1}$)	Excess amount adsorbed ($mol\ kg^{-1}$)	Total amount adsorbed		Pressure (bar)	Temp. (K)	Ref.
				($mol\ kg^{-1}$)	($mol\ L^{-1}$)			
MOF-210	6240	3.60	9.36	14.78	3.71	35	298	[51]
MOF-200	4530	3.59	8.17	13.57	2.99	35	298	[51]
AX-21 activated carbons	4880^L	1.64	11.59	14.06	6.88	35	298	[58]
Zeolite 13X	616	0.27	2.89	3.30	4.73	35.5	298	[114, 115]

L: Langmuir surface area

Table 2.4: Representative literature for CO adsorption.

Adsorbent	Low pressure			High pressure			Enthalpy of adsorption At zero coverage ($kJ\ mol^{-1}$)	Ref.
	Excess amount adsorbed ($mol\ kg^{-1}$)	Pressure (bar)	Temp. (K)	Excess amount adsorbed ($mol\ kg^{-1}$)	Pressure (bar)	Temp. (K)		
IRMOF-1	0.58	1	298	7.2^g	40	298	9.3	[116]
IRMOF-3	0.6^g	1	298	7.2^g	40	298	10.1	[116]
Zn/DABCO	–	–	–	7.8^g	40	298	12	[116]
Cu-BTC	1.4	1	295	9.1	43	295	24	[117]
MIL-101	0.89	1	295	6.6	68	295	44	[117]
Ni/DOBDC	5.6	0.8	303	–	–	–	58	[118]
MIL-53(Al)	0.30	1	303	–	–	–	16.4	[102]
Zeolite 13X	1.17	1.1	303	3.12	10.2	303	20	[119]
Silicalite	0.27	1.2	305	1.0	7.3	305	16.7	[120]

g: data obtained from GCMC simulations

Table 2.5: Representative literature for N_2 adsorption.

Adsorbent	**Low pressure**			**High pressure**			**Enthalpy of adsorption at zero coverage (kJ mol^{-1})**	**Ref.**
	Excess amount adsorbed (mol kg^{-1})	**Pressure (bar)**	**Temp. (K)**	**Excess amount adsorbed (mol kg^{-1})**	**Pressure (bar)**	**Temp. (K)**		
IRMOF-1	–	–	–	4.8[g]	40	298	8.4	[116]
RMOF-3	–	–	–	4.85[g]	40	298	9	[116]
Zn/DABCO	–	–	–	5.2[g]	40	298	11	[116]
	–	–	–	1.48	15	298	–	[92]
Ni/DABCO	–	–	–	1.46	15	298	–	[92]
MIL-53(Al)	0.20	1	303	–	–	–	15.9	[102]
Cu-BTC	0.31	1	295	2.32	10	298	–	[121, 30]
MOF-177	0.2	1	293	–	–	–	10	[14]
Mg/DOBDC	1.1	1	293	–	–	–	18	[14]
Ni/DOBDC	1.02	1	298	6.45	100	298	–	[90]
Zeolite 13X	0.8	2	298	–	–	–	–	[93]
	–	–	–	2.5	100	288	14 – 9.1	[122]
Silicalite	0.27	1.2	305	1.0	7.3	305	16.7	[120]
Norit R1	0.39	1.1	298	4.1	59.8	298	–	[123]

g: data obtained from GCMC simulations

Table 2.6: Representative literature for C_2H_6 adsorption.

Adsorbent	Low pressure			High pressure			Enthalpy of adsorption at zero coverage (kJ mol^{-1})	Ref.
	Excess amount adsorbed (mol kg^{-1})	Pressure (bar)	Temp (K)	Excess amount adsorbed (mol kg^{-1})	Pressure (bar)	Temp (K)		
Cu-BTC	1.0	0.1	295	4.8	1	295	–	[30]
MOF-5	–	–	–	1.9	1	297	15.1	[124]
MIL-101	3.0	1	298	15.5	8.5	298	45-30	[125]
Mg/DOBDC	1.5	0.1	298	6.3	1	298	27	[126]
Fe/DOBDC	1.03	0.1	318	6.6	1	318	25	[66]
Zeolite 13X	0.4	0.1	323	1.6	1	323	29.22	[127]
Silicalite	1.9	1	308	2.4	20	308	29	[95]
Zeolite 5A	1.4	1	293	2.22	13.9	293	10	[128]

Table 2.7: Representative literature for C_3H_8 adsorption.

Adsorbent	**Low pressure**			**High pressure**			**Enthalpy of adsorption at zero coverage (kJ mol^{-1})**	**Ref.**
	Excess amount adsorbed	**Pressure (bar)**	**Temp (K)**	**Excess amount adsorbed**	**Pressure (bar)**	**Temp (K)**		
Cu-BTC	5.2	0.1	318	7.2	1	303	44	[129]
MOF-5	17.5	0.1	300	19	1	300	20.17	[130]
MIL-53(Cr)	2.4	0.1	303	4.0	1	303	–	[131]
MIL-53(Fe)	0.0	0.1	303	2.4	1	303	–	[131]
Mg/DOBDC	7.1	0.1	298	8.2	1	298	33	[126]
Fe/DOBDC	4.6	0.1	318	5.3	1	318	33	[66]
NaX	3	0.1	293	3.2	1	293	34.4	[132]
Silicalite	1.66	0.1	308	1.94	1	308	41	[95]
activated carbon ASA	5.0	0.1	273	8.3	1	273	40.7	[133]

Table 2.8: Representative literature for O_2 adsorption.

Adsorbent	Low pressure			High pressure			Enthalpy of adsorption at zero coverage (kJ mol^{-1})	Ref.
	Excess amount adsorbed (mol kg^{-1})	Pressure (bar)	Temp (K)	Excess amount adsorbed (mol kg^{-1})	Pressure (bar)	Temp (K)		
Cu-BTC	0.3	1	295	–	–	–	13.88	[30]
MIL-53(Al)	0.13	1	303	–	–	–	14.5	[107]
Zn/DABCO	0.4	2.5	298	–	–	–	–	[92]
Fe/DOBDC	3.75	0.1	226	5.4	1	226	41	[15]
Zeolite 13X	0.2	1	306	–	–	–	15	[134]
Silicalite	0.15	1	305	–	–	–	16.3	[135]
Zeolite 5A	0.18	0.96	296	1.8	17.7	296	10	[136]
AC (BPL)	0.42	1.6	303	3.4	37.4	303	–	[137]

References

(1) Li, H.; Eddaoudi, M.; O'Keeffe, M.; Yaghi, O. M. Design and Synthesis of an Exceptionally Stable and Highly Porous Metal Organic Framework. *Nature* **1999**, *402*, 276–279.

(2) Chen, B.; Eddaoudi, M.; Hyde, S. T.; O'Keeffe, M.; Yaghi, O. M. Interwoven Metal-Organic Framework on a Periodic Minimal Surface with Extra-Large Pores. *Science* **2001**, *291*, 1021–1023.

(3) Yaghi, O. M.; O'Keeffe, M.; Ockwig, N. W.; Chae, H. K.; Eddaoudi, M.; Kim, J. Reticular Synthesis and the Design of New Materials. *Nature* **2003**, *423*, 705–714.

(4) Yaghi, O. M.; Li, H. Hydrothermal Synthesis of a Metal-Organic Framework Containing Large Rectangular Channels. *J. Am. Chem. Soc.***1995**, *117*, 10401–10402.

(5) Kitagawa, S.; Kitaura, R.; Noro, S. Functional Porous Coordination Polymers. *Angew. Chem. Int. Ed.* **2004**, *43*, 2334–2375.

(6) Kesanli, B.; Lin, W. Chiral Porous Coordination Networks: Rational Design and Applications in Enantioselective Processes. *Coord. Chem. Rev.* **2003**, *246*, 305–326.

(7) Lin, J. B.; Zhang, J. P.; Chen, X. M. Nonclassical Active Site for Enhanced Gas Sorption in Porous coordination polymer. *J. Am. Chem. Soc.* **2010**, *132*, 6654–6656.

(8) Park, K. S.; Ni, Z.; Cote, A. P.; Choi, J. Y.;Huang, R. D.; Uriberomo, F. J.; Chae, H. K.; O'Keeffe, M.; Yaghi, O. M. Exceptional Chemical and Thermal Stability of Zeolitic Imidazolate Frameworks. *Proc. Natl. Acad. Sci.* USA **2006**, *103*, 10186–10191.

(9) Wang, Z.; Cohen, S. M. Post-synthetic Modification of Metal-Organic Frameworks. *Chem. Soc. Rev.* **2009**, *38*, 1315–1329.

(10) Zhou, W.; Wu, H.; Yildirim, T. Enhanced H_2 Adsorption in Isostructural Metal-Organic Frameworks with Open Metal Sites: Strong Dependence of the Binding Strength on Metal Ions. *J. Am. Chem. Soc.* **2008**, *130*, 15268–15269.

(11) Collins, D. J.; Zhou, H. C. Hydrogen Storage in Metal-Organic Frameworks. *J. Mater. Chem.* **2007**, *17*, 3154–3160.

(12) Peng, Y.; Krungleviciute, V.; Eryazici, I.; Hupp, J. T.; Farha, O. K.; Yildirim, T. Methane Storage in Metal-Organic Frameworks: Current Records, Surprise Findings, and Challenges. *J. Am. Chem. Soc.* **2013**, *135*, 11887–11894.

(13) Herm, Z. R.; Swisher, J. A.; Smit, B.; Krishna, R.; Long, J. R. Metal-Organic Frameworks as Adsorbents for Hydrogen Purification and Pre-combustion Carbon Dioxide Capture. *J. Am. Chem. Soc.* **2011**, *133*, 5664–5667.

(14) Mason, J. A.; Sumida, K.; Herm, Z. R.; Krishna, R.; Long, J. R. Evaluating Metal-Organic Frameworks for Post-Combustion Carbon Dioxide Capture via Temperature Swing Adsorption. *Energy Environ. Sci.* **2011**, *4*, 3030–3040.

(15) Bloch, E. D.; Murray, L. J.; Queen, W. L.; Chavan, S.; Maximoff, S. N.; Bigi, J. P.; Krishna, R.; Peterson, V. K.; Grandjean, F.; Long, G. J. Selective Binding of O_2 over N_2 in a Redox-Active Metal-Organic Framework with Open Iron(II) Coordination Sites. *J. Am. Chem. Soc.* **2011**, *133*, 14814–14822.

(16) Couck, S.; Denayer, J. F. M.; Baron, G. V.; Remy, T.; Gascon, J.;́ Kapteijn, F. An Amine Functionalized MIL-53 Metal-Organic Framework with Large Separation Power for CO_2 and CH_4. *J. Am. Chem. Soc.* **2009**, *131*, 6326–6327.

(17) Zhao, C ; Dai, X ; Yao, T ; Chen, C ; Wang, X ; Wang, J ; Yang, J ; Wei, S ; Wu, Y ; Li, Y Ionic Exchange of Metal-Organic Frameworks to Access Single Nickel Sites for Efficient Electro-reduction of CO_2. *J. Am. Chem. Soc.* **2017**, *139*, 8078–8081.

(18) Horcajada, P.; Serre, C.; Vallet-Regi, M.; Sebban, M.; Taulelle, F.; Férey, G. Metal Organic Frameworks as Efficient Materials for Drug Delivery. *Angew. Chem., Int. Ed.* **2006**, *45*, 5974–5978.

(19) Fei, H.; Rogow, D. L.; Oliver, S. R. J. Reversible Anion Exchange and Catalytic Properties of Two Cationic Metal-Organic Frameworks Based on Cu(I) and Ag(I). *J. Am. Chem. Soc.* **2010**, *132*, 7202–7209.

(20) Loiseau, T.; Serre, C.; Huguenard, C.; Fink, G.; Taulelle, F.; Henry, M.; Bataille, T.; Férey, G. A Rationale for the Large Breathing of the Porous Aluminum Terephthalate (MIL–53) upon Hydration. *Chem. Eur. J.* **2004**, *10*, 1373–1382.

(21) Bourrelly, S.; Llewellyn, P. L.; Serre, C.; Millange, F.; Loiseau, T.; Férey, G. Different Adsorption Behaviors of Methane and Carbon Dioxide in the Isotypic Nanoporous Metal-Terephthalates MIL–53 and MIL–47. *J. Am. Chem. Soc.* **2005**, *127*, 13519–13521.

(22) Yazaydin, A. O.; Snurr, R. Q.; Park, T.-H.; Koh, K.; Liu, J.; LeVan, M. D.; Benin, A. I.; Jakubczak, P.; Lanuza, M.; Galloway, D. B.; Low, J. J.; Willis, R. R. Screening of Metal-

Organic Frameworks for Carbon Dioxide Capture from Flue Gas Using a Combined Experimental and Modeling Approach. *J. Am. Chem. Soc.* **2009**, *131*, 18198–18199.

(23) Long, J. R.; Yaghi O. M. The Pervasive Chemistry of Metal-Organic Frameworks. *Chem. Soc. Rev.* **2009**, *38*, 1213–1214.

(24) Hoskins, B. F.; Robson, R. Design and Construction of a New Class of Scaffolding–Like Materials Comprising Infinite Polymeric Frameworks of 3d-Linked Molecular Rods. A Reappraisal of the $Zn(CN)_2$ and $Cd(CN)_2$ Structures and the Synthesis and Structure of the Diamond-Related Frameworks $[N(CH_3)_4][Cu^{I}Zn^{II}(CN)_4]$ and Cu^{I}[4,4′,4″,4‴ Tetra cyano tetraphenyl methane] $BF_4 \cdot xC_6H_5NO_2$. *J. Am. Chem. Soc.* **1990**, *112*, 1546–1554.

(25) Chui, S. S.-Y.; Lo, S. M.-F.; Charmant, J. P. H.; Orpen, A. G.; Williams, I. D., A Chemically Functionalizable Nanoporous Material $[Cu_3(TMA)_2(H_2O)_3]_n$. *Science* **1999**, *283*, 1148–1150.

(26) Eddaoudi, M.; Kim, J.; Rosi, N.; Vodak, D.; Wachter, J.; O'Keeffe, M.; Yaghi, O. M., Systematic Design of Pore Size and Functionality in Isoreticular MOFs and Their Application in Methane Storage. *Science* **2002**, 295, 469–472.

(27) Cohen, S. M. Postsynthetic Methods for The Functionalization of Metal-organic Frameworks. *Chemical reviews* **2012**, *112*, 970–1000.

(28) Férey, G.; Mellot-Draznieks, C.; Serre, C.; Millange, F.; Dutour, J.; Surblé, S.; Margiolaki, I. A Chromium Terephthalate-Based Solid with Unusually Large Pore Volumes and Surface Area. *Science* **2005**, *309*, 2040–2042.

(29) Mishra, P.; Edubilli, S.; Mandal, B.; Gumma, S. Adsorption Characteristics of Metal Organic Frameworks Containing Coordinatively Unsaturated Metal Sites: Effect of Metal Cations and Adsorbate Properties. *J. Phys. Chem. C* **2014**, *118*, 6847–6855.

(30) García-Pérez, E.; Gascón, J.; Morales-Flórez, V.; Castillo, J. M.; Kapteijn, F.; Calero, S. Identification of Adsorption Sites in Cu-BTC by Experimentation and Molecular Simulation. *Langmuir* **2009**, *25*, 1725–1731.

(31) Rowsell, J. L. C.; Yaghi, O. M. Metal-organic Frameworks: A New Class of Porous Materials. *Microporous and Mesoporous Mater.* **2004**, *73*, 3–14.

(32) Li, H.; Eddaoudi, M.; Groy, T. L.; Yaghi, O. M. Establishing Microporosity in Open Metal-Organic Frameworks: Gas Sorption Isotherms for Zn(BDC) (BDC ¼ 1,4-benzenedicarboxylate). *J. Am. Chem. Soc.* **1998**, *120*, 8571–8572.

(33) Yakovenko, A. A.; Reibenspies, J. H.; Bhuvanesh, N.; Zhou, H. C. Generation and Applications of Structure Envelopes for Porous Metal-organic Frameworks. *J. Appl. Crystallogr.* **2013**, *46*, 346–353.

(34) Eddaoudi, M.; Li, H.; Yaghi, O. M.; Highly Porous and Stable Metal-organic Frameworks: Structure Design and Sorption Properties. *J. Am. Chem. Soc.* **2000,** *122*, 1391–1397.

(35) Chowdhury, P.; Bikkina, C.; Gumma, S. Gas Adsorption Properties of The Chromium-Based Metal Organic Framework MIL-101. *J. Phys. Chem.C.* **2009**, *113*, 6616–6621.

(36) Arstad, B.; Fjellvåg, H.; Kongshaug, K.; Swang, O.; Blom, R. Amine Functionalised Metal Organic Frameworks (MOFs) as Adsorbents for Carbon dioxide. *Adsorption* **2008,** *14*, 755–762.

(37) Millward, A. R.; Yaghi, O. M. Metal Organic Frameworks with Exceptionally High Capacity for Storage of Carbon Dioxide at Room Temperature. *J. Am. Chem. Soc.* **2005,** *127,* 17998–17999.

(38) Wu, H.; Zhou, W.; Yildirim, T. High-Capacity Methane Storage in Metal–Organic Frameworks M_2(dhtp): The Important Role of Open Metal Sites. *J. Am. Chem. Soc.* **2009,** *131,* 4995–5000.

(39) Senkovska, I.; Hoffmann, F.; Froeba, M.; Getzschmann, J.; Boehlmann, W.; Kaskel, S. New Highly Porous Aluminum Based Metal-organic Frameworks: Al(OH)(ndc) (ndc = 2,6-naphthalene dicarboxylate) and Al(OH)(bpdc) (bpdc =4,4'-biphenyl dicarboxylate). *Microporous Mesoporous Mater.* **2009**, *122,* 93–98.

(40) Chowdhury, P.; Bikkina, C; Meister, D; Dreisbach, F.; Gumma, S. Comparison of Adsorption Isotherms on Cu-BTC Metal Organic Frameworks Synthesized from Different Routes. *Microporous and Mesoporous Mater.* **2009,** *117,* 406–413.

(41) Sumida, K.; Her, J.-H.; Dinc_a, M.; Murray, L. J.; Schloss, J. M.; Pierce, C. J.; Thompson, B. A.; FitzGerald, S. A.; Brown, C. M.; Long, J. R. A Metal-Organic Framework with Exposed Cr^{2+} Sites. *J. Phys. Chem. C* **2011,** *115,* 8414–8421.

(42) Gándara, F.; Furukawa, H.; Lee, S.; Yaghi, O. M. High Methane Storage Capacity in Aluminum Metal-Organic Frameworks. *J. Am. Chem. Soc.* **2014**, *136,* 5271– 5274.

(43) Huang, L.; Wang, H.; Chen, J.; Wang, Z.; Sun, J.; Zhao, D.; Yan, Y. Synthesis, Morphology Control, and Properties of Porous Metal-organic Coordination Polymers. *Microporous Mesoporous Mater.* **2003**, *58,* 105–114.

(44) Stock, N.; Biswas, S. Synthesis of Metal-Organic Frameworks (MOFs): Routes to Various MOF Topologies, Morphologies, and Composites. *Chem. Rev.* **2012**, *112*, 933–967.

(45) Alternative Fuels Data Center–Fuel Properties Comparison, 2013.

http://www.afdc.energy.gov/fuels/fuel_comparison_chart.pdf.

(46) Yeh, S. An Empirical Analysis on the Adoption of Alternative Fuel Vehicles: The Case of Natural Gas Vehicles. *Energy Policy* **2007**, *35*, 5865–5875.

(47) Whyatt, G. A. Issues Affecting Adoption of Natural Gas in Light- and Heavy Duty Vehicles **2010**, PNNL-19745.

(48) Menon, V. C.; Komarneni, S. Porous Adsorbents for Vehicular Natural Gas Storage: A Review. *J. Porous Mater.* **1998**, *5*, 43–58.

(49) Munson, R. A.; Clifton, Jr., R. A. Natural gas storage with zeolites. *Bureau of Mines Nonmetallic Minerals Program, U.S. Dept. Interior* **1971**, *38*, 12.

(50) Matranga, K. R.; Myers, A. L.; Glandt, E. D. Storage of Natural Gas by Adsorption on Activated Carbon. *Chem. Eng. Sci.* **1992**, *47*, 1569–1579.

(51) Furukawa, H.; Ko, N.; Go, Y. B.; Aratani, N.; Choi, S. B.; Choi, E.; Yazaydin, A. O.; Snurr, R. Q.; O'Keeffe, M.; Kim, J.; Yaghi, O. M. Ultra-high Porosity in Metal-Organic Frameworks. *Science* **2010,** *329,* 424–428.

(52) Ma, S.; Sun, D.; Simmons, J. M.; Collier, C. D.; Yuan, D.; Zhou, H.-C. Metal-Organic Framework from an Anthracene Derivative Containing Nanoscopic Cages Exhibiting High Methane Uptake. *J. Am. Chem. Soc.* **2008**, *130,* 1012–1016.

(53) Stoeck, U.; Krause, S.; Bon, V.; Senkovska, I.; Kaskel, S. A highly Porous Metal-organic Framework, Constructed from a Cuboctahedral Super-molecular Building Block, with Exceptionally High Methane Uptake. *Chem. Commun.* **2012**, *48*, 10841–10843.

(54) Peng, Y.; Srinivas, G.; Wilmer, C. E.; Eryazici, I.; Snurr, R. Q.; Hupp, J. T.; Yildirim, T.; Farha, O. K. Simultaneously High Gravimetric and Volumetric Methane Uptake Characteristics of the Metal-Organic Framework NU-111. *Chem. Commun.* **2013**, *49*, 2992–2994.

(55) Li, B.; Zhang, Z.; Li, Y.; Yao, K.; Zhu, Y.; Deng, Z.; Yang, F.; Zhou, X.; Li, G.; Wu, H.; Nijem, N.; Chabal, Y. J.; Lai, Z.; Han, Y.; Shi, Z.; Feng, S.; Li, J. Enhanced Binding Affinity, Remarkable Selectivity, and High Capacity of CO_2 by Dual Functionalization of a rht- type Metal-organic Framework. *Angew. Chem. Int. Ed.* **2012**, *51*, 1412−1415.

(56) Peng, Y.; Krungleviciute, V.; Eryazici, I.; Hupp, J. T.; Farha, O. K.; Yildirim, T. Methane Storage in Metal–Organic Frameworks: Current Records, Surprise Findings, and Challenges. *J. Am. Chem. Soc.* **2013**, *135*, 11887–11894.

(57) Gandara, F.; Furukawa, H.; Lee, S.; Yaghi, O. M. High Methane Storage Capacity in Aluminum Metal Organic Frameworks. *J. Am. Chem. Soc.* **2014**, *136*, 5271–5274.

(58) Mason, J. A.; Veenstrab, M.; Long, J. R. Evaluating Metal-Organic Frameworks for Natural Gas Storage. *Chem. Sci.* **2014**, *5*, 32–51.

(59) Herm, Z. R.; Swisher, J. A.; Smit, B.; Krishna, R.; Long, J. R. Metal-Organic Frameworks as Adsorbents for Hydrogen Purification and Pre combustion Carbon Dioxide Capture. *J. Am. Chem. Soc.* **2011**, *133*, 5664–5667.

(60) Herm, Z. R.; Krishna, R.; Long, J. R. CO_2/CH_4, CH_4/H_2 and $CO_2/CH_4/H_2$ Separations at High Pressures Using Mg_2(dobdc). *Microporous and Mesoporous Mater.* **2012**, *151*, 481–487.

(61) Mason, J. A.; Sumida, K.; Herm, Z. R.; Krishna, R.; Long, J. R. Evaluating Metal-Organic Frameworks for Post-combustion Carbon Dioxide Capture via Temperature Swing Adsorption. *Energy Environ. Sci.* **2011**, *4*, 3030–3040.

(62) Krishna, R. Adsorptive Separation of CO_2/CH_4/CO Gas Mixtures at High Pressures. *Microporous and Mesoporous Mater.* **2012**, *156*, 217–223.

(63) Xiang, S.; He, Y.; Zhang, Z.; Wu, H.; Zhou, W.; Krishna, R.; Chen, B. Microporous metal-organic framework with potential for carbon dioxide capture at ambient conditions. *Nat. Commun.* **2012**, *3*, 954–962.

(64) Bloch, E. D.; Murray, L. J.; Queen, W. L.; Chavan, S.; Maximoff, S. N.; Bigi, J.P.; Krishna, R.; Peterson, V. K.; Grandjean, F.; Long, G.; Smit, B.; Bordiga, S.; Brown, C. M.; Long, J. R. Selective Binding of O_2 over N_2 in a Redox-Active Metal-Organic Framework with Open Iron(II) Coordination Sites. *J. Am. Chem. Soc.* **2011**, *133*, 14814–14822.

(65) Bae, Y. S.; Lee, C. Y.; Kim, K. C.; Farha, O. K.; Nickias, P.; Hupp, J. T.; Nguyen, S. B. T.; Snurr, R. Q. High Propene/Propane Selectivity in Isostructural Metal-Organic Frameworks with High Densities of Open Metal Sites. *Angew. Chem., Int. Ed.* **2012**, *51*, 1857–1860.

(66) Bloch, E. D.; Queen, W. L.; Krishna, R.; Zadrozny, J. M.; Brown, C. M.; Long, J. R. Hydrocarbon Separations in a Metal Organic Framework with Open Iron(II) Coordination Sites. *Science* **2012**, *335*, 1606–1610.

(67) Biswas, S.; Vanpoucke, D E. P.; Verstraelen, T.; Vandichel, M.; Couck, S.; Leus, K.; Liu, Y.-Y.; Waroquier, M.l; Van Speybroeck, V.; Denayer, J. F. M.; Van der Voort, P. New Functionalized Metal−Organic Frameworks MIL-47-X (X = −Cl, −Br, $-CH_3$, $-CF_3$, −OH, $-OCH_3$): Synthesis, Characterization, and CO_2 Adsorption Properties. *J. Phys. Chem. C* **2013**, *117*, 22784−22796.

(68) Jasuja, H.; Huang, Y.-g.; Walton, K. S. Adjusting The Stability of Metal-Organic Frameworks Under Humid Conditions by Ligand Functionalization. *Langmuir* **2012**, *28*, 16874−16880.

(69) Lin, X.; Telepeni, I.; Blake, A. J.; Dailly, A.; Brown, C. M.; Simmons, J. M.; Zoppi, M.; Walker, G. S.; Thomas, K. M.; Mays, T. J.; Hubberstey, P.; Champness, N. R.; Schröder, M. High Capacity Hydrogen Adsorption in Cu(II) Tetracarboxylate Framework Materials: The Role of Pore Size, Ligand Functionalization, and Exposed Metal Sites. *J. Am. Chem. Soc.* **2009**, *131*, 2159–2171.

(70) Lan, Y.-Q.; Li, S.-L.; Jiang, H.-L.; Xu, Q. Tailor-Made Metal-Organic Frameworks From Functionalized Molecular Building Blocks and Length-Adjustable Organic Linkers via Stepwise Synthesis. *Chem.-Eur. J.* **2012**, *18*, 8076–8083.

(71) Wang, Y.; Tan, C.; Sun, C. Z.; Xue, Z.; Zhu, Q.; Shen, C.; Wen, Y.; Hu, Sh.; Wang, Y.; Sheng, T.; Wu, X. Effect of Functionalized Groups on Gas-Adsorption Properties: Syntheses of Functionalized Microporous Metal−Organic Frameworks and Their High Gas-Storage Capacity. *Chem. -Eur. J.* **2014**, *20*, 1341−1348.

(72) Wang, Z.; Cohen, S. M. Post Synthetic Modification of Metal Organic Frameworks. *Chem. Soc. Rev.* **2009**, *38*, 1315–1329.

(73) Himsl, D.; Wallacher, D.; Hartmann, M. Improving the Hydrogen-Adsorption Properties of a Hydroxy-Modified MIL-53(Al) Structural Analogue by Lithium Doping. *Angew. Chem. Int. Ed.* **2009**, *48*, 4639–4642.

(74) Xiang, Z.; Hu, Z.; Yang, W.; Cao, D. Lithium Doping on Metal-Organic Frameworks for Enhancing H_2 Storage. *Int. J. Hydrogen Energy* **2012**, *37*, 946–950.

(75) Ferey, G.; Mellot-Draznieks, C.; Serre, C.; Millange, F.; Dutour, J.; Surble, S.; Margiolaki, I. A Chromium Terephthalate-Based Solid with Unusually Large Pore Volumes and Surface Area. *Science* **2005**, *309*, 2040–2042.

(76) Krishna, R. Adsorptive Separation of CO_2/CH_4/CO Gas Mixtures at High Pressures. *Microporous and Mesoporous Mater.* **2012**, *156*, 217–223.

(77) Chavan, S.; Vitillo, J. G.; Larabi, C.; Quadrelli, E. A.; Dietzel, P. DC; Bordiga, S. Functionalization of CPO–27–Ni Through Metal Hexacarbonyls: The Role of Open Ni^{2+} Sites. *Microporous Mesoporous Mater.* **2012**, *157*, 56−61.

(78) Dietzel, P. D. C.; Johnsen, R. E.; Blom, R.; Fjellvag, H. Structural Changes and Coordinatively Unsaturated Metal Atoms on Dehydration of Honeycomb Analogous Microporous Metal-Organic Frameworks. *Chem. Eur. J.* **2008**, *14*, 2389−2397.

(79) Zhang, Z.; Zhao, Y.; Gong, Q.; Li, Z.; Li, J. MOFs for CO_2 Capture and Separation from Flue Gas Mixtures: The Effect of Multifunctional Sites on Their Adsorption Capacity and Selectivity. *Chem. Commun.* **2013**, *49*, 653–661.

(80) Yang, Q.; Liu, D.; Zhong, C.; Li, J. -R. Development of Computational Methodologies for Metal-Organic Frameworks and Their Application in Gas Separations. *Chem. Rev.* **2013**, *113*, 8261–8323.

(81) Frost, H.; Dùren, T.; Snurr, R. Q. Effects of Surface Area, Free Volume, and Heat Of Adsorption on Hydrogen Uptake in Metal-Organic Frameworks. *J. Phys. Chem. B* **2006,** *110,* 9565–9670.

(82) Wilmer, C. E.; Leaf, M.; Lee, C. Y.; Farha O. K.; Hauser B. G.; Hupp, J. T.; Snurr, R. Q. Large-Scale Screening of Hypothetical Metal–Organic Frameworks. *Nature Chemistry* **2012**, *4,* 83–98.

(83) Krishna, R. Diffusion in Porous Crystalline Materials. *Chem. Soc. Rev.* **2012**, *41*, 3099–3118.

(84) Jhon, Y. H.; Cho, M.; Jeon, H. R.; Park, I.; Chang, R.; Rowsell, J. L. C.; Kim, J. Simulations of Methane Adsorption and Diffusion within Alkoxy–Functionalized IRMOFs Exhibiting Severely Disordered Crystal Structures. *J. Phys. Chem. C* **2007**, *111,* 16618–16625.

(85) Watanabe, T., and Sholl, D. S. Accelerating Applications of Metal–Organic Frameworks for Gas Adsorption and Separation by Computational Screening of Materials. *Langmuir* **2012**, *28,* 14114–14128.

(86) Chung, Y. G., Gomez–Gualdron, D. A., Li, P., Leperi, K. T., Deria, P., Zhang, H. D. In Silico Discovery of Metal–Organic Frameworks for Pre Combustion CO_2 Capture Using A Genetic Algorithm. *Sci. Adv.* **2016**, *2*, 1–9.

(87) Bourrelly Farrusseng, D.; Daniel, C.; Gaudillere, C.; Ravon, U.; Schuurman, Y.; Mirodatos, C.; Dubbeldam, D.; Frost, H.; Snurr, R.Q. Heats of Adsorption for Seven Gases in Three Metal-Organic Frameworks: Systematic Comparison of Experiment and Simulation. *Langmuir* **2009,** *25,* 7383–7388.

(88) Llewellyn, P. L.; Bourrelly, S.; Serre, C.; Vimont, A.; Daturi, M.; Hamon, L.; Weireld, G. D.; Chang, J.-S.; Hong, D.-Y.; Hwang, Y. K.; Jhung, S. H.; Férey, G. High Uptakes of CO_2 and CH_4 in Mesoporous Metals Organic Frameworks MIL-100 and MIL-101. *Langmuir* **2008**, *24*, 7245–7250.

(89) Chowdhury, P.; Mekala, S.; Dreisbach, F.; Gumma, S. Adsorption of CO, CO_2 and CH_4 on Cu-BTC and MIL-101 Metal Organic Frameworks: Effect of Open Metal Sites and Adsorbate Polarity. *Microporous and Mesoporous Mater.* **2012**, *152*, 246–252.

(90) Dietzel, P. D. C.; Besikiotis, V.; Blom, R. Application of Metal-organic Frameworks with Coordinatively Unsaturated Metal Sites in Storage and Separation of Methane and Carbon Dioxide. *J. Mater. Chem.* **2009,** *19*, 7362–7370.

(91) Caskey, S. R.; Wong-Foy, A. G.; Matzger, A. J. Dramatic Tuning of Carbon Dioxide Uptake via Metal Substitution in a Coordination Polymer with Cylindrical Pores. *J. Am. Chem. Soc.* **2008,** *130*, 10870–10871.

(92) Liang, Z.; Marshall, M.; Chaffee, A. L. CO_2 adsorption, selectivity and water tolerance of pillared-layer metal organic frameworks. *Microporous and Mesoporous Mater.* **2010,** *132*, 305–310.

(93) Liang, Z.; Marshall, M.; Chaffee, A. L. CO_2 Adsorption-Based Separation by Metal Organic Framework [Cu-BTC] versus Zeolite [13X]. *Energy & Fuels* **2009,** *23*, 2785–2789.

(94) Naik, S. P.; Chiang, S. T.; Thompson, R. W.; Huang, F. C. Formation of Silicalite-1 Hollow Spheres by the Self-assembly of Nanocrystals. *Chem. Mater.* **2003,** *15*, 787–792.

(95) Sun, M. S.; Shah, D. B.; Xu, H. H.; Talu, O. Adsorption Equilibria of C_1 to C_4 Alkanes, CO_2, and SF_6 on Silicalite. *J. Phys. Chem. B* **1998,** *102,* 1466–1473.

(96) Lu, Z.; Du, L.; Tang, K.; Bai, High H_2 and CH_4 Adsorption Capacity of a Highly Porous (2,3,4)-Connected Metal–Organic Framework. *J. Cryst. Growth Des.* **2013,** *13,* 2252–2255.

(97) He, Y.; Zhou, W.; Yildirim, T.; Chen, B. A Series of Metal-Organic Frameworks with High Methane Uptake and An Empirical Equation for Predicting Methane Storage Capacity. *Energy Environ. Sci.* **2013,** *6,* 2735–2744.

(98) Guo, Z.; Wu, H.; Srinivas, G.; Zhou, Y.; Xiang, S.; Chen, Z.; Yang, Y.; Zhou, W.; O'Keeffe, M.; Chen, B. A Metal-Organic Framework with Optimized Open Metal Sites and Pore Spaces for High Methane Storage at Room Temperature. *Angew. Chem. Int. Ed.* **2011,** *50,* 3178–3181.

(99) Wang, X. -S.; Ma, S; Rauch, K.; Simmons, J. M.; Yuan, D.; Wang, X.; Yildirim, T.; Cole, W. C; L´opez, J. J.; Meijere, A.; Zhou, H. -C. Metal-Organic Frameworks Based on Double-Bond-Coupled Di-Isophthalate Linkers with High Hydrogen and Methane Uptakes. *Chem. Mater.* **2008,** *20,* 3145–3152.

(100) Sun, D.; Ma, S.; Simmons, J. M.; Li, J. -R.; Yuan D.; Zhou, H.-C. An Unusual Case of Symmetry-Preserving Isomerism. *Chem. Commun.* **2010,** *46,* 1329–1331.

(101) Lin, X.; Telepeni, I.; Blake, A. J.; Dailly, A.; Brown, C. M.; Simmons, J. M.; Zoppi, M.; Walker, G. S.; Thomas, K. M.; Mays, T. J.; Hubberstey, P.; Champness, N. R.; Schröder, M. High Capacity Hydrogen Adsorption in Cu(II) Tetracarboxylate Framework Materials: The Role

of Pore Size, Ligand Functionalization and Exposed Metal Sites. *J. Am. Chem. Soc.* **2009,** *131*, 2159–2171.

(102) Rallapalli, P.; Prasanth, K. P.; Patil, D.; Somani, R. S.; Jasra, R. V.; Bajaj, H. C. Sorption Studies of CO_2, CH_4, N_2, CO, O_2 and Ar on Nanoporous Aluminum Terephthalate [MIL-53(Al)]. *J. Porous Mater*. **2011**, *18***,** 205–210.

(103) Wilmer, C. E.; Farha, O. K.; Yildirim, T.; Eryazici, I.: Krungleviciute, V.; Sarjeant, A. A.; Snurr, R. Q.; Hupp, J. T. Gram-Scale, High-Yield Synthesis of A Robust Metal–Organic Framework for Storing Methane and Other Gases. *Energy Environ. Sci.* **2013,** *6*, 1158–1163.

(104) Wiersum, A. D.; Chang, J. -S.; Serre C.; Llewellyn, P. L. An Adsorbent Performance Indicator as a First Step Evaluation of Novel Sorbents for Gas Separations: Application to Metal–Organic Frameworks. *Langmuir* **2013,** *29,* 3301–3309.

(105) Rowsell, J. L. C.; Yaghi, O. M. Effects of Functionalization, Catenation, and Variation of the Metal Oxide and Organic Linking Units on the Low-Pressure Hydrogen Adsorption Properties of Metal-Organic Frameworks. *J. Am. Chem. Soc.* **2006,** *128*, 1304–1315.

(106) He, Y.; Furukawa, H.; Wu, C.; O'Keeffe, M.; Krishna R.; Chen, B. Low-Energy Regeneration and High Productivity in A Lanthanide-Hexacarboxylate Framework for High-Pressure CO_2-CH_4-H_2 Separation. *Chem. Commun.* **2013,** *49*, 6773–6775.

(107) Peng, Y.; Srinivas, G.; Wilmer, C. E.; Eryazici, I.; Snurr, R. Q.; Hupp, J. T.; Yildirim, T.; Farha, O. K. Simultaneously High Gravimetric and Volumetric Methane Uptake Characteristics of The Metal–Organic Framework NU-111. *Chem. Commun.* **2013,** *49*, 2992–2994.

(108) Yuan, D.; Zhao, D.; Sun, D.; Zhou, H. -C. An Isoreticular Series of Metal–Organic Frameworks with Dendritic Hexacarboxylate Ligands and Exceptionally High Gas-Uptake Capacity. *Angew. Chem. Int. Ed.* **2010,** *49,* 5357–5361.

(109) Klein, N.; Senkovska, I.; Baburin, I. A.; Grünker, R.; Stoeck, U.; Schlichtenmayer, M.; Streppel, B; Mueller, U.; Leoni, S.; Hirscher, M.; Kaskel, S. Route to a Family of Robust, Non-interpenetrated Metal–Organic Frameworks with pto-like Topology. *Chem.–Eur. J.* **2011,** *17,* 13007–13016.

(110) Prasad, T. K.; Suh, M. P. Control of Interpenetration and Gas-Sorption Properties of Metal–Organic Frameworks by a Simple Change in Ligand Design. *Chem.–Eur. J.* **2012,** *18,* 8673–8680.

(111) Perez-Pellitero, J.; Amrouche, H.; Siperstein, F. R.; Pirngruber, G.; Nieto-Draghi, C.; Chaplais, G.; Masseron, A. S.; Bachi, D. B.; Peralta, D.; Bats, N. Adsorption of CO_2, CH_4, and N_2 on Zeolitic Imidazolate Frameworks: Experiments and Simulations. *Chem.–Eur. J.* **2010,** *16,* 1560–1571.

(112) Feldblyum, J. I.; Dutta, D.; Wong-Foy, A. G.; Dailly, A.; Imirzian, J.; Gidley, D. W.; Matzger, A. J. Interpenetration, Porosity, and High-Pressure Gas Adsorption in Zn_4O(2,6-Naphthalene Dicarboxylate)$_3$. *Langmuir* **2013,** *29,* 8146–8153.

(113) Yan, Y.; Yang, S.; Blake, A. J.; Lewis, W.; Poirier, E.; Barnett, S. A.; Champness, N. R.; Schröder, M. A Mesoporous Metal-Organic Framework Constructed From A Nanosized C3-Symmetric Linker and [Cu_{24}(Isophthalate)$_{24}$] Cuboctahedra. *Chem. Commun.* **2011,** *47,* 9995–9997.

(114) Rolniak, P. D.; Kobayashi, R. Adsorption of Methane and Several Mixtures of Methane and Carbon Dioxide at Elevated Pressures and Near Ambient Temperatures on 5A and 13X Molecular Sieves by Tracer Pertubation Chromatography. *AIChE J.* **1980,** *26,* 616–625.

(115) Dirar, Q. H.; Loughlin, K. F. Intrinsic Adsorption Properties of CO_2 on 5A and 13X Zeolite. *Adsorption* **2013,** *19,* 1149–1163.

(116) Karra, J. R.; Walton, K. S. Molecular Simulations and Experimental Studies of CO_2, CO, and N_2 Adsorption in Metal Organic Frameworks. *J. Phys. Chem. C* **2010**, *114*, 15735–15740.

(117) Serre, C.; Mellot-Draznieks, C.; Surble, S.; Audebrand, N.; Filinchuk, Y.; Férey, G. Role of Solvent-Host Interactions That Lead to Very Large Swelling of Hybrid Frameworks. *Science* **2007**, *315*, 1828–1831.

(118) Chavan, S.; Vitillo, J. G.; Groppo, E.; Bonino, F.; Lamberti, C.; Dietzel, P. D. C.; Bordiga, S. CO Adsorption on CPO-27-Ni Coordination Polymer: Spectroscopic Features and Interaction Energy. *J. Phys. Chem. C* **2009,** *113*, 3292–3299.

(119) Belmabkhout, Y.; Pirngruber, G.; Jolimaitre, E.; Methivier, A. A Complete Experimental Approach for Synthesis Gas Separation Studies Using Static Gravimetric and Column Breakthrough Experiments. *Adsorption* **2007,** *13,* 341–349.

(120) Golden, T. C.; Sircar, S. Gas Adsorption on Silicalite. *J. Coll. Inter. Sci.* **1994,** *162,* 182–188.

(121) Liu, J.; Culp, J.T.; Natesakhawat, S.; Bockrath, B.C.; Zande, B.; Sankar, S.G.; Garberoglio, G.; Karl Johnson, J. Experimental and Theoretical Studies of Gas Adsorption in $Cu_3(BTC)_2$: An Effective Activation Procedure *J. Phys. Chem. C.* **2007,** *111,* 9305–9313.

(122) Salem, M.M.K.; Braeuer, P.; Szombathely, MV; Heuchel, M.; Harting, P.; Quitzsch, K.; Jaroniec, M. Thermodynamics of High-Pressure Adsorption of Argon, Nitrogen, and Methane on Microporous adsorbents. *Langmuir*, **1998,** *14*, 3376–3389.

(123) Dreisbach, F.; Staudt, R.; Keller, J. U. High Pressure Adsorption Data of Methane, Nitrogen, Carbon Dioxide and their Binary and Ternary Mixtures on Activated carbon. *Adsorption* **1999,** *5*, 215–227.

(124) Stallmach, F.; Groger, S.; Kunzel, V.; Karger, J.; Yaghi, O. M.; Hesse, M.; Muller, U. NMR Studies on the Diffusion of Hydrocarbons on the Metal-Organic Framework Material MOF-5. *Angew. Chem. Int. Ed.* **2006,** *45*, 2123–2126.

(125) Pires, J.; Pinto, M. L. Granadeiro, C. M.; Barbosa, A.D. S.; Cunha-Silva, L.; Balula, S. S.; Saini, V. K. Effect on Selective Adsorption of Ethane and Ethylene of The Polyoxometalates Impregnation in The Metal-Organic Framework MIL-101. *Adsorption* **2014**, *20*, 533–543.

(126) Bao, Z.; Alnemrat, S.; Yu, L.; Vasiliev, I.; Ren, Q.; Lu, X.; Deng, S. Adsorption of Ethane, Ethylene, Propane, and Propylene on a Magnesium-Based MetalOrganic Framework. *Langmuir* **2011**, *27*, 13554–13562.

(127) Hyun, S. H.; Danner, R. P. Equiilbrium Adsorption of Ethane, Ethylene, Isobutane, Carbon Dioxide, and Their Binary Mixtures on 13X Molecular Sieves. J. *Chem. Eng. Data* **1982,** *27*, 196–200.

(128) Nam, Gi-M.; Jeong, B. -M.; Kang, S. -H.; Lee, B. -K.; Choi, D. -K. Equilibrium Isotherms of CH_4, C_2H_6, C_2H_4, N_2, and H_2 on Zeolite 5A Using a Static Volumetric Method. J. *Chem. Eng. Data* **2005,** *50*, 72–76.

(129) Rubes, M.; Wiersum, A. D.; Llewellyn, P. L.; Grajciar, L.; Bludsky, O.; Nachtigall, P. Adsorption of Propane and Propylene on Cu-BTC Metal-Organic Framework: Combined Theoretical and Experimental Investigation. *J. Phys. Chem. C* **2013,** *117*, 11159–11167.

(130) Jiang, J.; Sandler, S. I. Monte Carlo Simulation for the Adsorption and Separation of Linear and Branched Alkanes in IRMOF-1. *Langmuir* **2006**, *22*, 5702–5707.

(131) Llewellyn, P. L.; Horcajada, P.; Maurin, G.; Devic, T.; Rosenbach, N.; Bourrelly, S.; Serre, C.; Vincent, D.; Loera-Serna, S.; Filinchuk, Y.; Férey, G. Complex Adsorption of Short Linear Alkanes in the Flexible Metal-Organic-Framework MIL-53(Fe). *J. Am. Chem. Soc.* **2009**, *131***,** 13002–13008.

(132) Siperstein, F. R.; Myers, A.L. Mixed-Gas Adsorption. *AIChE J.* **2001,** *47*, 1141–1159.

(133) Herden, H.; Löffler, U.; Schöllner, R. Adsorption of Hydrocarbons on Activated Carbons. *J. Colloid Interface Sci.* **1991**, *144*, 477–482.

(134) Dunne, J. A.; Rao, M.; Sircar, S.; Gorte, R. J.; Myers, A. L. Calorimetric Heats of Adsorption and Adsorption Isotherms. 2. O_2, N_2, Ar, CO_2, CH_4, C_2H_6, and SF_6 on NaX, H-ZSM-5, and Na-ZSM-5 Zeolites. *Langmuir* **1996,** *12*, 5896–5904.

(135) Dunne, J.A.; Mariwala, R.; Rao, M.; Sircar, S.; Gorte, R.J.; Myers A. L. Calorimetric Heats of Adsorption and adsorption Isotherms. 1. O_2, N_2, Ar, CO_2, CH_4, C_2H_6, and SF_6 on Silicalite. *Langmuir* **1996,** *12*, 5888–5895.

(136) Talu, O.; Li, J.; Kumar, R.; Mathias, P. M.; Moyer, J. D. Jr.; Schork, J. M. Measurement and Analysis of Oxygen/Nitrogen/5A-Zeolite Adsorption Equilibria for Air Separation. *Gas. Sep. Purif.* **1996,** *10*, 149–159.

(137) Belmabkhout, Y.; De Weireld, G.; Frère, M. High-Pressure Adsorption Isotherms of N_2, CH_4, O_2, and Ar on Different Carbonaceous Adsorbents. *J. Chem. Eng. Data,* **2004,** *49*, 1379–1391.

CHAPTER 3

Theory

This chapter includes the theory related to adsorption, types of adsorption, and various adsorption isotherm models were presented. Some important thermodynamic properties such as Henry's constant, enthalpy of adsorption, and selectivity predictions using Ideal Adsorbed Solution Theory (IAST) were also included.

3.1 Phase Rule

In general, phase equilibrium indicates equality of thermal, mechanical, and chemical potentials. Adsorption is a surface phenomenon. Due to the extra intensive variable caused by lack of mechanical equilibrium, adsorption has one extra degree of freedom compared to that of bulk phase equilibria. So the phase rule for adsorption is [1],

$$F = C - X + 3 \qquad 3.1$$

Where F=number of degrees of freedom

C=number of chemical species

X=number of phases

3.2 Equilibrium Adsorption Isotherm

Due to an additional degree of freedom, the amount of adsorbed for pure gas adsorption at equilibrium is a function of two variables, i.e., pressure and temperature.

$$N = I\{P, T\} \quad (3.2)$$

Where N is the amount adsorbed, P is the pressure, and T is the temperature. At constant temperature, the adsorbed amount is

$$N = I\{P\} \quad (3.3)$$

This relationship is commonly called an adsorption isotherm. Fugacity (f) is used instead of pressure to account for non–ideality in the gas phase at high pressures [2], and then the relationship becomes

$$N = I\{f\} \quad (3.4)$$

3.3 Henry's Constant

The linear relationship between fluid phase and adsorbed concentrations is known as Henry's law. Henry's constant is defined as the slope of the isotherm at the limit of zero pressure. Mathematically, Henry's constant (β) is written as

$$\beta = \left(\frac{N}{P}\right)_{P \to 0} \quad (3.5)$$

Henry's constant (β) is a measure of vertical interactions between adsorbate and adsorbent.

3.4 Models for Pure Gas Adsorption Isotherms

In this following section, various adsorption isotherm models were used in this work are presented. All the discussion presented here is related to excess adsorption.

3.4.1 Langmuir Isotherm

The Langmuir model is based on the following assumptions:

(i) Fixed number of adsorption sites

(ii) Each site can hold only one molecule

(iii) All sites are equally energetic

(iv) No lateral interactions between adsorbate–adsorbate molecules

Based on the above assumption Langmuir equation is formulated as

$$N = \frac{N^{max}\beta f}{1 + \beta f} \tag{3.6}$$

Where N (mol kg^{-1}) is the amount adsorbed, f (bar) is the fugacity, N^{max} (mol kg^{-1}) is the saturation capacity, β (mol kg^{-1} bar^{-1}) is Henry's constant. Saturation capacity is considered to be independent of temperature, and the temperature dependency for Henry's constant is expressed by

$$\beta = \beta^{(0)}\exp(\beta^{(1)}/T) \tag{3.7}$$

Where T is temperature in K. The two parameters $\beta^{(0)}$ and $\beta^{(1)}$ are related to entropy and enthalpy of adsorption at zero loading, respectively.

3.4.2 Dual Site Langmuir (DSL) Isotherm

The Dual Site Langmuir (DSL) model demonstrates two types of adsorption sites with different energetic. Each site follows a Langmuir adsorption behavior. A DSL isotherm model is given by [3],

$$N = \frac{{N_1}^{max}\beta_1 f}{1 + \beta_1 f} + \frac{{N_2}^{max}\beta_2 f}{1 + \beta_2 f} \tag{3.8}$$

Where N_1^{max} and N_2^{max} (mol kg^{-1}) are the saturation capacities for sites 1 and 2, respectively; β_1 and β_2 (bar^{-1}) are the affinity parameters for sites 1 and 2, respectively. Saturation capacities (N_1^{max} and N_2^{max}) are considered to be independent of temperature, and the usual temperature dependency was considered for the affinity parameters (Eq. 3.9 and 3.10)

$$\beta_1 = \beta_1{}^{(0)} \exp(\beta_1{}^{(1)}/T) \quad 3.9$$

$$\beta_2 = \beta_2{}^{(0)} \exp(\beta_2{}^{(1)}/T) \quad 3.10$$

The Henry's constant (β) in this model can be calculated as

$$\beta = N_1^{max}\beta_1 + N_2^{max}\beta_2 \quad 3.11$$

3.4.3 Virial Isotherm

A virial isotherm is versatile as it can accommodate the heterogeneity in adsorption. A simple Virial isotherm with three parameters is expressed as follows [3]

$$\ln\left(\frac{f}{N}\right) = bN + cN^2 - \ln(\beta) \quad 3.12$$

Where b and c are second and third Virial coefficients for adsorption. The temperature dependency for these parameters is

$$b = b^{(0)} + \frac{b^{(1)}}{T} \quad 3.13$$

$$c = c^{(0)} + \frac{c^{(1)}}{T} \quad 3.14$$

The temperature dependency for β is the same as that in Eq. 3.7.

Since the equation is open-ended, this isotherm has no limit on the amount adsorbed as the pressure (fugacity) increases. Thus extrapolation of virial equation beyond the experimental measurements is not suggested. However, within the experimental range of temperature and pressure data, the virial equation is flexible and thermodynamically consistent.

In general, an adsorption isotherm is plotted in N vs. f domain. However, from an experimental data analysis perspective, isotherm in a virial domain [$ln(P/N)$ vs. N] can be extremely useful. The intercept [$-ln(\beta)$] of the Virial domain plot can directly be used to obtain Henry's constant (β). In addition, the slope of the virial domain plot reflects the energetics of adsorption. Any step or inflection in the virial domain plot indicates the heterogeneity in the adsorbent. This type of information is not easily recognizable from isotherm plotted in the conventional domain.

3.4.4 Virial–Langmuir (VL) Isotherm

The Langmuir equation is derived for only energetic homogeneous surfaces, which is generally not possible in a realistic situation. On the other hand, the flexible virial equation is versatile and can describe adsorption on a variety of surfaces. However, this equation does not account for the saturation at high pressure, which is usually observed in most cases. Thus, Langmuir and virial models are combined in a Langmuir–virial model [3] (Eq. 3.15) to overcome the limitations in either case.

$$\ln\left(\frac{f}{N}\right) = bN + cN^2 + \ln\frac{N^{max}}{\beta(N^{max} - N)} \qquad 3.15$$

This model correctly captures a saturation uptake of N^{max} at high pressure. The temperature dependency of Henry's constant is given by Eq. 3.7 and Virial parameters b and c are given by Eq. 3.13 and Eq. 3.14.

3.5 Enthalpy of Adsorption

Enthalpy of adsorption indirectly gives the strength of adsorbate and adsorbent binding and thus can be used to characterize the adsorption properties of any adsorbent. Enthalpy of adsorption at zero loading indicates the energy required for regeneration of adsorbent. For example, lower enthalpy of adsorption at zero coverage will result in easier regeneration of the adsorbent. The enthalpy of adsorption (Δh_{ads}) can be readily calculated from the model parameters of adsorption isotherms using the following equation [4]

$$\Delta h_{ads} = -R \left.\frac{\partial(\ln f)}{\partial(1/T)}\right|_N \qquad 3.16$$

Where R is the universal gas constant, the enthalpy of adsorption for each model was obtained *via.* Eq. 3.16 is given in Table 3.1.

Table 3.1: Enthalpy of adsorption of relevant isotherm models.

Model	**Enthalpy of Adsorption (Δh_{ads})**	**Eq. No.**	**Ref.**

Langmuir	$-R\beta^{(1)}$	3.17	[3]
Dual–Site Langmuir	$-R\left(\frac{\beta_1^{(0)}{N_1}^{max}\beta_1(1+\beta_2 f)^2+\beta_2^{(0)}{N_2}^{max}\beta_2(1+\beta_1 f)^2}{{N_1}^{max}\beta_1(1+\beta_2 f)^2+{N_2}^{max}\beta_2(1+\beta_1 f)^2}\right)$	3.18	[3]
Virial	$-R(\beta^{(1)}-b^{(1)}N-c^{(1)}N^2)$	3.19	[3]
Langmuir–virial	$-R(\beta^{(1)}-b^{(1)}N-c^{(1)}N^2)$	3.20	[3]

3.6 Spreading Pressure

Since adsorbed phase is thermodynamically two–dimensional, pressure cannot be considered as an intensive variable. Therefore, pressure and its corresponding extensive variable volume are not appropriate for a work term in the two–dimensional adsorbed phase [5]. A different intensive variable known as spreading pressure (π) is defined for the adsorbed phase to fix its state [6]. It has units of N m^{-1}, which is the same as that of surface tension. The corresponding extensive variable is the molar area (area of the solid per mole of adsorbed gas), *a*. Thus, the mechanical work term for the adsorbed phase per mole of solid can be calculated as πa; this is analogous to PV in bulk. Since the amount adsorbed *N* is generally expressed for a unit mass of the adsorbent, the area is also represented on the same basis as specific area *A* and has the units of m^2 kg^{-1}. For a single component system, the Gibbs' adsorption isotherm at constant *T* is given by [7, 8] Eq. No. 3.21,

$$-A.d\pi + RTN.d\ln P = 0 \qquad 3.21$$

From the above equation, the reduced spreading pressure, ψ is given by

$$\psi = \frac{\pi.A}{RT} = \int_0^P \frac{N}{P}.dP \qquad 3.22$$

The quantity ψ unis are moles per unit mass of adsorbent. It is also often used synonymously with π. At $P = 0$, the spreading pressure is zero due to no adsorption. Since the spreading pressure cannot be measured experimentally, Eq. 3.22 is used to calculate its value for a pure gas adsorption either by numerical integration or from isotherm model. The expression for ψ using various isotherm models is given below in Table 3.2. These expressions are essential for Ideal Adsorption Solution Theory (IAST) calculation discussed in the next section.

Table 3.2: Spreading pressure for relevant isotherm models.

Model	**Expression for ψ**	**Eq. No.**	**Ref.**

Langmuir	$N^{max}\ln(N^{max}+\beta f)$	3.23	[3]
Dual–Site Langmuir	$N_1{}^{max}\ln(1+\beta_1 f)+N_2{}^{max}\ln(1+\beta_1 f)$	3.24	[3]
Virial	$N+\frac{1}{2}bN^2+\frac{2}{3}cN^3$	3.25	[3]
Langmuir–virial	$\frac{1}{2}bN^2+\frac{2}{3}cN^3-N^{max}\ln\left(\frac{N^{max}-N}{N^{max}}\right)$	3.26	[3]

3.7 Ideal Adsorbed Solution Theory (IAST)

A thermodynamic solution approach yields the following phase equilibrium relation for equality of fugacities in bulk and the adsorbed phases.

$$y_i P \emptyset_i{}^{gas} = x_i \gamma_i P_i^0 \qquad 3.27$$

Where y_i is bulk gas mole fraction, P is the pressure, $\emptyset_i{}^{gas}$ is fugacity coefficient of bulk gas to account for non–ideality, x_i is adsorbed phase mole fraction, γ_i is activity coefficient in adsorbed phase (to account for non–ideal adsorbate mixture) and P_i^0 is pressure at the standard state. A convenient standard state is pure gas at the same temperature and spreading pressure as that of the mixture. If the adsorbate mixture is ideal, Eq. No. 3.27 simplifies to

$$y_i P = x_i P_i^0 \qquad 3.28$$

With this phase equilibrium relations along with an equation for total amount adsorbed (N), one can predict binary gas adsorption equilibria (*i.e.,* finding partial amount adsorbed N_i for a given gas mixture of mole fraction y_i at T and P) [9]. For example, in case of binary equilibrium, the following eight equations need to be solved.

$$y_1 P = x_1 P_1^0 \quad (3.29)$$

$$y_2 P = x_2 P_2^0 \quad (3.30)$$

$$I_1\{N_1^0, P_1^0\} = 0 \quad (3.31)$$

$$I_2\{N_2^0, P_2^0\} = 0 \quad (3.32)$$

$$I_3\{N_1^0, P_1^0, \psi\} = 0 \quad (3.33)$$

$$I_4\{N_2^0, P_2^0, \psi\} = 0 \quad (3.34)$$

$$x_1 + x_2 = 1 \quad (3.35)$$

$$\frac{1}{N} = \frac{x_1}{N_1^0} + \frac{x_2}{N_2^0} \quad (3.36)$$

I_1 and I_2 are isotherm models relating N_1^0 to P_1^0 and N_2^0 to P_2^0 for pure gas 1 and pure gas 2, respectively [Eqns. 3.6, 3.8, 3.12 and 3.15]. I_3 and I_4 are relations for spreading pressure ψ *via.* Eq. No. 3.22, as given in Table 3.2 for the respective model [Eq. No. 3.23 – 3.26].

References

(1) Smith, J. M. and Van Ness H. C. Introduction to Chemical Engineering Thermodynamics. *Fourth Edition, McGraw-Hill, New York,* **1987.**

(2) Talu, O. Needs, Status, Techniques and Problems with Binary Gas Adsorption Experiments. *Advances in Colloid and Interface Science* **1998,** *76-77,* 227–269.

(3) Chowdhury, P. Gas Adsorption on Cu-BTC and Cr-BDC Metal Organic Frameworks (MOFs). **PhD Dissertation,** *Indian Institute of Technology, Guwahati* (**2010**).

(4) Herden, H.; Loffler, U.; Schollner, R. Adsorption of Hydrocarbons on Activated Carbons. Journal of Colloid and Interface Science **1991**, *144*, 477–482.

(5) Van Ness, H. C. Adsorption of Gases on Solids. *I & EC Fundamentals* **1969,** *8,* 464–473.

(6) Steele, W. A. The Interaction of Gases with Solid Surfaces. *Pergamon press, New York,* **1974**.

(7) Do, D. D. Adsorption Analysis: Equilibria and Kinetics. *Imperial College Press, London,* **1998**.

(8) Gumma, S. On Measurement, Analysis and Modeling of Mixed gas Adsorption Equilibria. **PhD Dissertation**, *Cleveland State University* (**2003**).

(9) Myers, A. L.; Prausnitz, J. M. Thermodynamics of Mixed Gas Adsorption. *AIChE J.* **1965,** *11*,121–127.

CHAPTER 4

Experimental

This chapter details the various experimental protocols performed in this work. Firstly, a general synthesis procedure was explained, followed by synthesis of different MOFs worked on are included. Details of the calculation methodologies for converting raw experimental data into the appropriate domain are presented. Physical properties and purities of gases used in this work are also included.

4.1 General Synthesis procedure for MOFs

MOFs are made of two major components: a metal ion (or metal cluster) and an organic linker. The organic linkers donate multiple lone pairs of electrons to the metal ions. In contrast, the metal ions are consisting of vacant orbital shells that accept these lone pairs of electrons to form MOF structures. In general solvothermal synthesis, metal precursors, and organic linkers are dissolved in a solvent and placed in a closed reaction vessel for the self-assembly and formation of MOF crystals. The common solvents used include N,N–dimethylformamide (DMF), N,N–dimethylformamide (DEF), methanol, ethanol and acetonitrile, etc. The synthesis temperature is generally below 493 K, and the crystallization time varies from hours to several days. The resulting solid was filtered to remove all residual solvent and stored in methanol.

4.2 Synthesis of MOFs studied

4.2.1 Synthesis of Cu–abtc

Organic linker abtc was synthesized using the procedure reported by Lee et al. [1]. A mixture of 5–nitroisophthalic acid (19 g, 90 mmol, Merck) and NaOH (50 g, 1250 mmol, Merck) in 250 ml of distilled water was placed in a 1 L round bottom flask, stirred vigorously at 334 K. To this slurry, 100 g of D–glucose dissolved in 150 ml of water was slowly added, the cream color solution changes to dark brown. This mixture was cooled down to room temperature, and air bubbled for 4 hours, and kept in a freeze at 283 K overnight. The solution was then filtered, and the obtained product is dissolved in water and acidified. The obtained orange color precipitate was centrifuged and air-dried. The resulted H_4abtc was dissolved in hot DMF, and the solution was filtered while hot to remove any insoluble material. The solution was allowed to stand at room temperature for one day to form orange crystals, which were filtered off and air-dried.

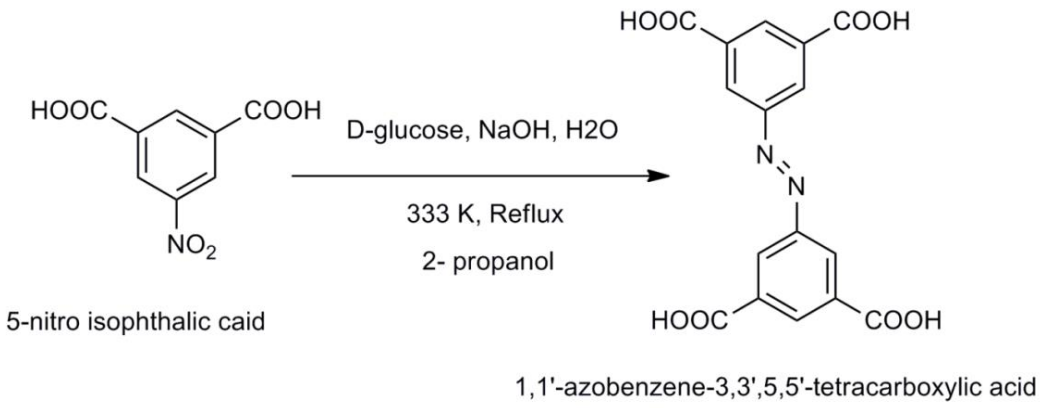

Figure 4.1: Synthesis of H_4abtc organic linker.

MOF synthesis was carried out as per the procedure suggested by Lee et al. [1]. Organic linker H_4abtc (0.065 g, 0.10 mmol) was dissolved in the mixture (7 mL, 4:3 v/v) of DMF and 1,4–dioxane and mixed with the aqueous solution (1 mL) of Cu $(NO_3)_2 \cdot 3H_2O$ (0.040 g, 0.19 mmol, Merck). The aqueous HNO_3 (61%) was added (2-3 drops) until the yellow-greenish turbid solution became clear. The solution mixture was placed in a polypropylene autoclave and heated

at 353 K for 24 h. The solution was cooled to room temperature, and green block-shaped crystals were retrieved. The crystals were filtered off and washed with fresh methanol 2 to 3 times in 24 hours. Additionally, to remove coordinately bonded DMF, methanol is used in the soxhlet extractor to remove excess DMF. Yield: 61 mg (79%).

4.2.2 Synthesis of Cu–hbtc

Organic linker H_4hbtc was synthesized according to the procedure reported in Lie et al. [1]. To 93.25 mL of ethanol, 1 g of H_4abtc (2.79 mmol) was added under stirring, followed by 50 ml of hydrazine hydrate (Merck) added slowly. The mixture was stirred at 333 K for 3 hours. Then ethanol evaporated, and water was added. After acidification to pH=1, a light yellow colored product was obtained.

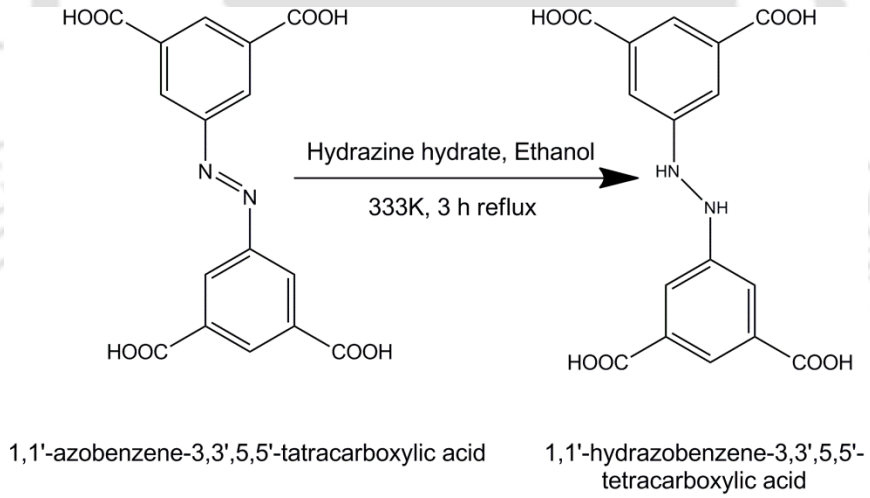

Figure 4.2: Synthesis of H_4hbtc organic linker.

A slightly modified procedure was followed to synthesize Cu–hbtc MOF, as Lee et al. [1] suggested. Organic linker H_4hbtc (0.065 g, 0.10 mmol) was dissolved in the mixture (7 mL, 4:3 v/v) of DMF and 1,4–dioxane and mixed with the aqueous solution (1 mL) of $Cu(NO_3)_2 \cdot 3H_2O$

(0.040 g, 0.19 mmol, Merck). HNO_3 (61%) was added (2–3 drops) until the yellow-greenish turbid solution became clear. The solution mixture was placed in polypropylene autoclaves and heated at 353 K for 24 h. The solution was cooled to room temperature, and the green block-shaped crystals were retrieved. The crystals were filtered off and washed with fresh methanol 2 to 3 times in 24 hours. Methanol was used in a soxhlet extractor to remove excess coordinately bonded DMF. Yield: 69 mg (81%).

4.2.3 Synthesis of Cu–BTC

Cu–BTC was synthesized using the procedure reported earlier [2]. 1,3,5 benzene tricarboxylic acid (H_3BTC) (1.0 g, Merck) is dissolved in 30 cm^3 of a 1:1 mixture of ethanol/ N,N dimethyl formamide (DMF) then added to a 15 cm^3 aqueous solution of $Cu(NO_3)_2.3H_2O$ (2.077 g, Merck) in a 60 cm^3 capped polypropylene bottle. The mixture is sonicated for 10 min and heated in an oven at 373 K for 10 h. The resulting blue precipitate is isolated by filtration and washed with methanol yielded 1.1 g of product.

4.2.4 Synthesis of Cu–(bromo)BTC

Organic linker 2–bromo–1,3,5–benzene tricarboxylic acid (H_3bromoBTC) was synthesized using the procedure reported earlier [3]. 2–bromomesitylene (20 g, Alfa Aesar) was added to an aqueous (250 mL) solution of NaOH (5 g, Merck). Potassium permanganate ($KMnO_4$, 85 g, Merck) was added in several batches to the solution over a period of 2 h with stirring and without heating. Next, the solution was heated to 368 K with stirring for 3 days. The resultant brown slurry was then filtered to remove the large amount of MnO_2, and the filtrate was acidified with concentrated HCl. The aqueous solution was continuously extracted with ethyl ether. Removal of the solvent (ethyl ether) in vacuum yields the product H_3bromoBTC (7.8 g).

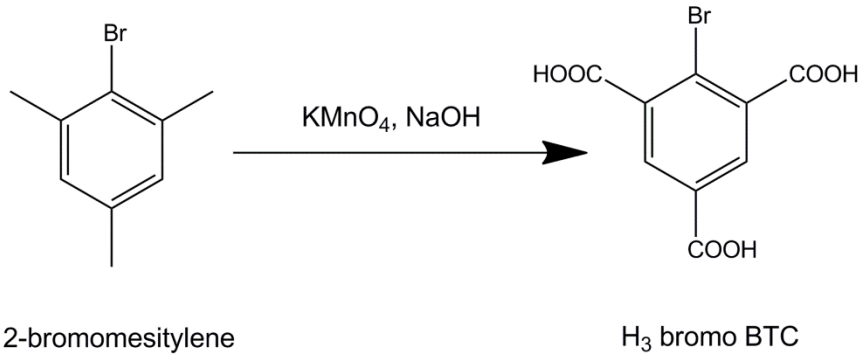

Figure 4.3: Synthesis procedure for H_3 bromo BTC.

Synthesis procedure for Cu–(bromo)BTC was followed reported earlier [4]**.** A mixture of $Cu(NO_3)_2 \cdot 3H_2O$ (72.48 mg, Merck), H_3bromoBTC (58 mg), and DMF with 15 equivalents formic acid (with respect to $Cu(NO_3)_2 \cdot 3H_2O$) was placed in a 30 ml PP bottle. The mixture was heated in a conventional oven at 363 K for 48 h and cooled to room temperature. The green crystal was obtained by filtration and washed with DMF. The yield was 52mg.

4.2.5 Synthesis of Cu–(iodo)BTC

Organic linker synthesis procedure reported earlier [3]. In a Preparation of organic linker 2–iodo–1,3,5–benzene tricarboxylic acid (H_3iodoBTC), Mesitylene (5 g, 0.042 mmol, Merck) was added to methanol (200 mL) solution of KI (8.715 g, 0.0525 mmol, Merck). Oxone (32.23 g, 0.0525 mmol, Alfa Aesar) was slowly added in several batches to the solution over a period of 2 h with stirring and without heating. And next, the solution was heated to 368 K with stirring overnight. The resulted yellowish solution was filtered to remove unreacted Oxone. The obtained solution was dried in a rotary evaporator. The resulted yield of 2–iodomesitylene was 6.7 g.

2–Iodomesitylene (3.0 g) was added to an aqueous (50 mL) solution of NaOH (2.5 g) and t–BuOH (50 mL, Merck). Potassium permanganate ($KMnO_4$, 17.38 g, Merck) was added in several

batches over a period of 2 h with stirring and without heating. Then the solution was heated to 368 K with stirring overnight. On the next day, around 20 mL of ethanol was added to remove the excess amount of $KMnO_4$. Then the hot solution was filtered and acidified to PH=1. The resulted solution was dried in a rotary evaporator. The yield was 4.2 g.

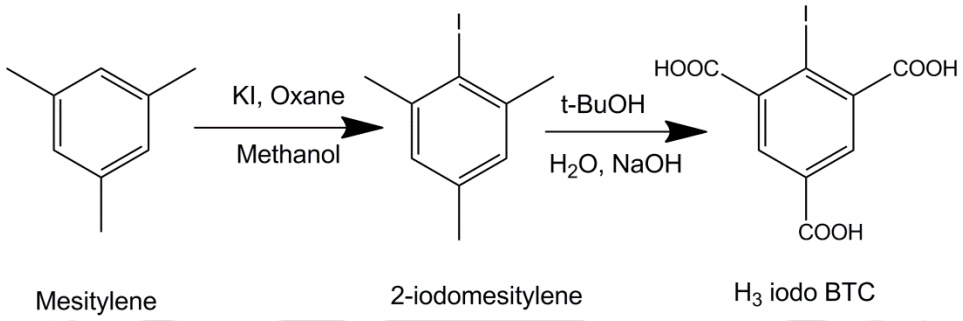

Figure 4.4: Synthesis procedure for H_3 iodo BTC.

To Synthesize Cu–(iodo)BTC MOF, a mixture of $Cu(NO_3)_2 \cdot 3H_2O$(217 mg), H_3iodoBTC (202 mg), and DMF (18 mL) with formic acid (0.52 mL) was placed in a 20 ml PP bottles. The mixture was heated in a conventional oven at 363 K for 48 h and cooled to room temperature. The green crystal was obtained by filtration and washed with DMF. The yield was 192 mg.

4.2.6 Synthesis of UiO–66

UiO–66 was synthesized using the following procedure reported in Katz et al. [4]. For UiO–66, in a 60 ml PP bottle was loaded with $ZrCl_4$ (125 mg, 0.54 mmol, Merck), terephthalic acid (123 mg, 0.75 mmol, Merck), DMF (10 mL), and concentrated HCl (1.0 mL) being sonicated for 20 minutes until fully dissolved. The remainder DMF of 5 mL was then added, and the mixture was sonicated an additional 20 minutes before being heated at 353K overnight. The resulting solid was then filtered and washed first with DMF (2x 10 mL) and then with methanol (2x 10 mL).

After removal of methanol by decanting, the sample was dried at 363 K to yield the final product.

4.2.7 Synthesis of UiO–66–NH_2

UiO–66–NH_2 was synthesized using the following procedure reported in Katz et al. [4]. A 20 mL PP bottle was loaded with $ZrCl_4$ (125 mg. 0.54 mmol, Merck), DMF (5 mL), and 1 mL concentrated HCl before being sonicated for 20 minutes until fully dissolved. The ligand 2–Aminoterephthalic acid (134 mg, 075 mmol, Alfa Aesar) and DMF (10 mL) were then added, and the mixture was sonicated an additional 20 minutes before being heated at 353K overnight. The resulting solid was then filtered and washed first with DMF (2x 10 mL) and then with methanol (2x 10 mL). After removing methanol by decanting, the sample was dried at 363 K to yield the final product.

4.2.8 Synthesis of UiO–66–NO_2

UiO–66–NO_2 was synthesized using the following procedure reported in Katz et al. [4]. A 20 ml PP bottle was loaded with $ZrCl_4$ (62.9 mg, 0.27 mmol, Merck), 2–Nitroterephthalic acid (62.8 mg, 0.38 mmol, Alfa Aesar), DMF (4 mL), and concentrated HCl (0.5 mL) being sonicated for 20 minutes until fully dissolved. The remainder DMF of 3.5 mL was then added, and the mixture was sonicated an additional 20 minutes before being heated at 353 K overnight. The resulting solid was then filtered and washed first with DMF (2x10 mL) and then with methanol (2x10 mL). After removing methanol by decanting, the sample was dried at 363 K to yield the final product.

4.2.9 Synthesis of UiO–66–COOH and UiO–66– $(COOH)_2$

Synthesis of UiO–66–COOH and UiO–66–$(COOH)_2$ used the following procedure reported in Zhang et al. [5]. In a round-bottom flask equipped with a reflux condenser and magnetic stirrer, organic linker (1,2,4–Benzenetricarboxylic acid (3.25 g, 10 mmol, Alfa Aesar) or 1,2,4,5–benzene tetracarboxylic acid (H_4BTEC) (2.54 g, 10 mmol, Alfa Aesar) and zirconium tetrachloride ($ZrCl_4$) (2.43 g, 10.4 mmol, Merck) were dispersed in distilled water (60 mL) and acetic acid (40 mL) at room temperature under stirring and then heated at 373 K for 24 h to yield a powder product. The product was soaked in anhydrous methanol for 3 days at room temperature, during which time the extract was decanted, and fresh methanol was added every day. This process was carried out to wash out residual reagents in the pores. After removing methanol by decanting, the sample was dried at 363 K to yield the final product of UiO–66–COOH or UiO–66–$(COOH)_2$.

4.3 Characterization

Powder X-ray diffraction (PXRD) patterns of all samples synthesized in this work were measured on a Bruker D8 advance instrument operating at 40 kV and 40 mA using Cu Kα (λ=1.5406 Å) radiation.

Thermogravimetric analysis (TGA) of all materials was performed between 298 K to1074 K with a heating rate of 5 K min^{-1} on a thermogravimetric analyzer (Make: Netzsch, Model: STA449F3A00) under a flow of argon at 40 cm^3 min^{-1}. About 10 mg of the MOF was placed in an alumina crucible sample holder for all experiments. Based on the TGA profile of the sample, the out-gassing temperature was determined during subsequent surface area/pore volume analysis and isotherm measurement.

The Brunauer–Emmett–Teller (BET) surface area and pore volume of the material were estimated from N_2 isotherms at 77K using a Quantachrome Autosorb–IQ MP instrument. Prior to nitrogen physisorption, all samples were activated under a flow of helium. The different activation temperatures followed were reported in Table 4.2. The specific surface area was calculated by using the BET model in the relative pressure (P/P_0) range 0.05–0.2. The pore volume was estimated at a predetermined relative pressure (P/P_0) of 0.98 using the Barrett–Joyner–Halenda (BJH) method.

4.4 Experimental System Used for Pure Gas Measurements

The experimental setup used for pure gas adsorption measurements consists of a Rubotherm Magnetic Suspension balance. The balance was connected to the pool of various gases through networks of stainless tubes, as shown in Figure 4.1. Mass flow controllers, temperature transducers, and pressure transducers were incorporated at appropriate locations. Pneumatic valves were used for the ease of experimentation.

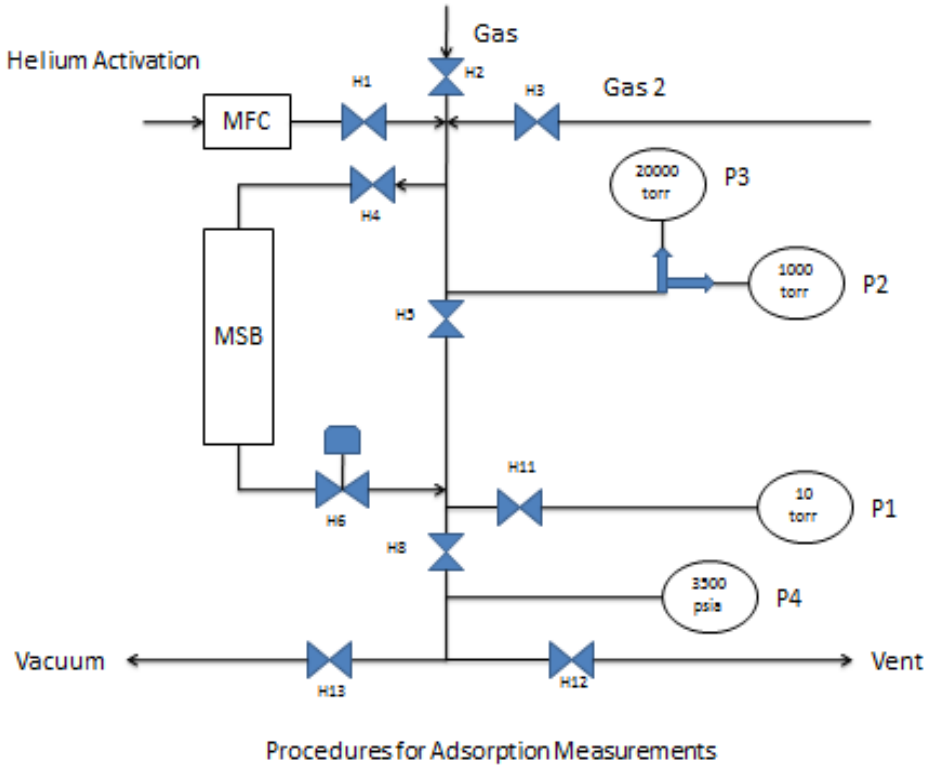

Figure 4.5: Schematic of gravimetric adsorption measurement unit used in this work.

Nomenclature

MSB # Magnetic Suspension Balance

MFC # Mass Flow Controller

H1, H2, H3, H4, H5, H6, H8, H11, H12, H13 # Pneumatic Valves

P1, P2, P3, P4 # Pressure Transducers

In addition to the above mentioned instruments, Swagelok fittings and stainless steel tubing (of 1/4″ and 1/8″) were used for connecting various sections in the experimental assembly.

More details on major hardware components used in this setup are given in Table 4.1.

Table 4.1: List of instruments used in the gravimetric experimental setup.

Component	**Model**	**Manufactu-rer**	**Range**	**Accuracy**	**Resol-ution**
Gravimetric Balance	3–position Magnetic suspension balance	Rubotherm	0–25 g	±20 μg	10 μg
Mass flow controller	GFC–17	Diegler Aalborg	0–200 cc min^{-1}	2% of full scale	1cc min^{-1}
Pressure transducers	627B11TDCAB	MKS Instruments	0–10 torr	±0.12% of full scale	0.001 torr
	627D18TBC1B		0–1000 torr		0.1 torr
	627B24TBC1B		0–20000 torr		1 torr
	PX41C0–3500PSIA	Omegadyne	0–3500 psi	±0.5% of full scale	1psi
Thermocouples	JK Type		0–1200 ^{o}C	±2% of full scale	1 ^{o}C
Temperature indicators		Masibus			
Heated and refrigerated circulator	RW–2025 G	Jeio Tech	–25 to 150 ^{o}C	±0.05 ^{o}C	0.1 ^{o}C
Vacuum pump	DUO 2.5	Pfeiffer Vacuum	$<6\times10^{-3}$ torr	N/A	N/A
Compressor	HS–WP–1	High speed appliances	0–100 psi	N/A	N/A

4.5 Equilibrium Adsorption Measurement

At first, the adsorbent was loaded into the bucket in the balance system, and then the system is hermetically sealed. An adsorbent sample of about 1 g or more was used to avoid measurement errors. Thereafter, activation of the sample was done by heating it at a higher temperature (Table 4.2 for more details) under vacuum (and about 20 cm^3 min^{-1} purge flow of helium). Activation of the sample was ensured when no significant reduction in its weight occurs with time. The activated sample was cooled to the experimental temperature under a vacuum. The first measurement point on the isotherm was obtained by charging the desired adsorbate to the target pressure inside the adsorption cell; sufficient time was allowed to reach equilibrium. Usually, the first few measurements were done at very low pressures (below 0.05 bar) in order to obtain accurate Henry's constant. Subsequent measurements for the isotherm were obtained by increasing the pressure in the incremental doses. Equilibrium adsorption was measured at approximately 15–20 points within the entire pressure range to get more reliable isotherm model parameters. After completing the isotherm experiment, the sample was again activated at a higher temperature under vacuum, as described earlier. The Excess amount adsorbed was calculated from raw measurements using buoyancy corrections (as described next). The impenetrable solid volume of adsorbent for buoyancy correction was obtained from helium measurements at 294 K in the pressure range of 0−25 bar, using non–adsorbing helium assumption.

Table 4.2: Details of activation protocols used for different MOFs.

MOF	Temperature (K)	Activation Time (hours)
Cu–abtc	443	3
Cu–hbtc	443	3
Cu–BTC	443	3
Cu–(bromo)BTC	443	3
Cu–(iodo)BTC	443	3
UiO–66	423	3
UiO–66–NH_2	423	3
UiO–66–NO_2	423	3
UiO–66–COOH	423	3
UiO–66–$(COOH)_2$	423	3

4.5.1 Calculation of Amount Adsorbed

When an activated sample is equilibrated with a gas at a particular temperature and pressure, Gibbs' excess amount adsorbed (M_{ex}) is calculated as

$$M_{ex} = M_{eq} - M_0 + V_{buoyancy}\rho^{gas} \qquad 4.1$$

Where M_0 is true adsorbent weight, including bucket weight in vacuo, M_{eq} is adsorbent plus bucket weight at equilibrium. M_0 and M_{eq} can directly be obtained from the magnetic suspension balance reading taken during the experiments from the following equation.

$$M_{eq} = MP1 - ZP \quad \text{(at equilibrium)} \tag{4.2}$$

$$M_0 = MP1 - ZP \quad \text{(at vacuo)} \tag{4.3}$$

Where *ZP* is the weight measurement at zero point position, *MP1* is the weight measurement when the only bucket was lifted, and *MP2* is the weight measurement when both bucket and sinker were lifted.

The last term in Eq. No. 4.1 is used for buoyancy correction to the sample and bucket. $V_{buoyancy}$ is the buoyancy volume, and ρ^{gas} is the bulk gas density.

4.6 Different Types of Amount Adsorbed

The bulk density was obtained from the virial equation of state

$$\rho^{gas} = \left(\frac{-1 + \sqrt{\frac{1 + 4B^{gas}P}{RT}}}{2B^{gas}} \right) M_w \tag{4.4}$$

Where M_w is the molar mass of the gas, P is the pressure, T is the temperature, R is the gas constant, and B^{gas} is the gas phase second virial coefficient.

The usual temperature dependency for B^{gas} is taken as

$$B^{gas} = B_1 + \frac{B_2}{T} + \frac{B_3}{T^3} + \frac{B_4}{T^8} + \frac{B_5}{T^9} \qquad 4.5$$

The values of B_i for the gases used in this study are tabulated in Table 4.3.

Table 4.3: Second virial coefficients for different gases [6].

Gas	$B_1 \times 10^2$	$B_2 \times 10^{-1}$	$B_3 \times 10^{-5}$	$B_4 \times 10^{-15}$	$B_5 \times 10^{-17}$
	$m^3\ kmol^{-1}$	$m^3\ kmol^{-1}\ K$	$m^3\ kmol^{-1}\ K^3$	$m^3\ kmol^{-1}\ K^8$	$m^3\ kmol^{-1}\ K^9$
He	1.400	-3.540	-5.950E-06	3.610E-13	-7.940E-15
CO_2	5.440	-3.635	-14.960	85.900	-139.700
CH_4	5.438	-2.714	-2.135	0.920	-0.785
CO	5.122	-1.709	-0.742	0.046	-0.029
N_2	4.670	-1.495	-0.611	0.081	-0.046
O_2	3.900	-1.554	-0.848	0.164	-0.115
C_2H_6	8.095	-6.171	-14.350	67.600	-97.400
C_3H_8	11.250	-10.000	-43.140	-18.000	-165.000

Fugacity was used instead of pressure to handle the gas phase non–ideality at higher pressures [7]. It was obtained from the virial equation for the bulk gas phase using

$$ln\left(\frac{f}{P}\right) = \left[\frac{B^{gas}P}{RT}\right] \qquad 4.6$$

4.6.1 Determination of Buoyancy Volume for the Various Reference States

For the calculation of buoyancy volume V_{buoyancy}, helium is used as probe gas. With non-adsorbing assumption for helium, LHS of Eq. No. 4.1 is taken as zero.

$$0 = M_{eq} - M_0 + V_{buoyancy}\rho^{gas} \qquad 4.7$$

M_{eq} and ρ^{gas} were obtained at 294 K at several pressures between 0–25 bar. The slope of M_{eq} vs ρ^{gas} was used to obtain the buoyancy volume for isotherm measurements.

4.7 Conversion of Units

In general, the amount adsorbed is expressed per unit kilogram of adsorbent. However, to understand the effect of metal atom substitution in the framework, specific units are not suitable; since the molar masses of the different metal atoms are different, the formula mass of the resultant unit cell also varies. Thus, the unit of "amount adsorbed" is converted from 'mol kg^{-1}' to 'molecules $unit\ cell^{-1}$' using.

$$N_u = \frac{NM_f}{1000} \qquad 4.8$$

Where N_u is the amount adsorbed in molecules $unit\ cell^{-1}$, N is the amount adsorbed in mol kg^{-1}, M_f is the molecular weight of unit cell in g. The amount adsorbed per metal atom (N_m) can be further calculated from

$$N_m = \frac{N_u}{n} \qquad 4.9$$

Where n is the number of metal atoms in one unit cell.

Volumetric adsorption uptakes are also important for practical applications in gas storage and separation. Gravimetric uptakes (N) can easily be converted to volumetric uptakes (N_v) following Eq. No. 4.10.

$$N_v = N\rho_c \qquad 4.10$$

Where N_v (mol L^{-1}) is the volumetric amount adsorbed, N is the amount adsorbed in mol kg^{-1} and ρ_c (g cm^{-3}) is the crystal density of the adsorbent.

It should be noted here that Eq. 4.10 is valid with the strict assumption of no void space between two crystals or two particles of adsorbent. In a real scenario, there will always be some void fraction within the adsorbent material. Thus the volumetric uptake obtained from Eq. 4.10 is the maximum possible uptake. In reality, the experimentally achieved value of volumetric uptake is lower than that obtained through Eq. 4.10 and depends upon the packing of adsorbent [8].

4.8 Experimental Conditions

Adsorption equilibria of various gases on several MOFs in this work were measured gravimetrically for a wide range of temperatures and pressures. The details of the experimental conditions at which adsorption measurements were performed are given in Table 4.4.

Table 4.4: Experimental ranges for various adsorption isotherm measurements.

Adsorbent	**Adsorbate**	**Temperatures (K)**	**Pressure Range (bar)**
Cu–abtc Cu–hbtc	CO_2	294, 317, 356	0–30
	CO	294, 317, 356	0–70
	CH_4	294, 317, 356	0–80
	N_2	294, 317, 356	0–100
	O_2	294, 317, 356	0–36
	C_2H_6	294, 317, 356	0 – 20
	C_3H_8	294, 317, 356	0–7
Cu–BTC Cu–(bromo)BTC Cu–(iodo)BTC	CO_2	294, 317, 356	0–25
	CO	294, 317, 356	0–45
	CH_4	294, 317, 356	0–75
	N_2	294, 317, 356	0–75
UiO–66 UiO–66–NH_2 UiO–66–NO_2 UiO–66–COOH UiO–66–$(COOH)_2$	CO_2	294, 317, 356	0–25
	CO	294, 317, 356	0–40
	CH_4	294, 317, 356	0–60
	N_2	294, 317, 356	0–80

4.9 Details of Gases Used

The details of various studied gases were mentioned in Table 4.5. All the gases were more than 99% in purity. No further purification has been done.

Table 4.5: Details of gases used in this study.

Gas	Supplier	Minimum Percentage Purity (Approximately)
He	Assam Air Products	99.995
CO_2		99.9
N_2		99.99
O_2		99.9
CO	Vadilal Gases Limited, India	99.95
CH_4		99.95
C_2H_6		99.5
C_3H_8		99.5

4.10 Physical Properties of Studied Gases

The physical properties of all studied gases in this work were given in Table 4.6 [9].

Table 4.6: Physical properties of gases used in this study.

Gas	Molecular Weight	Kinetic Diameter	Polarizability	Dipole Moment	Quadrupole Moment
	(g mol^{-1})	(Å)	($\times 10^{25}$ cm^3)	($\times 10^{18}$ esu cm)	($\times 10^{40}$ C m^2)
He	4	2.58	2.06	0	0
CO_2	44	3.3	26.3	0.0	14.3
CO	28	3.76	19.5	0.112	2.5
CH_4	16	3.8	26	0.0	0.0
N_2	28	3.64	17.6	0.0	1.52
O_2	32	3.5	16	0.0	1.3
C_2H_6	30	4.4	44.7	0.0	0.65
C_3H_8	44	4.3	62.9	0.0	4.0

References

(1) Lee, Y. G.; Moon, H. R.; Cheon, Y. E.; Suh, M. P. A Comparison of the H_2 Sorption Capacities of Isostructural Metal-Organic Frameworks With and Without Accessible Metal Sites: [{Zn_2(abtc)(dmf)$_2$}$_3$] and [{Cu_2(abtc)(dmf)$_2$}$_3$] versus [{Cu_2(abtc)}$_3$]. *Angew. Chem. Int.- Ed.* **2008**, *47*, 7741–7745.

(2) Liu, J.; Culp, J.T.; Natesakhawat, S.; Bockrath, B.C.; Zande, B.; Sankar, S.G.; Garberoglio, G.; Karl Johnson, J. Experimental and Theoretical Studies of Gas Adsorption in Cu_3(BTC)$_2$: An Effective Activation Procedure *J. Phys. Chem. C.* **2007**, *111*, 9305–9313.

(3) Cai, Y.; Kulkarni, A. R.; Huang, Y.-G.; Sholl, D. S.; Walton, K.S. Control of Metal Organic Framework Crystal Topology by Ligand Functionalization: Functionalized HKUST-1 Derivatives. *Cryst. Growth Des.* **2014**, *14*, 6122–6128.

(4) Karz, M. J; Brown, Z. J; Colon, y. J; Siu, P. W; Scheidt, K. A; Snurr, R. Q; Hupp, J, T; Farha, O. K. A facile Synthesis of UiO-66, UiO-67 and Their Derivatives. *Chem. Commun.* **2013**, *49*, 9449–9451.

(5) Zhang, X.; Hu, Q.; Xia, T.; Zhang, J.; Yang, Y.; Cui, Y.; Chen, B.; Qian, G. Turn-On and Ratiometric Luminescent Sensing of Hydrogen Sulfide Based on Metal-Organic Frameworks. *ACS Appl. Mater. Interfaces* **2016**, *8*, 32259–32265.

(6) http://dippr.byu.edu/student.asp.

(7) Talu, O. Needs, Status, Techniques and Problems With Binary Gas Adsorption Experiments. *Advances in Colloid and Interface Science* **1998**, *76-77*, 227–269.

(8) Peng, Y.; Krungleviciute, V.; Eryazici, I.; Hupp, J. T.; Farha, O. K.; Yildirim, T. Methane Storage in Metal–Organic Frameworks: Current Records, Surprise Findings, and Challenges. *J. Am. Chem. Soc.* **2013,** *135*, 11887–11894.

(9) Chowdhury, P. Gas Adsorption on Cu-BTC and Cr-BDC Metal Organic Frameworks (MOFs). **PhD Dissertation,** *Indian Institute of Technology, Guwahati* (**2010**).

CHAPTER 5

A Comparison of Adsorption Capacities of Cu–abtc Versus Cu–hbtc MOFs

In this chapter, the adsorption characteristics of CO_2, CO, N_2, CH_4, C_2H_6, C_3H_8, and O_2 on Di–Isophthalate MOFs were evaluated at three different temperatures viz. 294, 317, and 356 K and pressures ranging from 0–100 bar. This is an attempt to understand the affinity of functional group NH–NH presented in Cu–hbtc over N=N in Cu–abtc. In addition, the effect of polarity, polarizability, and open metal sites present in the framework of these MOFs on the adsorption characteristics also can be understand by this work.

5.1 Background

The adsorption characteristics of 3,3′,5,5′–azobenzenetetracarboxylic acid (H_4abtc) organic linker contained MOFs recently reported in the field of gases adsorption [1–5], gases separation [6, 7], drug delivery [8], dye removal [9], and magnetic thermal properties, etc. [10–13]. In these MOFs, {$M_2(CO_2)_4$}(M= metal) type of paddlewheel SBU is formed from M^{2+} ions with abtc ligand. The H_4abtc is one kind of aromatic tetracarboxylate ligand that possesses many advantages, including photochromatic and luminescence properties, etc. The binding modes and the geometrical configuration of the MOF resulting from the four carboxylic groups on the ligand increase it's the thermal stability and rigidity [19].

One of the research interests lies in understanding the effect of the functional groups present on the ligand on the gas adsorption properties of the MOF. We hypothesized that a subtle change by

the reduction of the azo group in the H_4abtc linker to form 3,3′,5,5′ hydrazinebenzenetetracarboxylatic acid (H_4hbtc) would influence the structure and the adsorption characteristics of the resultant MOF, shown in Figure 5.1.

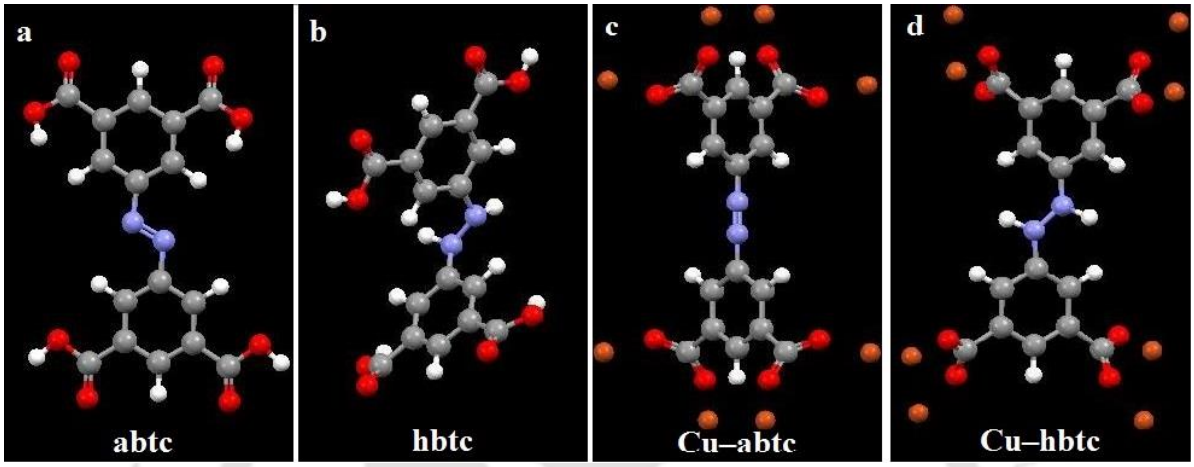

Figure 5.1: DFT optimized structures of (a) abtc, (b) hbtc organic linkers; After Cu metalation (c) Cu–abtc and (d) Cu–hbtc (Cu, orange; C, gray; O, red; H, white; N, blue).

In this work, we report the gas adsorption properties of the two porous structures formed from these two ligands, viz. [{Cu_2(abtc)}$_3$] (**Cu–abtc**) and [{Cu_2(hbtc)}$_3$] (**Cu–hbtc**). In both materials, a pair of Cu^{II} centers form a {$Cu_2(O_2CR)_4$} (R=organic ligand) square-shaped SBU is linked by four rectangular organic linkers, and extend infinitely giving rise to MOFs Cu–abtc and Cu–hbtc**.**

In this chapter, the adsorption properties of CO_2, CO, N_2, CH_4, C_2H_6, C_3H_8, and O_2 on Cu–abtc and Cu–hbtc MOFs at three different temperatures (294, 317, and 356 K) and a wide range of pressures were studied. We attempted to understand a subtle change by replacing the azo group, i.e., N=N in the abtc linker, with HN–NH group. To understand the effect of functional groups of those ligands on the gas adsorption characteristics of the MOF, thermodynamic properties such as the Henry's constant and enthalpy of adsorption were calculated for each MOF at

different conditions. In addition, IAST was also used to understand the effect of functionalization on selectivities for various binary mixtures.

5.2 Characterization of Frameworks Synthesized

Cu–abtc and Cu–hbtc frameworks were synthesized by the procedure reported in the literature and was discussed in Section 4.2.1–4.2.2. The synthesized samples were analyzed using thermogravimetric, powder XRD and BET surface area analysis.

5.2.1 Powder X-ray Diffraction (Powder XRD) Analysis

The powder XRD patterns for Cu–abtc and Cu–hbtc are given in Figure 5.2. The patterns are almost identical, indicating that both the compounds are iso-structural. This is rather surprising, considering that the reduction of N=N group results in the loss of the planarity of the abtc linker framework. The DFT optimized geometry of Cu–hbtc showed that on metalation with Cu, the linker almost regains the structure comparable with the one reported for Cu–abtc [18].

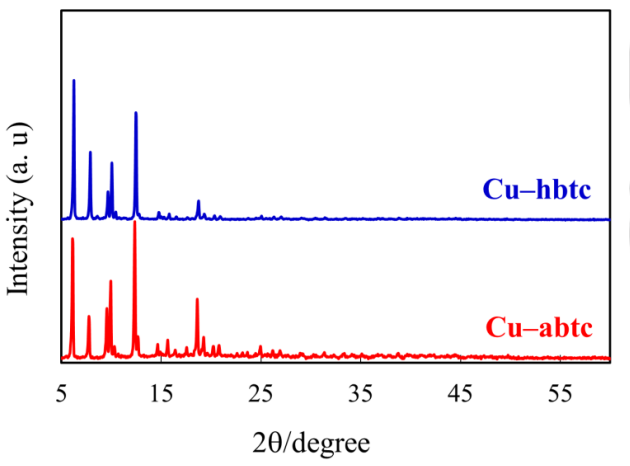

Figure 5.2: Powder X-ray diffractogram of Cu–abtc (red) and Cu–hbtc (blue).

5.2.2 Thermogravimetric Analysis (TGA)

Thermograms of Cu–abtc and Cu–hbtc were performed on a thermogravimetric analyzer (showed in Figure 5.3). The temperature was ramped from 298 K to 1074 K with a heating rate of 5 K min^{-1}, and the measurements were performed under argon atmosphere. There is a total of three weight-loss steps observed for each sample. The first weight loss step up to 377 K is relatively rapid and corresponds to the removal of solvent (methanol) and moisture. The second weight loss is due to the detachment of bonded 1,4–dioxane and DMF molecules. The final weight loss step corresponding to the decomposition and collapse of the framework happened around about of 575 K.

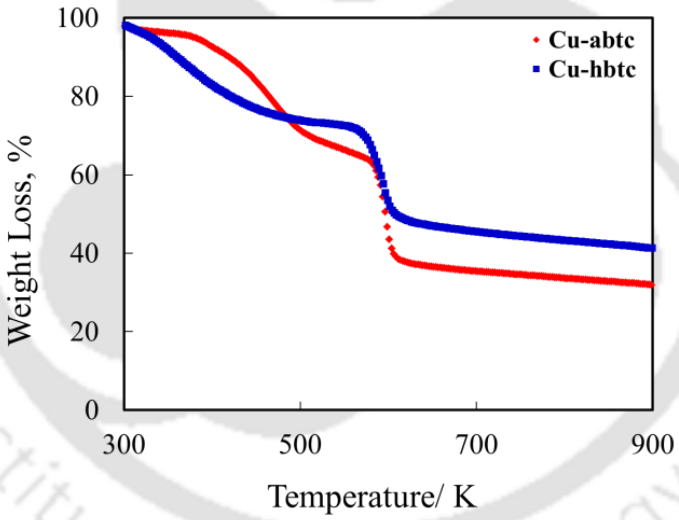

Figure 5.3: TGA analysis of Cu–abtc (red) and Cu–hbtc (blue) at a heating rate of 5 K min^{-1} under argon flow.

5.2.3 Surface Area and Pore Volume Analysis

N_2 adsorption isotherms of Cu–abtc and Cu–hbtc at 77 K are shown in Figure 5.4. Both were activated prior to isotherm measurement at 443 K under vacuum. Cu–hbtc shows more N_2 loading per unit gram than Cu–abtc. The surface area and pore volume calculated from these

isotherms are given in Table 5.1. A significant increase (~ 45 %) in the surface area and pore volume is observed for Cu–hbtc.

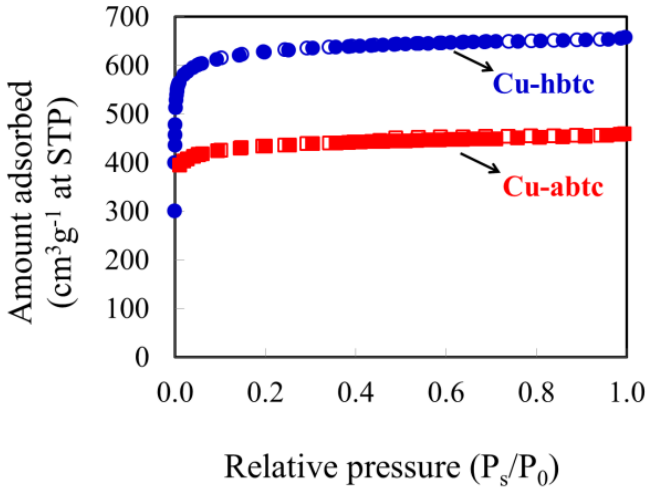

Figure 5.4: N_2 adsorption of Cu–abtc (red) and Cu–hbtc (blue) at 77 K.

Table 5.1: BET surface area and pore volume of Cu–abtc and Cu–hbtc

compound	Surface area	Pore volume
	m^2g^{-1}	cm^3g^{-1}
Cu–abtc	1311	0.711
Cu–hbtc	1904	1.019

5.3 Adsorption Isotherms

Adsorption isotherms of CO_2, CO, N_2, CH_4, C_2H_6, C_3H_8, and O_2 were measured on Cu–abtc and Cu–hbtc MOFs. The subtle difference in the constituent ligand in the two MOFs affects its interaction with adsorbates, thereby changing its adsorption characteristics. This effect will also depend on the polarity and polarizability of the adsorbate. The isotherms were modeled to get

insights into adsorption. For polar gases, i.e., CO_2 and CO, Langmuir–virial domain [ln (f/N) vs. N] Plot is useful for analyzing low-pressure experimental data. For other adsorbates (i.e., N_2, O_2, CH_4, C_2H_6, and C_3H_8), the Langmuir model [N vs. f] is sufficient to fit the experimental data.

5.3.1 CO_2 Isotherms

The adsorption isotherms for CO_2 are shown in Figure 5.5. Among all the studied gases, CO_2 had the highest adsorption capacity and it was found to be 2.9 mol kg^{-1} and 3.7 mol kg^{-1} at 1 bar and 294 K for Cu–abtc and Cu–hbtc. However, CO_2 uptakes are lower compared to that of Zn–DOBDC (4.6 mol kg^{-1}) [21], Cu–BTC (5.8 mol kg^{-1}) [22], Co–DOBDC (6.7 mol kg^{-1}) [23], Ni–DOBDC (6.9 mol kg^{-1}) [24] and Mg/DOBDC (7.57 mol kg^{-1}) [14] and higher than MOF–5 (1.0 mol kg^{-1}) [21], Zn–DABCO (2.0 mol kg^{-1}) [25], Ni–DABCO (2.0 mol kg^{-1}) [25], MIL–53 (Al) (2.3 mol kg^{-1}) [16], and MIL–47 (2.5 mol kg^{-1}) [16]. The CO_2 adsorption capacity of Cu–abtc is comparable to MIL–101 (2.8 mol kg^{-1}) [26]. The experimental results suggest that NH–NH bonds in Cu–hbtc may have more affinity towards CO_2 molecules than N=N bonds in Cu–abtc.

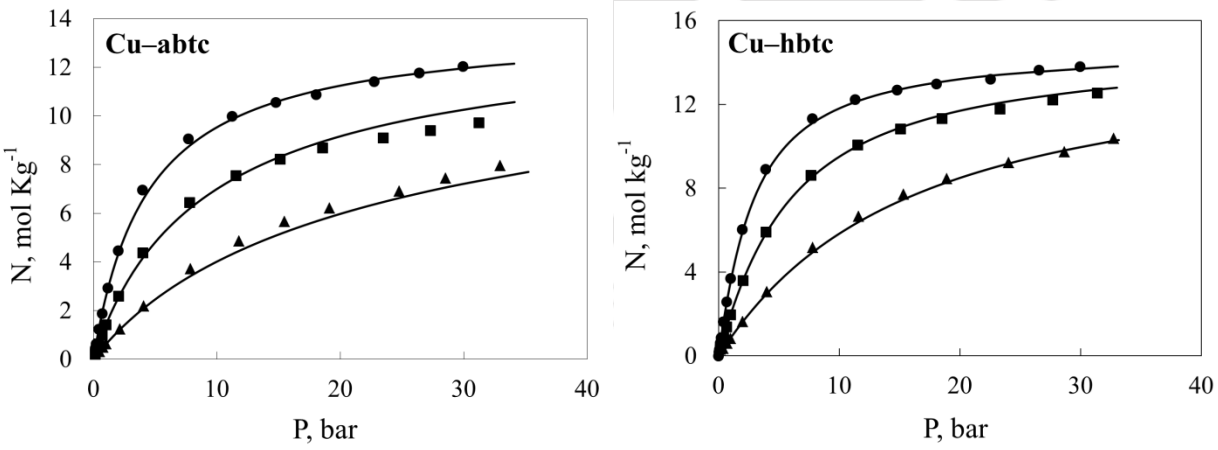

Figure 5.5: CO_2 isotherms of Cu–abtc and Cu–hbtc MOFs. Symbols are experimental data at 294 K (●), 317 K (■), and 356 K (▲); lines are fits obtained using Langmuir-virial isotherm parameters from Table 5.2.

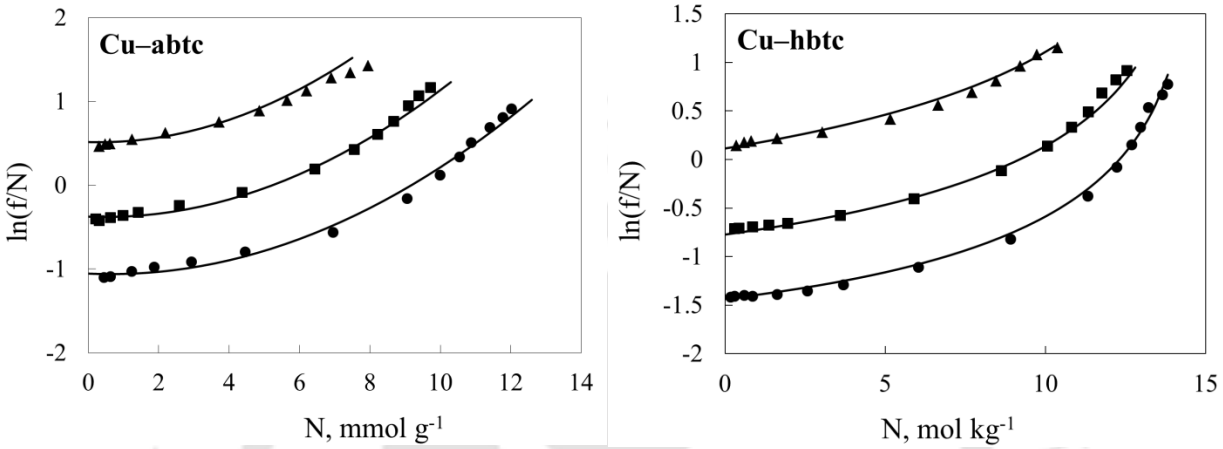

Figure 5.6: CO_2 isotherms of Cu–abtc and Cu–hbtc MOFs in Langmuir-virial domain. Symbols are experimental data at 294 K (●), 317 K (■), and 356 K (▲); lines are fits obtained using Langmuir-virial isotherm parameters from Table 5.2.

5.3.2 CO Isotherms

The CO loading capacity on Cu–abtc and Cu–hbtc at 1 bar and 294 K (See in Figure 5.7) is 0.64 and 1.02 mol kg^{-1} respectively. These CO uptakes are less compared to other adsorbents such Ni–DOBDC (5.9 mol kg^{-1}) [33] and Cu–BTC (1.4 mol kg^{-1}) [22] and higher than MIL–53(Al) (0.3 mol kg^{-1}) [29] and silicalite (0.27 mol kg^{-1}) [34]. In addition, CO uptakes are comparable to IRMOF–1 (0.58 mol kg^{-1}) [35] and IRMOF–3 (0.6 mol kg^{-1}) [35] for Cu–abtc, and Zeolite 13X (1.17 mol kg^{-1}) [36] for Cu–hbtc**.**

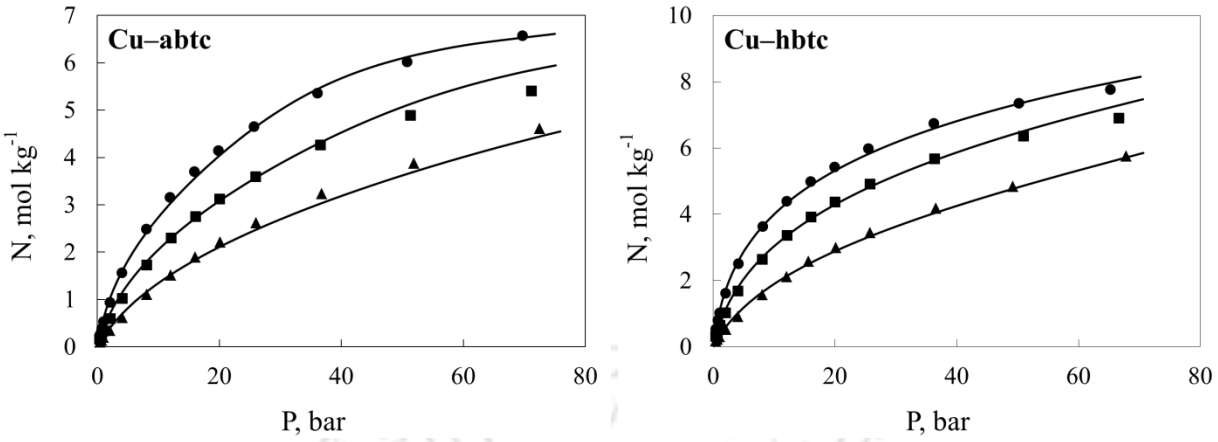

Figure 5.7: CO isotherms of Cu–abtc and Cu–hbtc MOFs. Symbols are experimental data at 294 K (●), 317 K (■), and 356 K (▲); lines are fits obtained using Langmuir-virial isotherm parameters from Table 5.3.

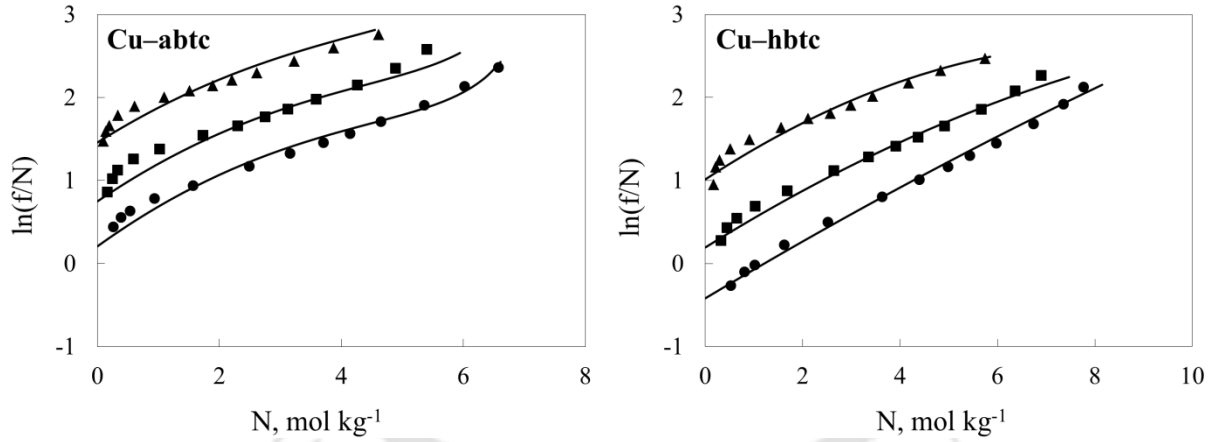

Figure 5.8: CO isotherms of Cu–abtc and Cu–hbtc MOFs in Langmuir-virial domain. Symbols are experimental data at 294 K (●), 317 K (■), and 356 K (▲); lines are fits obtained using Langmuir-virial isotherm parameters from Table 5.3.

5.3.3 CH_4 Isotherms

The adsorption isotherms of CH_4 for Cu–abtc and Cu–hbtc are shown in Figure 5.9. The adsorption capacities are found around 7.3 mol kg^{-1} for Cu–abtc and 8.4 mol kg^{-1} for Cu–hbtc at 294 K, 35 bar. However, these values are lower compared to Mg/DOBDC (9.82 mol kg^{-1}) [27], Cu–BTC (11.38 mol kg^{-1}) [27], NOTT–109 (11.16 mol kg^{-1}) [28], NOTT–101 (12.77 mol kg^{-1}) [28], comparable to Co–DOBDC (8.4 mol kg^{-1}) [27], Ni–DOBDC (8.6 mol kg^{-1}) [27], MIL–53 (Al) (8.4 mol kg^{-1}) [29] and higher than Zeolite 13X (3.3 mol kg^{-1})[30].

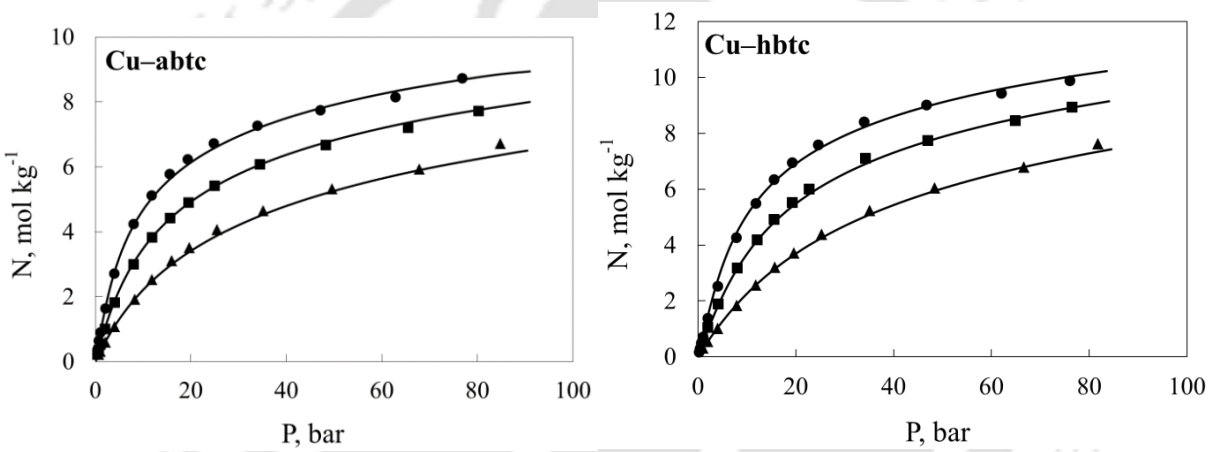

Figure 5.9: CH_4 isotherms of Cu–abtc and Cu–hbtc MOFs in Langmuir domain. Symbols are experimental data at 294 K (●), 317 K (■), and 356 K (▲); lines are fits obtained using Langmuir isotherm parameters from Table 5.4.

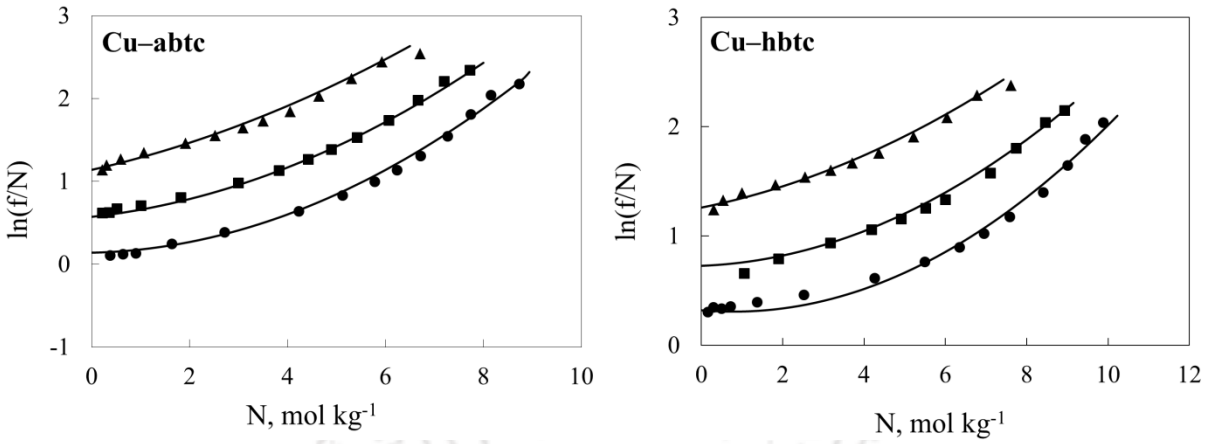

Figure 5.10: CH_4 isotherms of Cu–abtc and Cu–hbtc MOFs in Langmuir domain. Symbols are experimental data at 294 K (●), 317 K (■), and 356 K (▲); lines are fits obtained using Langmuir isotherm parameters from Table 5.4.

5.3.4 N_2 Isotherms

The N_2 adsorption isotherm on Cu–abtc and Cu–hbtc is shown in Figure 5.11. The adsorption capacity is found 0.27 mol kg^{-1} and 0.24 mol kg^{-1} respectively for Cu–abtc and Cu–hbtc at 1 bar, 294 K. As compared to CO_2 and CH_4 adsorption capacities, N_2 having relatively non–polar with low quadrupole moment attributed to such lower adsorption capacities. Hence, unlike in CO_2 and CH_4, their adsorption capacity on Cu–hbtc is slightly higher (as compared to that on Cu–abtc**).** As a result of this behavior, the selectivity for CO_2 over N_2 will be significantly higher for Cu–hbtc compared to Cu–abtc. However, these uptake capacities are lower than Mg/DOBDC (1.1 mol kg^{-1}) [15], Ni/DOBDC (1.02 mol kg^{-1}) [24], Zeolite 13X (0.8 mol kg^{-1}) [31] and comparable to MIL–53 (Al) (0.20 mol kg^{-1}) [29], Cu–BTC (0.31 mol kg^{-1}) [32].

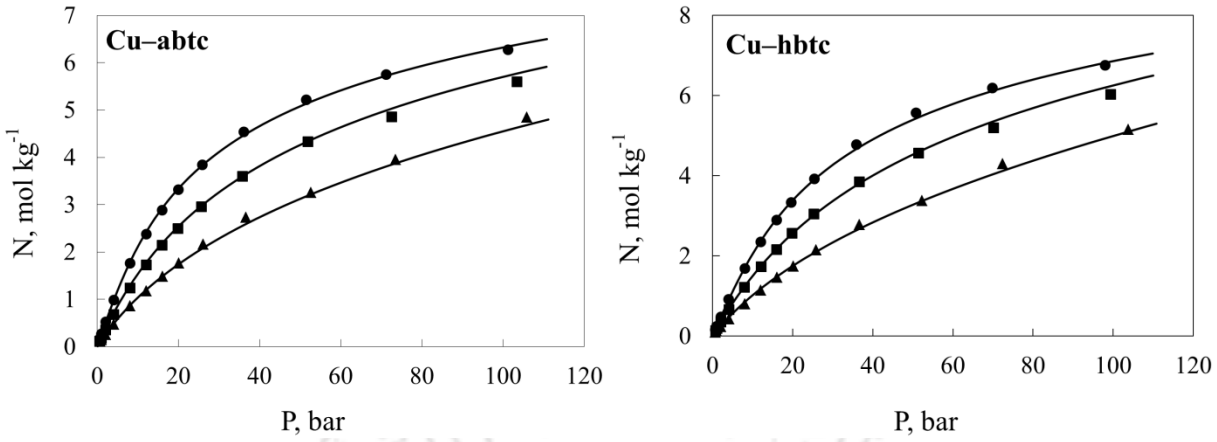

Figure 5.11: N_2 isotherms of Cu–abtc and Cu–hbtc MOFs in Langmuir domain. Symbols are experimental data at 294 K (●), 317 K (■), and 356 K (▲); lines are fits obtained using Langmuir isotherm parameters from Table 5.5.

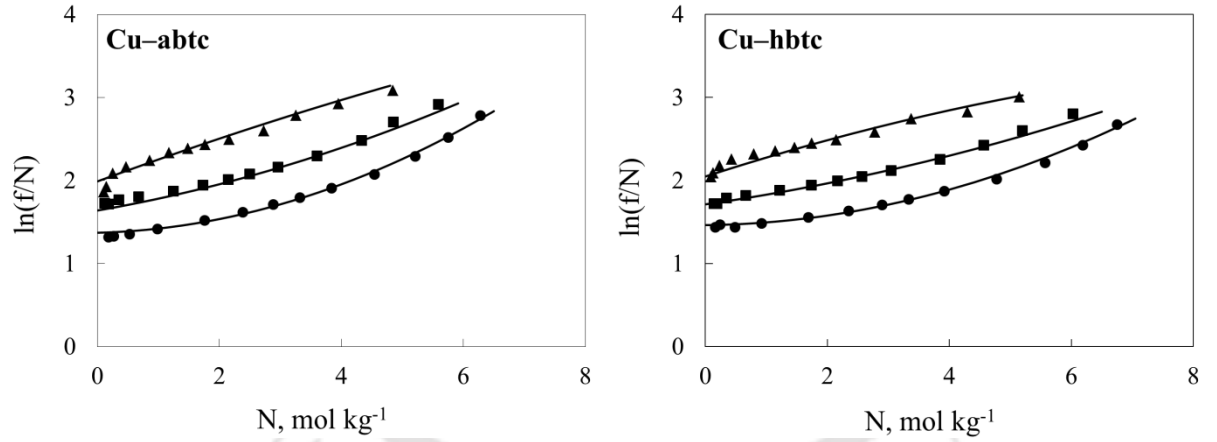

Figure 5.12: N_2 isotherms of Cu–abtc and Cu–hbtc MOFs in Langmuir domain. Symbols are experimental data at 294 K (●), 317 K (■), and 356 K (▲); lines are fits obtained using Langmuir isotherm parameters from Table 5.5.

5.3.5 C_2H_6 Isotherms

The adsorption isotherm for C_2H_6 is given in Figure 5.13. The loading for C_2H_6 on Cu–abtc and Cu–hbtc measured in this work are 6.2 mol kg^{-1} and 7.5 mol kg^{-1} respectively at 1 bar, 294 K. This loading capacity of C_2H_6 on Cu–abtc can be comparable to Mg/DOBDC (6.3 mol kg^{-1})[37], Fe–DOBDC (6.6 mol kg^{-1}) [38] and higher than on Cu–BTC (4.8 mol kg^{-1}) [39], MOF–5 (1.9 mol kg^{-1}) [40], Zeolite 13X (1.6 mol kg^{-1}) [41], Silicalite (2.4 mol kg^{-1}) [42].

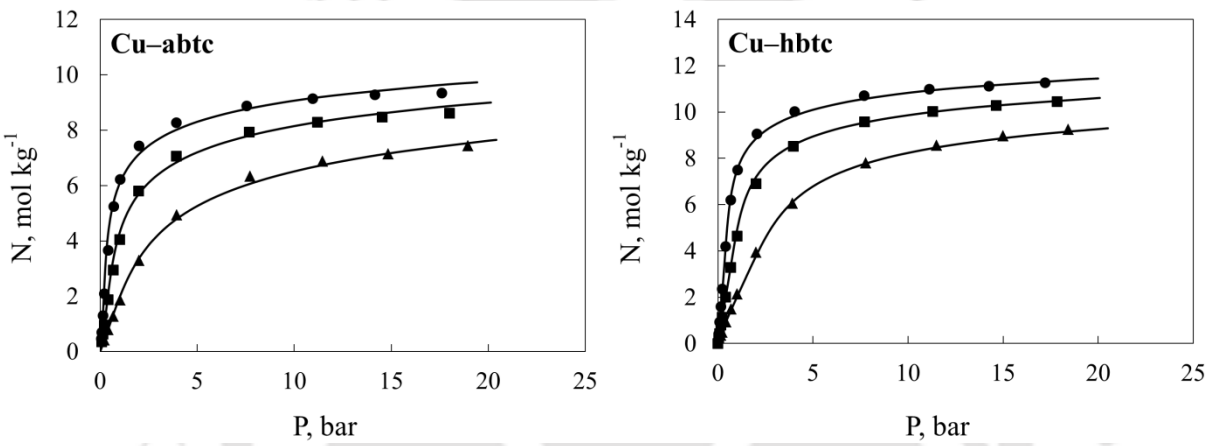

Figure 5.13: C_2H_6 isotherms of Cu–abtc and Cu–hbtc MOFs. Symbols are experimental data at 294 K (●), 317 K (■), and 356 K (▲); lines are fits obtained using Langmuir isotherm parameters from Table 5.6.

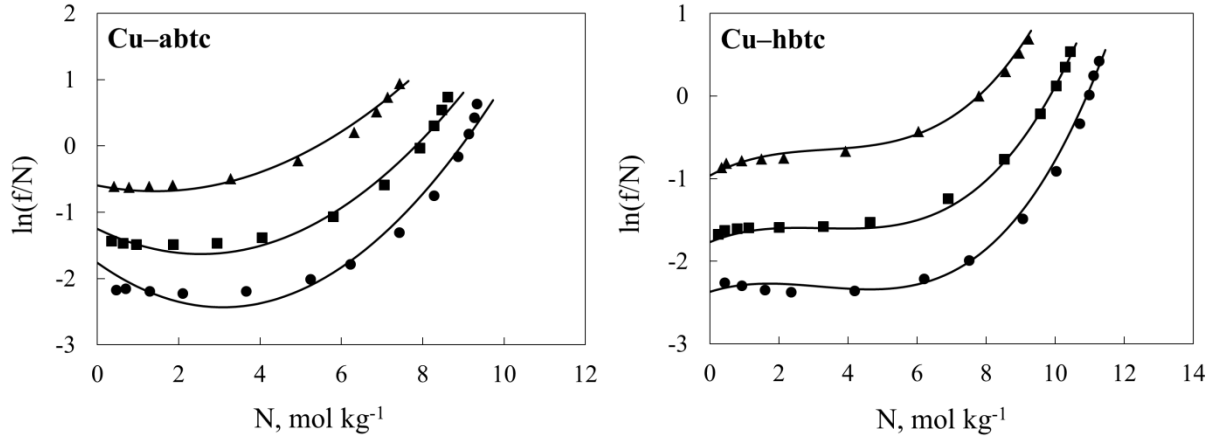

Figure 5.14: C_2H_6 isotherms of Cu–abtc and Cu–hbtc MOFs in Langmuir domain. Symbols are experimental data at 294 K (●), 317 K (■), and 356 K (▲); lines are fits obtained using Langmuir isotherm parameters from Table 5.6.

5.3.6 C_3H_8 Isotherms

At 294 K and 1 bar, the loading capacity of C_3H_8 on Cu–abtc found around 7.23 mol kg^{-1}. It is comparable to Cu–BTC (7.2 mol kg^{-1})[43] and higher than MIL–53 (Cr) (4.0 mol kg^{-1}) [44], Fe–DOBDC (5.3 mol kg^{-1})[40], Silicalite (3.2 mol kg^{-1})[45]. However, this value is lower than Mg/DOBDC (8.2 mol kg^{-1})[39]. To the best of our knowledge, the loading capacity of C_2H_6 and C_3H_8 on Cu–hbtc found around 7.5 mol $kg^{-1}$and 8.7 mol kg^{-1} respectively, and it is the highest loading capacity ever measured on MOFs at 294 K and 1bar. In general, as expected, the adsorption capacity increases with carbon chain length due to the increase in polarizability of the gases.

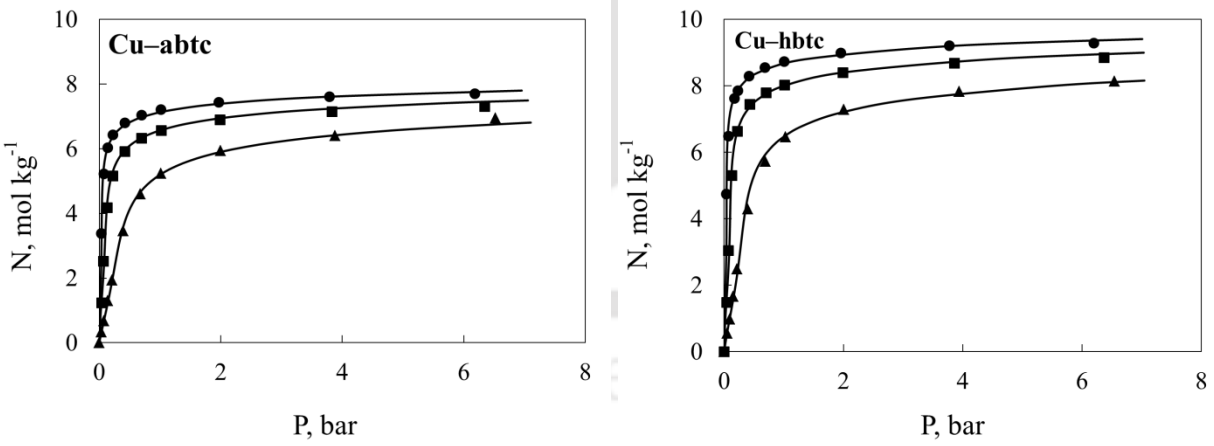

Figure 5.15: C_3H_8 isotherms of Cu–abtc and Cu–hbtc MOFs in Langmuir domain. Symbols are experimental data at 294 K (●), 317 K (■), and 356 K (▲); lines are fits obtained using Langmuir isotherm parameters from Table 5.7.

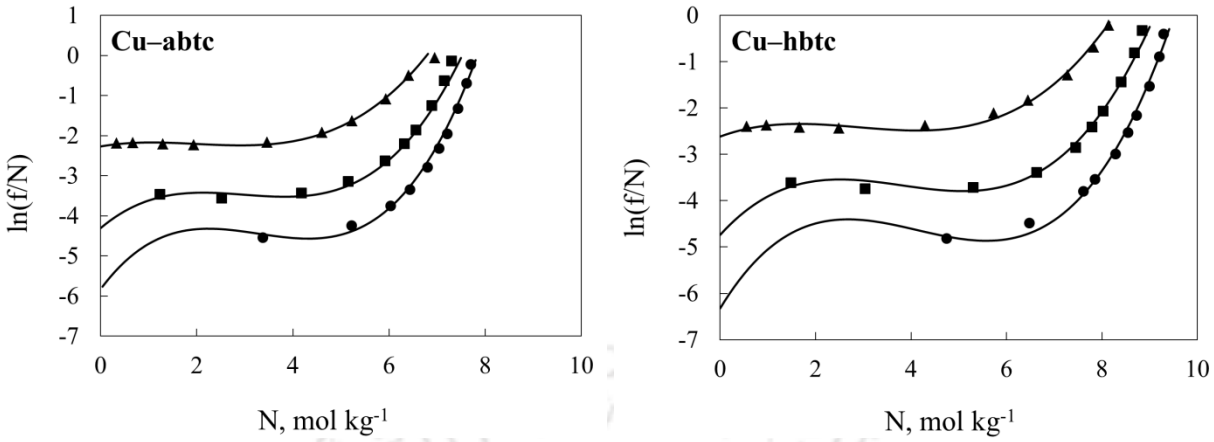

Figure 5.16: C_3H_8 isotherms of Cu–abtc and Cu–hbtc MOFs in Langmuir domain. Symbols are experimental data at 294 K (●), 317 K (■), and 356 K (▲); lines are fits obtained using Langmuir isotherm parameters from Table 5.7.

5.3.7 O_2 Isotherms

O_2 adsorption isotherms on Cu–abtc and Cu–hbtc are shown in Figure 5.17. The uptake capacities were found to be 0.22 mol kg^{-1} and 0.24mol kg^{-1} for Cu–abtc and Cu–hbtc. However, these capacities are lower than Cu–BTC (0.3 mol kg^{-1}) [39] and comparable to Zeolite 13X (0.2 mol kg^{-1}) [46] and higher than MIL–53(Al) (0.13 mol kg^{-1}) [29] and silicalite (0.15 mol kg^{-1}) [47]. For both Cu–abtc and Cu–hbtc, the uptake capacities of N_2 and O_2 were found to be approximately similar. Therefore, very low selectivity is observed for N_2 over O_2.

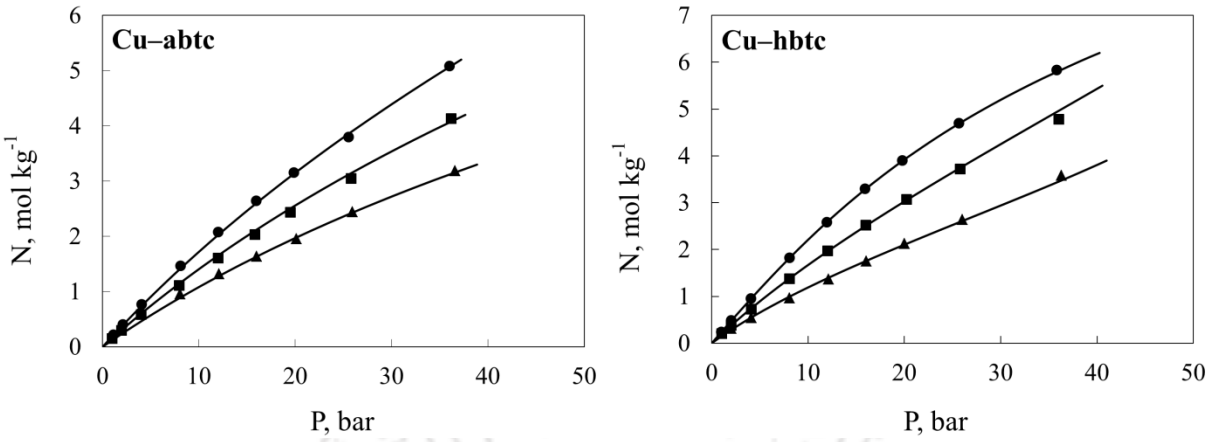

Figure 5.17: O_2 isotherms of Cu–abtc and Cu–hbtc MOFs. Symbols are experimental data at 294 K (●), 317 K (■), and 356 K (▲); lines are fits obtained using Langmuir isotherm parameters from Table 5.8.

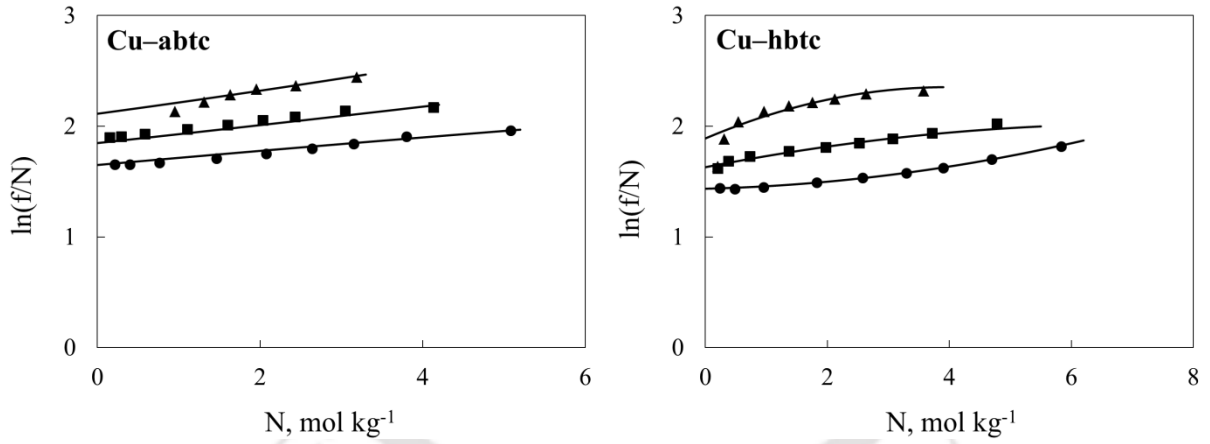

Figure 5.18: O_2 isotherms of Cu–abtc and Cu–hbtc MOFs in Langmuir domain. Symbols are experimental data at 294 K (●), 317 K (■), and 356 K (▲); lines are fits obtained using Langmuir isotherm parameters from Table 5.8.

5.4 Isotherm Modeling

The adsorption isotherms for the polar gases, i.e., CO_2 and CO, Langmuir–virial model [48] was used to fit the experimental data.

$$\ln\left(\frac{f}{N}\right) = bN + cN^2 + \ln\frac{N^{max}}{\beta(N^{max} - N)} \tag{5.1}$$

The temperature dependency for the Henry's constant (β) and virial parameters b, c are given by

$$\beta = \beta^{(0)}\exp(\beta^{(1)}/T) \tag{5.2}$$

$$b = b^{(0)} + \frac{b^{(1)}}{T} \tag{5.3}$$

$$c = c^{(0)} + \frac{c^{(1)}}{T} \tag{5.4}$$

Where T is temperature in K. The two parameters $\beta^{(0)}$ and $\beta^{(1)}$ are related to entropy and enthalpy of adsorption at zero loading, respectively.

For other adsorbates (i.e., N_2, O_2, CH_4, C_2H_6, and C_3H_8), the Langmuir model was sufficient to fit the experimental data. The following form of the model was used in this work.

$$N = \frac{N^{max}\beta f}{1 + \beta f} \tag{5.5}$$

Where N (mol kg^{-1}) is the amount adsorbed, f (bar) is the fugacity, N^{max} (mol kg^{-1}) is the saturation capacity, β (mol kg^{-1} bar^{-1}) is Henry's constant. The saturation capacity is considered independent of temperature.

Table 5.2: Fit parameters of Virial–Langmuir isotherm of CO_2.

Parameters	**Cu–abtc**	**Cu–hbtc**
$\beta^{(0)}$, mol kg^{-1} bar^{-1}	4.5812	6.6754
$\beta^{(1)}$, K	-941.4673	-2368.7657
$b^{(0)}$, mol^{-1} kg	2.0705	0.1973
$b^{(1)}$, mol^{-1} kg K	-345.6298	-75.6350
$c^{(0)}$, mol^{-2} kg^2	-0.1702	-0.0051
$c^{(1)}$, mol^{-2} kg^2 K	29.5265	2.3623
N^{max}, mol kg^{-1}	11.762	15.0739

Table 5.3: Fit parameters of Virial–Langmuir isotherm of CO.

Parameters	**Cu–abtc**	**Cu–hbtc**
$\beta^{(0)}$, mol kg^{-1} bar^{-1}	6.6001	7.9548
$\beta^{(1)}$, K	-1924.5808	-2589.9934
$b^{(0)}$, mol^{-1} kg	1.25	0.0791
$b^{(1)}$, mol^{-1} kg K	-207.9349	148.948
$c^{(0)}$, mol^{-2} kg^2	-0.2637	-0.0663
$c^{(1)}$, mol^{-2} kg^2 K	67.8528	-0.9633
N^{max}, mol kg^{-1}	7.9320	8.3044

Table 5.4: Fit parameters of Langmuir isotherm of CH_4.

Parameters	**Cu–abtc**	**Cu–hbtc**
N^{max}, mol kg^{-1}	9.1927	11.105
$\beta^{(0)} \times 10^{-5}$, bar^{-1}	7.69	9.21
$\beta^{(1)}$, bar^{-1}	2112.049	1986.467

Table 5.5: Fit parameters of Langmuir isotherm of N_2.

Parameters	**Cu–abtc**	**Cu–hbtc**
N^{max}, mol kg^{-1}	7.9536	9.1819
$\beta^{(0)} \times 10^{-5}$, bar^{-1}	2.00	2.00
$\beta^{(1)}$, bar^{-1}	1551.6961	1479.25

Table 5.6: Fit parameters of Langmuir isotherm of C_2H_6.

Parameters	**Cu–abtc**	**Cu–hbtc**
N^{max}, mol kg^{-1}	9.4848	11.5513
$\beta^{(0)} \times 10^{-5}$, bar^{-1}	3.41	4.91
$\beta^{(1)}$, bar^{-1}	3151.681	3025.89

Table 5.7: Fit parameters of Langmuir isotherm of C_3H_8.

Parameters	**Cu–abtc**	**Cu–hbtc**
N^{max}, mol kg^{-1}	7.5222	9.0846
$\beta^{(0)}\times 10^{-5}$, bar^{-1}	1.16	7.16
$\beta^{(1)}$, bar^{-1}	4284.6582	4469.2789

Table 5.8: Fit parameters of Langmuir isotherm of O_2.

Parameters	**Cu–abtc**	**Cu–hbtc**
N^{max}, mol kg^{-1}	16.2653	15.5123
$\beta^{(0)}\times 10^{-5}$, bar^{-1}	5.00	3.00
$\beta^{(1)}$, bar^{-1}	951.5605	1209.1654

5.5 Effect of physical properties of gases

The adsorption isotherms of CO_2, CO, and CH_4 on Cu–abtc and Cu–hbtc at 294 K are shown in Figure 5.19. Due to accessible metal sites [18] in both frameworks, electrostatic interactions are likely to be present. Thus CO with a significant dipole moment has higher adsorption capacity at lower pressures than CH_4. However, these metal sites are occupied at higher pressures, and adsorption occurs mainly due to dispersion interactions. As a result, the adsorption uptake for CH_4 (which has higher polarizability) is more than CO in the high-pressure region. This "cross–

over" in selectivity between CO and CH_4 occurs at about 0.2 bar for Cu–abtc and 4 bar for Cu–hbtc shown in Figure 5.19.

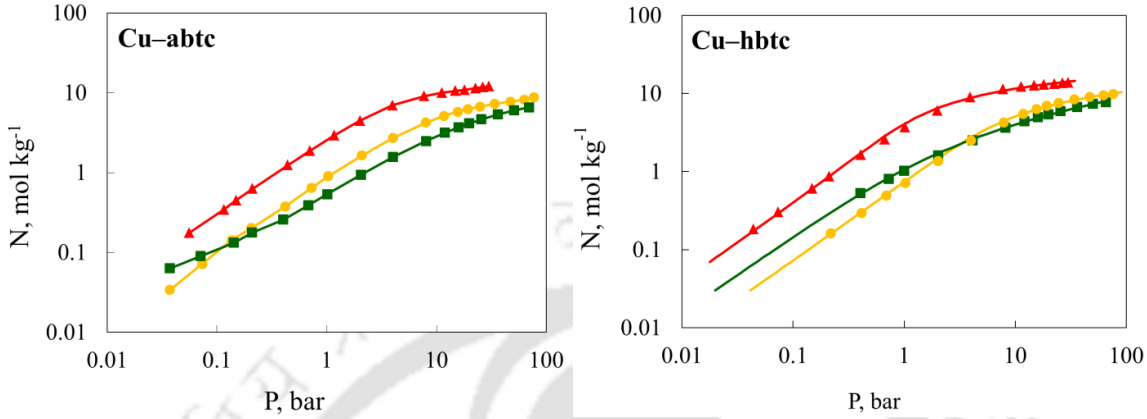

Figure 5.19: Adsorption Isotherms of CO_2 (▲), CO (■), and CH_4 (●) at 294 K for Cu–abtc and Cu–hbtc MOFs.

The comparative adsorption capacities for the non–polar gases at 294 K on Cu–abtc and Cu–hbtc are shown in Figure 5.20. The adsorption capacities are the lowest for N_2 and O_2 due to their low polarizability. For hydrocarbons (CH_4, C_2H_6, and C_3H_8), the adsorption capacity at lower pressures increases with carbon chain length (and hence polarizability). However, as the molecular size increases, the saturation loading decreases at higher pressure.

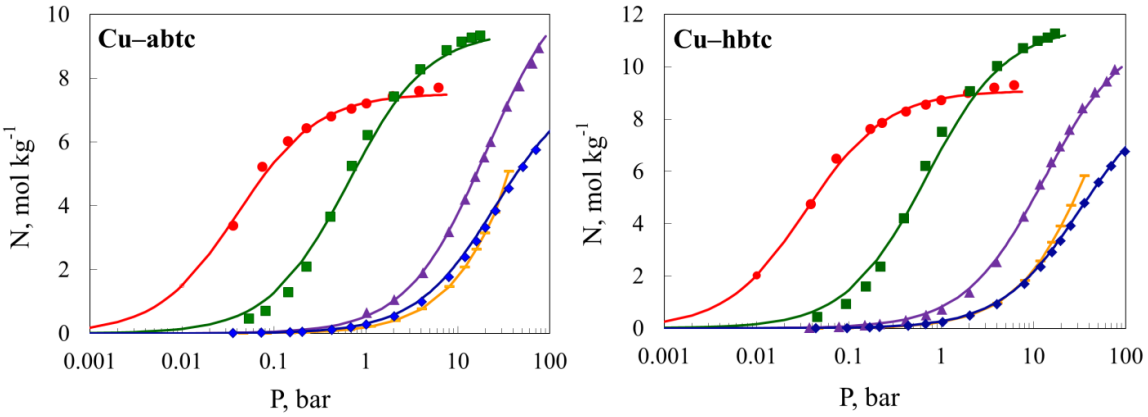

Figure 5.20: Adsorption Isotherms of C_3H_8(●), C_2H_6 (■), CH_4 (▲), N_2(♦), and O_2(⊖) at 294 K on Cu–abtc and Cu–hbtc MOFs.

5.6 Henry's Constants and Adsorption Enthalpy

The Henry's constant (β) at 294 K and the adsorption enthalpy at zero loading ($\Delta h_{ads,0}$) calculated from the model fit the parameters (From Table 5.2–Table 5.8). These plots help in understanding the effect of polarity and polarizability separately on adsorbate–adsorbent interactions. Both the quantities varied almost linearly for less polar gases (N_2, CH_4, C_2H_6, C_3H_8, and O_2). This behavior is similar to that obtained for the M/DOBDC series of MOFs [49]. However, for polar gases (CO_2 and CO) on compound Cu–hbtc, higher values of β and $\Delta h_{ads,0}$ are observed (Shown in Figure 5.22), highlighting significant electrostatic interactions (with the adsorbent) exist for the polar gases. However, such difference is minimal in Cu–abtc (shown in Figure 5.21).

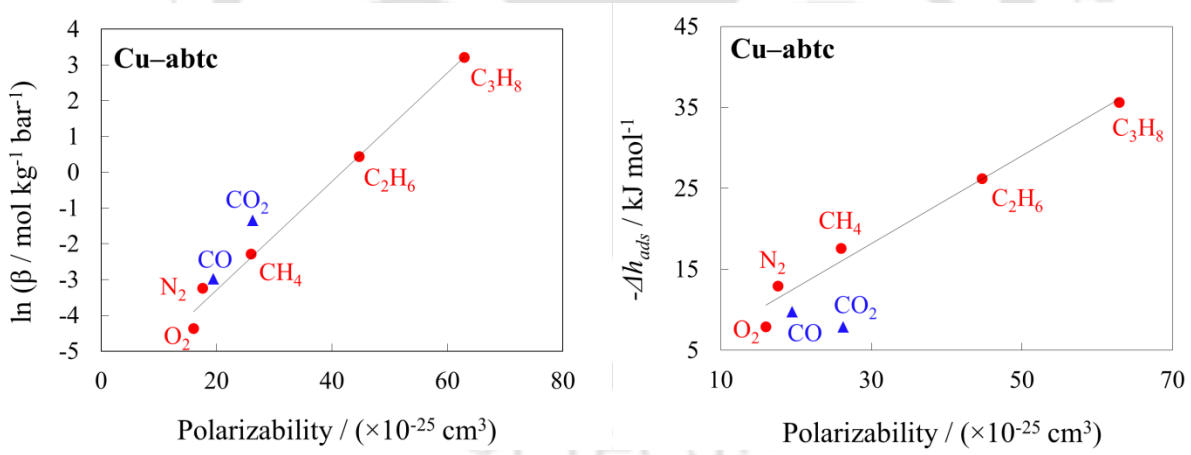

Figure 5.21: Henry's constant at 294 K and enthalpy of adsorption at zero occupancy as a function of the polarizability of the adsorbate for Cu–abtc; linear trend lines for nonpolar gases are also shown.

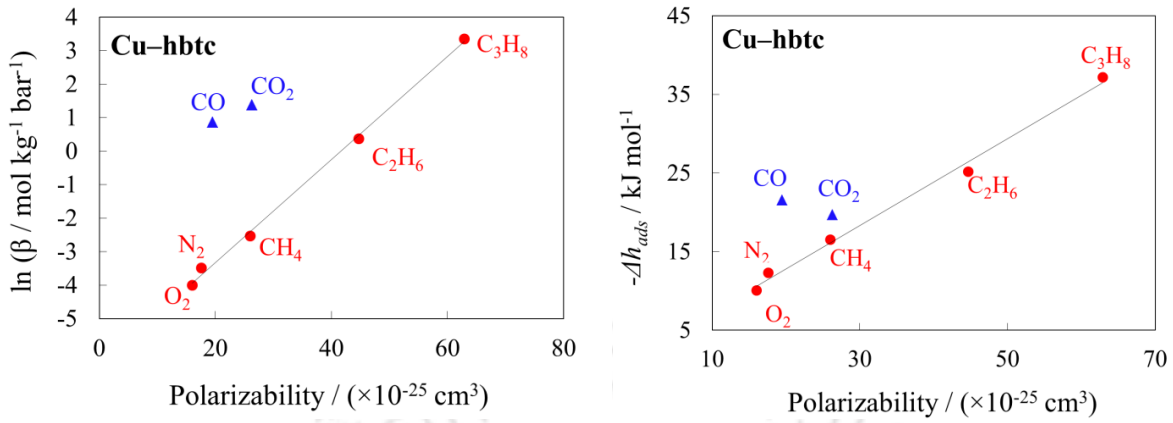

Figure 5.22: Henry's constant at 294 K and enthalpy of adsorption at zero occupancy as a function of the polarizability of the adsorbate for Cu–hbtc; linear trend lines for nonpolar gases are also shown.

The enthalpy of adsorption for CO_2 and N_2 on Cu–abtc and Cu–hbtc are shown in Figure 5.23. The adsorption enthalpy for CO_2 is slightly higher on Cu–hbtc compared to that of Cu–abtc, indicating a greater affinity of the NH–NH bond for the adsorbates. With an increase in loading, the adsorption enthalpy increases slightly for CO_2, possibly due to increased lateral interactions. However, in N_2, adsorption enthalpy on Cu–hbtc is only marginally lower than that on Cu–abtc**.** As a result of this behavior, the selectivity of CO_2 over N_2 will be significantly higher for Cu–hbtc compared to that on Cu–abtc.

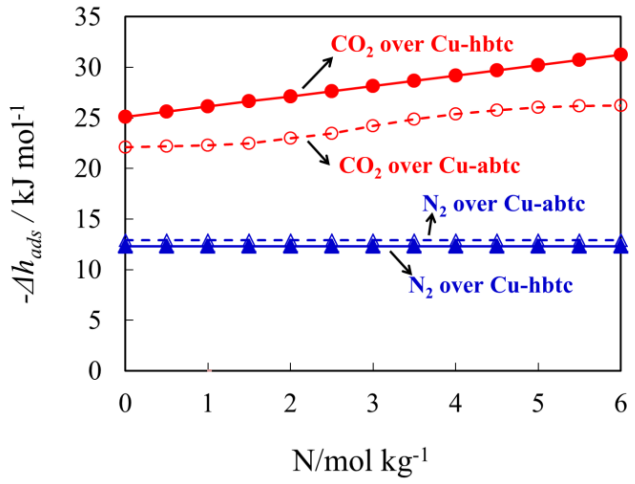

Figure 5.23: Variation of adsorption enthalpy of CO_2 (●) and N_2 (▲) with loading for Cu–abtc (open symbol) and Cu–hbtc (closed symbol).

The adsorption enthalpy for CO_2 on Cu–hbtc varies between 25.1 and 31.2 kJ mol^{-1} (shown in Figure 5.23). This value is lower than that on MOFs like MIL–53 [16], MIL–100[26] and MIL–101 [26], and Cu–BTC [22]. On the other hand, the adsorption enthalpy for CH_4 on Cu–hbtc is 18.4 kJ mol^{-1} (shown in Figure 5.24). It is comparable to that on MOFs such as Zn–DABCO [48], MIL–53 [16], MIL–100 [26] and slightly higher than that on a large pore MOF like IRMOF–3 [17].

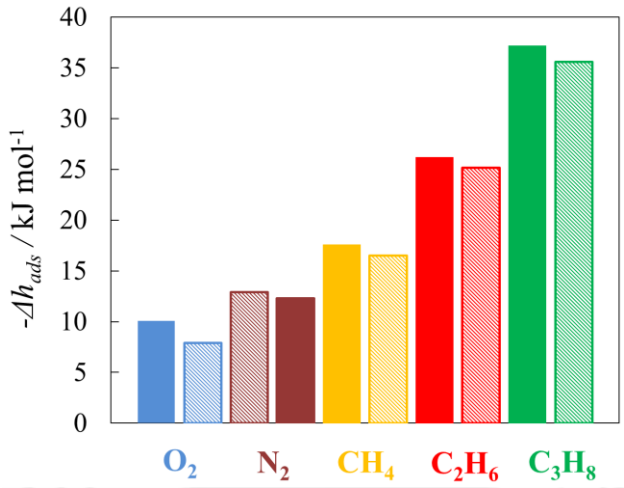

Figure 5.24: Adsorption enthalpy at zero coverage for N_2, O_2, CH_4, C_2H_6, and C_3H_8 on Cu–abtc (hatch pattern) and Cu–hbtc (solid fill).

For the gases like O_2, CH_4, C_2H_6, and C_3H_8, the enthalpy of adsorption on Cu–hbtc is slightly higher than that on Cu–abtc. However, in the case of N_2, the enthalpy of adsorption for Cu–abtc is somewhat more compared to Cu–hbtc (shown in Figure 5.24).

5.7 Prediction of Binary Selectivity using IAST

To understand the affinity of HN–NH over N=N in the framework on the binary selectivity for gas mixture, selectivities of various binary mixtures are calculated using IAST. At 294 K, the variation in CO_2 selectivity over N_2 with pressure for 20% CO_2 in the binary mixture is shown in Figure 5.25. The CO_2 selectivity over N_2 is significantly higher on Cu–hbtc than on Cu–abtc.

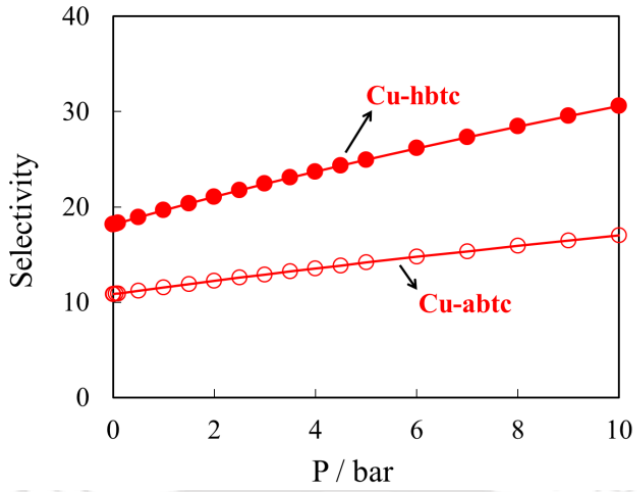

Figure 5.25: Variation of CO_2 selectivity over N_2 for Cu–abtc (open symbol) and Cu–hbtc (closed symbol). CO_2 mole fraction in all binary mixtures is 20%; lines are drawn as a guide to the eyes.

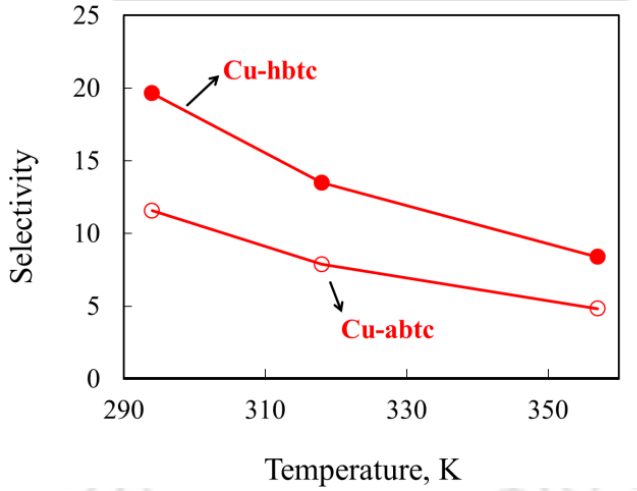

Figure 5.26: Effect of temperature on CO_2 selectivity (for 20% molar composition of CO_2) over N_2 for Cu–abtc (open symbol) and Cu–hbtc (closed symbol), at 1 bar; lines are drawn as a guide to the eyes.

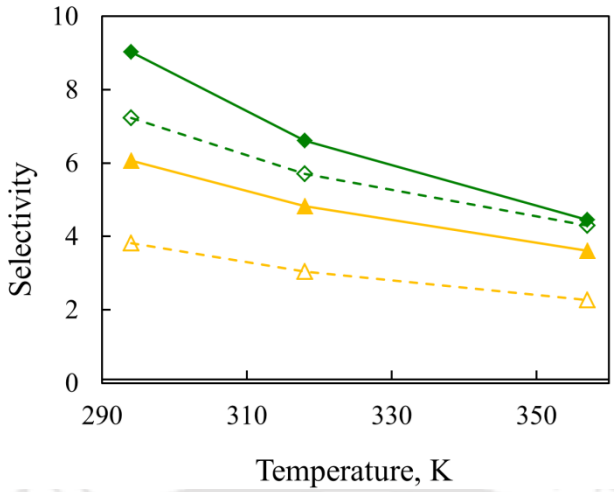

Figure 5.27: Effect of temperature on CO_2 selectivity (for 20% molar composition of CO_2) over CO (green) and CH_4 (yellow) for Cu–abtc (open symbol) and Cu–hbtc (closed symbol) at 1 bar; lines are drawn as a guide to the eyes.

In addition, the effect of temperature on selectivity is also studied (shown in figure 5.26 and figure 5.27). CO_2 selectivity over N_2 (Figure 5.26) for a binary gas mixture (20% of CO_2 at 1 bar) decreases with an increase in temperature. This decrease is attributed to the decline in electrostatic forces of CO_2 over N_2. Similar behavior is also observed for CO_2 selectivity over CH_4 and CO (Figure 5.27). However, CO_2 selectivity over CO and CH_4 does not change appreciably since both gases have polarity; Thus, decrease in selectivity with increasing temperature will be smaller for a polar pair than that for a polar–nonpolar pair adsorbates.

5.8 Summary

This work demonstrates adsorption characteristics various adsorbents to understand the affinity of the HN–NH group presented in Cu–hbtc over N=N in Cu–abtc MOFs. In both compounds, significant accessible metal sites are present. Due to the accessible metal sites present in the framework, CO loading increases progressively with pressure until gas molecules occupy metal

sites (up to 2.5 molKg^{-1} for Cu–hbtc and 2.0 molKg^{-1} for Cu–abtc). After that, CH_4 showed preferentially more adsorption capacity due to more polarizability. Type–I isotherm was observed for all gases, and a modified Virial model was used for polar gases (CO_2, CO), and the Langmuir model was used for less–polar gases (O_2, N_2, CH_4, C_2H_6, C_3H_8). Fitting parameters were utilized to calculate enthalpies of adsorption. An increase in adsorption enthalpy is observed with loading, attributed to lateral interactions. The CO_2 selectivity over N_2 increases significantly with an increase in pressure. However, the CO_2 selectivity over N_2 for compound Cu–hbtc is more than compound Cu–abtc due to the strong affinity of functional group and framework adsorbate interactions.

References

(1) Liu, Y.; Eubank, J. F.; Cairns, A. J.; Eckert, J.; Kravtsov, V. C.; Luebke, R.; Eddaoudi, M. Assembly of Metal-Organic Frameworks (MOFs) Based on Indium-Trimer Building Blocks: A Porous MOF with Soc Topology and High Hydrogen Storage. *Angew. Chemie - Int. Ed.* **2007**, *46*, 3278–3283.

(2) Miller, S. R.; Alvarez, E.; Fradcourt, L.; Devic, T.; Wuttke, S.; Wheatley, P. S.; Steunou, N.; Bonhomme, C.; Gervais, C.; Laurencin, D.; Morris, R. E.; Vimont, A.; Daturi, M.; Horcajada, P.; Serre, C. A Rare Example of a Porous Ca-MOF for the Controlled Release of Biologically Active NO. *Chem. Commun.* **2013**, *49*, 7773–7775.

(3) Mowat, J. P. S.; Miller, S. R.; Slawin, A. M. Z.; Seymour, V. R.; Ashbrook, S. E.; Wright, P. A. Synthesis, Characterisation and Adsorption Properties of Microporous Scandium Carboxylates with Rigid and Flexible Frameworks. *Microporous Mesoporous Mater.* **2011**, *142*, 322–333.

(4) Pang, M.; Cairns, A. J.; Liu, Y.; Belmabkhout, Y.; Zeng, H. C.; Eddaoudi, M. Synthesis and Integration of Fe-Soc-MOF Cubes into Colloidosomes via a Single-Step Emulsion-Based Approach. *J. Am. Chem. Soc.* **2013**, *135*, 10234–10237.

(5) Wang, X. Sen; Shengqian, M.; Rauch, K.; Simmons, J. M.; Yuan, D.; Wang, X.; Yildirim, T.; Cole, W. C.; López, J. J.; De Meijere, A.; Zhou, H. -C. Metal-Organic Frameworks Based on Double-Bond-Coupled Di-Isophthalate Linkers with High Hydrogen and Methane Uptakes. *Chem. Mater.* **2008**, *20*, 3145–3152.

(6) Osta, R. El; Frigoli, M.; Marrot, J.; Guillou, N.; Chevreau, H.; Walton, R. I.; Millange, F. A Lithium–Organic Framework with Coordinatively Unsaturated Metal Sites That Reversibly Binds Water. *Chem. Commun.* **2012**, *48*, 10639–10641.

(7) Mendes, P.; Rodrigues, A.; Horcajada, P.; Eubank, J.; Devic, T.; Serre, C.; Silva, J. Separation of Hexane Isomers on Rigid Porous Metal Carboxylate-Based Metal-Organic Frameworks. *Adsorpt. Sci. Technol.* **2014**, *32*, 475–488.

(8) Cunha, D.; Ben Yahia, M.; Hall, S.; Miller, S. R.; Chevreau, H.; Elkaïm, E.; Maurin, G.; Horcajada, P.; Serre, C. Rationale of Drug Encapsulation and Release from Biocompatible Porous Metal-Organic Frameworks. *Chem. Mater.* **2013**, *25*, 2767–2776.

(9) Du, P. Y.; Li, H.; Fu, X.; Gu, W.; Liu, X. A 1D Anionic Lanthanide Coordination Polymer as an Adsorbent Material for the Selective Uptake of Cationic Dyes from Aqueous Solutions. *Dalt. Trans.* **2015**, *44*, 13752–13759.

(10) Zhao, J.; Li, D. S.; Ke, X. J.; Liu, B.; Zou, K.; Hu, H. M. Auxiliary Ligand-Directed Structural Variation from 2D→3D Polythreaded Net to 3-Fold Interpenetrating 3D Pillar-Layered Framework: Syntheses, Crystal Structures and Magnetic Properties. *Dalt. Trans.* **2012**, *41*, 2560–2563.

(11) Fan, L.; Fan, W.; Li, B.; Liu, X.; Zhao, X.; Zhang, X. Structural Diversities and Related Properties of Four Coordination Polymers Synthesized from Original Ligand of 3,3′,5,5′-Azobenzenetetracarboxylic Acid. *Dalt. Trans.* **2015**, *44*, 2380–2389.

(12) Zhang, S.; Duan, E.; Cheng, P. An Exceptionally Stable 3D Gd^{III}-Organic Framework for Use as a Magnetocaloric Refrigerant. *J. Mater. Chem. A* **2015**, *3*, 7157–7162.

(13) Paquin, F.; Rivnay, J.; Salleo, A.; Stingelin, N.; Silva, C. Multi-Phase Semicrystalline Microstructures Drive Exciton Dissociation in Neat Plastic Semiconductors. *J. Mater. Chem. C* **2015**, *3*, 10715–10722.

(14) Herm, Z. R.; Swisher, J. A.; Smit, B.; Krishna, R.; Long, J. R. Metal-Organic Frameworks as Adsorbents for Hydrogen Purification and Pre-combustion Carbon Dioxide Capture. *J. Am. Chem. Soc.* **2011**, *133*, 5664–5667.

(15) Mason, J. A.; Sumida, K.; Herm, Z. R.; Krishna, R.; Long, J. R. Evaluating Metal-Organic Frameworks for Post-Combustion Carbon Dioxide Capture via Temperature Swing Adsorption. *Energy Environ. Sci.* **2011**, *4*, 3030–3040.

(16) Bourrelly, S.; Llewellyn, P. L.; Serre, C.; Millange, F.; Loiseau, T.; Ferey, G. Different Adsorption Behaviors of Methane and Carbon Dioxide in the Isotypic Nanoporous Metal-Terephthalates MIL-53 and MIL-47. *J. Am. Chem. Soc.* **2005**, *127*, 13519–13521.

(17) Yazaydin, A. Ö.; Snurr, R. Q.; Park, T. H.; Koh, K.; Liu, J.; LeVan, M. D.; Benin, A. I.; Jakubczak, P.; Lanuza, M.; Galloway, D. B.; Low, J. J.; Willis, R. R. Screening of Metal-Organic Frameworks for Carbon Dioxide Capture from Flue Gas Using a Combined Experimental and Modeling Approach. *J. Am. Chem. Soc.* **2009**, *131*, 18198–18199.

(18) Lee, Y. G; Moon, H. R; Cheon, Y. E; Suh, M. P. A Comparison of the H_2 Sorption Capacities of Isostructural Metal-Organic Frameworks with and without Accessible Metal Sites:[{Zn_2(abtc)(dmf)$_2$}$_3$] and [{Cu_2(abtc)(dmf)$_2$}$_3$] versus [{Cu_2(abtc)}$_3$]. *Angew. Chemie - Int. Ed.* **2008**, *47*, 7741–7745.

(19) Zhang, S; Ma, J; Zhang, X; Duan, E; Cheng, P. Assembly of Metal-Organic Frameworks Based on 3,3′,5,5′-Azobenzene-tetracarboxylic Acid: Photoluminescences, Magnetic Properties, and Gas Separations. *Inorg. Chem.* **2015**, *54*, 586–595.

(20) Talu, O. Needs, Status, Techniques and Problems with Binary Gas Adsorption Experiments. *Adv. Colloid Interface Sci.* **1998**, *76–77*, 227–269.

(21) Millward, A. R.; Yaghi, O. M. Metal-Organic Frameworks with Exceptionally High Capacity for Storage of Carbon Dioxide at Room Temperature. *J. Am. Chem. Soc.* **2005,** *127*, 17998–17999.

(22) Chowdhury, P.; Mekala, S.; Dreisbach, F.; Gumma, S. Adsorption of CO, CO_2 and CH_4 on Cu-BTC and MIL-101 Metal-organic Frameworks: Effect of Open Metal Sites and Adsorbate Polarity. *Microporous and Mesoporous Mater.* **2012**, *152*, 246–252.

(23) Caskey, S. R.; Wong-Foy, A. G.; Matzger, A. J. Dramatic Tuning of Carbon Dioxide Uptake via Metal Substitution in a Coordination Polymer with Cylindrical Pores. *J. Am. Chem. Soc.* **2008**, *130*, 10870–10871.

(24) Dietzel, P. D. C.; Besikiotis, V.; Blom, R. Application of Metal-Organic Frameworks with Coordinatively Unsaturated Metal Sites in Storage and Separation of Methane and Carbon dioxide. *J. Mater. Chem.*, **2009**, *19*, 7362–7370.

(25) Liang, Z.; Marshall, M.; Chaffee, A. L. CO_2 Adsorption, Selectivity and Water Tolerance of Pillared-Layer Metal-Organic Frameworks. *Microporous and Mesoporous Mater.* **2010**, *132*, 305–310.

(26) Llewellyn, P. L.; Bourrelly, S.; Serre, C.; Vimont, A.; Daturi, M.; Hamon, L.; Weireld, G. De; Chang, J.; Hong, D.; Hwang, Y. K.; Jhung, S. H.; Fe´rey, G. High Uptakes of CO_2 and CH_4 in Mesoporous Metal-Organic Frameworks MIL-100 and MIL-101. *Langmuir* **2008**, *24*, 7245–7250.

(27) Mason, J. A.; Veenstrab, M.; Long, J. R. Evaluating Metal-Organic Frameworks for Natural Gas Storage. *Chem. Sci.* **2014**, *5*, 32–51.

(28) He, Y.; Zhou, W.; Yildirim, T.; Chen, B. A Series of Metal-Organic Frameworks with High Methane Uptake and an Empirical Equation for Predicting Methane Storage Capacity. *Energy Environ. Sci.* **2013**, *6*, 2735–2744.

(29) Rallapalli, P.; Prasanth, K. P.; Patil, D.; Somani, R. S.; Jasra, R. V.; Bajaj, H. C. Sorption Studies of CO_2, CH_4, N_2, CO, O_2 and Ar on Nanoporous Aluminum Terephthalate [MIL-53(Al)]. *J. Porous Mater.* **2011**, *18*, 205–210.

(30) Rolniak, P. D.; Kobayashi, R. Adsorption of Methane and Several Mixtures of Methane and Carbon Dioxide at Elevated Pressures and Near Ambient Temperatures on 5A and 13X Molecular Sieves by Tracer Pertubation Chromatography. *AIChE J.* **1980**, *26*, 616–625.

(31) Liang, Z.; Marshall, M.; Chaffee, A. L. CO_2 Adsorption-Based Separation by Metal Organic Framework (Cu-BTC) versus Zeolite (13X). *Energy and Fuels* **2009**, *23*, 2785–2789.

(32) Liu, J.; Culp, J.T.; Natesakhawat, S.; Bockrath, B.C.; Zande, B.; Sankar, S.G.; Garberoglio, G.; Karl Johnson, J. Experimental and Theoretical Studies of Gas Adsorption in $Cu_3(BTC)_2$: An Effective Activation Procedure. *J. Phys. Chem. C.* **2007**, *111*, 9305–9313.

(33) Chavan, S.; Vitillo, J. G.; Groppo, E.; Bonino, F.; Lamberti, C.; Dietzel, P. D. C.; Bordiga, S. CO Adsorption on CPO-27-Ni Coordination Polymer: Spectroscopic Features and Interaction Energy. *J. Phys. Chem. C* **2009**, *113*, 3292–3299.

(34) Golden, T. C.; Sircar, S. Gas Adsorption on Silicalite. *J. Coll. Inter. Sci.* **1994**, *162*, 182–188.

(35) Karra, J. R.; Walton, K. S. Molecular Simulations and Experimental Studies of CO_2, CO and N_2 Adsorption in Metal-Organic Frameworks. *J. Phys. Chem. C* **2010**, *114*, 15735–15740.

(36) Belmabkhout, Y.; Pirngruber, G.; Jolimaitre, E.; Methivier, A. A complete Experimental Approach for Synthesis Gas Separation Studies Using Static Gravimetric and Column Breakthrough Experiments. *Adsorption* **2007**, *13*, 341–349.

(37) Bao, Z.; Alnemrat, S.; Yu, L.; Vasiliev, I.; Ren, Q.; Lu, X.; Deng, S. Adsorption of Ethane, Ethylene, Propane, and Propylene on a Magnesium-Based Metal Organic Framework. *Langmuir* **2011**, *27*, 13554–13562.

(38) Bloch, E. D.; Queen, W. L.; Krishna, R.; Zadrozny, J. M.; Brown, C. M.; Long, J. R. Hydrocarbon Separations in a Metal-Organic Framework with Open Iron(II) Coordination Sites. *Science* **2012**, *335*, 1606–1610.

(39) Elena, G. P.; Jorge, G.; Victor, M. F.; Castillo, J. M.; Kapteijn, F.; Calero, S. Identification of Adsorption Sites in Cu-BTC by Experimentation and Molecular Simulation. *Langmuir* **2009**, *25*, 1725–1731.

(40) Stallmach, F.; Groger, S.; Kunzel, V.; Karger, J.; Yaghi, O. M.; Hesse, M.; Muller, U. NMR Studies on the Diffusion of Hydrocarbons on the Metal-Organic Framework Material MOF-5. *Angew. Chem. Int - Ed.* **2006**, *45*, 2123–2126.

(41) Hyun, S. H.; Danner, R. P. Equilibrium Adsorption of Ethane, Ethylene, Iso-butane, Carbon Dioxide, and Their Binary Mixtures on 13X Molecular Sieves. *J. Chem. Eng. Data* **1982**, *27*, 196–200.

(42) Sun, M. S.; Shah, D. B.; Xu, H. H.; Talu, O. Adsorption Equilibria of C_1 to C_4 Alkanes, CO_2, and SF_6 on Silicalite. *J. Phys. Chem. B* **1998**, *102*, 1466–1473.

(43) Rubes, M.; Wiersum, A. D.; Llewellyn, P. L.; Grajciar, L.; Bludsky, O.; Nachtigall, P. Adsorption of Propane and Propylene on Cu-BTC Metal-Organic Framework: Combined Theoretical and Experimental Investigation. *J. Phys. Chem. C* **2013**, *117*, 11159–11167.

(44) Llewellyn, P. L.; Horcajada, P.; Maurin, G.; Devic, T.; Rosenbach, N.; Bourrelly, S.; Serre, C.; Vincent, D.; Loera-Serna, S.; Filinchuk, Y.; Férey, G. Complex Adsorption of Short Linear Alkanes in the Flexible Metal-Organic Framework MIL-53(Fe). *J. Am. Chem. Soc.* **2009**, *131*, 13002–13008.

(45) Siperstein, F. R.; Myers, A.L. Mixed-Gas Adsorption. *AIChE J.* **2001**, *47*, 1141–1159.

(46) Dunne, J. A.; Rao, M.; Sircar, S.; Gorte, R. J.; Myers, A. L. Calorimetric Heats of Adsorption and Adsorption Isotherms. 2. O_2, N_2, Ar, CO_2, CH_4, C_2H_6, and SF_6 on Na-X, H-ZSM-5, and NaZSM-5 Zeolites. *Langmuir* **1996**, *12*, 5896–5904.

(47) Dunne, J.A.; Mariwala, R.; Rao, M.; Sircar, S.; Gorte, R.J.; Myers A. L. Calorimetric Heats of Adsorption and adsorption Isotherms. 1. O_2, N_2, Ar, CO_2, CH_4, C_2H_6, and SF_6 on Silicalite. *Langmuir* **1996**, *12*, 5888–5895.

(48) Mishra, P.; Mekala, S.; Dreisbach, F.; Mandal, B.; Gumma, S. Adsorption of CO_2, CO, CH_4 and N_2 on Zinc Based Metal-Organic Framework. *Sep. Purif. Technol*. **2012**, *94*,124–130.

(49) Mishra, P.; Edubilli, S.; Mandal, B.; Gumma, S. Adsorption Characteristics of Metal-Organic Frameworks Containing Co-ordinatively Unsaturated Metal Sites: Effect of Metal Cations and Adsorbate Properties. *J. Phys. Chem. C* **2013**, *118*, 6847–6855.

CHAPTER 6

Selective Gas Adsorption on HKUST–1 Derivatives: Cu–BTC Versus Cu–(bromo)BTC Versus Cu–(iodo)BTC

In this chapter, the adsorption isotherms of CO_2, CH_4, CO, and N_2 on Cu–BTC, Cu–(bromo)BTC, and Cu–(iodo)BTC were evaluated at three different temperatures viz. 294, 317, and 356 K and a wide range of pressures. Similar to the previous chapter, the effect of functional groups presented in the framework is investigated on the adsorption characteristics of HKUST-1 derivatives. This work explains the affinity of functional groups, changes in pore structure, and adsorption selectivity by inserting halogen functional groups into the frameworks.

6.1 Background

The concept of reticular synthesis, which permits families of isostructural crystals to be produced by altering ligand length and functionality, is one of the most intriguing aspects of MOFs [1, 2]. Some of the widely studied isostructural families are IRMOFs [3], UIO–66 [4–6], and MIL–53 [7, 10], etc. However, little work has been done to modify the H_3BTC organic ligand for functionalizing Cu–BTC to optimize its properties for gases adsorption [11–13], separation [8, 9, 14, 15], drug delivery [17], ion exchanging [20], catalysis [21] and micro sensing [16, 22].

Cu–BTC is a well-studied material made up of Cu^{2+} metal clusters linked to a 1,3,5–benzenetricarboxylate (H_3BTC) organic linker, resulting in a three-dimensional structure with open metal sites. The resultant structure features big cavities with octahedral cages with a pore

diameter of 9 Å. Several studies revealed that Cu–BTC having good thermal stability does not suffer crystal structure damage during the adsorption and desorption cycles.

The adsorption equilibria of several gases on Cu–BTC frameworks up to saturation pressures showed heterogeneity in structure due to the presence of open metal sites in prior studies [18, 19]. In this chapter, we showed the effect of functionalization by comparing the gas adsorption properties of Cu–BTC versus Cu–(bromo)BTC versus Cu–(iodo)BTC over a wide range of temperatures and pressure. We have chosen four industrially important gases for comparative study of CO_2, CH_4, CO, and N_2 adsorption on these frameworks, i.e., Cu–BTC, Cu–(bromo)BTC, and Cu–(iodo)BTC.

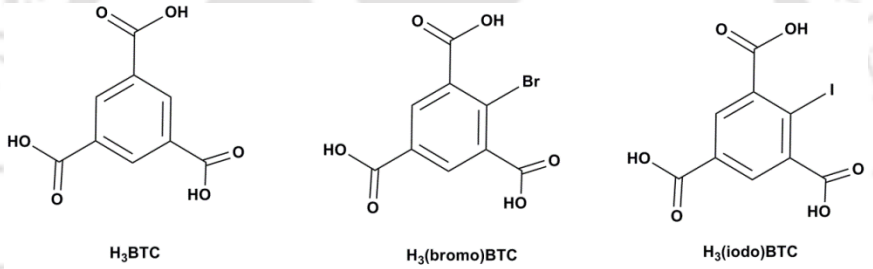

Figure 6.1: Organic linkers used to synthesize Cu–BTC, Cu–(bromo)BTC, and Cu–(iodo)BTC.

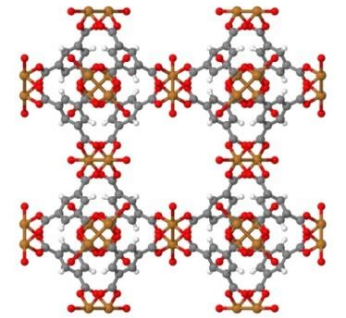

Figure 6.2: Framework structure of Cu–BTC (Brown: metal, red: oxygen, black: carbon, white: oxygen). Redrawn from CCDC deposition 943008.

6.2 Characterization of Frameworks Synthesized

Cu–BTC, Cu–(bromo)BTC, and Cu–(iodo)BTC frameworks were synthesized by the procedure reported in the literature and already discussed in chapter 4, section 4.2.3–4.2.5. The synthesized samples were analyzed using powder XRD, Thermogravimetric, and BET Surface area analysis.

6.2.1 Powder X-Ray Diffraction (PXRD)

The PXRD patterns for the synthesized MOFs are shown in Figure 6.3. Cu–BTC, Cu–(bromo)BTC, and Cu–(iodo)BTC frameworks have nearly identical XRD patterns, indicating that all three compounds are iso-structural.

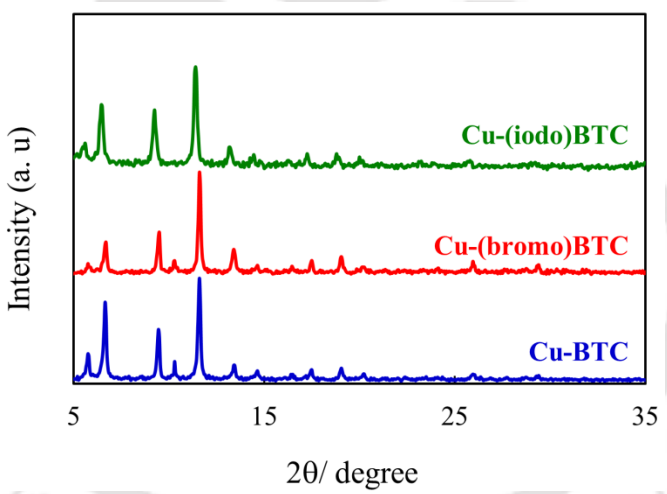

Figure 6.3: Powder X-ray diffractogram of Cu–BTC (blue), Cu–(bromo)BTC (red), and Cu–(iodo)BTC (green).

6.2.2 Thermogravimetric Analysis (TGA)

TGA patterns for all the materials are depicted in Figure 6.4. All the samples possessed high thermal stability. The first weight loss step is observed at around 400 K corresponds to the loss of moisture and other volatile solvents. However, for Cu–BTC, minimal weight loss is observed

compared to Cu–(bromo)BTC and Cu–(iodo)BTC (The moisture and volatile solvent content in the materials are widely different). The weight loss between the temperature range of 400 to 580 K is quite steady for all the samples. The second weight loss in the range of 580–635 K is happened due to the decomposition of the tricarboxylates linker in the MOF. The activation temperature for all the samples are fixed at 444 K based on thermogravimetric profiles.

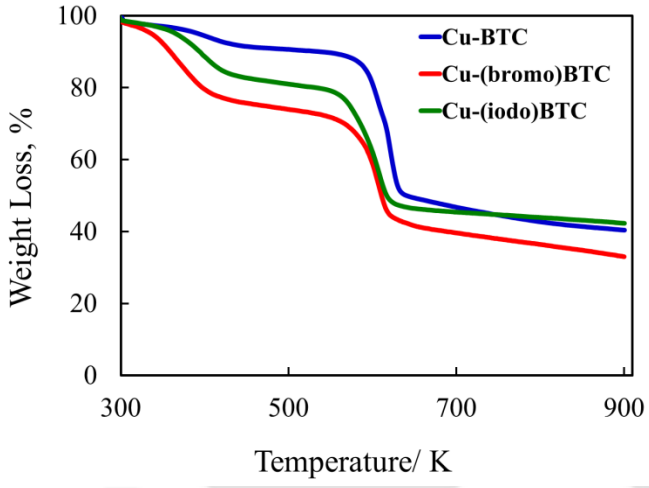

Figure 6.4: TGA analysis of compound Cu–BTC (blue), Cu–(bromo)BTC (red), and Cu–(iodo)BTC (green) at a heating rate of 5 K min^{-1} under the flow of Argon.

6.2.3 Surface Area and Pore Volume Analysis

N_2 adsorption isotherms of the samples at 77 K are shown in Figure 6.5. Samples were activated prior to isotherm measurement at 444 K under vacuum. The N_2 loading per unit gram for the synthesized MOFs is followed as Cu–BTC >Cu–(bromo)BTC>Cu–(iodo)BTC. The resultant surface area and pore volume are given in Table 1.

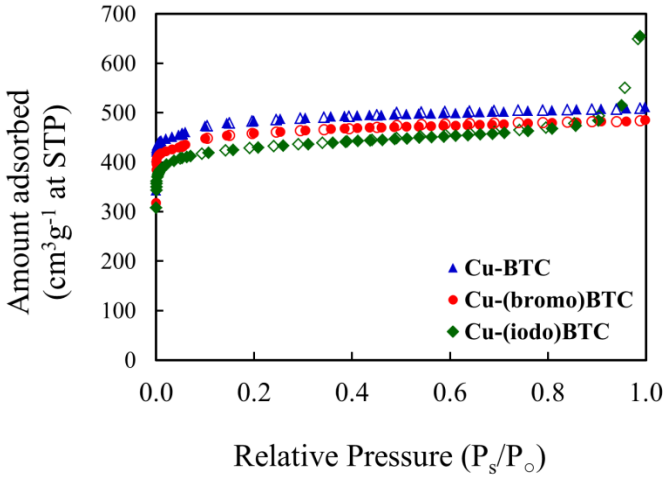

Figure 6.5: N_2 adsorption (closed symbol) and desorption (open symbol) of Cu–BTC (blue), Cu–(bromo)BTC (red), and Cu–(iodo)BTC (green) at 77 K.

Table 6.1: BET surface area and pore volume of Cu–BTC, Cu–(bromo)BTC, and Cu–(iodo)BTC.

MOF	Surface area	Pore volume
	m^2g^{-1}	cm^3g^{-1}
Cu–BTC	1663	0.75
Cu–(bromo)BTC	1558	0.89
Cu–(iodo)BTC	1307	1.01

6.3 Adsorption Isotherms

The adsorption isotherms of Cu–BTC, Cu–(bromo)BTC, and Cu–(iodo)BTC were evaluated gravimetrically on four industrially important gases CO_2, CH_4, CO, and N_2 at temperatures of 294, 317, 356 K. The isotherm are typically followed Type–I.

6.3.1 CO_2 Isotherms

Amongst all the studied gases, the adsorption capacity of CO_2 is found highest (shown in Figure 6.6). The adsorption capacities for CO_2 on Cu–BTC, Cu–(bromo)BTC and Cu– (iodo)BTC are found to be 5.2, 4.15 and 4.88 mol kg^{-1} respectively at 1 bar and 294 K. However, CO_2 uptakes are lower than Co–DOBDC (6.7 mol kg^{-1}) [23], Ni–DOBDC (6.9 mol kg^{-1}) [24] and Mg/DOBDC (7.57 mol kg^{-1}) [8] and significantly higher than MOF–5 (1.0 mol kg^{-1}) [25], Zn–DABCO (2.0 mol kg^{-1}) [25], Ni–DABCO (2.0 mol kg^{-1}) [26], MIL–53 (Al) (2.3 mol kg^{-1}) [16], MIL–47 (2.5 mol kg^{-1}) [16] and MIL–101 (2.8 mol kg^{-1}) [27]. CO_2 with higher polarity and polarizability is primarily responsible for these maximum absorption capacities.

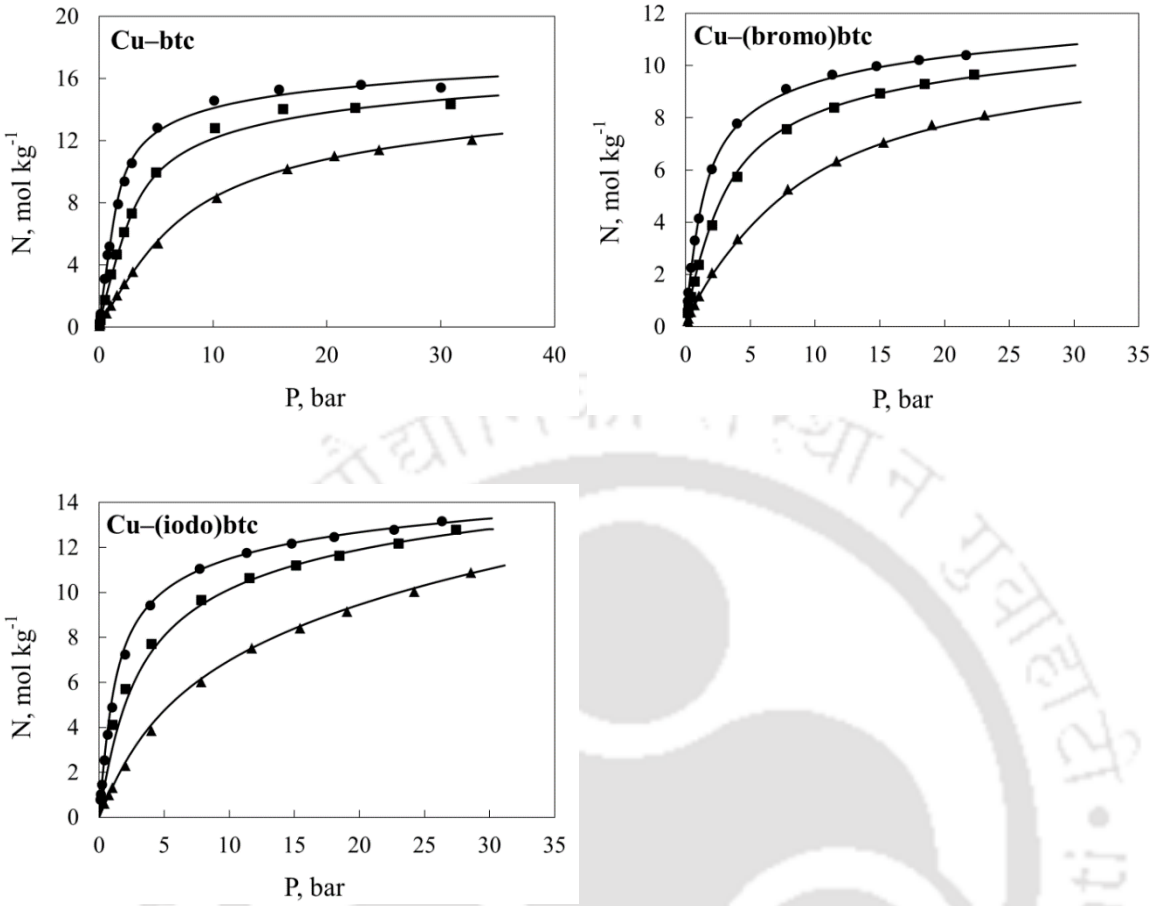

Figure 6.6: CO_2 isotherms of Cu–BTC, Cu–(bromo)BTC, and Cu–(iodo)BTC MOFs. Symbols are experimental data at 294 K (●), 317 K (■), and 356 K (▲); lines are fits obtained using Langmuir isotherm parameters from Table 6.2.

6.3.2 N_2 Isotherms

The adsorption capacities of N_2 on Cu–BTC, Cu–(bromo)BTC, and Cu–(iodo)BTC are found to be 0.18, 0.30, and 0.25 mol kg^{-1} respectively at 1 bar and 294 K (shown in Figure 6.7). N_2 is relatively non–polar with a low quadrupole moment attributed to lower adsorption capacities than other studied gases. However, these uptake capacities are lower than Mg–DOBDC (1.1 mol kg^{-1}) [9] and Ni–DOBDC (1.02 mol kg^{-1}) [24], Zeolite 13X (0.8 mol kg^{-1}) [28] and comparable to MIL–53 (Al) (0.20 mol kg^{-1}) [29].

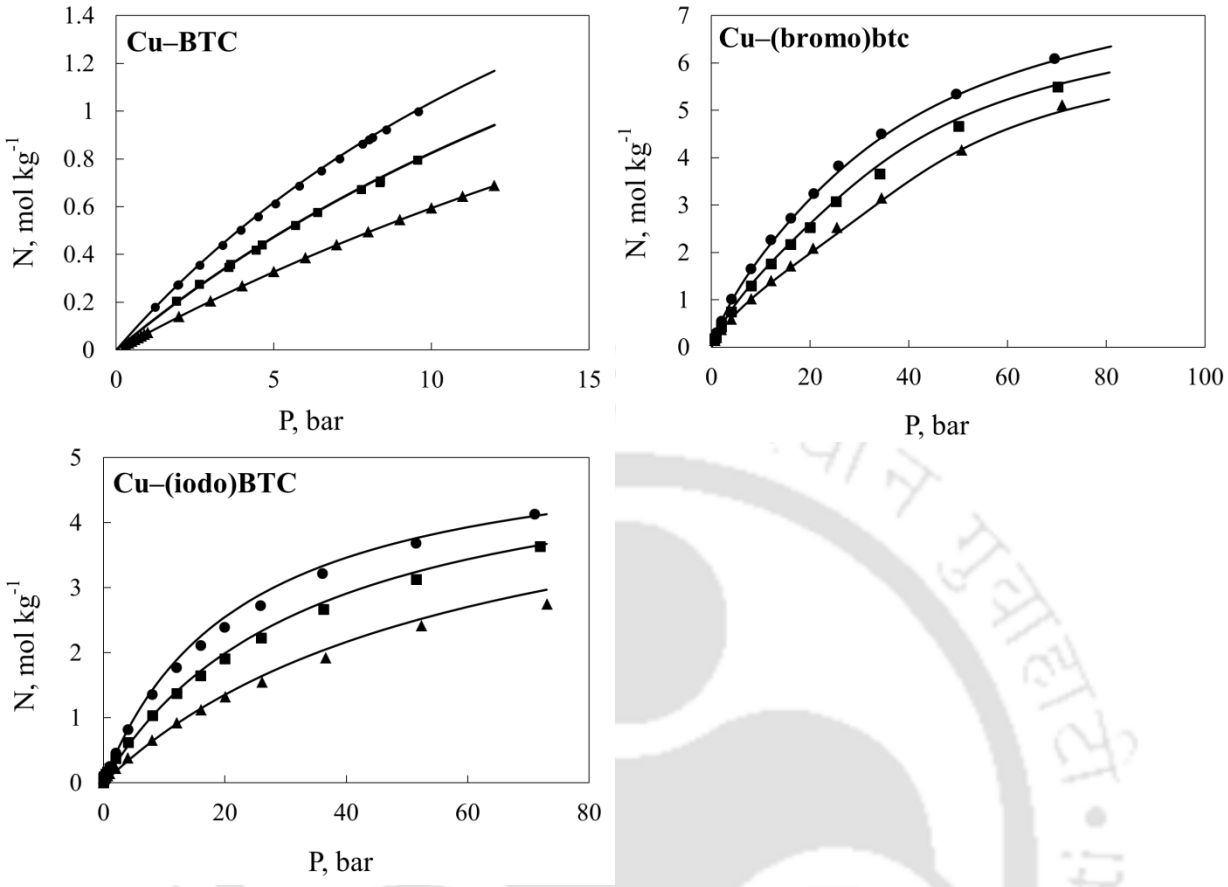

Figure 6.7: N_2 isotherms of Cu–BTC, Cu–(bromo)BTC, and Cu–(iodo)BTC MOFs. Symbols are experimental data at 294 K (●), 317 K (■), and 356 K (▲); lines are fits obtained using Langmuir isotherm parameters from Table 6.3.

6.3.3 CO Isotherms

The CO loading at 1 bar and 294 K (shown in Figure 6.8) is 1.43, 1.09, and 1.77 mol kg^{-1} for Cu–BTC, Cu– (bromo)BTC, and Cu–(iodo)BTC respectively. These CO uptakes are quite less compared to Ni–DOBDC (5.9 mol kg^{-1}) [30] and much higher than MIL–53(Al) (0.3 mol kg^{-1}) [29] and silicalite (0.27 mol kg^{-1}) [31], IRMOF–1 (0.58 mol kg^{-1}) [32], and IRMOF–3 (0.6 mol kg^{-1}) [32].

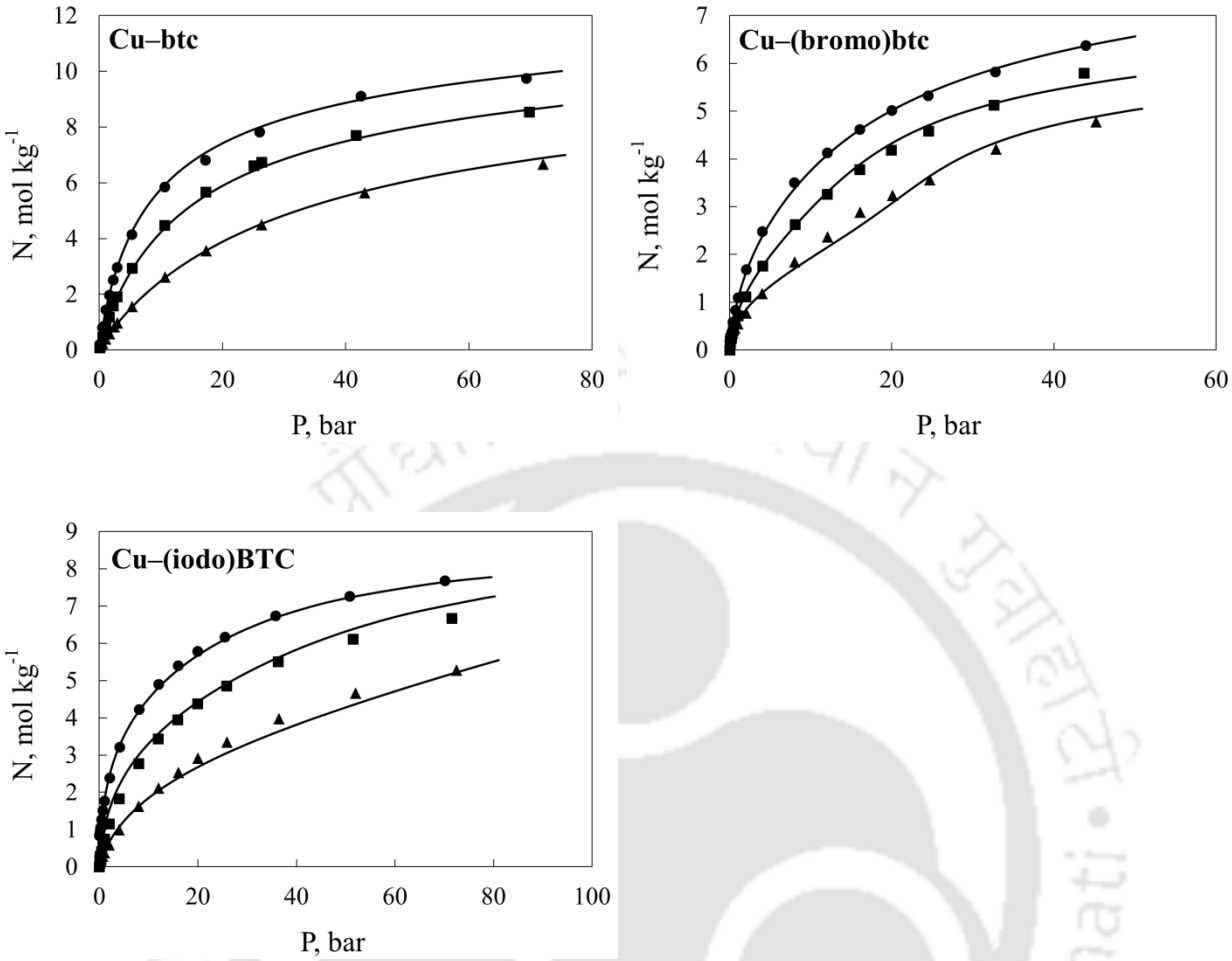

Figure 6.8: CO isotherms of Cu–BTC, Cu–(bromo)BTC, and Cu–(iodo)BTC MOFs. Symbols are experimental data at 294 K (●), 317 K (■), and 356 K (▲); lines are fits obtained using Langmuir isotherm parameters from Table 6.4.

6.3.4 CH_4 Isotherms

The adsorption isotherms of CH_4 on Cu–BTC, Cu–(bromo)BTC and Cu–(iodo)BTC are 9.5, 7.0 and 6.8 mol kg^{-1} respectively at 294 K, 35 bar and shown in Figure 6.9. However, these values are lower compared to NOTT–109 (11.16 mol kg^{-1}) [33] and NOTT–101 (12.77 mol kg^{-1}) [33]. Although these values are comparable to Co–DOBDC (8.4 mol kg^{-1}) [34], Ni–DOBDC (8.6 mol kg^{-1}) [34], MIL–53 (Al) (8.4 mol kg^{-1}) [29] and higher than Zeolite 13X (3.3 mol kg^{-1})[35].

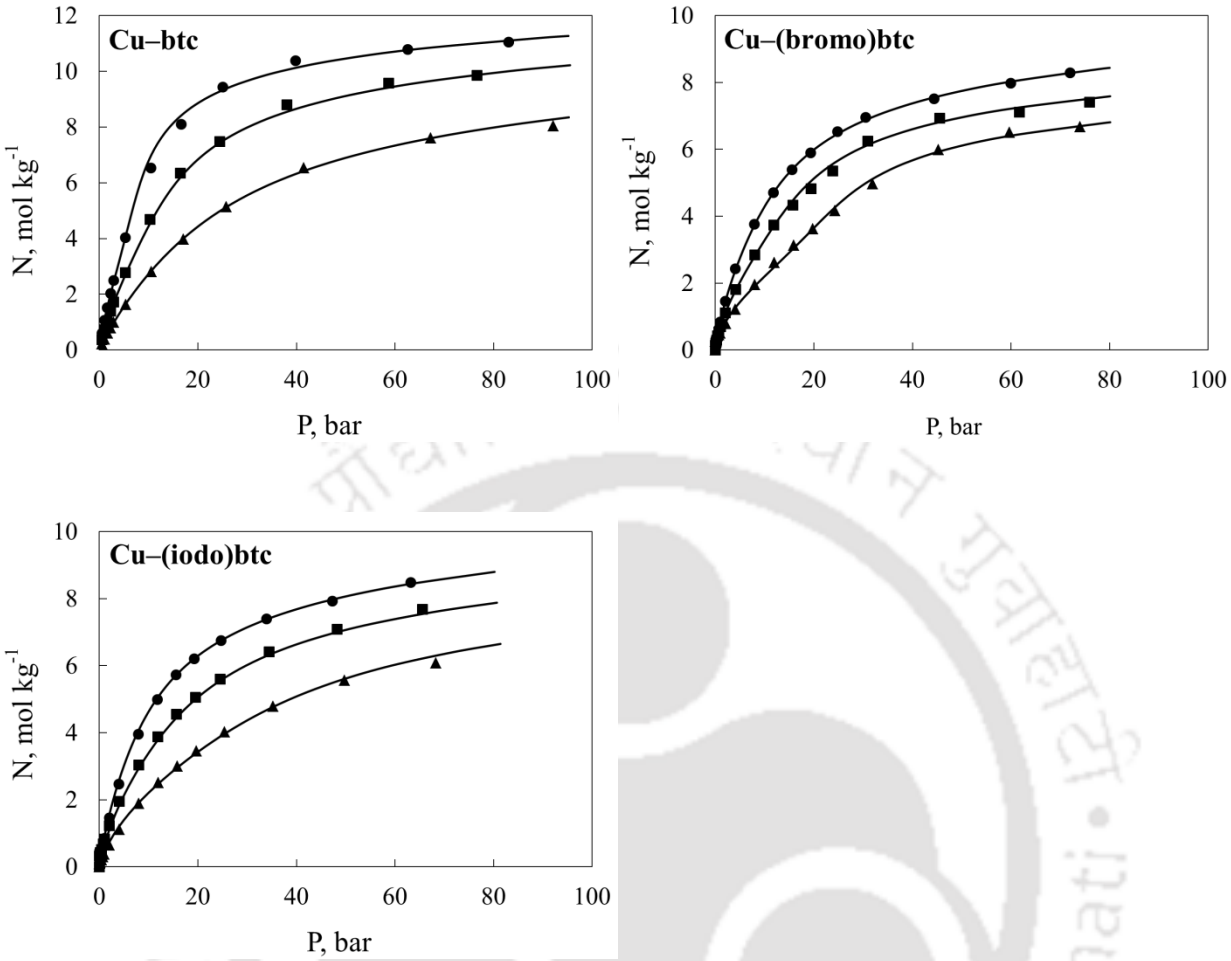

Figure 6.9: CH_4 isotherms of Cu–BTC, Cu–(bromo)BTC, and Cu–(iodo)BTC MOFs. Symbols are experimental data at 294 K (●), 317 K (■), and 356 K (▲); lines are fits obtained using Langmuir isotherm parameters from Table 6.5.

6.4 Isotherm Modeling

The accuracy of the models is mostly determined by the independent variables in the equation, Langmuir equation is fitted for all experimental data which basically used for homogeneous surfaces. In this case, the Langmuir model is well-fitting statistically, indicating that all sites are similarly energetic with no lateral interaction. Langmuir equation is

$$N = \frac{N^{max}\beta f}{1 + \beta f} \qquad 6.1$$

Where N (mol kg^{-1}) is the amount adsorbed, f (bar) is the fugacity, N^{max} (mol kg^{-1}) is the saturation capacity, β (mol kg^{-1} bar^{-1}) is Henry's constant. Saturation capacity is considered to be independent of temperature, and Henry's constant is expressed by

$$\beta = \beta^{(0)}\exp(\beta^{(1)}/T) \qquad 6.2$$

Where T is temperature in K. The two parameters $\beta^{(0)}$ and $\beta^{(1)}$ are related to entropy and enthalpy of adsorption at zero loading, respectively.

Table 6.2: Fit parameters of Langmuir isotherm of CO_2.

Parameters	**Cu–BTC**	**Cu–(bromo)BTC**	**Cu–(iodo)BTC**
N^{max}, mol kg^{-1}	16.4258	11.1506	13.6459
$\beta^{(0)}$, bar^{-1}	2.2E-05	6.4E-05	4.8E-05
$\beta^{(1)}$, bar^{-1}	2990.148	2668.639	2777.421

Table 6.3: Fit parameters of Langmuir isotherm of N_2.

Parameters	**Cu–BTC**	**Cu–(bromo)BTC**	**Cu–(iodo)BTC**
N^{max}, mol kg^{-1}	3.2218	9.8299	5.3898
$\beta^{(0)}$, bar^{-1}	8.0E-04	1.2E-03	2.0E-04
$\beta^{(1)}$, bar^{-1}	1196.343	885.0715	1586.416

Table 6.4: Fit parameters of Langmuir isotherm of CO.

Parameters	**Cu–BTC**	**Cu–(bromo)BTC**	**Cu–(iodo)BTC**
N^{max}, mol kg^{-1}	10.3081	7.16	7.6894
$\beta^{(0)}$, bar^{-1}	3.11E-05	3.0E-05	9.35E-05
$\beta^{(1)}$, bar^{-1}	2455.943	1751.174	2876.562

Table 6.5: Fit parameters of Langmuir isotherm of CH_4.

Parameters	**Cu–BTC**	**Cu–(bromo)BTC**	**Cu–(iodo)BTC**
N^{max}, mol kg^{-1}	12.471	9.5038	9.7411
$\beta^{(0)}$, bar^{-1}	4.66E-05	5.0E-04	1.0E-04
$\beta^{(1)}$, bar^{-1}	2262.666	1516.304	1924.127

6.5 Effect of the functionality on the framework

To understand the exact effect of functionalization in the frameworks, formula weight is eliminated; the adsorption capacities are converted from mol kg^{-1} to molecules unitcell^{-1}. Interestingly, for CO_2, CO and CH_4, the trend of adsorption capacities is followed in decreasing order Cu–(iodo)BTC>Cu–BTC>Cu–(bromo)BTC. For N_2, the trend is followed as Cu–(bromo)BTC>Cu–(iodo)BTC>Cu–BTC. In case of CO_2, CO, and CH_4 the adsorption, polarizability of functional groups drives the adsorption capacity. In case of for N_2, the surface area and pore size of structure are the responsible for possible adsorption.

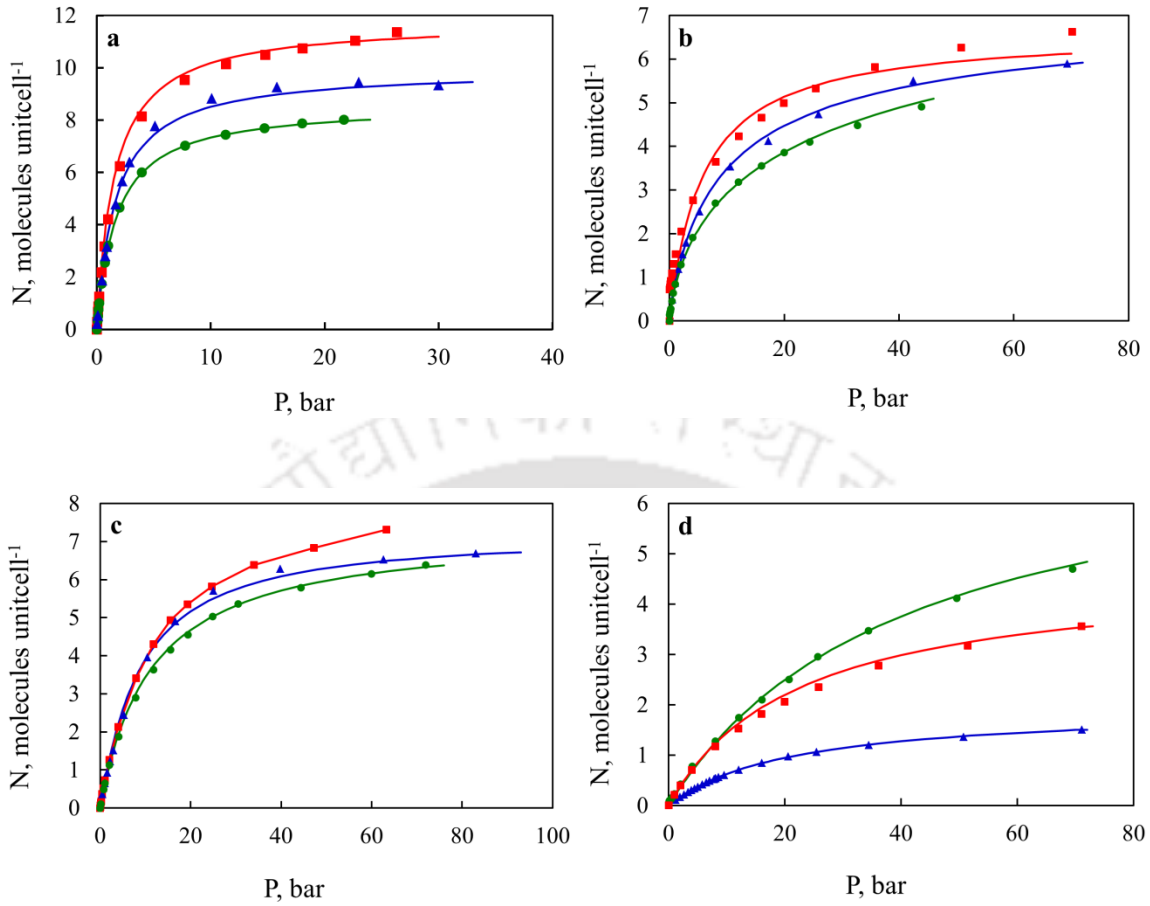

Figure 6.10: Adsorption Isotherms of (a) CO_2, (b) CO, (c) CH_4, and (d) N_2 on Cu–BTC (▲), Cu–(bromo)BTC (●), and Cu–(iodo)BTC (■) at 294 K; adsorption capacities compared in molecules/unit cell.

6.6 Effect of physical properties of gases

The adsorption isotherms of Cu–(bromo)BTC evaluated on CO_2, CO, CH_4, and N_2 at 294 K are shown in Figure 6.11. Due to the presence of open metal sites [19] in frameworks, electrostatic–dispersion interactions are observed. The adsorption capacity for CO_2 is higher than other studied gases due to more polarity and polarizability and for is lowest for N_2 due to low polarity and polarizability. However, in case of CO which having dipole moment is more adsorbed at lower

pressures than CH_4 due to electrostatic interactions. After CO has occupied open metal site, dispersion interaction takes over, and CH_4 has a higher adsorption capacity than CO due to its higher polarizability. Similar kind of interactions were observed for Cu–BTC and Cu–(iodo)BTC (shown in Figure 6.12).

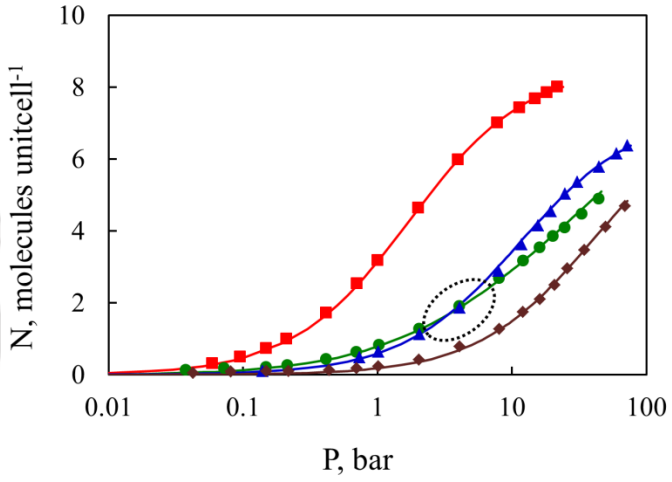

Figure 6.11: Due to the presence of open metal sites in framework, CH_4 isotherm overtake over CO; CO_2 (■), CH_4 (▲), CO (●), and N_2 (♦) at 294 K for Cu–(bromo)BTC; adsorption capacities compared in molecules/unit cell.

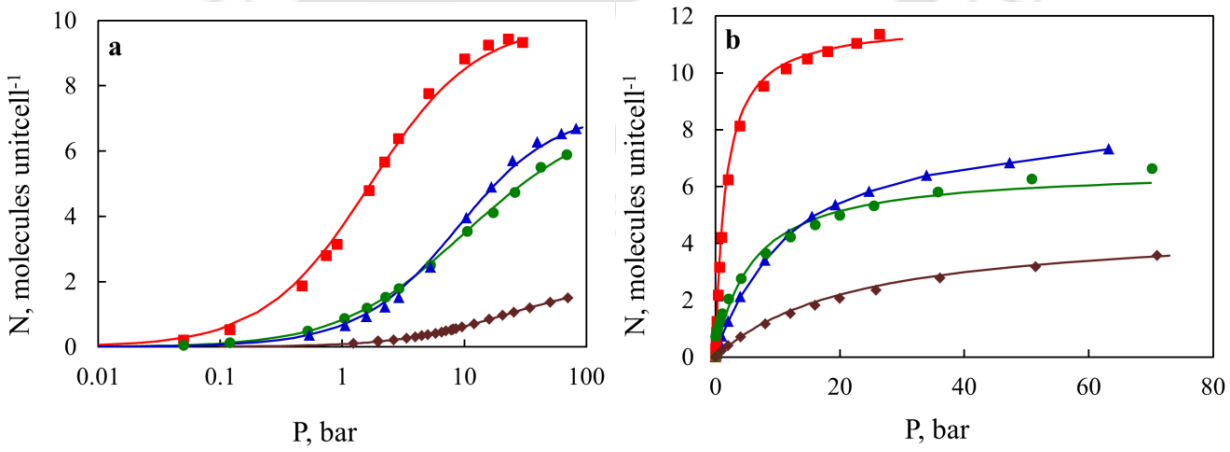

Figure 6.12: Due to the presence of open metal sites in the framework, CH_4 isotherm overtake over CO; CO_2 (■), CH_4 (▲), CO (●), and N_2 (♦) at 294 K for (a) Cu–BTC and (b) Cu–(iodo)BTC; adsorption capacities compared in molecules/unit cell.

6.7 Henry's Constants and Adsorption Enthalpy

The enthalpies of adsorption were calculated from the fit parameters using the Langmuir equation

$$\Delta h_{ads} = -R \frac{\partial(\ln f)}{\partial(1/T)}\Big|_N = -R\beta \qquad 6.3$$

Where R is the gas constant in kJ $mol^{-1}K^{-1}$.

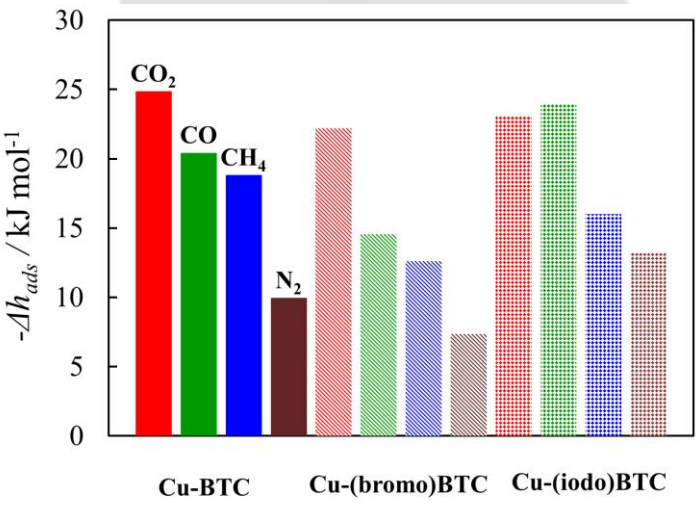

Figure 6.13: Variation of adsorption enthalpy at zero coverage on Cu–BTC versus Cu–(bromo)BTC versus Cu–(iodo)BTC.

From the enthalpy of adsorption data for CO_2, CO, CH_4, and N_2, it is possible to evaluate the Cu–BTC derivatives for adsorbent regeneration and gas separation application. The enthalpy of adsorption for CO_2 and CH_4 is shown highest for Cu–BTC (24.9 and 18.8 kJ/mol respectively)

followed by Cu–(iodo)BTC (23.1 and 16.0 kJ/mol) and Cu–(bromo)BTC (22.2 and 12.6 kJ/mol) respectively. Interestingly for CO and N_2, Cu–(iodo)BTC (23.9 and 13.2 kJ/mol) is shown the highest, followed by Cu–BTC (20.4 and 9.9 kJ/mol) and Cu–(bromo)BTC (14.6 and 7.4 kJ/mol) respectively. Thus, in both cases, the enthalpy of adsorption is governed by the polarizability of bigger functional groups, whereas electrostatic interactions play an important role in CO adsorption. However, for N_2 lowest enthalpy observed due to low polarity and polarizability. Enthalpy differences are observed between CO_2 and N_2, i.e. ($\Delta H(CO_2)$–$\Delta H(N2)$) ~ –9.9 kJ/mol for Cu–(iodo)BTC and approximately equal for Cu–(bromo)BTC and Cu–(iodo)BTC ~ –15.0 kJ/mol. These data are indicator for Cu–BTC and Cu–(bromo)BTC which are more selective for CO_2 over N_2 than Cu–(iodo)BTC.

6.8 Prediction of Binary Selectivity using IAST

Selectivities of various binary mixes are determined using IAST to understand the affinity of functional groups offered in the framework on the binary selectivity for gas mixture. At 294 K, the variation in CO_2 selectivity over N_2 with respect to the mole fraction of CO_2 is shown in Figure 6.14. At a lower mole fraction of CO_2, the selectivity of CO_2 is high for Cu–BTC over Cu–(bromo)BTC and Cu–(iodo)BTC. As mole fraction of CO_2 increases, the selectivity decreases. At CO_2 mole fraction of 0.2 (i.e., 20% of CO_2 in binary mixture of CO_2/N_2), the selectivity of CO_2 over N_2 is approximately 6 times more for Cu–BTC over Cu–(bromo)BTC and 3 times more over Cu–(iodo)BTC. Thus, Cu–BTC is more selective for CO_2 in CO_2/N_2 binary mixture.

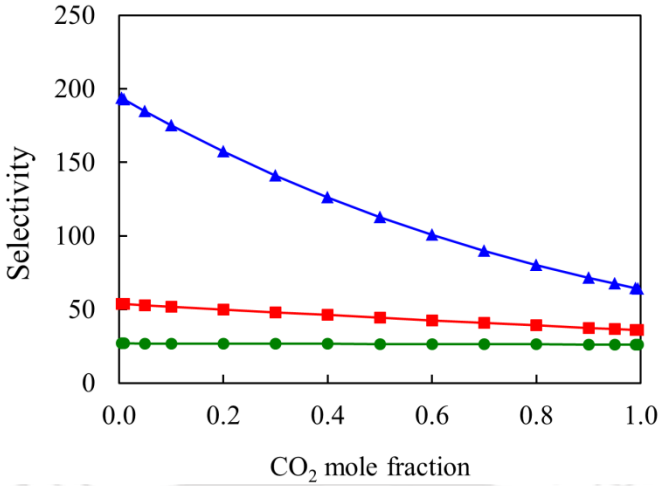

Figure 6.14: Variation of CO_2 selectivity over N_2 for Cu–BTC (▲), Cu–(bromo)BTC (●), and Cu–(iodo)BTC (■). CO_2 at 294 K and 1 bar; lines are drawn as a guide to the eyes.

At 294 K and 1 bar, the variation in CO_2 selectivity over CH_4 is shown in Figure 6.15. The selectivity of CO_2 over CH_4 is significantly more for Cu–(iodo)BTC over Cu–BTC and Cu–(bromo)BTC and no selectivity is observed in between Cu–BTC and Cu–(bromo)BTC.

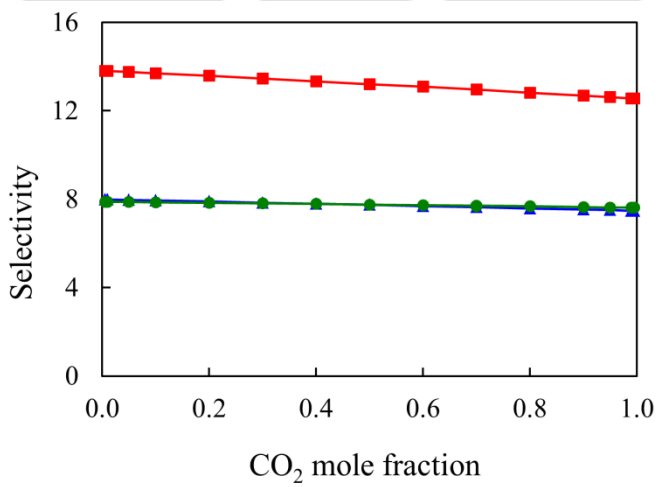

Figure 6.15: Variation of CO_2 selectivity over CH_4 for Cu–(iodo)BTC (■) over Cu–BTC (▲) and Cu–(bromo)BTC (●). CO_2 at 294 K and 1 bar; lines are drawn as a guide to the eyes.

6.9 Summary

This work is evaluated about adsorption of CO_2, CO, CH_4 and N_2 carried out over a wide range of pressures and three different temperatures on Cu–BTC, Cu–(bromo)BTC, and Cu–(iodo)BTC. For all gases Type–I isotherm is observed. The adsorption capacity of CO_2 is high due to more polarity and polarizability followed by CH_4, CO, and N_2. However, at lower pressure range, CO having more adsorption capacity than CH_4 due to electrostatic interaction of CO with open metal sites presented in frameworks. After CO molecules occupy an open metal site, dispersion processes take over, and CH_4 exhibits stronger adsorption due to its higher polarizability. In addition, the enthalpy of adsorption for CO_2 and CH_4 is shown highest for Cu–BTC followed by Cu–(iodo)BTC and Cu–(bromo)BTC respectively. However, for CO and N_2, the enthalpy of adsorption is observed for Cu–(iodo)BTC followed by Cu–BTC and Cu–(bromo)BTC respectively. Therefore, in both the cases enthalpy of adsorption is governed by polarizability of bigger functional groups, whereas electrostatic interactions plays an important role in CO. Selectivities of various binary mixtures are calculated using IAST. At 294 K and 1 bar, for Cu–BTC, CO_2 selectivity over N_2 significantly higher than Cu–(bromo)BTC and Cu–(iodo)BTC and such selectivity decreases with increase in CO_2 mole fraction.

References

(1) O'Keeffe, M. Design of MOFs and Intellectual Content in Reticular Chemistry: A Personal View. *Chem. Soc. Rev.* **2009**, *38*, 1215–1217.

(2) Yaghi, O. M.; O'Keeffe, M.; Ockwig, N. W.; Chae, H. K.; Eddaoudi, M.; Kim, J. Reticular Synthesis and The Design of New Materials. *Nature* **2003**, *423*, 705−714.

(3) Eddaoudi, M.; Kim, J.; Rosi, N.; Vodak, D.; Wachter, J.; O'Keeffe, M.; Yaghi, O. M. Systematic Design of Pore Size and Functionality in Isoreticular MOFs and Their Application in Methane Storage. *Science* **2002**, *295*, 469−472.

(4) Cmarik, G. E.; Kim, M.; Cohen, S. M.; Walton, K. S. Tuning the Adsorption Properties of UiO-66 via Ligand Functionalization. *Langmuir* **2012**, *28*, 15606−15613.

(5) Huang, Y.; Qin, W.; Li, Z.; Li, Y. Enhanced Stability and CO_2 Affinity of a UiO-66 Type Metal-Organic Framework Decorated with Dimethyl Groups. *Dalt. Trans.* **2012**, *41*, 9283–9285.

(6) Kandiah, M.; Nilsen, M. H.; Usseglio, S.; Jakobsen, S.; Olsbye, U.; Tilset, M.; Larabi, C.; Quadrelli, E. A.; Bonino, F.; Lillerud, K. P. Synthesis and Stability of Tagged UiO-66 Zr-MOFs. *Chem. Mater.* **2010**, *22*, 6632−6640.

(7) Biswas, S.; Ahnfeldt, T.; Stock, N. New Functionalized Flexible Al-MIL-53-X (X = -Cl, -Br, CH_3, $-NO_2$, $-(OH)_2$) Solids: Syntheses, Characterization, Sorption, and Breathing Behavior. *Inorg. Chem.* **2011**, *50*, 9518−9526.

(8) Herm, Z. R.; Swisher, J. A.; Smit, B.; Krishna, R.; Long, J. R. Metal-Organic Frameworks as Adsorbents for Hydrogen Purification and Precombustion Carbon Dioxide Capture. *J. Am. Chem. Soc.* **2011**, *133*, 5664-5667.

(9) Mason, J. A.; Sumida, K.; Herm, Z. R.; Krishna, R.; Long, J. R. Evaluating Metal Organic Frameworks for Post-Combustion Carbon Dioxide Capture via Temperature Swing Adsorption. *Energy Environ. Sci.* **2011**, *4*, 3030-3040.

(10) Serra-Crespo, P.; Gobechiya, E.; Ramos-Fernandez, E. V.; Juan-Alcañiz, J.; Martinez-Joaristi, A.; Stavitski, E.; Kirschhock, C. E. A.; Martens, J. A.; Kapteijn, F.; Gascon, J. Interplay of Metal Node and Amine Functionality in NH_2-MIL-53: Modulating Breathing Behavior through Intra-Framework Interactions. *Langmuir* **2012**, *28*, 12916–12922.

(11) Zhou, W.; Wu, H.; Yildirim, T. Enhanced H_2 Adsorption inIsostructural Metal Organic Frameworks with Open Metal Sites: Strong Dependence of the Binding Strength on Metal Ions. *J. Am. Chem. Soc.* **2008**, *130*, 15268−15269.

(12) Collins, D. J.; Zhou, H.-C. Hydrogen Storage in Metal-Organic Frameworks. *J. Mater. Chem.* **2007**, *17*, 3154−3160.

(13) Peng, Y.; Krungleviciute, V.; Eryazici, I.; Hupp, J. T.; Farha, O. K.; Yildirim, T. Methane Storage in Metal −Organic Frameworks: Current Records, Surprise Findings, and Challenges. *J. Am. Chem. Soc.* **2013**, *135*, 11887−11894.

(14) Bloch, E. D.; Murray, L. J.; Queen, W. L.; Chavan, S.; Maximoff, S. N.; Bigi, J. P.; Krishna, R.; Peterson, V. K.; Grandjean, F.; Long, G. J. Selective Binding of O_2 over N_2 in a Redox-Active Metal Organic Framework with Open Iron(II) Coordination Sites. *J. Am. Chem. Soc.* **2011**, *133*, 14814–14822.

(15) Couck, S.; Denayer, J. F. M.; Baron, G. V.; Remy, T.; Gascon, J.; Kapteijn, F. An Amine-Functionalized MIL-53 Metal-Organic Framework with Large Separation Power for CO_2 and CH_4. *J. Am. Chem. Soc.* **2009**, *131*, 6326–6327.

(16) Bourrelly, S.; Llewellyn, P. L.; Serre, C.; Millange, F.; Loiseau, T.; Férey, G. Different Adsorption Behaviors of Methane and Carbon Dioxide in the Isotypic Nanoporous Metal Terephthalates MIL-53 and MIL-47. *J. Am. Chem. Soc.* **2005**, *127*, 13519–13521.

(17) Zhao, C ; Dai, X ; Yao, T ; Chen, C ; Wang, X ; Wang, J ; Yang, J ; Wei, S ; Wu, Y ; Li, Y. Ionic Exchange of Metal-Organic Frameworks to Access Single Nickel Sites for Efficient Electroreduction of CO_2. *J. Am. Chem. Soc.* **2017**, *139*, 8078–8081.

(18) Chowdhury, P.; Mekala, S.; Dreisbach, F.; Gumma, S. Adsorption of CO, CO_2 and CH_4 on Cu-BTC and MIL-101 metal organic frameworks: Effect of Open Metal Sites and Adsorbate Polarity. *Microporous and Mesoporous Mater.* **2012**, *152*, 246–252.

(19) Duren, T.; Bae, Y. S.; Snurr, R. Q. Using Molecular Simulation to Characterize Metal Organic Frameworks for Adsorption Applications. *Chem. Soc. Rev.* **2009**, *38*, 1237–1247.

(20) Fei, H.; Rogow, D. L.; Oliver, S. R. J. Reversible Anion Exchange and Catalytic Properties of Two Cationic Metal-Organic Frameworks Based on Cu(I) and Ag(I). *J. Am. Chem. Soc.* **2010**, *132*, 7202–7209.

(21) Loiseau, T.; Serre, C.; Huguenard, C.; Fink, G.; Taulelle, F.; Henry, M.; Bataille, T.; Férey, G. A Rationale for the Large Breathing of the Porous Aluminum Terephthalate (MIL-53) upon Hydration. *Chem. Eur. J.* **2004**, *10*, 1373–1382.

(22) Yazaydin, A. Ö.; Snurr, R. Q.; Park, T. H.; Koh, K.; Liu, J.; LeVan, M. D.; Benin, A. I.; Jakubczak, P.; Lanuza, M.; Galloway, D. B.; Low, J. J.; Willis, R. R. Screening of Metal-Organic Frameworks for Carbon Dioxide Capture from Flue Gas Using a Combined Experimental and Modeling Approach. *J. Am. Chem. Soc.* **2009**, *131*, 18198–18199.

(23) Caskey, S. R.; Wong-Foy, A. G.; Matzger, A. J. Dramatic Tuning of Carbon Dioxide Uptake via Metal Substitution in a Coordination Polymer with Cylindrical Pores. *J. Am. Chem. Soc.* **2008**, *130*, 10870–10871.

(24) Dietzel, P. D. C.; Besikiotis, V.; Blom, R. Application of Metal-Organic Frameworks with Coordinatively Unsaturated Metal Sites in Storage and Separation of Methane and Carbon Dioxide. *J. Mater. Chem.* **2009**, *19*, 7362–7370.

(25) Millward, A. R.; Yaghi, O. M. Metal Organic Frameworks with Exceptionally High Capacity for Storage of Carbon Dioxide at Room Temperature. *J. Am. Chem. Soc.* **2005,** *127*, 17998–17999.

(26) Liang, Z.; Marshall, M.; Chaffee, A. L. CO_2 Adsorption, Selectivity and Water Tolerance of Pillared-Layer Metal Organic Frameworks. *Microporous Mesoporous Mater.* **2010**, *132*, 305–310.

(27) Llewellyn, P. L.; Bourrelly, S.; Serre, C.; Vimont, A.; Daturi, M.; Hamon, L.; Weireld, G. D.; Chang, J. S.; Hong, D. Y.; Hwang, Y. K.; Jhung, S. H.; Fe'rey, G. High Uptakes of CO_2 and CH_4 in Mesoporous Metals Organic Frameworks MIL-100 and MIL-101. *Langmuir* **2008**, *24*, 7245–7250.

(28) Liang, Z.; Marshall, M.; Chaffee, A. L. CO_2 Adsorption-Based Separation by Metal Organic Framework (Cu-BTC) versus Zeolite (13X). *Energy and Fuels* **2009**, *23*, 2785–2789.

(29) Rallapalli, P.; Prasanth, K. P.; Patil, D.; Somani, R. S.; Jasra, R. V.; Bajaj, H. C. Sorption Studies of CO_2, CH_4, N_2, CO, O_2 and Ar on Nanoporous Aluminum Terephthalate [MIL-53(Al)]. *J. Porous Mater.* **2011**, *18*, 205–210.

(30) Chavan, S.; Vitillo, J. G.; Groppo, E.; Bonino, F.; Lamberti, C.; Dietzel, P. D. C.; Bordiga, S. CO Adsorption on CPO-27-Ni Coordination Polymer: Spectroscopic Features and Interaction Energy. *J. Phys. Chem. C* **2009**, *113*, 3292-3299.

(31) Golden, T. C.; Sircar, S. Gas Adsorption on Silicalite. *J. Coll. Inter. Sci.* **1994**, *162*, 182–188.

(32) Karra, J. R.; Walton, K. S. Molecular Simulations and Experimental Studies of CO_2, CO, and N_2 Adsorption in Metal Organic Frameworks. *J. Phys. Chem. C* **2010**, *114*, 15735–15740.

(33) He, Y.; Zhou, W.; Yildirim, T.; Chen, B. A Series of Metal-Organic Frameworks with High Methane Uptake and an Empirical Equation for Predicting Methane Storage Capacity. *Energy Environ. Sci.* **2013**, *6*, 2735–2744.

(34) Mason, J. A.; Veenstrab, M.; Long, J. R. Evaluating Metal-Organic Frameworks for Natural Gas Storage. *Chem. Sci.* **2014**, *5*, 32–51.

(35) Rolniak, P. D.; Kobayashi, R. Adsorption of Methane and Several Mixtures of Methane and Carbon Dioxide at Elevated Pressures and Near Ambient Temperatures on 5A and 13X Molecular Sieves by Tracer Pertubation Chromatography. *AIChE J.* **1980**, *26*, 616–625.

CHAPTER 7

A Comparative Study of Effect of Functionality on CO_2, CH_4, CO, and N_2 Adsorption in UiO–66 Derivatives

In this chapter, the adsorption characteristics of CO_2, CH_4, CO, and N_2 are measured on UiO–66 MOF derivatives. To know the affinity of various functional groups on gas adsorption, numerous functional groups from simple to complex such as –H, –NH_2, –NO_2, –COOH, and –$(COOH)_2$ are introduced. This work focuses on a comparative study of the effect of functional groups in the framework over unfunctionalized UiO–66 MOF. In addition, the role of functional groups over selectivity also can be understood by this work.

7.1 Background

Adsorption and separation of gases play an important role in industrial applications such as carbon capture from flue gas, natural gas sweetening, and CO_2 separation from CO [1]. Several important factors are considered while choosing an adsorbent for adsorption and separation processes. The adsorbent must possess high uptake capacity, stability, easily generable, stable in the presence of process conditions and high selectivity [2]. However, there are still a number of issues with MOFs in terms of stability. One MOF that has been successfully synthesized with many organic linkers with different functional groups and exhibited exceptional properties such as thermally stable, moisture stable, low cost, and good adsorption properties (UiO–66 (UiO = University of Oslo) [3]. Significant research work is reported in the literature on UiO–66, UiO–66–NH_2, UiO–66–NO_2, UiO–66–COOH, and UiO–66–$(COOH)_2$ [4–8, 11–16, 19].

The family of UiO–66 MOF is comprised of Twelve BDC linkers coordinated with metal atoms of the $Zr_6O_4(OH)_4$ cluster with one of their carboxylate groups. The resultant structure exhibited good porosity with octahedral and tetrahedral cages with a pore opening of 9 Å and 7 Å. Similar isostructural MOFs with the same metal atoms with varying functional groups in organic linker is studied as IRMOF [20, 21] (IRMOF = isoreticular MOF) and DMOF [22–24] (DMOF = DABCO MOF). A significant change was observed in the adsorption capacities of these MOFs by introducing polar functional groups such as amino, nitro, alkoxy, and nitro functional groups [20] and other non-polar naphthyl functional groups [25, 26].

The objective of this work is study the effect of functionality by comparing the gas adsorption properties in UiO–66, UiO–66–NH_2, UiO–66–NO_2, UiO–66–COOH, and UiO–66–$(COOH)_2$ over a wide range of temperature and pressure. Four industrially important gases with a wide range of polarity and polarizability such as CO_2, CO, CH_4, and N_2 have chosen for comparative gas adsorption study on these frameworks. In addition, the enthalpy of adsorption is also calculated for each material respect to adsorbate. Finally, IAST is performed to find the potential separation of CO_2/N_2, CO_2/CH_4, and CO_2/CO mixture for targeted applications including carbon capture, natural gas sweetening, steam reforming, coal gasification, and partial oxidation of hydrocarbons, etc.

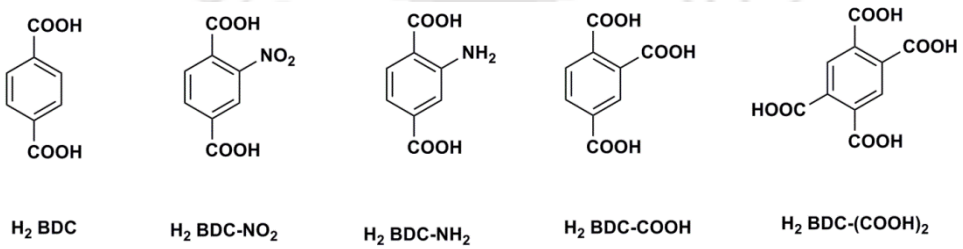

Figure 7.1: Organic linkers used for synthesizing UiO–66 derivatives.

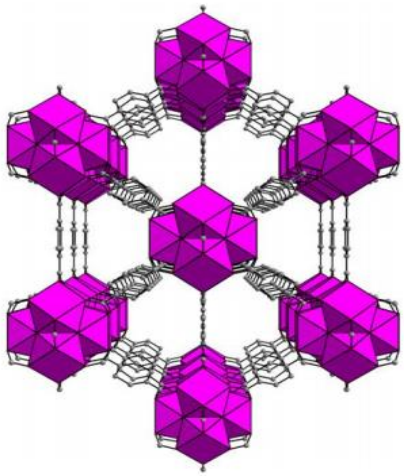

Figure 7.2: Crystal structure of UiO–66 MOF (Twelve BDC linkers coordinate to the metal atoms of the cluster with one of their carboxylate groups).

7.2 Characterization of Frameworks Synthesized

UiO–66 derivatives were synthesized as per the procedure reported in the literature in chapter 4, section 4.2.6–4.2.10. The synthesized samples were characterized using various techniques such as thermogravimetric, powder XRD, and BET surface area analysis.

7.2.1 Powder X-Ray Diffraction (PXRD)

The powder XRD patterns for UiO–66, UiO–66–NO_2, UiO–66–NH_2, UiO–66–COOH, and UiO–66–$(COOH)_2$ are shown in Figure 7.3. The XRD peaks are almost identical, indicating that all the compounds are isostructural in nature.

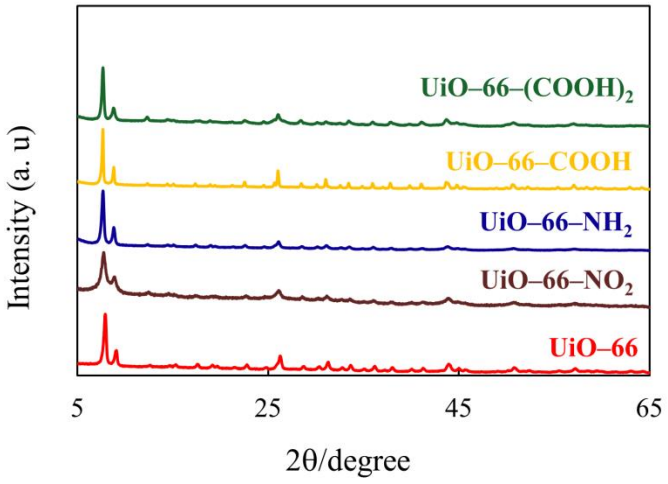

Figure 7.3: Powder X-ray diffractogram of UiO–66 (red), UiO–66–NO_2 (brown), UiO–66–NH_2 (blue), UiO–66–COOH (yellow) and UiO–66–$COOH)_2$ (green).

7.2.2 Thermogravimetric Analysis (TGA)

Thermograms of UiO–66, UiO–66–NO_2, UiO–66–NH_2, UiO–66–COOH, and UiO–66–$(COOH)_2$ are shown in Figure 7.4. The temperature was ramped from 300 to 1100 K with a heating rate of 5 K min^{-1}, and the measurements were performed under argon atmosphere. The initial weight loss step is observed at 363 K corresponds to the removal of solvent (methanol) and moisture for UiO–66 and UiO–66–COOH MOFs. The final weight loss step is occurred at 800 K due to total decomposition and subsequent collapse of the framework. In case of UiO–66–NH_2, UiO–66–NO_2, and UiO–66–$(COOH)_2$, total three weight loss steps are seen in Figure 7.4. The first weight loss step up to 363 K is relatively rapid, and corresponds to the removal solvent (methanol) and moisture. The second weight loss is due to detachment of bonded DMF molecules. The third and final weight loss step is observed due to the decomposition and collapse of the framework at 750 K.

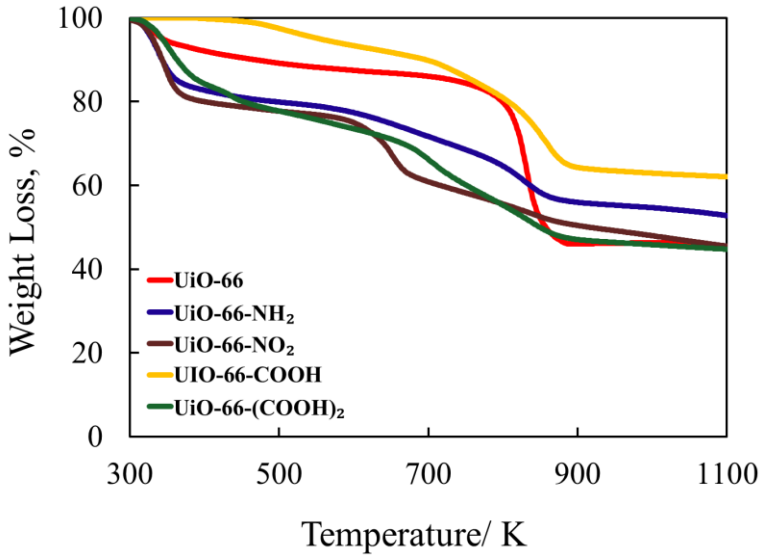

Figure 7.4: TGA analysis of UiO–66 (red), UiO–66–NO_2 (brown), UiO–66–NH_2 (blue), UiO–66–COOH (yellow), and UiO–66–$(COOH)_2$ (green).

7.2.3 Surface Area and Pore Volume Analysis

N_2 adsorption isotherms of the all samples at 77 K are shown in Figure 7.5. Samples were activated prior to isotherm measurement at 423 K under vacuum. The N_2 loading per unit gram is followed as UiO–66>UiO–66–NH_2>UiO–66–COOH>UiO–66–NO_2>UiO–66–$(COOH)_2$. The surface area and pore volume calculated from these isotherms are given in Table 7.1.

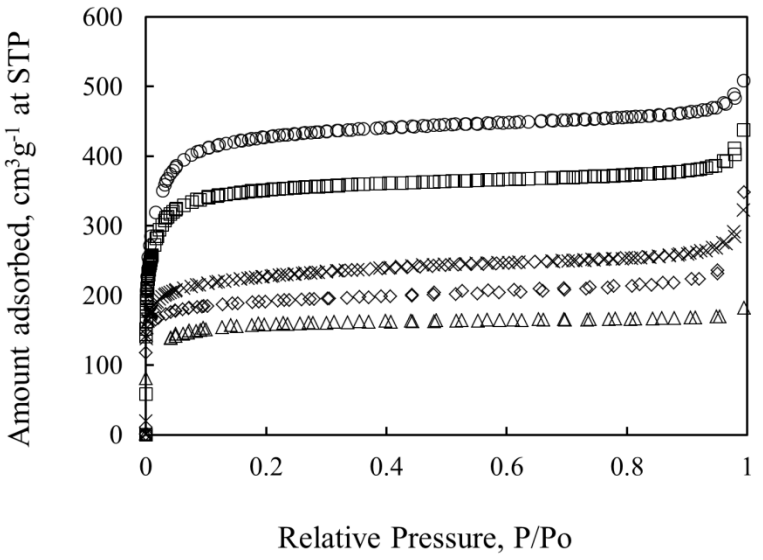

Figure 7.5: N_2 adsorption isotherms at 77 K on UiO–66 (○), UiO–66–NH_2 (□), UiO–66–NO_2 (×), UiO–66–COOH (◊), and UiO–66–$(COOH)_2$ (Δ).

Table 7.1: BET surface area and pore volume of UiO–66 derivatives used in this chapter.

MOF	Surface area	Pore volume
	m^2g^{-1}	cm^3g^{-1}
UiO–66	1460	0.79
UiO–66–NH_2	1192	0.68
UiO–66–NO_2	706	0.47
UiO–66–COOH	654	0.53
UiO–66–$(COOH)_2$	547	0.28

7.3 Adsorption Isotherms

Adsorption isotherms of CO_2, CH_4, CO, and N_2 were measured on UiO–66, UiO–66–NH_2, UiO–66–NO_2, UiO–66–COOH, and UiO–66–$(COOH)_2$ MOFs. The isotherms were modeled to get insights into adsorption. For all measured gases, the Virial domain [ln(f/N) vs. N] Plot is used to analyze the experimental data.

7.3.1 CO_2 Isotherms

Adsorption isotherms of CO_2 on all samples at 294, 317, and 356 K are shown in Figure 7.6. All isotherms exhibits Type–I isotherm; it means UiO–66 MOF derivatives are microporous in nature. Among the studied temperatures, the highest uptake capacity is observed at 294 K followed by 317 K and 356 K. At 294 K and 1 bar pressure, CO_2 uptakes for UiO–66–$(COOH)_2$, UiO–66–COOH, UiO–66–NH_2, UiO–66, and UiO–66–NO_2 are 1.91 mol kg^{-1}, 1.90 mol kg^{-1},

1.83 mol kg^{-1}, 1.42 mol kg^{-1} and 1.14 mol kg^{-1} respectively. These values are comparable to Zn–DABCO (2.0 mol kg^{-1}) [30], Ni–DABCO (2.0 mol kg^{-1}) [30] and higher than MOF–5 (1.0 mol kg^{-1}) [21]. However, these uptakes are lower than compare of Zn–DOBDC (4.6 mol kg^{-1}) [21], Cu–BTC (5.8 mol kg^{-1}) [31], Co–DOBDC (6.7 mol kg^{-1}) [32], Ni–DOBDC (6.9 mol kg^{-1}) [33] and Mg–DOBDC (7.57 mol kg^{-1}) [9].

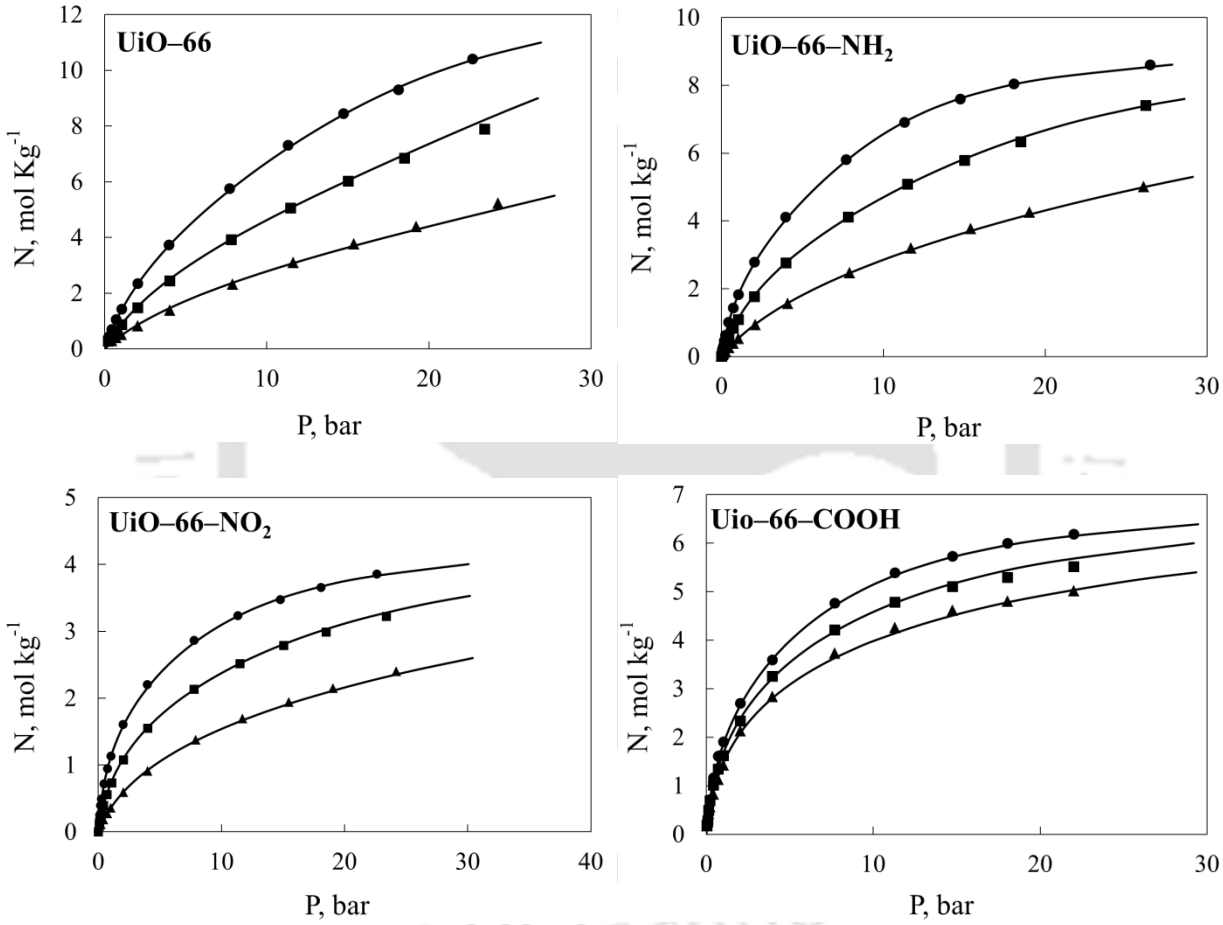

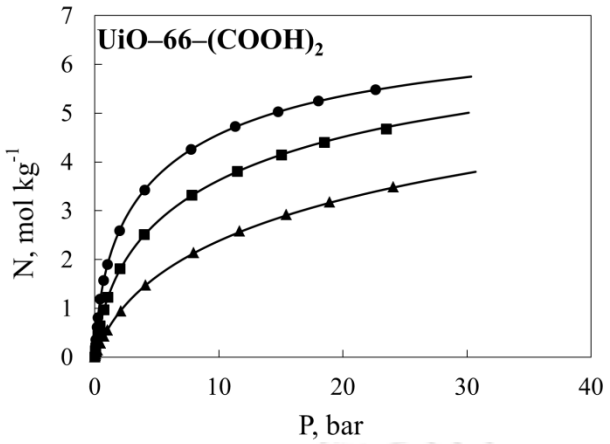

Figure 7.6: CO_2 isotherms of UiO–66, UiO–66–NH_2, UiO–66–NO_2, UiO–66–COOH, and UiO–66–$(COOH)_2$ MOFs. Symbols are experimental data at 294 K (●), 317 K (■), and 356 K (▲); lines are fits obtained using Virial isotherm parameters from Table 7.2.

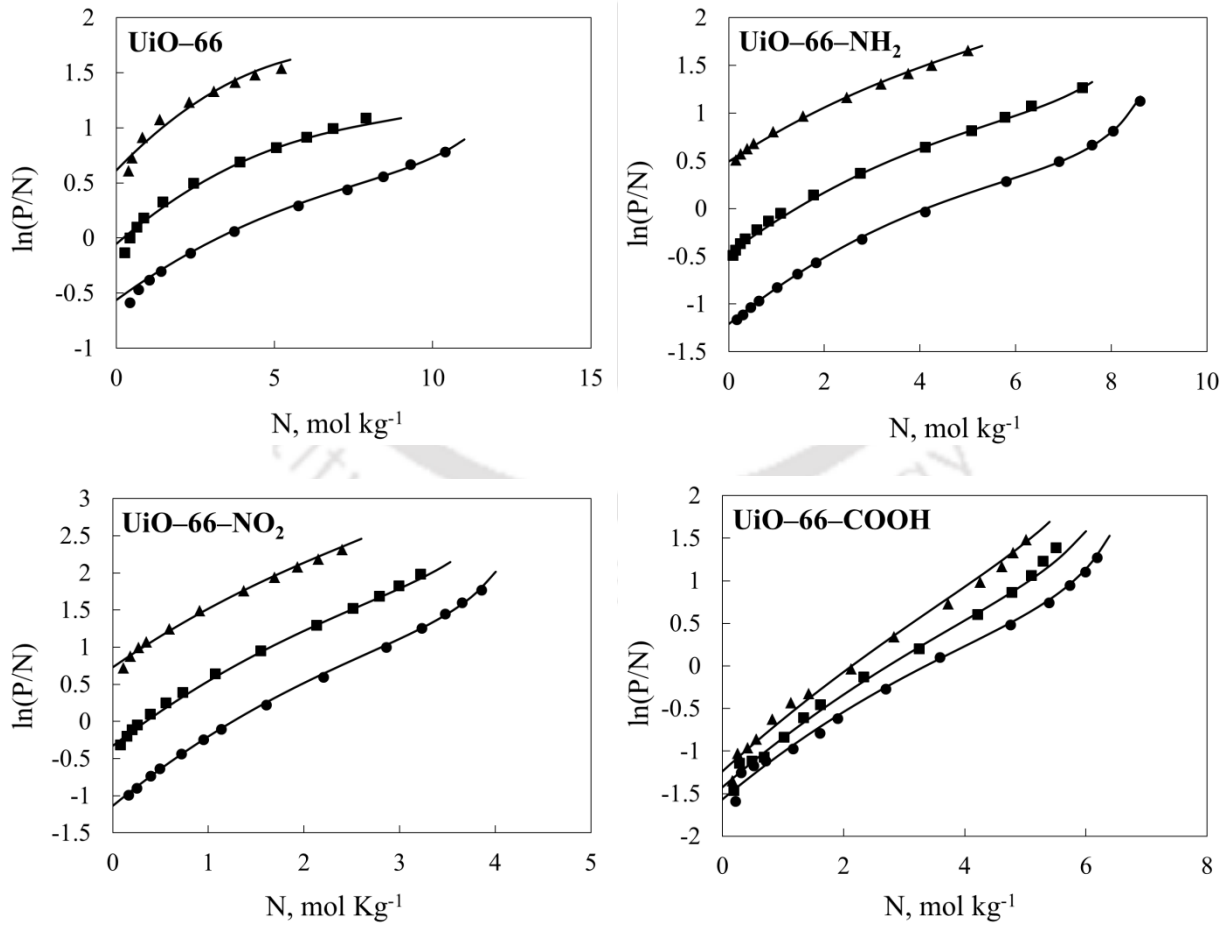

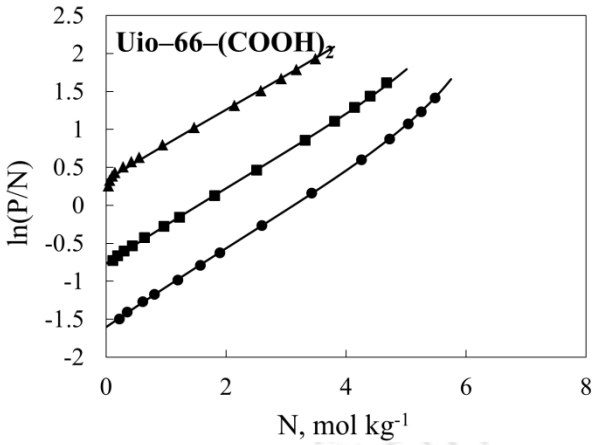

Figure 7.7: CO_2 isotherms of UiO–66, UiO–66–NH_2, UiO–66–NO_2, UiO–66–COOH, and UiO–66–$(COOH)_2$ MOFs in the Virial domain. Symbols are experimental data at 294 K (●), 317 K (■), and 356 K (▲); lines are fits obtained using the Virial isotherm parameters from Table 7.2.

7.3.2 CH_4 Isotherms

The adsorption isotherms of CH_4 on UiO–66 derivatives MOFs at three different temperatures are shown in Figure 7.8. In contrast to CO_2, CH_4 loading on UiO–66 MOFs are comparable to that on Cu–abtc/Cu–hbtc MOFs (studied in the chapter 5) over the entire range of pressure and temperature. The adsorption capacities for UiO–66, UiO–66–NH_2, UiO–66–COOH, UiO–66–$(COOH)_2$, and UiO–66–NO_2 were 5.0 mol kg^{-1}, 4.3 mol kg^{-1}, 3.4 mol kg^{-1}, 3.0 mol kg^{-1} and 2.8 mol kg^{-1} respectively at 294 K temperature and 35 bar pressure. All these uptakes are significantly lower than Cu–BTC (11.38 mol kg^{-1}) [34], NOTT–109 (11.16 mol kg^{-1}) [35], Co–DOBDC (8.4 mol kg^{-1}) [34], Ni–DOBDC (8.6 mol kg^{-1}) [34], MIL–53 (Al) (8.4 mol kg^{-1}) [36], Mg–DOBDC (9.82 mol kg^{-1}) [34]. However, CH_4 adsorption capacities of UiO–66–COOH, UiO–66– $(COOH)_2$, UiO–66–NO_2 can be comparable to Zeolite 13X (3.3 mol kg^{-1})[37].

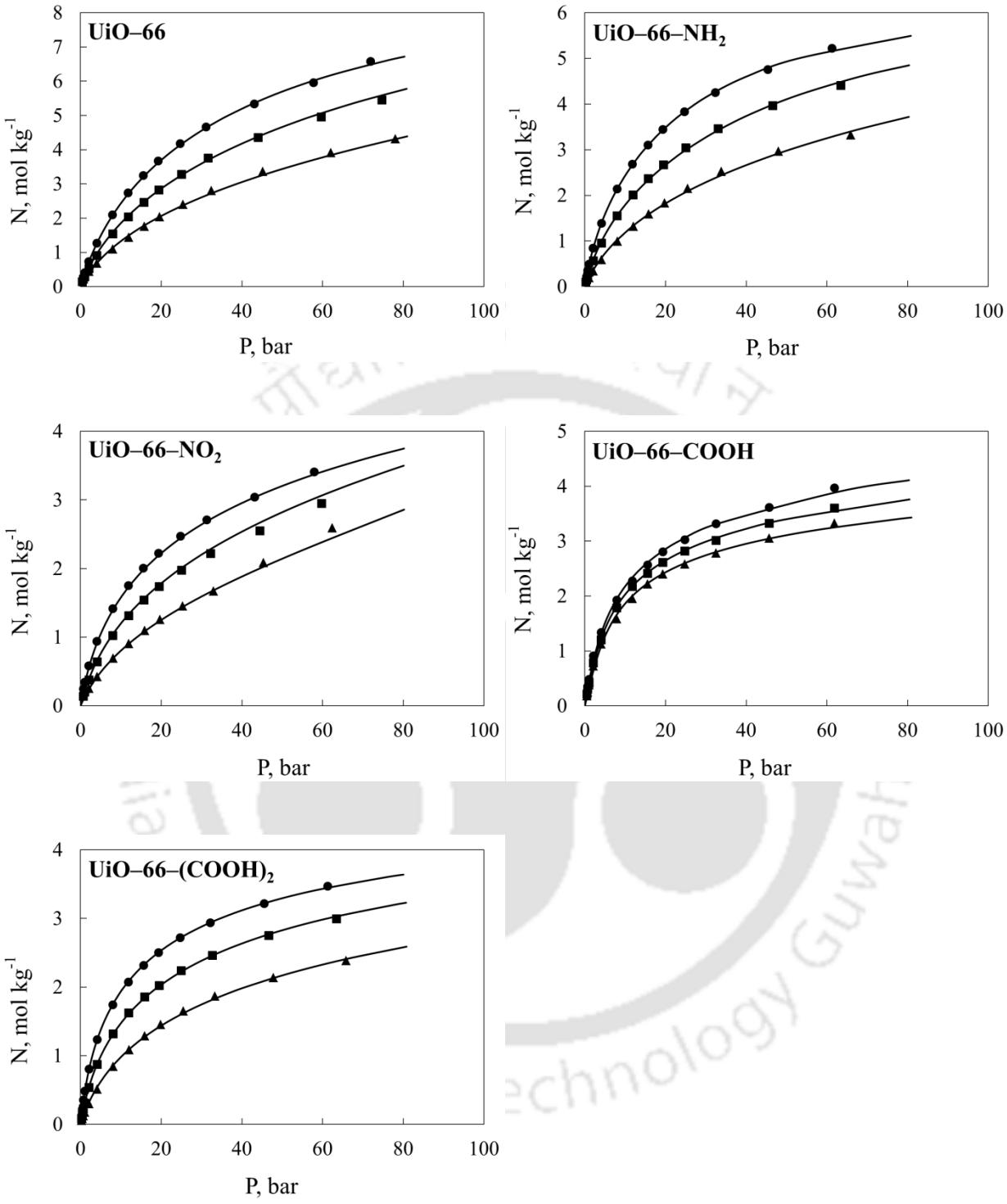

Figure 7.8: CH_4 isotherms of UiO–66, UiO–66–NH_2, UiO–66–NO_2, UiO–66–COOH, and UiO–66–$(COOH)_2$ MOFs. Symbols are experimental data at 294 K (●), 317 K (■), and 356 K (▲); lines are fits obtained using Virial isotherm parameters from Table 7.3.

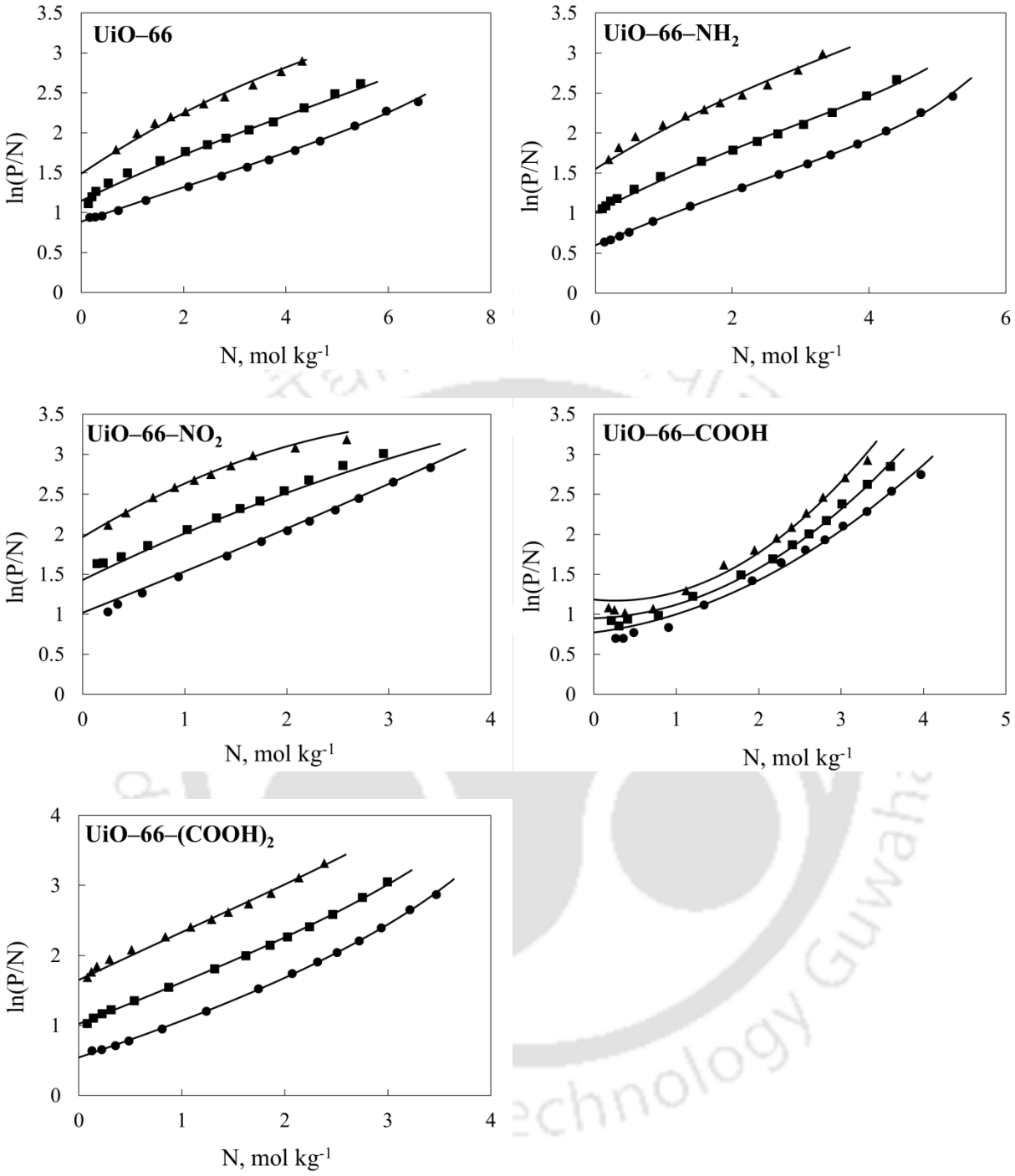

Figure 7.9: CH_4 isotherms of UiO–66, UiO–66–NH_2, UiO–66–NO_2, UiO–66–COOH, and UiO–66–$(COOH)_2$ MOFs in the Virial domain. Symbols are experimental data at 294 K (●), 317 K (■), and 356 K (▲); lines are fits obtained using Virial isotherm parameters from Table 7.3.

7.3.3 CO and N_2 Isotherms

CO isotherms of UiO–66, UiO–66–NH_2, UiO–66–NO_2, UiO–66–COOH, and UiO–66–$(COOH)_2$ MOFs are shown in Figure 7.10. For CO, at 294 K and 1 bar, uptake is varies in between 0.15 mol kg^{-1} to 0.2 mol kg^{-1}. However these uptakes are significantly lower than Cu–BTC (1.4 mol kg^{-1}) [31], IRMOF–1 (0.58 mol kg^{-1}) [38] and IRMOF–3 (0.6 mol kg^{-1}) [38] and Zeolite 13X (1.17 mol kg^{-1}) [39]. Similarly for N_2, shown in Figure 7.12, at 294 K and 1 bar, uptake is varied in between 0.1 mol kg^{-1} and 0.15 mol kg^{-1}. These adsorption capacities are significantly lower than Mg–DOBDC (1.1 mol kg^{-1}) [10] and Ni–DOBDC (1.02 mol kg^{-1}) [33], Zeolite 13X (0.8 mol kg^{-1}) [40] and approximately comparable to MIL–53 (Al) (0.20 mol kg^{-1}) [36].

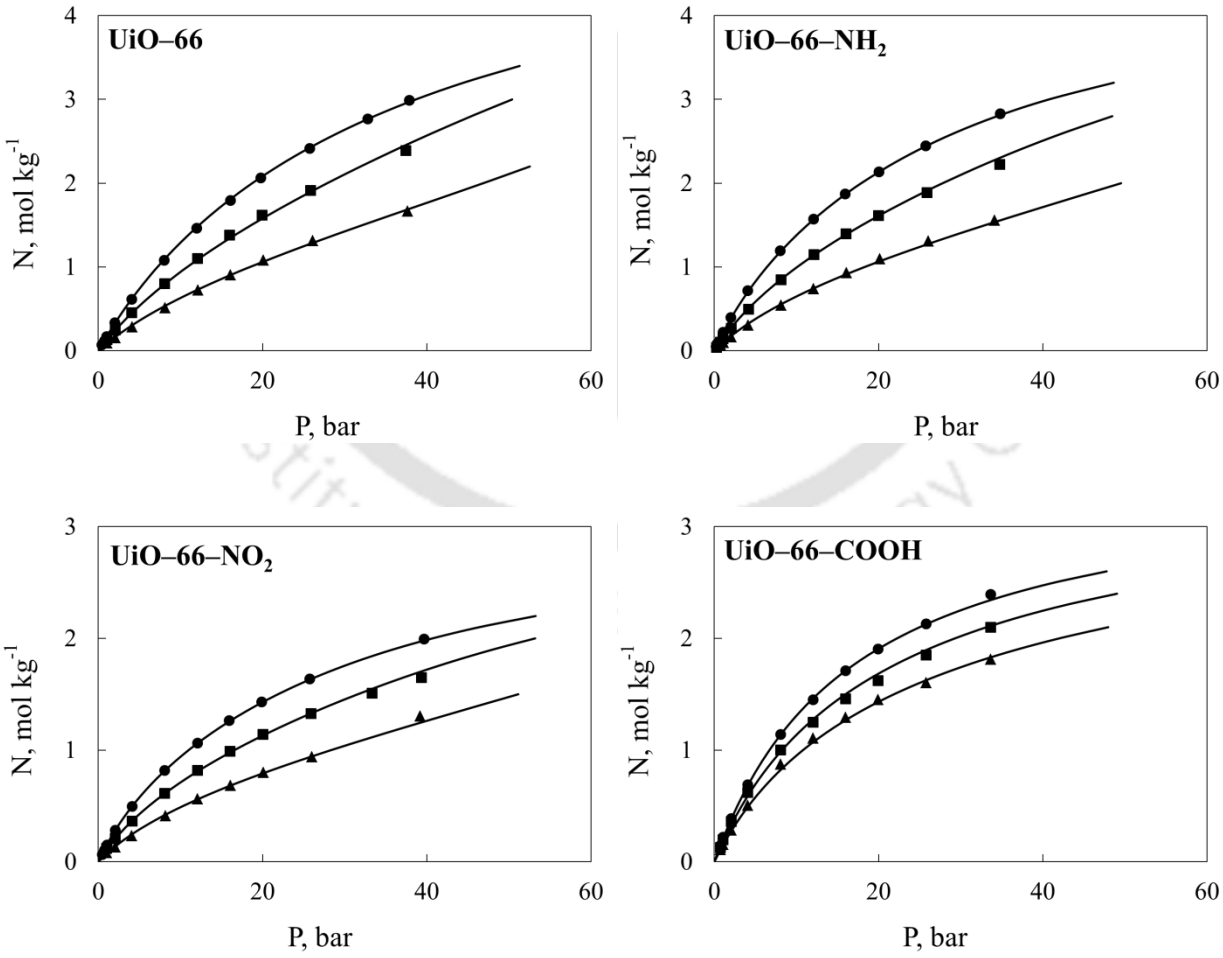

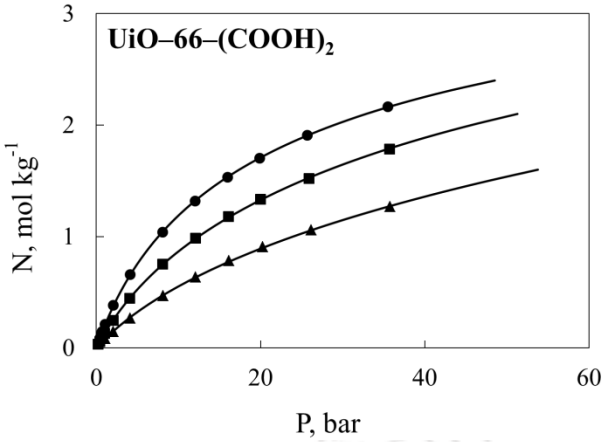

Figure 7.10: CO isotherms of UiO–66, UiO–66–NH_2, UiO–66–NO_2, UiO–66–COOH, and UiO–66–$(COOH)_2$ MOFs. Symbols are experimental data at 294 K (●), 317 K (■), and 356 K (▲); lines are fits obtained using Virial isotherm parameters from Table 7.4.

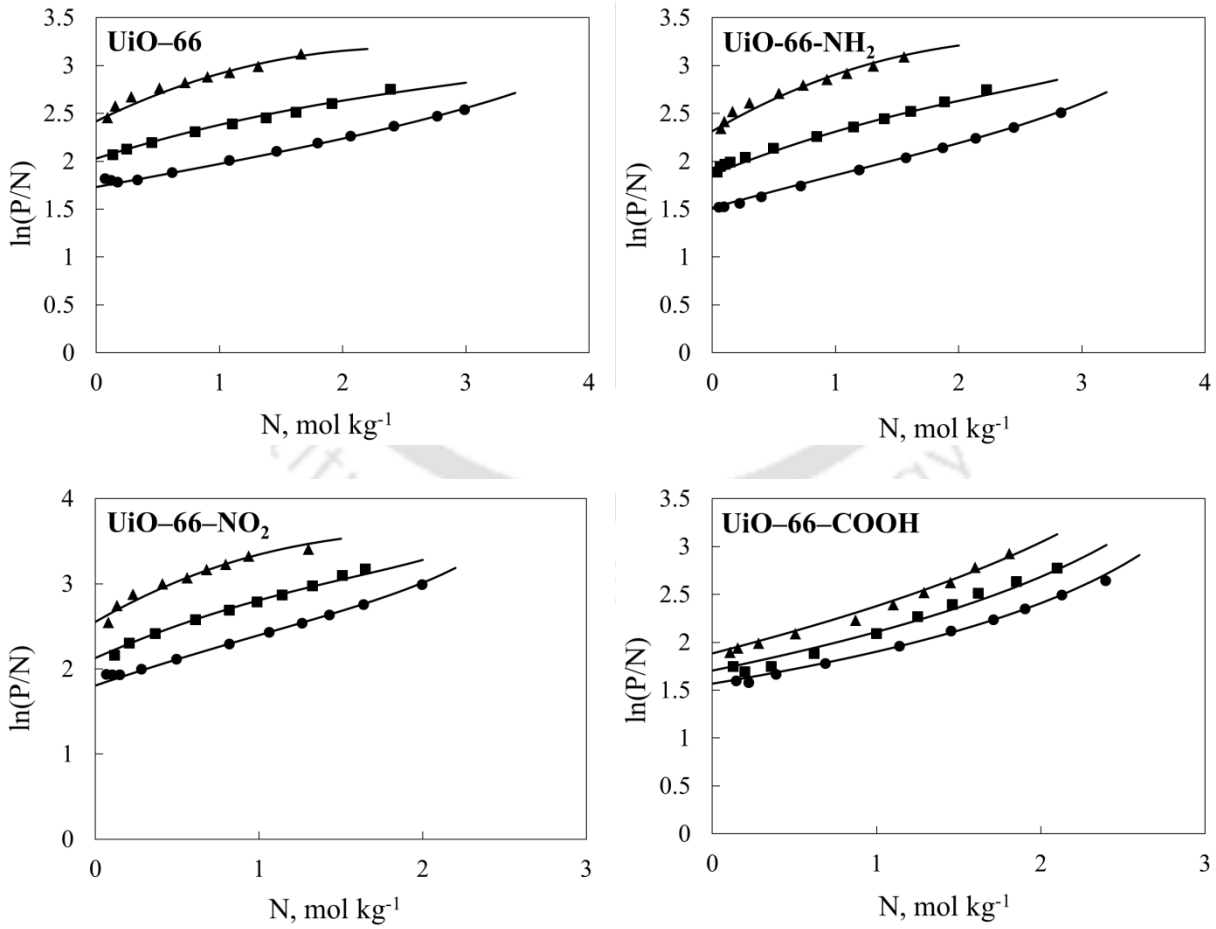

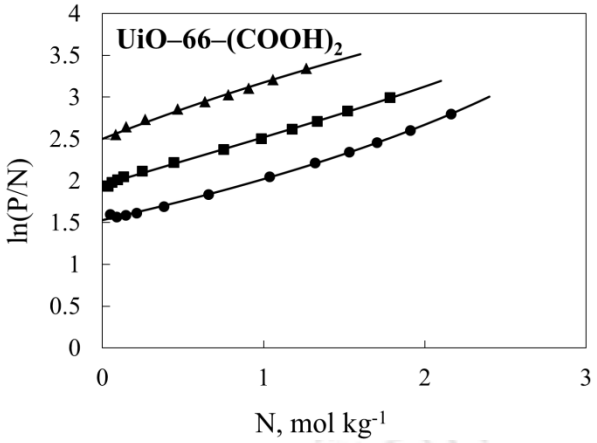

Figure 7.11: CO isotherms of UiO–66, UiO–66–NH_2, UiO–66–NO_2, UiO–66–COOH, and UiO–66–$(COOH)_2$ MOFs in the Virial domain. Symbols are experimental data at 294 K (●), 317 K (■), and 356 K (▲); lines are fits obtained using Virial isotherm parameters from Table 7.4.

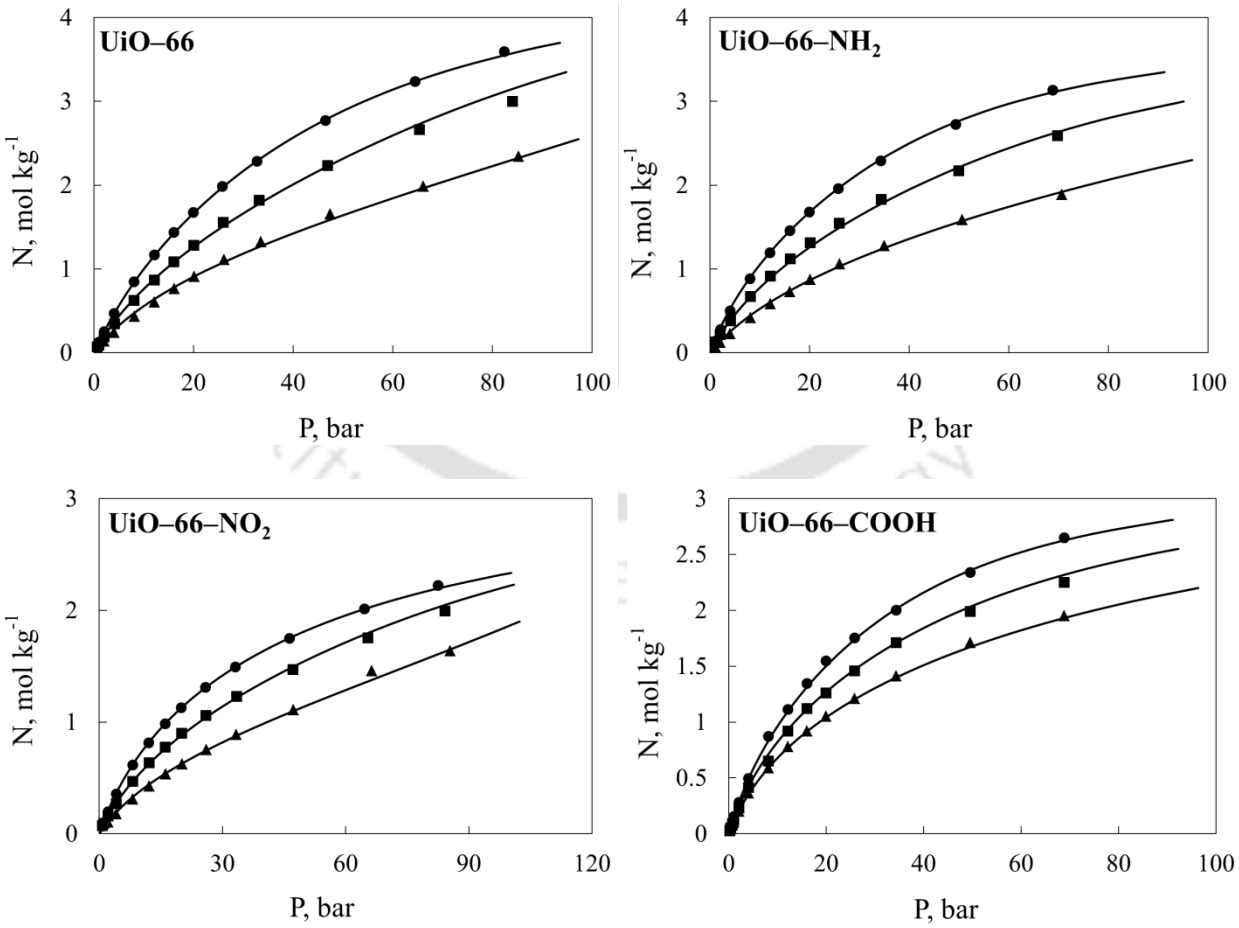

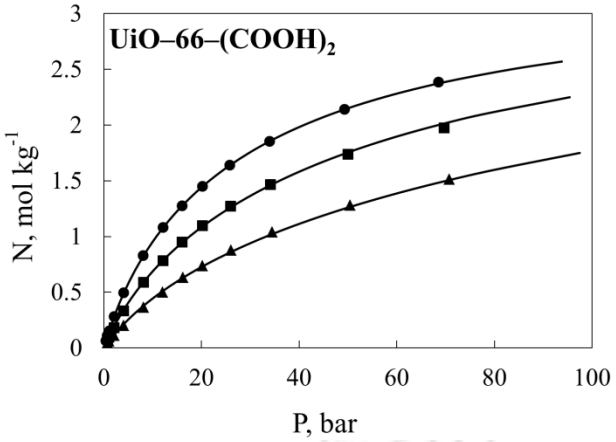

Figure 7.12: N_2 isotherms of UiO–66, UiO–66–NH_2, UiO–66–NO_2, UiO–66–COOH, and UiO–66–$(COOH)_2$ MOFs. Symbols are experimental data at 294 K (●), 317 K (■), and 356 K (▲); lines are fits obtained using Virial isotherm parameters from Table 7.5.

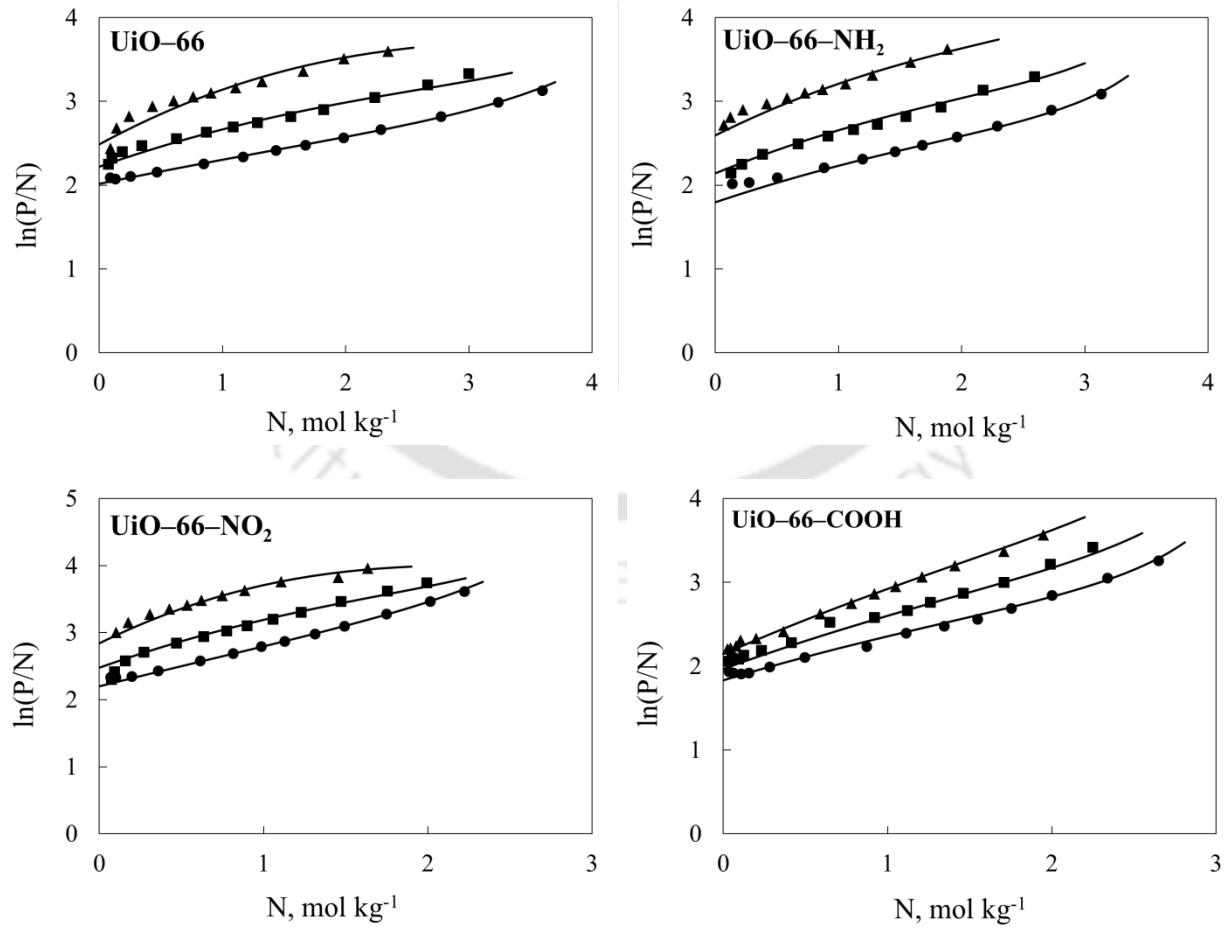

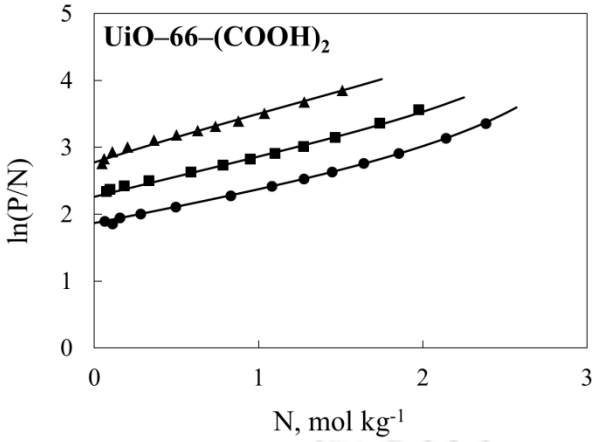

Figure 7.13: N_2 isotherms of UiO–66, UiO–66–NH_2, UiO–66–NO_2, UiO–66–COOH, and UiO–66–$(COOH)_2$ MOFs in the Virial domain. Symbols are experimental data at 294 K (●), 317 K (■), and 356 K (▲); lines are fits obtained using Virial isotherm parameters from Table 7.5.

7.4 Isotherm Modeling

The adsorption isotherms for all measured gases CO_2, CH_4, CO, and N_2, the Virial model [41] was used up to two virial coefficients to fit the experimental data.

$$\ln\left(\frac{f}{N}\right) = bN + cN^2 - \ln(\beta) \qquad 7.1$$

Where N (mol kg^{-1}) is the amount adsorbed, f (bar) is the fugacity, β (mol kg^{-1} bar^{-1}) is temperature dependency of Henry's constant, and b, c are virial parameters

$$b = b^{(0)} + \frac{b^{(1)}}{T} \qquad 7.2$$

$$c = c^{(0)} + \frac{c^{(1)}}{T} \qquad 7.3$$

$$\beta = \beta^{(0)}\exp(\beta^{(1)}/T) \qquad 7.4$$

Where $\beta^{(0)}$ and $\beta^{(1)}$ are related to entropy and enthalpy of adsorption at zero loading, respectively, and T is the temperature in K.

Table 7.2: Fit parameters of Virial isotherm of CO_2.

Parameters	UiO-66	UiO-66-NH_2	UiO-66-NO_2	UiO-66-COOH	UiO-66-$(COOH)_2$
$\beta^{(0)}\times10^4$, mol kg^{-1}bar^{-1}	7.97	4.78	8.83	8.37	8.88
$\beta^{(1)}$, K	-2676.71	-1568.37	-2902.83	667.052	-3060.77
$b^{(0)}$, mol^{-1} kg	0.3021	1.45	0.9142	0.5762	0.5274
$b^{(1)}$, mol^{-1} kg K	9.3235	-368.52	-11.7824	45.3355	-18.75
$c^{(0)}$, mol^{-2} kg^2	-0.0563	-0.1687	-0.292	0.0462	-0.08
$c^{(1)}$, mol^{-2} kg^2 K	12.9484	47.6007	73.67	13.4031	27.95

Table 7.3: Fit parameters of Virial isotherm of CH_4.

Parameters	UiO-66	UiO-66-NH_2	UiO-66-NO_2	UiO-66-COOH	UiO-66-$(COOH)_2$
$\beta^{(0)}\times10^4$, mol kg^{-1}bar^{-1}	4.15	5.62	6.20	3.04	6.55
$\beta^{(1)}$, K	-951.746	-1472.9	-1532.07	-663.555	-1752.97
$b^{(0)}$, mol^{-1} kg	1.4822	1.74	1.8212	-1.1547	1.8534
$b^{(1)}$, mol^{-1} kg K	-377.853	-416.308	-360.198	376.017	-421.836
$c^{(0)}$, mol^{-2} kg^2	-0.1548	-0.2725	-0.5478	0.647	-0.3021
$c^{(1)}$, mol^{-2} kg^2 K	47.0063	81.6541	155.4473	-160.596	109.662

Table 7.4: Fit parameters of Virial isotherm of CO.

Parameters	UiO-66	UiO-66-NH_2	UiO-66-NO_2	UiO-66-COOH	UiO-66-$(COOH)_2$
$\beta^{(0)}\times10^4$, mol $kg^{-1}bar^{-1}$	5.12	5.89	5.83	3.61	6.85
$\beta^{(1)}$, K	-988.74	-1282.0	-1174.02	-598.644	-1556.53
$b^{(0)}$, mol^{-1} kg	3.1665	2.7322	3.5667	0.342	2.3546
$b^{(1)}$, mol^{-1} kg K	-869.18	-704.103	-885.42	-173.55	-574.5
$c^{(0)}$, mol^{-2} kg^2	-1.0641	-0.9239	-1.7493	0.8933	-0.8034
$c^{(1)}$, mol^{-2} kg^2 K	318.5448	273.1076	518.657	-236.775	260.8166

Table 7.5: Fit parameters of Virial isotherm of N_2.

Parameters	UiO-66	UiO-66-NH_2	UiO-66-NO_2	UiO-66-COOH	UiO-66-$(COOH)_2$
$\beta^{(0)}\times10^4$, mol $kg^{-1}bar^{-1}$	4.55	6.08	5.67	3.51	6.80
$\beta^{(1)}$, K	-738.95	-1246.67	-1011.33	-487.299	-1438.55
$b^{(0)}$, mol^{-1} kg	3.2574	2.2531	4.1455	2.4676	2.5209
$b^{(1)}$, mol^{-1} kg K	-884.796	-548.067	-1062.44	-586.083	-626.796
$c^{(0)}$, mol^{-2} kg^2	-0.8206	-0.5914	-1.9459	0-0.3797	-0.6547
$c^{(1)}$, mol^{-2} kg^2 K	246.115	174.8051	585.4791	117.6848	220.4058

7.5 The effect of organic linker functionality

The adsorption characteristics of CO_2, CH_4, CO, and N_2 are measured on UiO–66, UiO–66–NH_2, UiO–66–NO_2, UiO–66–COOH, and UiO–66–$(COOH)_2$. For all studied gases, Type–I isotherm is observed. The adsorption capacity is enhanced due to introduction of polar and complex functional groups such as –H, –NH_2, –NO_2, –COOH, and –$(COOH)_2$. These groups are also helped to reduce free volume, which have a negative impact on adsorption. At low pressure region, MOF functionality is played a dominant role, whereas at saturation pressure level pore volume of the MOF is responsible for more uptake capacity.

On CO_2 adsorption: Since this work focuses on CO_2 adsorption, it can be observed two distinct effects of pure CO_2 adsorption with respect to organic linker functionalization. At the low-pressure region, the CO_2 uptake (shown in Figure 7.14) is improved by the introduction of polar functional groups, and such improvement is more pronounced for functional groups with larger polarity. This kind of consistent behavior is observed for reported IRMOFs [20, 21]. The main reason is that at pressures up to 1 bar (low-pressure region), larger functional group that provides optimized pore diameter, therefore CO_2 molecules in the pores are tightly attached, attributing to the interactions between CO_2 molecules and functionalized framework. The CO_2 uptake in the MOFs at a specific temperature is in the same order as the respective polarity of the functional groups. The highest adsorption is found for UiO–66–$(COOH)_2$ and followed by UiO–66–COOH, UiO–66–NO_2, UiO–66–NH_2 and UiO–66 at three different temperatures viz., 294 K, 317 K, 356 K, at low pressure region.

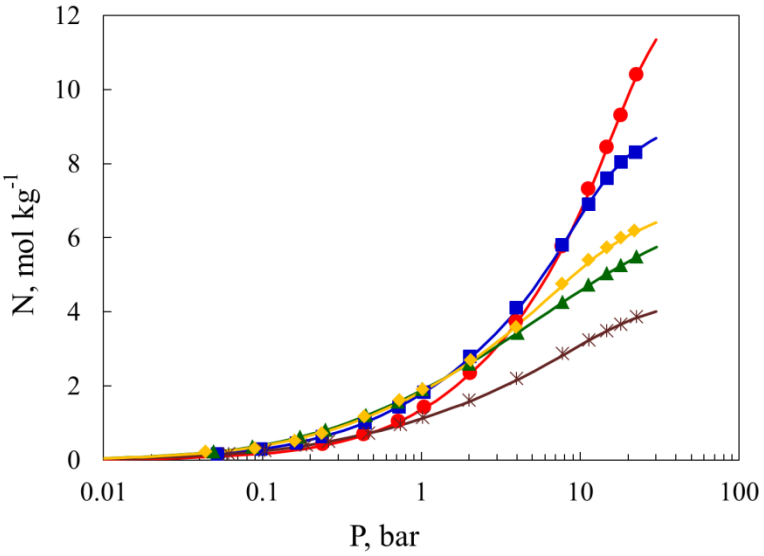

Figure 7.14: Adsorption isotherms of CO_2 at 294 K on UiO–66 (●), UiO–66–NH_2 (■), UiO–66–NO_2 (×), UiO–66–COOH (♦), and UiO–66– $(COOH)_2$ (▲).

As with substantial increment of pressure up to saturation (30 bar) levels, the advantage of the polar functional groups becomes less evident, and the highest uptake capacity was followed with respect to the pore volume of the MOF. The highest up take is observed for UiO-66 followed by UiO–66–NH_2, UiO–66–COOH, UiO–66–NO_2 and UiO–66–$(COOH)_2$ at 294 K and 30 bar. Similar loading capacities are also observed at temperature of 317 K and 356 K.

On CH_4 adsorption: In CH_4 adsorption at 294 K, a low-pressure region (shown in Figure 7.15), CH_4 adsorption is improved by functionalization. The highest uptake is observed for UiO–66–$(COOH)_2$ and followed by UiO–66–NH_2, UiO–66–COOH, and UiO–66. This subtle difference is mainly driven by the polarity of functional groups presented in the framework. The order of uptake at the low-pressure region is approximately equaled to UiO–66–$(COOH)_2$ and UiO–66–NH_2 and then followed by UiO–66–COOH and UiO–66. In contrast to CO_2 adsorption, the lowest uptake is seen for UiO–66–NO_2 in entire region of low pressure, attributes to small pore

collapse in framework. However, as pressure is reached to 60 bar, improvement in adsorption is observed. At high pressure region, gas uptake capacities are reached to saturation due to pore volume of MOF. The order of uptake at 294 K is highest for UiO–66 and followed by UiO–66–NH_2, UiO–66–COOH, UiO–66–NO_2, and UiO–66–$(COOH)_2$.

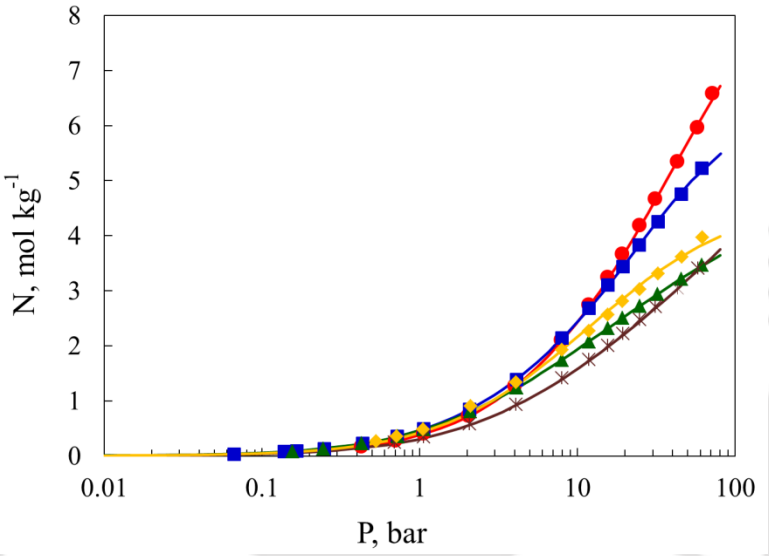

Figure 7.15: Adsorption isotherms of CH_4 at 294 K on UiO–66 (●), UiO–66–NH_2 (■), UiO–66–NO_2 (×), UiO–66–COOH (♦), and UiO–66–$(COOH)_2$ (▲).

On CO and N_2 adsorption: In CO and N_2 adsorption at 294K are shown (Figure 7.16 and Figure 7.17 respectively), at the low-pressure region, UiO–66 and UiO–66–NH_2 showing approximately equal uptake capacities, which have higher uptakes, followed by UiO–66–COOH, UiO–66–$(COOH)_2$ and UiO–66–NO_2. UiO–66–NO_2 showing the lowest entire region of adsorption same as in CH_4 adsorption. As with increase in saturation pressure, the highest uptake is found for UiO–66 and followed by UiO–66–NH_2, UiO–66–COOH, UiO–66–$(COOH)_2$, and UiO–66–NO_2. Similar kind of trends are also observed at 317 K and 356 K. At the low-pressure region, polar gasses (CO_2) and polar functional groups more evident for polar–polar strong interaction.

On the other hand, non–polar and polar interactions are weaker in the case of CH_4, CO, and N_2 adsorption.

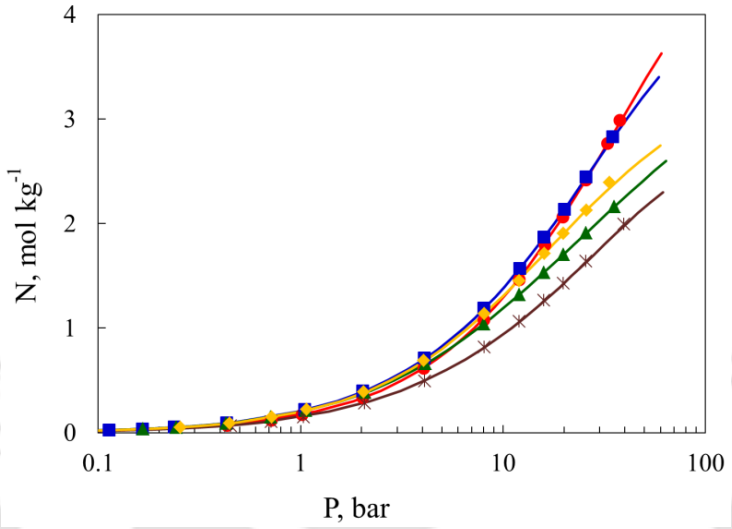

Figure 7.16: Adsorption isotherms of CO at 294 K on UiO–66 (●), UiO–66–NH_2 (■), UiO–66–NO_2 (×), UiO–66–COOH (♦), and UiO–66–$(COOH)_2$ (▲).

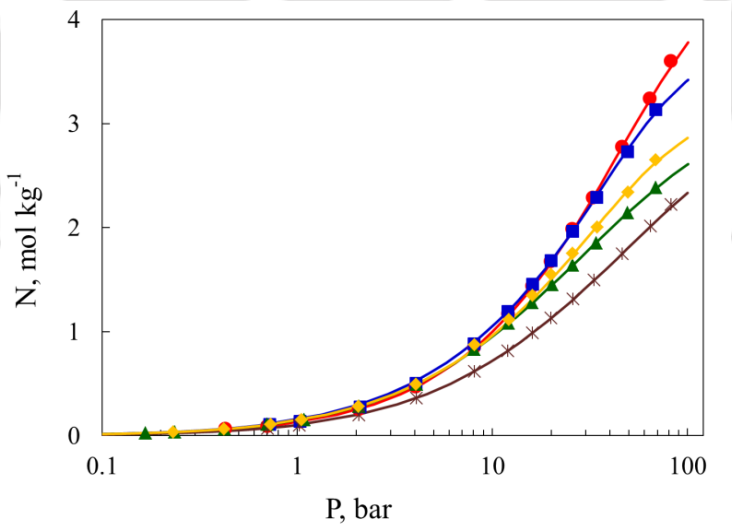

Figure 7.17: Adsorption isotherms of N_2 at 294 K on UiO–66 (●), UiO–66–NH_2 (■), UiO–66–NO_2 (×), UiO–66–COOH (♦), and UiO–66–$(COOH)_2$ (▲).

7.6 Henry's Constants and Adsorption Enthalpy

Henry's constant is a measure of interaction between the adsorbate and the solid surface of the adsorbent. Henry's constant at 294 K for all the studied gases is plotted are shown in Figure 7.18. It is observed that at Henry's region of low pressure for polar gases such as CO_2, the values are significantly higher than the rest of the studied gases. In case of CO (polar gas in nature), due to negligible unsaturated metal sites presence in framework, it is showing less henry's constant value than CH_4 which has higher polarizability. In case of CH_4, CO and N_2, Henrys constant is become insensitive.

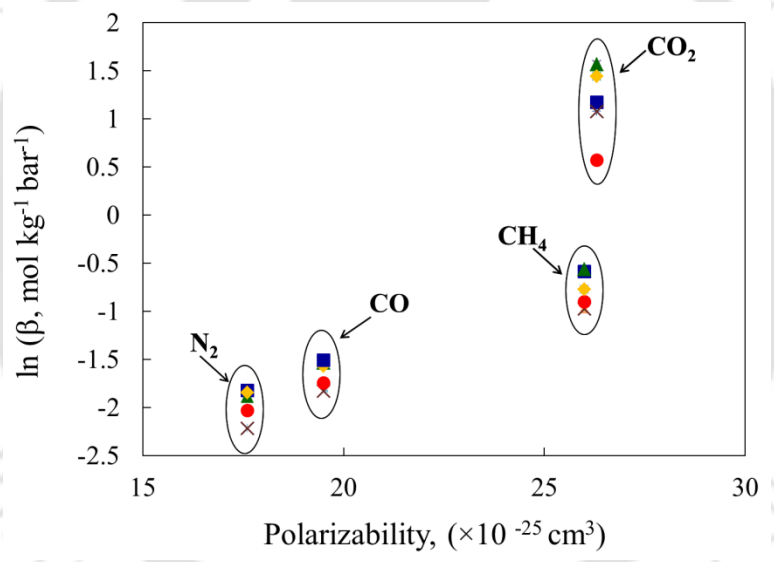

Figure 7.18: Henry's constant at 294 K as a function of the polarizability of the adsorbate for the UiO–66–$(COOH)_2$ adsorbent.

The enthalpies of adsorption on UiO–66, UiO–66–NH_2, UiO–66–COOH, UiO–66–NO_2, and UiO–66–$(COOH)_2$ for CO_2, CH_4, CO, and N_2 are calculated using the model fit parameters.

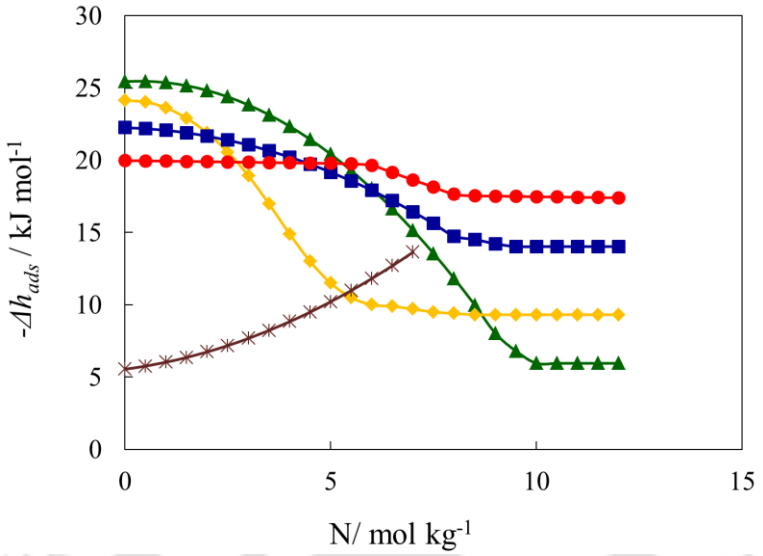

Figure 7.19: Variation of enthalpy of adsorption of CO_2 on UiO–66 (●), UiO–66–NH_2 (■), UiO–66–COOH (×), UiO–66–NO_2 (♦), and UiO–66– $(COOH)_2$ (▲).

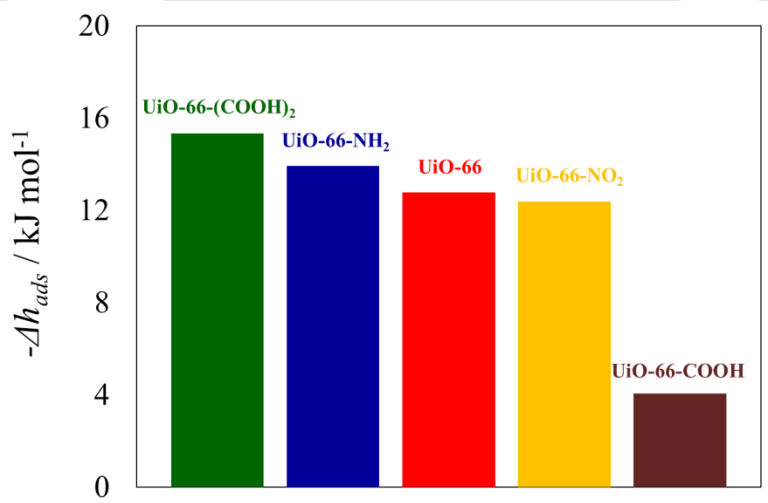

Figure 7.20: Variation of enthalpy of adsorption at zero coverage of N_2 on UiO–66 (red), UiO–66–NH_2 (blue), UiO–66–COOH (yellow), UiO–66–NO_2 (brown), and UiO–66–$(COOH)_2$ (green).

In case of CO_2, the enthalpy of adsorption at zero coverage (shown in Figure 7.19) is varied in between 20.0–26.0 kJ mol^{-1} for UiO–66, UiO–66–NH_2, UiO–66–NO_2, and UiO–66–$(COOH)_2$ MOFs. However, it is 5.5 kJ mol^{-1} for UiO–66–COOH; such low value is mainly governed by less isosteric heat of adsorption. The order of enthalpy of adsorption at zero coverage for CO_2 is followed as UiO–66–$(COOH)_2$>UiO–66–NO_2>UiO–66–NH_2>UiO–66>UiO–66–COOH and thus, attributing to the polarity of functional groups presented in the framework. As CO_2 loading increases, the effect of functional groups becomes less effective, so enthalpy gradually decreases with an increase in CO_2 loading. However, in the case of UiO–66–COOH, the enthalpy of adsorption gradually increases to a rise in CO_2 loading. These calculated enthalpies of adsorption at zero loading ($-\Delta h_{ads,0}$) for CO_2 on the studied MOFs (~4.4–26.0 kJ mol^{-1}) is considerably lower than MIL–53 [17], MIL–100[42] and MIL–101 [42], Cu–BTC [31], M/DOBDC[43] and slightly higher than to large pore MOF like IRMOF–3 [18]. Here, we can understand the two factors by the introduction of more complex functional groups to the linkers: one is as enthalpy factor that increases the interactions between the framework and CO_2, contributing positively to the CO_2 uptake, and the other is which reduces the free volume of the material (for N_2, $\Delta h_{ads,0}$ shown in Figure 7.20).

7.7 Prediction of Binary Selectivity using IAST

To understand the functionalization in the framework on the binary selectivity in the gas mixture, selectivities of various binary mixtures are calculated using IAST. At 294 K, the variation in CO_2 selectivity over N_2 with pressure for 20% CO_2 in the binary mixture is shown in Figure 7.21. The CO_2 selectivity over N_2 gradually increased as sites are progressively filled. However, in the case of UiO–66–NO_2, it progressively decreases the selectivity. The selectivity of CO_2 over N_2 following order is UiO–66–$(COOH)_2$>UiO–66–COOH>UiO–66–NH_2>UiO–66> UiO–66–NO_2

at saturation level reached. In CO_2 selectivity over CO (shown in Figure 7.22), UiO–66–$(COOH)_2$ shows ~2.2 times more selective over unfunctionalized UiO–66. In the case of UiO–66–COOH and UiO–66–NH_2 is ~2 fold more selective over UiO–66. Initially, for UiO–66–COOH and UiO–66–NO_2 having more selective over UiO–66, as gradually pressure increases the selectivity is decreased, for UiO–66– $(COOH)_2$ is a small increment in selectivity and whereas in UiO–66 and UiO–66–NH_2 does not change appreciably.

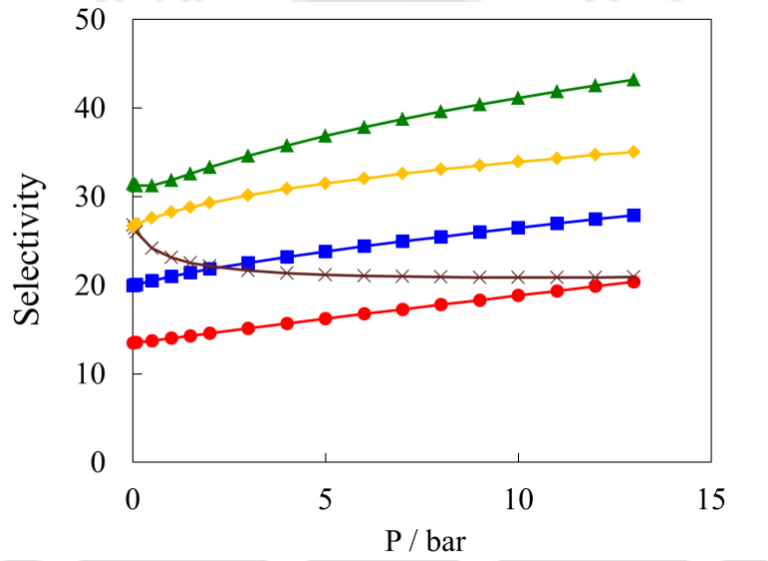

Figure 7.21: Variation of CO_2 selectivity over N_2 for UiO–66 (●), UiO–66–NH_2 (■), UiO–66–COOH (♦), UiO–66–NO_2 (×), and UiO–66–$(COOH)_2$ (▲); CO_2 mole fraction in all binary mixture is 20%; lines are drawn as a guide to the eyes.

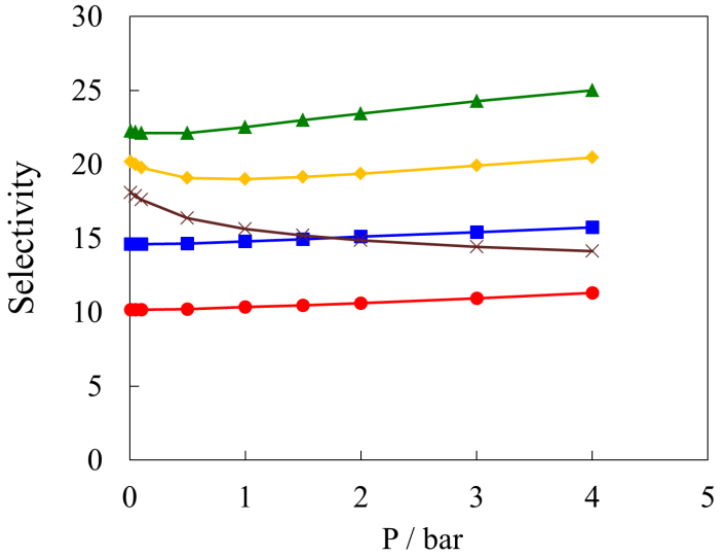

Figure 7.22: Variation of CO_2 selectivity over CO for UiO–66 (●), UiO–66–NH_2 (■), UiO–66–COOH (♦), UiO–66–NO_2 (×), and UiO–66–$(COOH)_2$ (▲). CO_2 mole fraction in all binary mixtures is 20%; lines are drawn as a guide to the eyes.

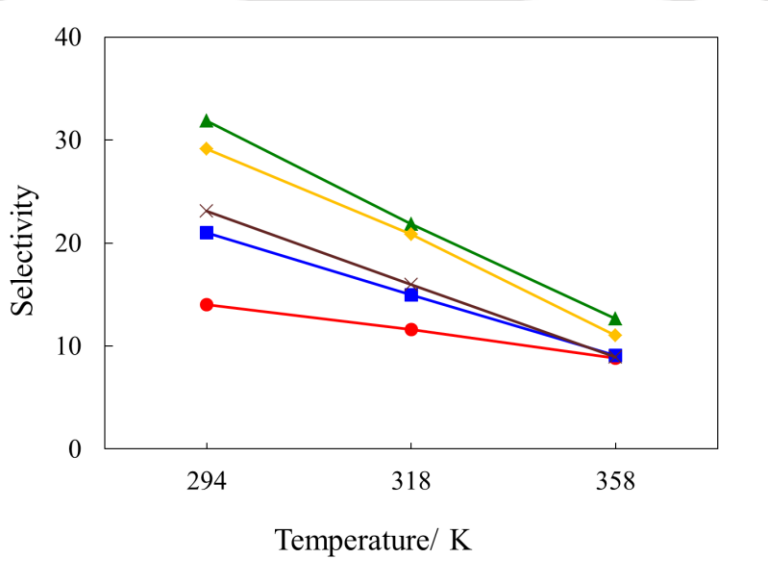

Figure 7.23: Effect of temperature on CO_2 selectivity (for 20% molar composition of CO_2) over N_2 for UiO–66 (●), UiO–66–NH_2 (■), UiO–66–COOH (♦), UiO–66–NO_2 (×), and UiO–66–$(COOH)_2$ (▲); lines are drawn as a guide to the eyes.

In addition, the effect of temperature on selectivity is also calculated (shown in Figure 7.23). CO_2 selectivity over N_2 for a binary gas mixture (20% molar composition of CO_2 at 1 bar) decreases with an increase in temperature. From Figure 7.23, two kinds of trends can observe, (1) the larger affinity of functional groups means the quicker decrease of selectivity with increasing in temperature; (2) at a lower temperature, the larger the difference in selectivity in different functionalized UiO–66 MOFs and such difference may disappear at high temperature. This indicates that the modification of MOFs by introducing functional groups into the linkers is more effective under low-temperature conditions. This strategy may not be beneficial when used for high-temperature applications.

7.8 Summary

This work demonstrates organic linker functionality on adsorption characteristics of CO_2, CH_4, CO, and N_2 over a wide range of pressure and three different temperatures. Through linker functionalization, introducing more polar and complex functional groups such as $–NH_2$, $–NO_2$, –COOH, and –(COOH) can improve the adsorption capacity. It also reduces the free volume may negatively contribute to adsorption. In low-pressure regions, polar functional groups play a dominant role, whereas at saturation level reaches pore volume, and free space available can be attributed to more adsorption. CO_2 adsorption at low pressure follows the order UiO–66–$(COOH)_2$>UiO–66–COOH>UiO–66–NO_2>UiO–66–NH_2>UiO–66 with adsorption enthalpies varies ranging between 5.5 and 26.0 kJ mol^{-1}. The selectivity of CO_2 over CH_4, CO, and N_2 in presence of larger and complex functional groups results in sudden decrease in selectivity with an increase in temperature; such difference is observed more at lower temperatures and could be negligible at higher temperatures. Therefore, MOFs should be designed in such a way as to increase affinity for targeted gases adsorption caused by complex polar functional groups at

lower pressure, and such influence may disappears as pressure increases. The linker functionality is also more evident at lower temperatures, and such influence decreases with an increase in temperature due to interaction between framework and adsorbate.

References

(1) D'Alessandro, D. M.; Smit, B.; Long, J. R. Carbon Dioxide Capture: Prospects for New Materials. *Angew. Chemie - Int. Ed.* **2010**, *49*, 6058–6082.

(2) Cmarik, G. E; Kim, M: Cohen, S. M; Walton, K. S. Tuning the Adsorption Properties of UiO-66 via Ligand Functionalization. *Langmuir* **2012**, *28*, 15606−15613.

(3) Cavka, J. H.; Jakobsen, S.; Olsbye, U.; Guillou, N.; Lamberti, C.; Bordiga, S.; Lillerud, K. P. A New Zirconium Inorganic Building Brick Forming Metal Organic Frameworks with Exceptional Stability. *J. Am. Chem. Soc.* **2008**, *130*, 13850–13851.

(4) Blandez, J. F.; Santiago-Portillo, A.; Navalón, S.; Giménez-Marqués, M.; Álvaro, M.; Horcajada, P.; García, H. Influence of Functionalization of Terephthalate Linker on the Catalytic Activity of UiO-66 for Epoxide Ring Opening. *J. Mol. Catal. A Chem.* **2016**, *425*, 332–339.

(5) Cirujano, F. G.; Corma, A.; Llabrés i Xamena, F. X. Conversion of Levulinic Acid into Chemicals: Synthesis of Biomass Derived Levulinate Esters over Zr-Containing MOFs. *Chem. Eng. Sci.* **2015**, *124*, 52–60.

(6) Cunha, D.; Gaudin, C.; Colinet, I.; Horcajada, P.; Maurin, G.; Serre, C. Rationalization of the Entrapping of Bioactive Molecules into a Series of Functionalized Porous Zirconium Terephthalate MOFs. *J. Mater. Chem. B* **2013**, *1*, 1101–1108.

(7) DeStefano, M. R.; Islamoglu, T.; Garibay, S. J.; Hupp, J. T.; Farha, O. K. Room-Temperature Synthesis of UiO-66 and Thermal Modulation of Densities of Defect Sites. *Chem. Mater.* **2017**, *29*, 1357–1361.

(8) Garibay, S. J.; Cohen, S. M. Isoreticular Synthesis and Modification of Frameworks with the UiO-66 Topology. *Chem. Commun.* **2010**, *46*, 7700–7702.

(9) Herm, Z. R.; Swisher, J. A.; Smit, B.; Krishna, R.; Long, J. R. Metal-Organic Frameworks as Adsorbents for Hydrogen Purification and Pre-combustion Carbon Dioxide Capture. *J. Am. Chem. Soc.* **2011**, *133*, 5664–5667.

(10) Mason, J. A.; Sumida, K.; Herm, Z. R.; Krishna, R.; Long, J. R. Evaluating Metal-Organic Frameworks for Post-Combustion Carbon Dioxide Capture via Temperature Swing Adsorption. *Energy Environ. Sci.* **2011**, *4*, 3030–3040.

(11) Kandiah, M.; Nilsen, M. H.; Usseglio, S.; Jakobsen, S.; Olsbye, U.; Tilset, M.; Larabi, C.; Quadrelli, E. A.; Bonino, F.; Lillerud, K. P. Synthesis and Stability of Tagged UiO-66 Zr-MOFs. *Chem. Mater.* **2010**, *22*, 6632–6640.

(12) Ploskonka, A. M.; Marzen, S. E.; DeCoste, J. B. Facile Synthesis and Direct Activation of Zirconium Based Metal-Organic Frameworks from Acetone. *Ind. Eng. Chem. Res.* **2017**, *56*, 1478–1484.

(13) Rada, Z. H.; Abid, H. R.; Sun, H.; Wang, S. Bifunctionalized Metal Organic Frameworks, UiO-66-NO_2-N (N = -NH_2, -$(OH)_2$, -$(COOH)_2$), for Enhanced Adsorption and Selectivity of CO_2 and N_2. *J. Chem. Eng. Data* **2015**, *60*, 2152–2161.

(14) Zhang, X.; Hu, Q.; Xia, T.; Zhang, J.; Yang, Y.; Cui, Y.; Chen, B.; Qian, G. Turn-on and Ratiometric Luminescent Sensing of Hydrogen Sulfide Based on Metal-Organic Frameworks. *ACS Appl. Mater. Interfaces* **2016**, *8*, 32259–32265.

(15) Biswas, S.; Zhang, J.; Li, Z.; Liu, Y. Y.; Grzywa, M.; Sun, L.; Volkmer, D.; Van Der Voort, P. Enhanced Selectivity of CO_2 over CH_4 in Sulphonate-, Carboxylate- and Iodo-Functionalized UiO-66 Frameworks. *Dalt. Trans.* **2013**, *42*, 4730–4737.

(16) Biswas, S.; Van Der Voort, P. A General Strategy for the Synthesis of Functionalised UiO-66 Frameworks: Characterisation, Stability and CO_2 Adsorption Properties. *Eur. J. Inorg. Chem.* **2013**, *12*, 2154–2160.

(17) Bourrelly, S.; Llewellyn, P. L.; Serre, C.; Millange, F.; Loiseau, T.; Férey, G. Different Adsorption Behaviors of Methane and Carbon Dioxide in the Isotypic Nanoporous Metal Terephthalates MIL-53 and MIL-47. *J. Am. Chem. Soc.* **2005**, *127*, 13519–13521.

(18) Yazaydin, A. Ö.; Snurr, R. Q.; Park, T. H.; Koh, K.; Liu, J.; LeVan, M. D.; Benin, A. I.; Jakubczak, P.; Lanuza, M.; Galloway, D. B.; Low, J. J.; Willis, R. R. Screening of Metal-Organic Frameworks for Carbon Dioxide Capture from Flue Gas Using a Combined Experimental and Modeling Approach. *J. Am. Chem. Soc.* **2009**, *131*, 18198–18199.

(19) Reinsch, H.; Bueken, B.; Vermoortele, F.; Stassen, I.; Lieb, A.; Lillerud, K. P.; De Vos, D. Green Synthesis of Zirconium-MOFs. *Cryst. Eng. Comm.* **2015**, *17*, 4070–4074.

(20) Deng, H.; Doonan, C. J.; Furukawa, H.; Ferreira, R. B.; Towne, J.; Knobler, C. B.; Wang, B.; Yaghi, O. M. Multiple Functional Groups of Varying Ratios in Metal-Organic Frameworks. *Science* **2010**, *327*, 846–850.

(21) Millward, A. R.; Yaghi, O. M. Metal Organic Frameworks with Exceptionally High Capacity for Storage of Carbon Dioxide at Room Temperature. *J. Am. Chem. Soc.* **2005,** *127*, 17998–17999.

(22) Dybtsev, D. N.; Chun, H.; Kim, K. Rigid and Flexible: A Highly Porous Metal-Organic Framework with Unusual Guest-Dependent Dynamic Behavior. *Angew. Chemie - Int. Ed.* **2004**, *43*, 5033–5036.

(23) Uemura, K.; Onishi, F.; Yamasaki, Y.; Kita, H. Syntheses, Crystal Structures, and Water Adsorption Behaviors of Jungle-Gym-Type Porous Coordination Polymers Containing Nitro Moieties. *J. Solid State Chem.* **2009**, *182*, 2852–2857.

(24) Zhao, Y.; Wu, H.; Emge, T. J.; Gong, Q.; Nijem, N.; Chabal, Y. J.; Kong, L.; Langreth, D. C.; Liu, H.; Zeng, H.; Li, J. Enhancing Gas Adsorption and Separation Capacity through Ligand Functionalization of Microporous Metal-Organic Framework Structures. *Chem. - A Eur. J.* **2011**, *17*, 5101–5109.

(25) Comotti, A.; Bracco, S.; Sozzani, P.; Horike, S.; Matsuda, R.; Chen, J.; Takata, M.; Kubota, Y.; Kitagawa, S. Nanochannels of Two Distinct Cross-Sections in a Porous Al-Based Coordination Polymer. *J. Am. Chem. Soc.* **2008**, *130*, 13664–13672.

(26) Paranthaman, S.; Coudert, F.-X.; Fuchs, A. H. Water Adsorption in Hydrophobic MOF Channels. *Phys. Chem. Chem. Phys.* **2010**, *12*, 8123–8129.

(27) Katz, M. J; Brown, Z. J; Colon, y. J; Siu, P. W; Scheidt, K. A; Snurr, R. Q; Hupp, J, T; Farha, O. K. A Facile Synthesis of UiO-66, UiO-67 and Their Derivatives. *Chem. Commun.* **2013**, *49*, 9449–9451.

(28) Zhang, X.; Hu, Q.; Xia, T.; Zhang, J.; Yang, Y.; Cui, Y.; Chen, B.; Qian, G. Turn-On and Ratiometric Luminescent Sensing of Hydrogen Sulfide Based on Metal-Organic Frameworks. *ACS Appl. Mater. Interfaces* **2016**, *8*, 32259–32265.

(29) Talu, O. Needs, Status, Techniques and Problems with Binary Gas Adsorption Experiments. *Adv. Colloid Interface Sci.* **1998**, *76–77*, 227–269.

(30) Liang, Z.; Marshall, M.; Chaffee, A. L. CO_2 Adsorption, Selectivity and Water Tolerance of Pillared-Layer Metal-Organic Frameworks. *Microporous and Mesoporous Mater.* **2010**, *132*, 305–310.

(31) Chowdhury, P.; Mekala, S.; Dreisbach, F.; Gumma, S. Adsorption of CO, CO_2 and CH_4 on Cu-BTC and MIL-101 Metal-organic Frameworks: Effect of Open Metal Sites and Adsorbate Polarity. *Microporous and Mesoporous Mater.* **2012**, *152*, 246–252.

(32) Caskey, S. R.; Wong-Foy, A. G.; Matzger, A. J. Dramatic Tuning of Carbon Dioxide Uptake via Metal Substitution in a Coordination Polymer with Cylindrical Pores. *J. Am. Chem. Soc.* **2008**, *130*, 10870–10871.

(33) Dietzel, P. D. C.; Besikiotis, V.; Blom, R. Application of Metal-Organic Frameworks with Coordinatively Unsaturated Metal Sites in Storage and Separation of Methane and Carbon dioxide. *J. Mater. Chem.* **2009**, *19*, 7362–7370.

(34) Mason, J. A.; Veenstrab, M.; Long, J. R. Evaluating Metal-Organic Frameworks for Natural Gas Storage. *Chem. Sci.* **2014**, *5*, 32–51.

(35) He, Y.; Zhou, W.; Yildirim, T.; Chen, B. A Series of Metal-Organic Frameworks with High Methane Uptake and an Empirical Equation for Predicting Methane Storage Capacity. *Energy Environ. Sci.* **2013**, *6*, 2735–2744.

(36) Rallapalli, P.; Prasanth, K. P.; Patil, D.; Somani, R. S.; Jasra, R. V.; Bajaj, H. C. Sorption Studies of CO_2, CH_4, N_2, CO, O_2 and Ar on Nanoporous Aluminum Terephthalate [MIL-53(Al)]. *J. Porous Mater*. **2011**, *18*, 205–210.

(37) Rolniak, P. D.; Kobayashi, R. Adsorption of Methane and Several Mixtures of Methane and Carbon Dioxide at Elevated Pressures and Near Ambient Temperatures on 5A and 13X Molecular Sieves by Tracer Pertubation Chromatography. *AIChE J.* **1980**, *26*, 616–625.

(38) Karra, J. R.; Walton, K. S. Molecular Simulations and Experimental Studies of CO_2, CO and N_2 Adsorption in Metal-Organic Frameworks. *J. Phys. Chem. C* **2010**, *114*, 15735–15740.

(39) Belmabkhout, Y.; Pirngruber, G.; Jolimaitre, E.; Methivier, A. A complete Experimental Approach for Synthesis Gas Separation Studies Using Static Gravimetric and Column Breakthrough Experiments. *Adsorption* **2007**, *13*, 341–349.

(40) Liang, Z.; Marshall, M.; Chaffee, A.L. CO_2 Adsorption-based Separation by Metal-Organic Framework (Cu-BTC) Versus Zeolite (13X). *Energy and Fuels* **2009**, *23*, 2785–2789.

(41) Mishra, P.; Mekala, S.; Dreisbach, F.; Mandal, B.; Gumma, S. Adsorption of CO_2, CO, CH_4 and N_2 on Zinc Based Metal-Organic Framework. *Sep. Purif. Technol*. **2012**, *94*,124–130.

(42) Llewellyn, P.L.; Bourrelly, S.; Serre, C.; Vimont, A.; Daturi, M.; Hamon, L.; Weireld, G.D.; Chang, J. S.; Hong, D. Y.; Hwang, Y.K.; Jhung, S.H.; Férey, G. High Uptakes of CO_2 and CH_4 in Mesoporous Metal-Organic Frameworks MIL-100 and MIL-101, *Langmuir* **2008**, *24*, 7245–7250.

(43) Mishra, P.; Edubilli, S.; Mandal, B.; Gumma, S. Adsorption Characteristics of Metal-Organic Frameworks Containing Co-ordinatively Unsaturated Metal Sites: Effect of Metal Cations and Adsorbate Properties. *J. Phys. Chem. C* **2014**, *118*, 6847–6855.

CHAPTER 8

Conclusions and Future Scope

This chapter summarizes the major inferences drawn from the research work presented in this dissertation and recommendations for further extension of this work in the future.

8.1 Conclusions

The main objective of this work was to systematically investigate the effect of the functionality on adsorption characteristics of selected MOFs. MOFs from various categories were chosen based on industrial applications that must possess low cast, high uptake capacity, be easily generable, stability in the presence of process conditions, and selectivity. Accordingly, Cu–abtc/Cu–hbtc MOFs are studied in the first part exhibits photo–chromatic nature, binding modes, and geometrical configuration of four carboxylic groups on the ligand increases the thermal stability and rigidity of the MOF. The next two parts study focuses on the effect of the functionality on adsorption characteristics of Cu–BTC and UiO–66 derivatives. Various industrially important gases (viz. CO_2, CO, CH_4, N_2, C_2H_6, C_3H_8, and O_2) were chosen to represent a wide range of polarity and polarizability. The adsorption measurements were correlated with the physical properties of gases. To get an insight into adsorption, isotherms were modeled to find Henry's constant and enthalpy of adsorption. The major accomplishments in this work were summarized in the following sections.

8.1.1 Affinity of functional group HN–NH in Cu–hbtc over N=N in Cu–abtc

The adsorption characteristics of Cu–abtc and Cu–hbtc were evaluated by measuring adsorption isotherms over selective industrially important gases covering a wide range of polarity and polarizability, *viz.* CO_2, CO, CH_4, N_2, C_2H_6, C_3H_8, and O_2. This work systematically demonstrated adsorption characteristics of Cu–abtc and Cu–hbtc to understand the affinity of functional group HN–NH presented in Cu–hbtc over N=N in Cu–abtc**.** In both compounds, significant accessible metal sites are present. Due to accessible metal sites present in the framework, CO loading increases progressively with pressure until sites are occupied by gas molecules (up to 2.5 mol kg^{-1} for Cu–hbtc and 2.0 mol kg^{-1} for Cu–abtc). After that, CH_4 showed preferentially more adsorption capacity due to more polarizability. To best our knowledge, the loading capacity of C_2H_6 and C_3H_8 on Cu–hbtc was 7.5 mol $kg^{-1}$and 8.7 mol kg^{-1}, respectively, is the highest loading capacity ever measured on MOFs 294 K and 1 bar. For all measured gases, Type–I isotherm were observed, and a modified Virial model was used for polar gasses (CO_2, CO), Langmuir model used for less–polar gasses (O_2, N_2, CH_4, C_2H_6, C_3H_8). Fitting parameters were utilized to calculate enthalpies of adsorption. An increase in adsorption enthalpy is observed with loading, attributed to lateral interactions. The CO_2 Selectivity over N_2 increases significantly with an increase in pressure. However, the CO_2 selectivity over N_2 for compound Cu–hbtc is more than compound Cu–abtc due to the strong affinity of functional group and framework adsorbate interactions.

8.1.2 A comparative study of gas adsorption on Cu-BTC versus Cu-(bromo)BTC versus Cu-(iodo)BTC

Cu–BTC is one of the most widely studied MOFs which is comprised of Cu^{2+} metal clusters coordinated to 1,3,5-benzenetricarboxylate (H_3BTC) organic linker. Although Cu–BTC has been well studied, limited work has been done to modify the H_3BTC ligand to functionalize Cu–BTC to optimize its properties for gas adsorption applications. This work evaluated adsorption characteristics of CO_2, CO, CH_4, and N_2 was carried out over a wide range of pressures and three different temperatures on Cu–BTC, Cu–(bromo)BTC, and Cu–(iodo)BTC. For all gases, Type–I isotherm were observed. CO_2 shown more adsorption capacity due to more polarity and polarizability, followed by CH_4, CO, and N_2 having low polarizability. However, CO showed more adsorption capacity at a lower pressure range than CH_4 due to the electrostatic interaction of CO and open metal sites presented in frameworks. After CO molecules occupy the open metal sites, dispersion effects dominate, and CH_4 shown more adsorption due to more polarizability. In addition, the enthalpy of adsorption for CO_2 and CH_4 shown highest for Cu–BTC followed by Cu–(iodo)BTC and Cu–(bromo)BTC, respectively. However, for CO and N_2, Cu–(iodo)BTC was shown highest, followed by Cu–BTC and Cu–(bromo)BTC. Therefore, in both cases, the enthalpy of adsorption is governed by the polarizability of bigger functional groups. In contrast, electrostatic interactions play an important role in CO. Selectivities of various binary mixtures is calculated using IAST. At 294 K, for Cu–BTC, 0.2 mole fraction of CO_2 selectivity over N_2 is significantly more than Cu–(bromo)BTC and Cu–(iodo)BTC and decreases with an increase in CO_2 mole fraction.

8.1.3 Effect of functionality (functional groups: –H, –NH_2, –NO_2, –COOH, –$(COOH)_2$) on adsorption characteristics of UiO–66 derivatives

This work demonstrated organic linker functionality of UiO–66 derivatives on adsorption characteristics of CO_2, CH_4, CO, and N_2. Through linker functionalization, introducing more polar and complex functional groups such as –NH_2, –NO_2, –COOH, and –$(COOH)_2$ can improve the adsorption capacity. It also reduces the free volume may negatively contribute to adsorption. In a low-pressure region, polar functional groups play a dominant role, whereas at saturation level reaches pore volume, and free space can be attributed to more adsorption. CO_2 adsorption at low pressure follows the order UiO–66–$(COOH)_2$>UiO–66–COOH>UiO–66–NO_2>UiO–66–NH_2>UiO–66 with adsorption enthalpies varies ranging between 5.5 to 26.0 kJ mol^{-1}. The selectivity of CO_2 over CH_4, CO, and N_2 showing that introducing larger and complex functional groups means a sudden decrease in selectivity with an increase in temperature; such difference is more at lower temperatures and could be negligible at higher temperatures. Therefore, MOFs should be designed in such a way as to increase the adsorption capacity by introducing complex polar functional groups at lower pressure, and such influence may disappear as pressure increases.

8.2 Recommendation for Future Works

This work presents a systematic and detailed investigation to understand the adsorption characteristics of different categories of MOFs. There are undoubtedly several areas that merit further research attention.

- Although Cu–abtc and Cu–hbtc MOFs showed good uptake capacities for lower alkanes, these MOFs are susceptible to humid and oxygen environments. It would be interesting to improve the stability by subtle changes in organic ligand or with zirconium metalation.
- Cu–BTC MOF having the disadvantage of being hydrophilicity while exposed to moisture. Either functionalization or multivariate metal synthesis can improve the stability of MOF.
- In UiO–66, known for moisture stable and thermally stable up to 800 K. By introducing complex functional groups improved the adsorption capacity at low-pressure region. However, it resulted reduction of free volume, and decrease in adsorption capacity was observed at higher pressure. So to get optimal uptake capacity and selectivity, functional groups has to be chosen accordingly.

APPENDIX: A

Detail of the MOF activation procedure followed for adsorption measurements

Table A. Details of activation temperature and time used for different MOFs.

MOF	Temperature (K)	Activation Time (hours)
Cu–abtc	443	3
Cu–hbtc	443	3
Cu–BTC	443	3
Cu–(bromo)BTC	443	3
Cu–(iodo)BTC	443	3
UiO–66	423	3
UiO–66–NH_2	423	3
UiO–66–NO_2	423	3
UiO–66–COOH	423	3
UiO–66–$(COOH)_2$	423	3

APPENDIX:B

Excess Adsorption Isotherm Data on Studied MOFs

Table B1. Adsorption isotherm data of CO_2 on Cu–abtc and Cu–hbtc.

MOF	Gas	At 294 K		At 317 K		At 356 K	
		P (bar)	Amount adsorbed, N (mol kg^{-1})	P (bar)	Amount adsorbed, N (mol kg^{-1})	P (bar)	Amount adsorbed, N (mol kg^{-1})
Cu–abtc	CO_2	0.00	0.00	0.00	0.00	0.00	0.00
		0.15	0.45	0.14	0.21	0.48	0.30
		0.21	0.63	0.20	0.31	0.79	0.49
		0.44	1.24	0.43	0.63	1.02	0.62
		0.71	1.88	0.69	0.99	2.14	1.24
		1.17	2.93	1.02	1.41	4.08	2.19
		2.01	4.45	2.04	2.59	7.88	3.71
		3.97	6.95	4.01	4.38	11.78	4.86
		7.70	9.06	7.79	6.43	15.49	5.65
		11.25	9.99	11.54	7.55	19.13	6.20
		14.78	10.55	15.12	8.23	24.77	6.91
		18.05	10.88	18.57	8.68	28.52	7.44
		22.73	11.40	23.49	9.10	32.95	7.95
		26.40	11.77	27.31	9.39		
		29.95	12.03	31.23	9.72		
Cu–hbtc	CO_2	0.00	0.00	0.00	0.00	0.00	0.00
		0.04	0.18	0.15	0.31	0.41	0.35
		0.07	0.30	0.21	0.44	0.71	0.60
		0.15	0.61	0.43	0.86	1.00	0.83
		0.21	0.87	0.70	1.37	2.01	1.62
		0.41	1.64	1.01	1.96	4.02	3.05
		0.67	2.58	2.03	3.60	7.80	5.16
		1.02	3.69	3.94	5.90	11.62	6.66
		1.99	6.03	7.68	8.62	15.34	7.71
		3.92	8.91	11.53	10.06	18.93	8.46
		7.76	11.33	15.09	10.82	24.05	9.21
		11.31	12.23	18.54	11.33	28.66	9.73
		14.79	12.70	23.31	11.77	32.74	10.37
		18.07	12.97	27.68	12.20		
		22.54	13.21	31.39	12.55		
		26.55	13.64				
		29.95	13.81				

Table B2. Adsorption isotherm data of CO on Cu–abtc and Cu–hbtc

MOF	Gas	At 294 K		At 317 K		At 356 K	
		P (bar)	Amount adsorbed, N (mol kg^{-1})	P (bar)	Amount adsorbed, N (mol kg^{-1})	P (bar)	Amount adsorbed, N (mol kg^{-1})
Cu–abtc	CO	0.00	0.00	0.00	0.00	0.00	0.00
		0.40	0.26	0.39	0.16	0.43	0.10
		0.68	0.39	0.69	0.25	0.68	0.14
		1.01	0.54	1.02	0.33	1.02	0.19
		2.05	0.94	2.09	0.59	2.02	0.34
		4.01	1.57	4.07	1.02	4.06	0.61
		8.02	2.49	8.09	1.73	8.11	1.10
		11.91	3.16	12.08	2.30	12.06	1.51
		15.93	3.70	16.07	2.75	16.03	1.89
		19.86	4.14	20.03	3.13	20.09	2.21
		25.65	4.65	25.97	3.59	26.02	2.62
		36.06	5.36	36.56	4.26	36.81	3.23
		50.76	6.02	51.32	4.89	51.90	3.88
		69.71	6.57	71.20	5.40	72.53	4.61
Cu–hbtc	CO	0.00	0.00	0.00	0.00	0.00	0.00
		0.41	0.53	0.42	0.32	0.44	0.17
		0.73	0.80	0.68	0.44	0.71	0.22
		1.00	1.02	1.12	0.65	1.03	0.30
		2.03	1.62	2.05	1.03	2.06	0.52
		4.15	2.52	4.06	1.69	4.04	0.91
		8.14	3.63	8.08	2.64	8.03	1.56
		12.09	4.40	12.13	3.36	12.06	2.11
		15.98	4.99	16.07	3.92	15.67	2.57
		19.91	5.43	19.97	4.37	20.14	2.99
		25.49	5.98	25.73	4.91	25.76	3.44
		36.20	6.74	36.35	5.67	36.60	4.18
		50.20	7.35	50.98	6.36	49.22	4.84
		65.20	7.76	66.66	6.90	67.82	5.75

Table B3. Adsorption isotherm data of N_2 on Cu–abtc and Cu–hbtc

MOF	Gas	At 294 K		At 317 K		At 356 K	
		P (bar)	Amount adsorbed, N (mol kg^{-1})	P (bar)	Amount adsorbed, N (mol kg^{-1})	P (bar)	Amount adsorbed, N (mol kg^{-1})
Cu–abtc	N_2	0.00	0.00	0.00	0.00	0.00	0.00
		0.69	0.18	0.66	0.12	0.68	0.11
		1.02	0.27	1.02	0.18	1.01	0.15
		2.05	0.53	2.07	0.35	2.04	0.25
		4.06	0.99	4.11	0.68	4.06	0.47
		8.05	1.76	8.08	1.24	8.10	0.86
		12.04	2.38	12.08	1.73	12.10	1.18
		15.98	2.89	16.03	2.15	16.13	1.49
		19.95	3.32	19.93	2.50	20.09	1.76
		25.88	3.84	25.67	2.96	26.05	2.16
		36.10	4.54	35.76	3.60	36.60	2.73
		51.53	5.21	51.87	4.33	52.64	3.25
		71.22	5.75	72.57	4.85	73.51	3.95
		101.23	6.28	103.47	5.59	105.84	4.85
Cu–hbtc	N_2	0.00	0.00	0.00	0.00	0.00	0.00
		0.68	0.16	0.77	0.14	0.68	0.09
		1.04	0.24	1.07	0.19	1.02	0.13
		2.04	0.48	2.08	0.35	2.03	0.23
		4.05	0.92	4.08	0.66	4.08	0.43
		8.02	1.69	7.99	1.22	8.08	0.80
		12.04	2.35	12.12	1.73	12.06	1.15
		16.00	2.90	15.95	2.16	16.10	1.47
		19.65	3.34	19.89	2.56	20.15	1.74
		25.46	3.92	25.36	3.04	25.81	2.15
		35.88	4.78	36.62	3.85	36.68	2.78
		50.83	5.57	51.46	4.56	52.29	3.38
		69.82	6.19	70.10	5.20	72.43	4.30
		97.94	6.75	99.42	6.03	103.74	5.15

Table B4. Adsorption isotherm data of CH_4 on Cu–abtc and Cu–hbtc

MOF	Gas	At 294 K		At 317 K		At 356 K	
		P (bar)	Amount adsorbed, N (mol kg^{-1})	P (bar)	Amount adsorbed, N (mol kg^{-1})	P (bar)	Amount adsorbed, N (mol kg^{-1})
Cu–abtc	CH_4	0.00	0.00	0.00	0.00	0.00	0.00
		0.42	0.38	0.41	0.22	0.68	0.22
		0.73	0.64	0.68	0.37	1.03	0.31
		1.03	0.90	1.02	0.52	2.11	0.60
		2.09	1.64	2.04	1.01	4.08	1.07
		4.00	2.72	4.08	1.82	8.24	1.92
		8.00	4.23	7.98	3.00	11.87	2.52
		11.74	5.12	11.87	3.83	15.96	3.10
		15.60	5.78	15.64	4.43	19.70	3.51
		19.35	6.23	19.51	4.90	25.54	4.05
		24.81	6.72	24.93	5.42	35.14	4.64
		33.96	7.27	34.46	6.07	49.60	5.31
		47.10	7.74	48.29	6.67	67.84	5.93
		62.85	8.15	65.47	7.20	84.79	6.71
		76.85	8.73	80.29	7.72		
Cu–hbtc	CH_4	0.00	0.00	0.00	0.00	0.00	0.00
		0.22	0.16	2.04	1.06	1.05	0.31
		0.42	0.29	4.18	1.89	2.02	0.54
		0.69	0.49	8.07	3.17	4.02	1.00
		1.03	0.72	12.06	4.19	7.92	1.83
		2.03	1.37	15.60	4.91	11.84	2.56
		4.01	2.53	19.31	5.52	15.74	3.19
		7.88	4.26	22.70	6.00	19.61	3.71
		11.80	5.50	34.28	7.11	25.30	4.37
		15.56	6.34	47.02	7.74	35.15	5.23
		19.27	6.95	64.85	8.46	48.38	6.04
		24.57	7.59	76.47	8.94	66.62	6.78
		34.02	8.41			81.75	7.62
		46.74	9.01				
		62.08	9.44				
		76.00	9.89				

Table B5. Adsorption isotherm data of C_2H_6 on Cu–abtc and Cu–hbtc

MOF	Gas	At 294 K		At 317 K		At 356 K	
		P (bar)	Amount adsorbed, N (mol kg^{-1})	P (bar)	Amount adsorbed, N (mol kg^{-1})	P (bar)	Amount adsorbed, N (mol kg^{-1})
Cu–abtc	C_2H_6	0.00	0.00	0.00	0.00	0.00	0.00
		0.05	0.47	0.08	0.35	0.22	0.41
		0.08	0.70	0.15	0.64	0.42	0.78
		0.14	1.29	0.22	0.96	0.69	1.28
		0.23	2.10	0.42	1.87	1.02	1.86
		0.41	3.66	0.68	2.94	2.00	3.28
		0.70	5.24	1.02	4.05	3.95	4.94
		1.04	6.22	1.99	5.80	7.73	6.32
		2.01	7.43	3.93	7.06	11.46	6.87
		3.92	8.28	7.69	7.93	14.85	7.14
		7.55	8.87	11.20	8.28	18.95	7.43
		10.96	9.14	14.53	8.47		
		14.17	9.27	18.00	8.62		
		17.61	9.34				
Cu–hbtc	C_2H_6	0.00	0.00	0.00	0.00	0.00	0.00
		0.05	0.43	0.05	0.25	0.15	0.35
		0.09	0.92	0.08	0.43	0.21	0.48
		0.15	1.60	0.16	0.80	0.42	0.93
		0.22	2.36	0.23	1.13	0.69	1.49
		0.40	4.20	0.41	2.01	1.01	2.14
		0.68	6.20	0.68	3.29	2.01	3.93
		1.03	7.51	1.00	4.64	3.92	6.04
		2.05	9.06	1.99	6.90	7.77	7.79
		4.03	10.02	3.96	8.52	11.49	8.56
		7.68	10.71	7.71	9.57	15.00	8.96
		11.10	10.99	11.30	10.03	18.42	9.24
		14.24	11.11	14.63	10.29		
		17.20	11.27	17.83	10.44		

Table B6. Adsorption isotherm data of C_3H_8 on Cu–abtc and Cu–hbtc

MOF	Gas	At 294 K		At 317 K		At 356 K	
		P (bar)	Amount adsorbed, N (mol kg^{-1})	P (bar)	Amount adsorbed, N (mol kg^{-1})	P (bar)	Amount adsorbed, N (mol kg^{-1})
Cu–abtc	C_3H_8	0.00	0.00	0.00	0.00	0.00	0.00
		0.04	3.37	0.04	1.23	0.04	0.33
		0.07	5.22	0.07	2.52	0.08	0.67
		0.14	6.03	0.14	4.17	0.14	1.30
		0.23	6.43	0.22	5.15	0.21	1.94
		0.42	6.80	0.43	5.91	0.40	3.47
		0.69	7.04	0.70	6.32	0.67	4.60
		1.02	7.21	1.02	6.56	1.02	5.23
		1.97	7.43	1.99	6.89	1.99	5.93
		3.79	7.61	3.83	7.15	3.88	6.41
		6.18	7.70	6.34	7.30	6.52	6.95
Cu–hbtc	C_3H_8	0.00	0.00	0.00	0.00	0.00	0.00
		0.04	4.75	0.04	1.48	0.05	0.56
		0.07	6.48	0.07	3.04	0.09	0.97
		0.17	7.62	0.13	5.31	0.15	1.66
		0.23	7.86	0.22	6.64	0.22	2.49
		0.41	8.29	0.43	7.45	0.40	4.29
		0.68	8.55	0.70	7.79	0.69	5.73
		1.00	8.73	1.01	8.03	1.03	6.46
		1.96	8.99	2.00	8.40	2.01	7.28
		3.78	9.20	3.86	8.68	3.94	7.83
		6.20	9.29	6.37	8.84	6.54	8.14

Table B7. Adsorption isotherm data of O_2 on Cu–abtc and Cu–hbtc

MOF	Gas	At 294 K		At 317 K		At 356 K	
		P (bar)	Amount adsorbed, N (mol kg^{-1})	P (bar)	Amount adsorbed, N (mol kg^{-1})	P (bar)	Amount adsorbed, N (mol kg^{-1})
Cu–abtc	O_2	0.00	0.00	0.00	0.00	0.00	0.00
		1.13	0.22	1.00	0.15	8.05	0.96
		2.10	0.40	1.98	0.30	12.07	1.32
		4.06	0.77	4.03	0.59	16.00	1.64
		8.08	1.47	7.97	1.11	20.11	1.95
		11.98	2.08	11.98	1.60	25.91	2.44
		15.92	2.64	15.82	2.03	36.58	3.19
		19.83	3.15	19.50	2.43		
		25.53	3.80	25.80	3.05		
		36.00	5.09	36.17	4.14		
Cu–hbtc	O_2	0.00	0.00	0.00	0.00	0.00	0.00
		1.00	0.24	1.03	0.20	1.04	0.20
		2.03	0.49	2.03	0.38	2.05	0.31
		4.08	0.96	4.11	0.73	4.14	0.54
		8.09	1.83	8.08	1.37	8.09	0.96
		11.94	2.58	12.03	1.98	12.11	1.37
		15.93	3.30	15.99	2.52	16.04	1.76
		19.77	3.90	20.23	3.07	20.01	2.12
		25.66	4.70	25.80	3.72	26.04	2.64
		35.79	5.83	36.03	4.78	36.30	3.58

Table B8. Adsorption isotherm data of CO_2 on Cu–BTC derivatives

MOF	Gas	At 294 K		At 317 K		At 356 K	
		P (bar)	Amount adsorbed, N (mol kg^{-1})	P (bar)	Amount adsorbed, N (mol kg^{-1})	P (bar)	Amount adsorbed, N (mol kg^{-1})
Cu–BTC	CO_2	0.00	0.00	0.00	0.00	0.00	0.00
		0.05	0.35	0.05	0.18	0.06	0.08
		0.12	0.87	0.13	0.47	0.14	0.19
		0.47	3.10	0.52	1.73	0.67	0.89
		0.74	4.63	1.07	3.39	1.07	1.39
		0.91	5.20	1.56	4.66	1.58	2.02
		1.67	7.91	2.20	6.11	2.24	2.77
		2.23	9.37	2.87	7.32	2.98	3.55
		2.89	10.55	5.01	9.96	5.19	5.38
		5.13	12.84	10.19	12.81	10.35	8.31
		10.09	14.58	16.17	14.03	16.55	10.17
		15.81	15.29	22.51	14.11	20.68	10.99
		22.99	15.60	30.86	14.35	24.59	11.40
		30.00	15.41			32.77	12.04
Cu–(bromo)BTC	CO_2	0.00	0.00	0.00	0.00	0.00	0.00
		0.15	0.97	0.16	0.52	0.16	0.22
		0.21	1.31	0.23	0.69	0.22	0.30
		0.41	2.26	0.41	1.14	0.43	0.55
		0.70	3.31	0.68	1.73	0.68	0.82
		1.00	4.15	1.01	2.37	1.04	1.17
		2.01	6.04	2.03	3.88	2.04	2.05
		3.96	7.79	3.98	5.75	4.03	3.35
		7.74	9.11	7.80	7.57	7.90	5.25
		11.32	9.66	11.48	8.40	11.66	6.33
		14.73	9.98	15.03	8.93	15.29	7.05
		18.03	10.21	18.46	9.30	19.03	7.72
		21.67	10.41	22.30	9.65	23.10	8.09
Cu–(iodo)BTC	CO_2	0.00	0.00	0.00	0.00	0.00	0.00
		0.10	0.79	1.02	4.10	0.40	0.60
		0.14	1.01	2.03	5.70	0.75	0.97
		0.21	1.45	4.01	7.71	1.02	1.30
		0.41	2.53	7.85	9.66	2.04	2.28
		0.66	3.67	11.54	10.63	4.02	3.83
		1.00	4.88	15.12	11.20	7.86	6.01
		2.01	7.23	18.47	11.64	11.75	7.51
		3.94	9.43	23.01	12.16	15.43	8.39
		7.72	11.05	27.43	12.78	19.05	9.14
		11.35	11.75			24.21	10.03
		14.79	12.17			28.58	10.86
		18.06	12.45				
		22.68	12.79				
		26.35	13.17				

Table B9. Adsorption isotherm data of CO on Cu–BTC derivatives

MOF	Gas	At 294 K		At 317 K		At 356 K	
		P (bar)	Amount adsorbed, N (mol kg^{-1})	P (bar)	Amount adsorbed, N (mol kg^{-1})	P (bar)	Amount adsorbed, N (mol kg^{-1})
Cu–BTC	CO	0.00	0.00	0.00	0.00	0.00	0.00
		0.05	0.09	0.07	0.07	0.60	0.23
		0.12	0.21	0.13	0.12	1.08	0.39
		0.52	0.81	0.55	0.47	1.66	0.58
		1.04	1.43	1.06	0.84	2.45	0.82
		1.59	1.97	1.62	1.18	2.93	0.95
		2.26	2.51	2.27	1.58	5.37	1.54
		2.92	2.96	2.91	1.91	10.67	2.60
		5.28	4.15	5.32	2.93	17.35	3.56
		10.61	5.84	10.63	4.46	26.41	4.49
		17.22	6.81	17.28	5.67	43.12	5.63
		26.01	7.82	26.35	6.73	72.09	6.65
		42.50	9.10	41.68	7.70		
		69.30	9.75	69.79	8.53		
Cu–(bromo)BTC	CO	0.00	0.00	0.00	0.00	0.00	0.00
		0.15	0.28	0.15	0.23	0.14	0.19
		0.21	0.36	0.22	0.27	0.21	0.24
		0.41	0.59	0.43	0.41	0.42	0.35
		0.69	0.83	0.69	0.55	0.68	0.45
		1.02	1.09	1.05	0.72	1.03	0.54
		2.03	1.68	2.02	1.12	2.04	0.77
		4.03	2.48	4.07	1.76	4.04	1.17
		8.00	3.50	8.08	2.63	8.05	1.84
		12.04	4.13	12.04	3.26	12.12	2.36
		16.03	4.61	16.05	3.77	16.10	2.88
		20.01	5.01	19.94	4.18	20.11	3.23
		24.47	5.32	24.54	4.58	24.68	3.56
		32.75	5.82	32.63	5.12	32.89	4.20
		43.94	6.37	43.72	5.80	45.21	4.77
Cu–(iodo)BTC	CO	0.00	0.00	0.00	0.00	0.00	0.00
		0.04	0.83	0.08	0.18	0.03	0.06
		0.07	0.89	0.15	0.24	0.09	0.10
		0.15	0.98	0.20	0.28	0.15	0.13
		0.22	1.06	0.41	0.40	0.24	0.16
		0.43	1.27	0.71	0.57	0.42	0.21
		0.71	1.51	1.05	0.74	0.67	0.28
		1.05	1.77	2.00	1.15	1.06	0.37
		2.08	2.38	4.01	1.83	2.00	0.58
		4.11	3.21	8.02	2.77	4.07	0.99
		8.08	4.22	12.00	3.43	8.02	1.61
		12.06	4.90	15.91	3.94	12.04	2.10
		16.01	5.40	19.99	4.38	16.10	2.52
		19.96	5.78	25.84	4.85	20.07	2.91
		25.47	6.17	36.34	5.51	25.93	3.34
		35.78	6.74	51.53	6.12	36.52	3.96
		50.83	7.26	71.55	6.67	52.04	4.65
		70.19	7.68			72.53	5.28

Table B10. Adsorption isotherm data of CH_4 on Cu–BTC derivatives

MOF	Gas	At 294 K		At 317 K		At 356 K	
		P (bar)	Amount adsorbed, N (mol kg^{-1})	P (bar)	Amount adsorbed, N (mol kg^{-1})	P (bar)	Amount adsorbed, N (mol kg^{-1})
Cu–BTC	CH_4	0.00	0.00	0.00	0.00	0.00	0.00
		0.54	0.59	0.53	0.38	0.55	0.21
		1.06	1.07	1.06	0.72	1.07	0.39
		1.59	1.52	1.59	1.02	1.66	0.59
		2.25	2.02	2.26	1.39	2.27	0.79
		2.91	2.50	2.90	1.71	2.94	0.99
		5.28	4.04	5.24	2.77	5.35	1.62
		10.43	6.53	10.32	4.68	10.58	2.81
		16.66	8.10	16.47	6.35	17.08	3.97
		25.02	9.44	24.42	7.48	25.75	5.14
		39.78	10.38	38.02	8.79	41.53	6.53
		62.63	10.79	58.71	9.58	67.21	7.60
		83.06	11.04	76.67	9.86	92.11	8.04
Cu–(bromo)BTC	CH_4	0.00	0.00	0.00	0.00	0.00	0.00
		0.74	0.63	0.70	0.54	0.74	0.45
		1.01	0.84	1.03	0.69	1.01	0.51
		2.05	1.46	2.03	1.11	2.09	0.79
		4.07	2.43	4.09	1.81	4.04	1.21
		7.89	3.76	7.99	2.84	7.98	1.95
		11.77	4.71	11.87	3.74	12.00	2.60
		15.57	5.39	15.76	4.33	15.92	3.13
		19.36	5.90	19.45	4.82	19.82	3.62
		24.83	6.53	23.84	5.35	24.24	4.16
		30.53	6.96	30.92	6.24	31.94	4.97
		44.42	7.52	45.54	6.93	45.24	5.98
		59.93	7.98	61.71	7.12	59.67	6.50
		71.96	8.28	75.96	7.41	73.99	6.68
Cu–(iodo)BTC	CH_4	0.00	0.00	0.00	0.00	0.00	0.00
		0.20	0.20	1.03	0.82	0.44	0.21
		0.45	0.42	2.02	1.23	0.73	0.29
		0.68	0.61	4.09	1.95	1.00	0.37
		1.03	0.85	7.99	3.04	2.05	0.64
		2.03	1.46	11.83	3.88	4.04	1.11
		4.00	2.46	15.68	4.55	8.02	1.88
		7.93	3.95	19.49	5.06	11.93	2.50
		11.75	5.00	24.52	5.60	15.81	3.00
		15.56	5.72	34.46	6.41	19.65	3.46
		19.29	6.20	48.23	7.09	25.38	4.01
		24.68	6.75	65.59	7.67	35.21	4.78
		33.96	7.40			49.73	5.56
		47.27	7.92			68.29	6.08
		63.23	8.48				

Table B11. Adsorption isotherm data of N_2 on Cu–BTC derivatives

MOF	Gas	At 294 K		At 317 K		At 356 K	
		P (bar)	Amount adsorbed, N (mol kg^{-1})	P (bar)	Amount adsorbed, N (mol kg^{-1})	P (bar)	Amount adsorbed, N (mol kg^{-1})
Cu–BTC	N_2	0.00	0.00	0.00	0.00	0.00	0.00
		1.24	0.18	1.91	0.21	1.91	0.18
		1.96	0.27	2.64	0.27	2.64	0.25
		1.98	0.27	3.57	0.35	3.57	0.32
		2.65	0.36	3.63	0.36	3.63	0.34
		3.38	0.44	4.44	0.42	4.44	0.41
		3.97	0.50	4.63	0.44	4.63	0.43
		4.51	0.56	5.69	0.52	5.69	0.52
		5.05	0.61	6.40	0.58	6.40	0.58
		5.81	0.69	7.79	0.67	7.79	0.67
		6.52	0.75	8.36	0.70	8.36	0.70
		7.10	0.80	8.38	0.71	8.38	0.71
		7.82	0.86	9.56	0.79	9.56	0.79
		8.02	0.88				
		8.14	0.89				
		8.57	0.92				
		9.59	1.00				
Cu–(bromo)BTC	N_2	0.00	0.00	0.00	0.00	0.00	0.00
		0.70	0.23	0.69	0.18	0.70	0.14
		1.01	0.30	1.01	0.24	1.03	0.20
		2.03	0.55	2.07	0.43	2.04	0.37
		4.06	1.01	4.07	0.74	4.04	0.58
		8.04	1.66	8.06	1.29	8.10	1.02
		12.06	2.27	12.09	1.75	12.11	1.40
		16.07	2.73	16.04	2.16	16.08	1.71
		20.72	3.25	19.98	2.53	20.61	2.09
		25.69	3.83	25.31	3.07	25.48	2.53
		34.39	4.51	34.17	3.66	34.48	3.15
		49.56	5.35	50.07	4.66	50.73	4.16
		69.47	6.09	70.21	5.49	71.08	5.11
Cu–(iodo)BTC	N_2	0.00	0.00	0.00	0.00	0.00	0.00
		1.02	0.25	1.02	0.22	1.03	0.14
		2.02	0.46	2.04	0.37	2.02	0.22
		4.03	0.82	4.10	0.62	4.03	0.38
		8.03	1.36	8.11	1.03	8.05	0.66
		12.02	1.77	12.09	1.37	12.10	0.92
		15.99	2.11	16.04	1.65	16.11	1.12
		19.95	2.39	20.03	1.91	20.12	1.32
		25.83	2.72	25.99	2.22	26.12	1.55
		36.10	3.22	36.26	2.67	36.60	1.92
		51.46	3.68	51.59	3.13	52.43	2.41
		71.01	4.13	71.93	3.63	73.07	2.75

Table B12. Adsorption isotherm data of CO_2 on UiO–66 derivatives

MOF	Gas	At 294 K		At 317 K		At 356 K	
		P (bar)	Amount adsorbed, N (mol kg^{-1})	P (bar)	Amount adsorbed, N (mol kg^{-1})	P (bar)	Amount adsorbed, N (mol kg^{-1})
UiO–66	CO_2	0.00	0.00	0.00	0.00	0.00	0.00
		0.24	0.43	0.24	0.27	0.43	0.29
		0.44	0.70	0.43	0.43	0.72	0.39
		0.72	1.05	0.71	0.65	1.04	0.50
		1.05	1.42	1.04	0.87	2.05	0.83
		2.04	2.34	2.04	1.47	4.03	1.38
		3.97	3.73	4.02	2.44	7.90	2.31
		7.70	5.76	7.80	3.91	11.63	3.09
		11.30	7.31	11.47	5.06	15.37	3.75
		14.74	8.44	15.01	6.02	19.22	4.38
		18.12	9.30	18.50	6.85	24.26	5.22
		22.70	10.40	23.44	7.89		
UiO–66–NH_2	CO_2	0.00	0.00	0.00	0.00	0.00	0.00
		0.05	0.17	0.05	0.09	0.06	0.04
		0.10	0.30	0.09	0.14	0.11	0.07
		0.16	0.46	0.17	0.24	0.18	0.11
		0.24	0.63	0.25	0.34	0.25	0.15
		0.44	1.01	0.47	0.58	0.45	0.25
		0.72	1.43	0.73	0.83	0.73	0.39
		1.04	1.83	1.03	1.09	1.03	0.53
		2.02	2.79	2.04	1.77	2.08	0.93
		3.97	4.11	4.00	2.76	4.10	1.56
		7.71	5.81	7.83	4.11	7.90	2.47
		11.30	6.91	11.50	5.08	11.71	3.19
		14.76	7.60	15.02	5.78	15.40	3.76
		18.08	8.05	18.50	6.33	19.03	4.25
		26.50	8.60	26.23	7.40	26.10	5.01
UiO–66–NO_2	CO_2	0.00	0.00	0.00	0.00	0.00	0.00
		0.06	0.17	0.06	0.08	0.23	0.11
		0.10	0.25	0.12	0.15	0.44	0.18
		0.19	0.40	0.18	0.20	0.73	0.27
		0.26	0.49	0.25	0.26	1.03	0.35
		0.47	0.72	0.44	0.40	2.05	0.59
		0.74	0.95	0.71	0.56	4.02	0.91
		1.02	1.14	1.09	0.73	7.92	1.37
		2.00	1.60	2.04	1.07	11.71	1.69
		4.00	2.20	4.01	1.55	15.46	1.94
		7.76	2.86	7.79	2.13	19.08	2.15
		11.34	3.23	11.51	2.52	24.21	2.40
		14.76	3.48	15.06	2.79		
		18.08	3.65	18.51	2.99		
		22.63	3.86	23.38	3.22		

Contd. (Adsorption isotherm data of CO_2 on UiO–66 derivatives)

MOF	Gas	At 294 K		At 317 K		At 356 K	
		P (bar)	Amount adsorbed, N (mol kg^{-1})	P (bar)	Amount adsorbed, N (mol kg^{-1})	P (bar)	Amount adsorbed, N (mol kg^{-1})
UiO–66–COOH	CO_2	0.00	0.00	0.00	0.00	0.00	0.00
		0.04	0.22	0.04	0.19	0.04	0.17
		0.09	0.31	0.09	0.28	0.09	0.25
		0.16	0.52	0.16	0.49	0.16	0.42
		0.24	0.72	0.24	0.69	0.24	0.56
		0.44	1.17	0.44	1.01	0.44	0.82
		0.73	1.61	0.73	1.34	0.73	1.13
		1.02	1.90	1.03	1.62	1.02	1.42
		2.05	2.70	2.05	2.33	2.05	2.13
		3.97	3.59	3.97	3.25	3.97	2.84
		7.71	4.76	7.71	4.21	7.71	3.72
		11.31	5.39	11.31	4.78	11.31	4.25
		14.76	5.73	14.76	5.10	14.76	4.61
		18.06	6.00	18.06	5.29	18.06	4.80
		22.01	6.18	22.01	5.51	22.01	5.01
UiO–66–$(COOH)_2$	CO_2	0.00	0.00	0.00	0.00	0.00	0.00
		0.05	0.22	0.06	0.12	0.05	0.04
		0.09	0.35	0.10	0.19	0.09	0.07
		0.17	0.61	0.17	0.30	0.16	0.11
		0.25	0.81	0.26	0.44	0.23	0.15
		0.45	1.20	0.42	0.64	0.48	0.29
		0.71	1.57	0.73	0.97	0.75	0.43
		1.02	1.90	1.05	1.22	1.04	0.55
		2.00	2.60	2.06	1.81	2.10	0.95
		4.03	3.43	4.01	2.51	4.09	1.47
		7.77	4.26	7.84	3.32	7.96	2.14
		11.32	4.73	11.50	3.81	11.68	2.59
		14.77	5.03	15.04	4.15	15.43	2.92
		18.03	5.25	18.51	4.40	18.93	3.17
		22.62	5.48	23.50	4.68	24.07	3.49

Table B13. Adsorption isotherm data of CO on UiO–66 derivatives

MOF	Gas	At 294 K		At 317 K		At 356 K	
		P (bar)	Amount adsorbed, N (mol kg^{-1})	P (bar)	Amount adsorbed, N (mol kg^{-1})	P (bar)	Amount adsorbed, N (mol kg^{-1})
UiO–66	CO	0.00	0.00	0.00	0.00	0.00	0.00
		0.44	0.07	1.05	0.13	1.05	0.09
		0.72	0.12	2.07	0.25	2.05	0.16
		1.02	0.17	4.06	0.45	4.09	0.28
		2.03	0.33	8.06	0.80	8.12	0.51
		4.05	0.62	12.05	1.10	12.13	0.72
		8.04	1.08	16.00	1.38	16.06	0.91
		12.00	1.46	19.95	1.62	20.11	1.08
		16.07	1.80	25.87	1.91	26.10	1.31
		19.79	2.06	37.43	2.39	37.65	1.67
		25.72	2.42				
		32.78	2.77				
		37.87	2.99				
UiO–66–NH_2	CO	0.00	0.00	0.00	0.00	0.00	0.00
		0.24	0.05	0.26	0.04	0.72	0.07
		0.43	0.09	0.44	0.06	1.11	0.10
		1.05	0.22	0.72	0.10	2.05	0.17
		2.03	0.40	1.05	0.14	4.09	0.30
		4.09	0.72	2.07	0.27	8.12	0.54
		8.04	1.19	4.18	0.50	12.09	0.74
		12.07	1.57	8.12	0.85	16.11	0.93
		15.94	1.87	12.11	1.15	20.14	1.09
		20.06	2.14	16.06	1.40	26.06	1.31
		25.75	2.45	20.01	1.61	34.14	1.56
		34.80	2.83	25.89	1.89		
UiO–66–NO_2	CO	0.00	0.00	0.00	0.00	0.00	0.00
		0.45	0.07	1.02	0.12	1.02	0.08
		0.72	0.10	2.08	0.21	2.06	0.13
		1.03	0.15	4.09	0.37	4.07	0.23
		2.07	0.28	8.06	0.61	8.19	0.41
		4.10	0.49	12.06	0.82	12.06	0.56
		8.10	0.82	16.05	0.99	16.09	0.68
		12.06	1.06	20.05	1.14	20.10	0.80
		15.95	1.26	25.91	1.33	26.00	0.94
		19.87	1.43	33.35	1.51	39.20	1.30
		25.72	1.64	39.34	1.65		
		39.69	2.00				

Contd. (Adsorption isotherm data of CO on UiO–66 derivatives)

MOF	Gas	At 294 K		At 317 K		At 356 K	
		P (bar)	Amount adsorbed, N (mol kg^{-1})	P (bar)	Amount adsorbed, N (mol kg^{-1})	P (bar)	Amount adsorbed, N (mol kg^{-1})
UiO–66–COOH	CO	0.00	0.00	0.00	0.00	0.00	0.00
		0.72	0.15	0.72	0.13	0.72	0.11
		1.08	0.22	1.08	0.20	1.08	0.16
		2.05	0.39	2.05	0.36	2.05	0.28
		4.07	0.69	4.07	0.62	4.07	0.51
		8.08	1.14	8.08	1.00	8.08	0.87
		12.05	1.45	12.05	1.25	12.05	1.10
		15.98	1.71	15.98	1.46	15.98	1.29
		19.93	1.90	19.93	1.62	19.93	1.45
		25.79	2.13	25.79	1.85	25.79	1.60
		33.67	2.39	33.67	2.10	33.67	1.81
UiO–66–$(COOH)_2$	CO	0.00	0.00	0.00	0.00	0.00	0.00
		0.24	0.05	0.24	0.03	1.07	0.08
		0.43	0.09	0.43	0.06	2.07	0.15
		0.71	0.15	0.71	0.10	4.10	0.27
		1.06	0.21	1.03	0.13	8.11	0.47
		2.08	0.38	2.05	0.25	12.07	0.64
		4.14	0.66	4.08	0.44	16.12	0.78
		8.05	1.04	8.06	0.75	20.24	0.91
		12.05	1.32	12.07	0.99	26.18	1.06
		15.96	1.53	16.11	1.18	35.76	1.27
		19.87	1.70	20.00	1.33		
		25.71	1.91	25.88	1.52		
		35.49	2.16	35.71	1.78		

Table B14. Adsorption isotherm data of CH_4 on UiO–66 derivatives

MOF	Gas	At 294 K		At 317 K		At 356 K	
		P (bar)	Amount adsorbed, N (mol kg^{-1})	P (bar)	Amount adsorbed, N (mol kg^{-1})	P (bar)	Amount adsorbed, N (mol kg^{-1})
UiO–66	CH_4	0.00	0.00	0.00	0.00	0.00	0.00
		0.43	0.17	0.43	0.14	2.08	0.44
		0.70	0.27	0.71	0.21	4.07	0.68
		1.06	0.41	1.02	0.29	8.03	1.09
		2.04	0.73	2.09	0.53	11.96	1.44
		4.01	1.27	4.05	0.91	15.85	1.76
		7.91	2.10	8.05	1.54	19.64	2.04
		11.78	2.74	11.90	2.04	25.41	2.40
		15.57	3.25	15.71	2.46	32.44	2.80
		19.27	3.67	19.47	2.82	45.19	3.36
		24.73	4.18	25.06	3.28	62.06	3.91
		31.13	4.67	31.69	3.75	78.07	4.32
		43.07	5.34	44.05	4.36		
		57.73	5.96	59.72	4.96		
		71.88	6.58	74.69	5.46		
UiO–66–NH_2	CH_4	0.00	0.00	0.00	0.00	0.00	0.00
		0.25	0.13	0.29	0.10	1.02	0.19
		0.43	0.22	0.45	0.15	2.10	0.34
		0.72	0.35	0.70	0.22	4.13	0.59
		1.06	0.49	1.03	0.32	8.10	0.99
		2.07	0.84	2.08	0.57	12.03	1.32
		4.11	1.38	4.09	0.95	15.80	1.59
		7.99	2.14	8.05	1.55	19.76	1.83
		11.81	2.68	11.99	2.01	25.47	2.15
		15.61	3.10	15.73	2.36	33.84	2.52
		19.37	3.44	19.55	2.67	47.97	2.96
		24.71	3.83	25.09	3.04	65.88	3.32
		32.32	4.25	33.03	3.46		
		45.37	4.76	46.63	3.96		
		61.24	5.22	63.43	4.40		
UiO–66–NO_2	CH_4	0.00	0.00	0.00	0.00	0.00	0.00
		0.69	0.25	0.72	0.14	2.08	0.25
		1.06	0.34	1.03	0.20	4.10	0.42
		2.07	0.58	2.11	0.38	8.07	0.69
		4.09	0.94	4.10	0.64	11.97	0.90
		7.98	1.42	8.02	1.02	15.87	1.09
		11.85	1.75	11.92	1.31	19.67	1.26
		15.53	2.01	15.74	1.54	25.35	1.46
		19.37	2.22	19.49	1.74	32.99	1.67
		24.75	2.47	25.09	1.98	45.37	2.09
		31.30	2.71	32.27	2.22	62.40	2.59
		43.18	3.04	44.50	2.55		
		57.93	3.41	59.78	2.95		

Contd. (Adsorption isotherm data of CH_4 on UiO–66 derivatives)

MOF	Gas	At 294 K		At 317 K		At 356 K	
		P (bar)	Amount adsorbed, N (mol kg^{-1})	P (bar)	Amount adsorbed, N (mol kg^{-1})	P (bar)	Amount adsorbed, N (mol kg^{-1})
UiO–66–COOH	CH_4	0.00	0.00	0.00	0.00	0.00	0.00
		0.53	0.26	0.53	0.21	0.53	0.18
		0.72	0.36	0.72	0.31	0.72	0.25
		1.05	0.48	1.05	0.41	1.05	0.38
		2.10	0.91	2.10	0.78	2.10	0.72
		4.09	1.34	4.09	1.20	4.09	1.12
		7.94	1.92	7.94	1.78	7.94	1.58
		11.81	2.27	11.81	2.17	11.81	1.95
		15.58	2.57	15.58	2.41	15.58	2.22
		19.35	2.81	19.35	2.61	19.35	2.40
		24.79	3.02	24.79	2.82	24.79	2.58
		32.54	3.31	32.54	3.01	32.54	2.78
		45.74	3.62	45.74	3.32	45.74	3.05
		61.92	3.97	61.92	3.60	61.92	3.32
UiO–66–$(COOH)_2$	CH_4	0.00	0.00	0.00	0.00	0.00	0.00
		0.24	0.13	0.23	0.08	0.25	0.06
		0.43	0.22	0.43	0.14	0.46	0.09
		0.72	0.36	0.72	0.22	0.71	0.12
		1.06	0.48	1.06	0.31	1.10	0.17
		2.09	0.81	2.08	0.54	2.08	0.30
		4.12	1.24	4.10	0.87	4.09	0.51
		8.00	1.74	8.05	1.32	8.07	0.84
		11.84	2.07	11.92	1.62	12.01	1.09
		15.63	2.32	15.91	1.86	15.95	1.29
		19.32	2.51	19.48	2.02	19.91	1.45
		24.74	2.72	24.95	2.24	25.46	1.65
		32.15	2.94	32.68	2.46	33.36	1.87
		45.58	3.22	46.69	2.75	47.79	2.14
		61.24	3.47	63.43	3.00	65.83	2.39

Table B15. Adsorption isotherm data of N_2 on UiO–66 derivatives

MOF	Gas	At 294 K		At 317 K		At 356 K	
		P (bar)	Amount adsorbed, N (mol kg^{-1})	P (bar)	Amount adsorbed, N (mol kg^{-1})	P (bar)	Amount adsorbed, N (mol kg^{-1})
UiO–66	N_2	0.00	0.00	0.00	0.00	0.00	0.00
		0.70	0.09	0.70	0.07	1.04	0.09
		1.04	0.13	1.03	0.10	2.04	0.14
		2.07	0.25	2.07	0.19	4.08	0.24
		4.05	0.47	4.10	0.35	8.15	0.43
		8.08	0.85	8.07	0.63	12.16	0.60
		12.10	1.17	12.09	0.87	16.16	0.76
		16.04	1.44	16.05	1.09	20.16	0.91
		19.92	1.68	20.05	1.28	26.16	1.11
		25.79	1.99	25.99	1.55	33.49	1.32
		32.74	2.29	33.14	1.82	47.40	1.66
		46.47	2.77	46.94	2.24	66.13	1.99
		64.46	3.24	65.32	2.67	85.21	2.35
		82.38	3.60	84.01	3.00		
UiO–66–NH_2	N_2	0.00	0.00	0.00	0.00	0.00	0.00
		1.03	0.14	1.08	0.13	1.09	0.07
		2.10	0.28	2.05	0.22	2.06	0.12
		4.06	0.50	4.09	0.38	4.09	0.23
		8.04	0.88	8.11	0.67	8.14	0.42
		12.04	1.20	12.09	0.91	12.15	0.58
		16.05	1.46	16.11	1.12	16.07	0.73
		19.99	1.68	20.09	1.31	20.14	0.87
		25.82	1.96	25.99	1.55	26.06	1.06
		34.27	2.29	34.42	1.83	34.99	1.28
		49.36	2.73	49.96	2.17	50.67	1.59
		68.82	3.13	69.79	2.59	70.66	1.89
UiO–66–NO_2	N_2	0.00	0.00	0.00	0.00	0.00	0.00
		0.71	0.07	0.74	0.07	2.07	0.10
		1.03	0.10	1.04	0.09	4.08	0.18
		2.07	0.20	2.09	0.16	8.11	0.31
		4.08	0.36	4.08	0.27	12.14	0.43
		8.10	0.62	8.08	0.47	16.16	0.53
		12.01	0.81	12.09	0.64	20.17	0.62
		16.05	0.99	16.03	0.78	26.10	0.75
		19.94	1.13	20.06	0.90	33.36	0.89
		25.85	1.31	25.90	1.06	47.27	1.11
		33.12	1.49	33.40	1.23	66.33	1.46
		46.34	1.75	47.20	1.47	85.41	1.64
		64.52	2.01	65.45	1.75		
		82.51	2.22	84.20	2.00		

contd. (Adsorption isotherm data of N_2 on UiO–66 derivatives)

MOF	Gas	At 294 K		At 317 K		At 356 K	
		P (bar)	Amount adsorbed, N (mol kg^{-1})	P (bar)	Amount adsorbed, N (mol kg^{-1})	P (bar)	Amount adsorbed, N (mol kg^{-1})
UiO–66–COOH	N_2	0.00	0.00	0.00	0.00	0.00	0.00
		0.23	0.03	0.23	0.03	0.23	0.03
		0.42	0.06	0.42	0.05	0.42	0.05
		0.73	0.11	0.73	0.09	0.73	0.08
		1.05	0.15	1.05	0.13	1.05	0.11
		2.06	0.28	2.06	0.23	2.06	0.20
		4.07	0.50	4.07	0.42	4.07	0.37
		8.12	0.87	8.12	0.65	8.12	0.59
		12.18	1.11	12.18	0.92	12.18	0.78
		16.06	1.35	16.06	1.12	16.06	0.92
		19.98	1.55	19.98	1.26	19.98	1.05
		25.82	1.75	25.82	1.46	25.82	1.21
		34.39	2.00	34.39	1.71	34.39	1.41
		49.55	2.34	49.55	1.99	49.55	1.71
		68.82	2.65	68.82	2.25	68.82	1.95
UiO–66–$(COOH)_2$	N_2	0.00	0.00	0.00	0.00	0.00	0.00
		0.42	0.06	0.78	0.08	0.74	0.05
		0.70	0.11	1.02	0.10	1.02	0.06
		1.09	0.15	2.06	0.18	2.06	0.11
		2.08	0.28	4.08	0.33	4.08	0.20
		4.08	0.50	8.14	0.59	8.12	0.37
		8.06	0.83	12.08	0.78	12.05	0.50
		12.09	1.08	16.01	0.95	16.23	0.63
		16.01	1.28	20.15	1.10	20.15	0.74
		20.17	1.45	25.97	1.27	26.04	0.88
		25.82	1.64	34.10	1.47	34.47	1.04
		33.95	1.85	50.02	1.74	50.40	1.28
		49.30	2.14	69.66	1.98	70.79	1.51
		68.51	2.39				